



Combined EEG and MEG source analysis of epileptiform activity using calibrated realistic finite element head models

Dissertation
Zur Erlangung des akademischen Grades
Doktor-Ingenieur (Dr.-Ing.)

vorgelegt der Fakultät für Informatik und Automatisierung
Technischen Universität Ilmenau

von: Ümit Aydın
geboren am: 03.07.1983 in Bursa, Türkei

Gutachter:

1. Univ.-Prof. Dr.-Ing. habil. Jens Haueisen
2. Prof. Dr. Ceon Ramon
3. PD. Dr. rer. nat. Carsten Hermann Wolters (Betreuer/Doktorvater)

Tag der Einreichung: 12.01.2015

Tag der wissenschaftlichen Aussprache: 24.03.2015

Version 05/11/2015

A problem with the sign (color) of MEG topographies in Figure 6.1 on page 117 is corrected.

Abstract

In this thesis, a new experimental and methodological analysis pipeline for combining the complementary information contained in electroencephalography (EEG) and magnetoencephalography (MEG) is introduced. The forward problem is solved using high resolution finite element head models that are constructed from individual T1 weighted, T2 weighted and diffusion tensor (DT-) MRIs. For this purpose, scalp, skull spongiosa, skull compacta, cerebrospinal fluid, white matter (WM) and gray matter (GM) are segmented and included into the head models. In order to obtain highly accurate source reconstructions, the realistic geometry, tissue conductivity anisotropy (i.e., WM tracts) and individually estimated conductivity values are taken into account. To achieve this goal, the brain anisotropy is modeled using the information obtained from DT-MRI. A main focus is placed on the skull conductivity due to its high inter-individual variance and different sensitivities of EEG and MEG source reconstructions to it. In order to estimate individual skull conductivity values that fit best to the constructed head models, simultaneously acquired somatosensory evoked potential and field data measured for the same individuals are analyzed. As shown in this work, the constructed head models could be used to non-invasively localize interictal spike activity in patients suffering from pharmaco-resistant focal epilepsy with higher reliability. In addition, by using these advanced head models, tissue sensitivities of EEG, MEG and combined EEG/MEG (EMEG) are compared by means of altering the distinguished tissue types and their conductivities. Finally, the effects of spike averaging and signal-to-noise-ratios (SNRs) on source analysis are evaluated by localizing subaverages.

The results obtained in this thesis demonstrate the importance of using anisotropic and skull conductivity calibrated realistic finite element models not only for EEG but also for MEG and EMEG source analysis. By employing such advanced finite element models, it is possible to demonstrate that EMEG achieves accurate source reconstructions at early instants in time (epileptic spike onset), i.e., time points with low SNR, which are not yet subject to propagation and thus supposed to be closer to the origin of the epileptic activity. It is also shown that EMEG is able to reveal the propagation pathway at later time points in agreement with invasive stereo-EEG, while EEG or MEG alone reconstruct only parts of it. Spike averaging and SNR analysis reveal that subaveraging provides important and accurate information about both the center of gravity and the extent of the epileptogenic tissue that neither single nor

grand-averaged spike localizations could supply. Moreover, it is shown that accurate source reconstructions obtained with EMEG can be used to determine a region of interest, and new MRI sequences that acquire high resolution images in this restricted area can detect FCDs that were not detectable with other MRI sequences.

The pipelines proposed in this work are also tested for source analysis of somatosensory and auditory evoked responses measured from healthy subjects and the results are compared with the literature. In addition, the finite element head models are also used to assess the volume conductor effects on simulations of non-invasive brain stimulation techniques such as transcranial direct current and transcranial magnetic stimulation.

Zusammenfassung

In dieser Arbeit wird eine neue Pipeline, welche die komplementären Informationen der Elektroenzephalographie (EEG) und Magnetoenzephalographie (MEG) berücksichtigen kann, vorgestellt und experimentell sowie methodisch analysiert. Um das Vorwärtsproblem zu lösen, wird ein hochrealistisches Finite-Elemente-Kopfmodell aus individuell gemessenen T1-gewichteten, T2-gewichteten und Diffusion-Tensor (DT)-MRIs generiert. Dafür werden die Kompartments Kopfhaut, spongioser Schädel, kompakter Schädel, Liquor Cerebrospinalis (CSF), graue Substanz und weiße Substanz segmentiert und ein individuelles Kopfmodell erstellt. Um eine sehr akkurate Quellenanalyse zu garantieren werden die individuelle Kopfform, die Anisotropie der weißen Substanz und die individuell kalibrierte Schädelleitfähigkeiten berücksichtigt. Die Anisotropie der weißen Substanz wird anhand der gemessenen DT-MRI Daten berechnet und in das segmentierte Kopfmodell integriert. Da sich die Leitfähigkeit des schwach-leitenden Schädels für verschiedene Probanden sehr stark unterscheidet und diese die Ergebnisse der EEG Quellenanalyse stark beeinflusst, wird ein Fokus auf die Untersuchung der Schädelleitfähigkeit gelegt. Um die individuelle Schädelleitfähigkeit möglichst genau zu bestimmen werden simultan gemessene somatosensorische Potentiale und Felder der Probanden verwendet und ein Verfahren zur Kalibrierung der Schädelleitfähigkeit durchgeführt. Wie in dieser Studie gezeigt, können individuell generierte Kopfmodelle dazu verwendet werden um, in einem nicht-invasivem Verfahren, interiktale Aktivität für Patienten, welche an medikamentenresistenter Epilepsie leiden, mit einer sehr hohen Genauigkeit zu detektieren. Außerdem werden diese akkuraten Kopfmodelle dazu verwendet um die unterschiedlichen Sensitivitäten von EEG, MEG und einer kombinierten EEG und MEG (EMEG) Quellenanalyse in Bezug auf verschiedene Gewebeleitfähigkeiten zu untersuchen. Wie in dieser Studie gezeigt wird liefert eine kombinierte EMEG Quellenanalyse zuverlässigere und robustere Ergebnisse für die Lokalisierung epileptischer Aktivität als eine einfache EEG oder MEG Quellenanalyse. Zuletzt werden die Auswirkungen einer Spikemittelung sowie die Effekte verschiedener Signal-Rausch-Verhältnisse (SNRs) anhand verschiedener Teilmittlungen untersucht.

Wie in dieser Arbeit gezeigt wird sind realistische Kopfmodelle mit anisotroper weißer Substanz und kalibrierter Schädelleitfähigkeit nicht nur für die EEG Quellenanalyse, sondern auch für die MEG und EMEG Quellenanalyse vorteilhaft. Durch die

Anwendung dieser akkuraten Kopfmodelle konnte gezeigt werden, dass EMEG Quellenanalyse sehr gute Quellenrekonstruktionen auch schon zu Beginn des epileptischen Spikes liefert, wo nur eine sehr geringe SNR vorhanden ist. Da zu diesem Zeitpunkt noch keine Ausbreitung der epileptischen Aktivität eingesetzt hat ist die Lokalisation von frühen Quellen von besonderer Bedeutung. Während die EMEG Quellenanalyse auch Ausbreitungseffekte für spätere Zeitpunkte genau darstellen kann, können einfache EEG oder MEG Quellenanalysen diese nicht oder nur teilweise darstellen. Die Validierung der Ausbreitung wird anhand eines invasiv gemessenen Stereo-EEG durchgeführt. Durch die durchgeführten Spikemittelungen und die SNR Analyse wird verdeutlicht, dass durch eine Teilmittlung wichtige und exakte Informationen über den Mittelpunkt sowie die Größe des epileptischen Gewebes gewonnen werden können, welche weder durch eine einfachen noch einer "Grand-average" Lokalisation des Spikes erreichbar sind. Eine weitere Anwendung einer genauen EMEG Quellenanalyse ist die Bestimmung einer "region of interest" anhand von standardisierten MRT Messungen. Diese kleinen Gebiete werden dann später mit einer optimalen und höher aufgelösten MRT-Sequenz gemessen. Dank dieses optimierte Verfahren können auch sehr kleine FCDs entdeckt werden, welche auf dem standardisierten gemessenen MRT-Sequenzen nicht erkennbar sind.

Die Pipeline, welche in dieser Arbeit entwickelt wird, kann auch für gesunde Probanden angewendet werden. In einer ersten Studie wird eine Quellenanalyse der somatosensorischen und auditorisch-induzierten Reize durchgeführt. Die gewonnen Daten werden mit anderen Studien vergleichen und mögliche Gemeinsamkeiten diskutiert. Eine weitere Anwendung der realistischen Kopfmodelle ist die Untersuchung von Volumenleitungseffekten in nicht-invasiven Hirnstimulationsmethoden wie transkranielle Gleichstromstimulation und transkranielle Magnetstromstimulation.

Acknowledgement

I would like to show my gratitude to people who supported me during my PhD studies, especially:

- My thesis supervisor PD. Dr. rer. nat. Carsten Wolters for the opportunity to join his group, his valuable advices (both scientific and not-scientific) his professional guidance and supportive attitude.
- Prof. Dr.-Ing. Jens Haueisen for accepting me as a PhD student and his scientific support.
- Prof. Dr. Ceon Ramon for accepting to be a reviewer of this work and his valuable comments on how to improve this work.
- Jun.-Prof. Dr.-Ing. Daniel Baumgarten for accepting to be an examiner in the scientific debate.
- Prof. Dr.-Ing. Christo Pantev for giving me a "home" at the Institute for Biomagnetism and Biosignalanalysis in Münster and for sharing his scientific knowledge.
- My colleagues in the working group "Methods in Bioelectromagnetism" for their precious support, scientific discussions and for their friendly attitude.
- Johannes Vorwerk and Sven Wagner for proofreading the thesis and helping with the German abstract.
- All my colleagues at IBB for a friendly working environment.
- Prof. Dr. med. Dipl.-Phys. Bernd Lütkenhöner for fruitful discussions and his scientific advices regarding the study presented in Chapter 6.
- Karin, Hildegard and Ute for their help with the EEG, MEG, MRI measurements, and Andreas for having the solutions to all technical problems.
- Our project cooperation partners Dr. med. Stefan Rampp, Marcel Heers, Philipp Küpper; Dr. rer. nat. Harald Kugel; Dr. Andreas Galka; Laith Hamid; Dr.-Ing. Matthias Dümpelmann; PD. Dr. med. Christoph Kellinghaus; Prof. Dr. med. Jörg Wellmer and Prof. Dr. med. Hermann Stefan for a very productive collaboration and valuable scientific information exchange.

- My fiancée Agne not only for her support and caring but also for proofreading the thesis.
- My family for their support at all times. "Ayrıca aileme her zaman yanımda olup beni destekledikleri için teşekkür ederim."

Finally, I am grateful to the German Research Foundation (DFG) and PD. Dr. rer. nat. Carsten Wolters for funding this work through the project WO1425/2-1 and the Priority Program 1665 of the DFG (WO1425/5-1).

Contents

Nomenclature	x
1 Introduction	1
1.1 Motivation	1
1.2 Contributions	2
1.3 Scope of the Thesis	4
2 Fundamentals and Theory	6
2.1 Epilepsy	6
2.1.1 Zones in presurgical epilepsy diagnosis	7
2.2 Anatomy and Physiology of the Head and Brain	9
2.3 Electroencephalography and Magnetoencephalography	11
2.3.1 Sensitivity differences between EEG and MEG	13
2.3.2 Forward problem of bioelectromagnetism	15
2.3.2.1 Maxwell's equations and quasi-static assumption	15
2.3.2.2 Literature survey on the tissue sensitivities of EEG and MEG	18
2.3.2.3 Numerical techniques to solve the forward problem of EEG/MEG	20
2.3.3 Inverse problem of bioelectromagnetism	25
2.3.3.1 Combined EEG/MEG source analysis	25
2.3.3.1.1 Calculation of SNRs for whitening	26
2.3.3.1.2 Formulation of combined EEG/MEG (EMEG) problem	26
2.3.3.2 Inverse algorithms	27
2.3.3.2.1 Equivalent dipole approaches	27
2.3.3.2.2 Current density approaches	29
2.3.3.3 Source analysis in presurgical epilepsy diagnosis	30
2.3.3.3.1 Location and extent of the epileptogenic zone	31

2.3.3.3.2	Propagation/SNR balance in source reconstruction of epileptic activity	32
2.4	Magnetic Resonance Imaging	33
3	Study I: Volume Conduction Effects on EEG, MEG and EMEG in Presurgical Epilepsy Diagnosis	36
3.1	Patient and Methods	36
3.1.1	Patient information	36
3.1.2	MRI measurements	37
3.1.3	Post-processing of structural MRIs	38
3.1.4	Generation of the geometry-adapted hexahedral finite element mesh	41
3.1.5	Inclusion of gray and white matter conductivity tensors	42
3.1.6	Effective medium approach	44
3.1.7	Head models used in this study	45
3.1.8	EEG and MEG acquisition and preprocessing	46
3.1.8.1	Somatosensory evoked potentials (SEP) and fields (SEF)	48
3.1.8.2	Spontaneous measurements	49
3.1.9	Marking and clustering of interictal spikes	49
3.1.10	Forward approach	50
3.1.11	Construction of the source space	51
3.1.12	Source reconstruction of interictal spikes	51
3.1.13	Skull conductivity calibration procedure using SEP and SEF data	53
3.2	Results	56
3.2.1	Skull conductivity calibration and source analysis of the somatosensory evoked responses	56
3.2.2	Evaluation of interictal epileptic activity	58
3.2.2.1	Interictal spike marking, clustering and SNR improvement	58
3.2.2.2	Effects of varying skull conductivity on source reconstruction for the epileptic activity	58
3.2.2.3	Effects of six versus three compartment head modeling on EEG and MEG spike source reconstruction	61
3.2.2.4	Comparison of EMEG to single modality EEG or MEG source reconstruction	64
3.3	Discussion	66

4 Study II: Comparison of EEG, MEG and EMEG Localizations of Epileptic Activity at Different Propagation Phases via Sub-Averages	75
4.1 Methods	76
4.1.1 Detection of the epileptic spikes	76
4.1.2 Sub-averaging	76
4.1.3 Source reconstruction procedure	78
4.1.4 Stereo-EEG Measurements	78
4.1.5 Square distance index (SDI)	79
4.2 Results	79
4.2.1 Effects of epileptic spike averaging on source reconstruction . . .	81
4.2.2 Comparison of EEG, MEG and EMEG source reconstructions .	85
4.3 Discussion	94
4.3.1 Comparison of EEG, MEG and EMEG source reconstructions .	94
4.3.1.1 Propagation phenomenon: Problems and opportunities for noninvasive source reconstruction	94
4.3.1.2 EEG, MEG and EMEG source reconstructions at spike onset	96
4.3.1.3 Differences of EEG, MEG and EMEG source recon- structions in revealing the propagation pathway	96
4.3.2 Effects of epileptic spike averaging on source reconstruction . . .	98
4.3.3 Preselection criteria to improve single and sub-averaged spike source reconstructions	99
4.3.4 Estimation of the optimal sub-average number	99
4.3.5 Topology of the irritative zone	100
4.3.6 Relationship between size of dipole scatter, SNR and extent of the irritative zone	101
5 Study III: A Three Step MRI-EMEG-MRI Pipeline in Presurgical Epilepsy Diagnosis.	103
5.1 Methods	103
5.1.1 Simultaneous measurement of EEG/MEG	104
5.1.2 Acquisition of the first set of MRI data	104
5.1.3 Segmentation, head model construction, conductivity calibration and calculation of leadfield matrix	104
5.1.4 Marking of the epileptic spikes and source reconstruction procedure	105
5.1.5 Acquisition of a second set of MRI data	106

5.1.6	DTI tractography	106
5.2	Results and Discussion	106
6	Study IV: EMEG Source Analysis of Evoked Responses with Finite Element Head Models	114
6.1	Subject I: General Properties of Somatosensory and Auditory Evoked Responses	114
6.1.1	Head model	114
6.1.2	Somatosensory evoked potentials and fields	115
6.1.2.1	Stimulus properties, signals and topographies	115
6.1.2.2	EEG, MEG and EMEG source reconstructions for SER	116
6.1.3	Auditory evoked potentials and fields	118
6.1.3.1	Stimulus properties, signals and topographies	119
6.1.3.2	EEG, MEG and EMEG source reconstructions for AER	120
6.1.3.3	Source reconstructions for AERs for different stimulus frequencies	121
6.2	Subject II: Comparison Between the Primary and the Secondary Auditory Cortices	124
6.2.1	Experiment 1: Investigation of the long latency components	125
6.2.1.1	Properties of the stimulus and pre-processing	125
6.2.1.2	Results	125
6.2.1.2.1	Signals and topographies	125
6.2.1.2.2	Source reconstructions	128
6.2.2	Experiment 2: Investigation of the middle latency components	132
6.2.2.1	Properties of the stimulus and pre-processing	132
6.2.2.2	Results	132
6.2.2.2.1	Signals and topographies	132
6.2.2.2.2	Source reconstructions	134
6.2.3	Discussion	136
7	Other Studies: Simulation of Noninvasive Brain Stimulation Techniques with High Resolution Finite Element Head Models	141
7.1	Study I: Investigation of tDCS Volume Conduction Effects in a Highly Realistic Head Model	142
7.1.1	Effects on currents in scalp, skull and CSF	144
7.1.2	Effects on currents inside the brain	147
7.1.3	Conclusion	149

7.2	Study II: Assessing the Efficiency of Six Electrode Setups for Transcranial Direct Current Stimulation	150
7.3	Study III: The Influence of Sulcus Width on Simulated Electric Fields Induced by Transcranial Magnetic Stimulation	153
7.4	Contributions of the Author to the Presented Brain Stimulation Studies	155
8	Summary and Outlook	157
8.1	Summary	157
8.2	Outlook	159
	Bibliography	162
	Scientific Contributions	186
	Erklärung	190

List of Figures

2.1	Mean number of people with epilepsy per 1000 population in WHO regions and in the world	7
2.2	Structure of the brain	11
2.3	Layered structure of visual cortex layers 1 to 6 and the white matter .	12
2.4	EASYCAP EEG cap with 74 equidistant electrode positions (10/10-System)	13
2.5	The schematic representation of the sensors of the MEG system used in this thesis	14
2.6	Illustration of epileptogenic tissue	33
3.1	FDG-PET showing left fronto-temporal hypometabolism	37
3.2	Fiducials on T1 MRI	38
3.3	T1, T2 and the segmented (lower row) MRIs	40
3.4	Head model visualized with SCIRun	41
3.5	Geometry adapted and regular hexahedral meshes	42
3.6	A sample slice from the blip-up data, blip-down data and their difference before and after susceptibility correction	43
3.7	Main fiber directions (largest eigenvalues of diffusion tensors) weighted according to the fractional anisotropy	44
3.8	An example source space with 2 mm resolution limited to gray matter, the dipole scan map obtained for an epileptic spike and the final dipole when only visualizing the dipole that corresponds to the peak of the dipole scan map	52
3.9	Steps of <i>Algorithm 1</i>	54
3.10	RV obtained from <i>Algorithm 2</i> in step 2.d. for different skull conductivity parameters for 6C and 3C head models	57
3.11	The waveform and topography of a representative FT9 spike	59
3.12	Influence of skull conductivity on EEG and MEG localizations	60
3.13	Single spike localizations and corresponding centroid and spread sphere	62

3.14	Comparison of three and six compartment head models	63
3.15	Differences of EEG, MEG and EMEG localizations	64
3.16	Best three DS locations in terms of metrics for an exemplary MEG dipole scan for head model <i>6C_132</i> plotted on T1 MRI	69
4.1	Butterfly plots and topographies of EEG and MEG for the grand-average (average over all 200 single epileptic spikes)	77
4.2	The summary of the sEEG findings for all contacts	80
4.3	Locations of sEEG contacts inside the brain and epileptic activity mea- sured with sEEG and ldEEG	81
4.4	Average SNRs for EEG, MEG and EMEG	83
4.5	Centroid dipoles determined from the dipole scan peaks of EEG, MEG and EMEG for different sub-averages at 23 ms before the EEG spike peak	84
4.6	Peaks of the deviation scans of EEG, MEG and EMEG for different sub-averages	86
4.7	Square distance index and the percentage of dipoles closer than 10 mm for each sEEG contact	88
4.8	Dipole localizations of EEG, MEG and EMEG for sub-averages of 10 .	89
4.9	Average waveform of the spikes measured simultaneously with sEEG and 21 electrodes low density scalp EEG	90
4.10	EEG, MEG and EMEG deviation scan peaks of Av10 for time-points from -33 ms (spike onset) in steps of 10 ms until time-point -3 ms (late propagation phase close to EEG peak)	92
4.11	Square distance indexes and the percentage of dipoles closer than 10 mm for each sEEG contact	93
4.12	SDI values for EEG, MEG and EMEG at -33 ms	95
4.13	An example concave topology for single spike localizations with MEG .	100
5.1	Segmented MRI, T1 MRI, and the source space points shown on T1 MRI	105
5.2	Butterfly plots for MEG and EEG, and topographies of MEG and EEG for the averaged spike at 11 different time instances	108
5.3	Source localizations at -7 ms	109
5.4	Source localizations at -23 ms, slices selected according to the left hemi- spheric activity	110
5.5	Source localizations at -23 ms, slices selected according to the right hemispheric activity	111
5.6	The results of DTI tractography	112

5.7	The EMEG, EEG and MEG localizations at -23 ms and -7 ms	113
6.1	Healthy subject SEP(EEG)/SEF(MEG) butterfly plots and topographies for P14(m) and N20(m) components.	117
6.2	Source reconstructions for the N20(m) component for a healthy subject based on EEG, MEG and EMEG	118
6.3	AEP/AEF signals and topographies for 250 Hz, 1000 Hz, 4000 Hz sinusoidal tones	121
6.4	The EEG, MEG and EMEG source reconstructions for the rising flank of the N100(m) component for the stimulation with 1000 Hz	122
6.5	EMEG source reconstructions for auditory stimulation with sinusoidal tones with 250, 1000 and 4000 Hz	124
6.6	Left ear stimulation: Auditory evoked responses for 800 ms long sine tones	126
6.7	Right ear stimulation: Auditory evoked responses for 800 ms long sine tones	127
6.8	Left ear stimulation: MEG and EEG topographies recorded for 102 ms after 800 ms sine tones	129
6.9	Right ear stimulation: MEG and EEG topographies recorded at 107 ms after 800 ms sine tones.	130
6.10	Left ear stimulation: Auditory evoked responses for 20 ms long sine tones	134
6.11	Right ear stimulation: Auditory evoked responses for 20 ms long sine tones	135
6.12	Left ear stimulation for 20 ms sine tones: MEG and EEG topographies at the peak of the P1b(m) component at 57ms	136
6.13	Right ear stimulation for 20 ms sine tones: MEG and EEG topographies at the peak of the P1b(m) component at 59 ms	137
7.1	Current densities for three, four and five compartment models for a sample slice near auditory cortex	146
7.2	Current densities inside WM and GM	147
7.3	Investigation of the efficiencies of six electrode setups for tDSC	152
7.4	The electric field strengths on the surface of the GM for motor (M1) and occipital (Oz) cortex stimulation simulations with different electrode configurations	154

List of Tables

3.1	Head models used in this chapter	47
3.2	The number of spikes marked by each reviewer	50
3.3	Sensitivity of EEG and MEG spike source reconstruction with regard to skull conductivity	60
3.4	Euclidean distance between the EEG and MEG centroids and the ratio of intersecting spread sphere volumes of EEG and MEG to their union for FT9 and F9 spike clusters and for the different head models	61
3.5	Sensitivity of EEG and MEG spike source reconstruction with regard to three compartment (3C) or six compartment (6C) head modeling . .	63
3.6	Comparison of EEG and MEG spike cluster centroid results with the results of EMEG using the reference head model <i>6C_Cal</i>	65
3.7	Sensitivity of EMEG spike source reconstruction with regard to skull conductivity	66
6.1	Comparison of EEG and MEG source reconstructions of the auditory N100(m) with the results of EMEG for the left and right hemisphere .	122
6.2	The positions of the EMEG dipoles are given for the tested frequencies in the left and right hemisphere	123
6.3	Mean global field powers of sensors for P50(m) and N100(m) components. (800 ms sine tones)	127
6.4	Source localization results for N100(m) and P50(m) components	131
6.5	Mean global field powers of sensors for P30(m) and Pb1(m) components (20 ms sine tones)	133
6.6	Source localization results for P30(m) and Pb1(m) components	138
7.1	Head models used in this study	143
7.2	Conductivities used in this section	151

Nomenclature

AEF	Auditory evoked field
AEP	Auditory evoked potential
AER	Auditory evoked response
AMG-CG	Algebraic MultiGrid preconditioned Conjugate Gradient
BEM	Boundary element method
cGM	Cerebellar gray matter
CSF	Cerebrospinal fluid
CT	Computed tomography
cWM	Cerebellar white matter
DLPFC	Dorsolateral prefrontal cortex
DS	Dipole scan
DT-MRI	Diffusion tensor MRI
DTI	Diffusion tensor imaging
EC	Eddy current
EEG	Electroencephalography
EIT	Electrical impedance tomography
eLORETA	Exact low-resolution brain electromagnetic tomography
EMEG	Combined Electroencephalography/Magnetoencephalography
FCD	Focal cortical dysplasia
FDG-PET	Fluorodeoxyglucose positron emission tomography
FDM	Finite difference method
FE	Finite element
FEM	Finite element method
FLAIR	Fluid-attenuated inversion recovery
fMRI	functional MRI
GABA	Gamma-Aminobutyric acid
GM	Gray matter
GOF	Goodness-of-fit
IFG	Inferior frontal gyrus

ISI	Inter stimulus interval
ldEEG	low density electroencephalography
LES	Left ear stimulation
LH	Left hemisphere
LORETA	Laplacian weighted minimum norm
M1	Primary motor cortex
MEG	Magnetoencephalography
MGFP	Mean global field power
MNE	Minimum norm estimate
MR	Magnetic resonance
MRI	Magnetic resonance imaging
N100	The auditory evoked potential measured at around 100 ms after the stimulus.
N100(m)	The auditory evoked potential and field measured at around 100 ms after the stimulus.
N100m	The auditory evoked field measured at around 100 ms after the stimulus.
N20	The somatosensory evoked potential measured at around 20 ms after the stimulus for median nerve stimulation.
N20(m)	The somatosensory evoked potential and field measured at around 20 ms after the stimulus for median nerve stimulation.
N20m	The somatosensory evoked field measured at around 20 ms after the stimulus for median nerve stimulation.
NAS	Nasion
Oz	Occipital cortex
P14	The somatosensory evoked potential measured at around 14 ms after the stimulus for median nerve stimulation.
P14(m)	The somatosensory evoked potential and field measured at around 14 ms after the stimulus for median nerve stimulation.
P14m	The somatosensory evoked field measured at around 14 ms after the stimulus for median nerve stimulation.
PAL	left preauricular
PAR	right preauricular
PET	Positron emission tomography
RES	Right ear stimulation
RH	Right hemisphere

RV	Residual variance
SDI	Square distance index
sEEG	Stereo electroencephalography
SEF	Somatosensory evoked field
SEP	Somatosensory evoked potential
SER	Somatosensory evoked response
sLORETA	Standardized low resolution brain electromagnetic tomography
SNR	Signal-to-noise-ratio
SOA	Stimulus onset asynchrony
SPECT	Single-photon emission computed tomography
SWARM	sLORETA-weighted accurate minimum-norm
T1 MRI	T1 weighted MRI
T2 MRI	T2 weighted MRI
tACS	Transcranial alternating current stimulation
tDCS	Transcranial direct current stimulation
TMS	Transcranial magnetic stimulation
WHO	World health organization
WM	White Matter

1 Introduction

1.1 Motivation

Epilepsy surgery is often used to treat pharmaco-resistant focal epilepsy and its success depends profoundly on the correct determination of the epileptogenic zone. This zone is defined as the minimum amount of cortex that has to be resected (inactivated or completely disconnected) to produce seizure freedom [1]. This zone is estimated prior to surgery based on information available from initial seizure semiology, lesions in magnetic resonance images (MRI), video and electroencephalography (EEG) long-term monitoring, magnetoencephalography (MEG), single photon emission computed tomography (SPECT), positron emission tomography (PET), and neuropsychological examination. The irritative zone, one of the important zones for locating the epileptogenic zone, is identified by EEG and/or MEG. The irritative zone is defined as the brain area producing synchronous discharges of nerve cell clusters between seizures (interictal). The identification of the irritative zone has not only localizatory, but also prognostic value [2, 3, 4]. Multifocal or contralateral epileptic discharges are correlated to a less favorable postoperative outcome regarding seizure freedom [3]. Although the irritative zone might not always be identical to the epileptogenic zone, it holds important information regarding the location of the epileptogenic zone. An accurate identification of the irritative zone can therefore be of crucial importance.

EEG and MEG have been shown to contain complementary information both in theory and practice. It has, for example, been reported that some epileptic spikes could be recorded only in MEG and not in EEG and vice versa. Because of this complementarity, the combined analysis of EEG and MEG data is of increasing interest for the neuroscientific community in a wide range of applications including presurgical epilepsy diagnosis (by the reconstruction of epilepsy-characteristic electric potentials and magnetic fields), evoked response analysis and connectivity studies [5, 6, 7, 8, 9]. However, the interplay of single modality EEG or MEG and combined EEG/MEG (EMEG) source reconstructions with volume conduction effects using realistic head models has not yet been investigated satisfactorily. It is important to perform these

combined EEG/MEG studies not only for showing the advantages of using EMEG over EEG or MEG, but also disclosing the risks of EMEG and single modality EEG or MEG source reconstructions of interictal epileptic activity and to point out a guideline how to minimize the risks when working with simultaneously acquired data. This study thus contributes to important and long-standing questions on feasibility and accuracy of combined EEG/MEG versus single modality EEG or MEG source reconstruction not only with respect to application in epileptology, but also more generally for neuroscientific studies.

Another important issue in source analysis of epileptic activity is the propagation phenomenon. Epileptic activity should be localized as close as possible to the spike onset to avoid propagation. However, the low signal-to-noise-ratio (SNR) limits the confidence in source reconstructions at these early time instants. Thus, this work aimed to investigate if EMEG could increase the reliability in localizations compared to single modality EEG or MEG at early time instants.

The decision between localizing each single epileptic spike separately and averaging spikes with similar topographies before source reconstruction is another highly disputed issue in presurgical epilepsy diagnosis, and both approaches have their merits and drawbacks. Single spike localizations might be used to estimate the size of the irritative zone [10, 11, 12, 13, 14, 15]. However, these localizations suffer from low SNRs [16, 17, 18]. In contrast, averaging similar spikes might increase the SNR remarkably and, thus, also the reliability of the localizations [16], but information on the extent (size of the irritative zone) might get lost. Therefore, in this study the effects of SNR and averaging on EEG, MEG and EMEG source reconstructions were investigated by calculating multiple subaverages (e.g., instead of averaging all spikes only 10 spikes were averaged). This enabled comparison of the effects of averaging and the resulting SNRs in a step-by-step approach.

1.2 Contributions

One of the main contributions of this thesis is the introduction of a new experimental and methodological source analysis pipeline that benefits from the complimentary information in the combined simultaneously measured EEG and MEG data sets. In this context, conductivity calibrated six compartment high resolution head models of the patients were constructed and the forward problem was solved with finite element method (FEM). The conductivity of the skull was estimated using a calibration method, which relies on the differences in inverse solutions of simultaneously mea-

sured somatosensory evoked potentials and fields (one additional run that precedes the acquisition of multiple runs of epileptic discharges) and to the best of the author's knowledge, this is the first source analysis study for simultaneously measured EEG and MEG of epileptic activity using an individual, conductivity calibrated six compartment high resolution finite element model of the patient's head. This way, the feasibility and reliability of EMEG versus single modality EEG or MEG source reconstructions for localizing interictal epileptic activity and somatosensory evoked responses were studied. Furthermore, the design of this study allowed the investigation of the influence of the number of head tissue compartments (six versus the standard three compartment approach) as well as the effects of conductivities of compartments (individually calibrated versus standard skull conductivity parameters as found in the literature) on the localizations.

Another important contribution was the investigation of the optimal choice of the number of epileptic spikes in averaging to (1) sufficiently reduce the noise bias for an accurate determination of the center of gravity of the epileptic activity and (2) to still get an estimation of the extent of the irritative zone. For this purpose, motivated by the findings of Bast et al. [16] and Wennberg and Cheyne [17] for EEG, and Wennberg and Cheyne [18] for MEG source reconstructions, multiple subaverages were calculated in order to investigate the effects of SNRs and averaging on EEG, MEG and EMEG source reconstructions. The results showed that subaveraging provides important and accurate information about both the center of gravity and the extent of the epileptogenic tissue that neither single nor grand-averaged spike localizations can supply. Moreover, a strategy, which tracks the location changes in centroid dipoles for different subaverages in order to estimate the optimal subaverage number, was tested and confirmed.

The final contribution in presurgical epilepsy diagnosis was the introduction and evaluation of a three step MRI-EMEG source reconstruction-MRI pipeline. In this pipeline accurate source reconstructions obtained with EMEG were used to determine a region of interest (ROI) and a new MRI sequence that benefits from the new advancements in parallel transmit coils in MRI [19] was used to acquire high resolution images (ZOOMit MRI) in the predefined ROI (cubic voxels with 0.5 mm edge length). The ability to restrict the area enabled to reach these high resolutions within reasonable acquisition times with special 3T MRIs. To the best of the authors knowledge, this is the first study that uses this function coupled with source analysis and it might be very relevant in future studies aiming to detect cortical malformations that cannot be seen in lower resolution MRI images.

The head modeling pipeline, proposed in this work, was coupled with the combined information supplied by EMEG and was used to study auditory (AER) and somatosensory (SER) evoked responses that were obtained from two healthy subjects. In this direction, special emphasis was put on the AERs measured from a subject for whom the audiogram, clinical examination and radiologic examination showed no pathology, but the AERs in one hemisphere was mainly silent for components up to 100 ms. To the best of the author's knowledge, this is the first study to show such a case for a subject without any detectable brain lesion or pathology and is an important demonstration of the high variance of the brain activities even within the healthy population.

In addition to the applications in EEG and MEG source analysis, the finite element head models constructed with the pipeline presented here were also used for studying the volume conductor effects in non-invasive brain stimulation techniques such as transcranial direct current stimulation and transcranial magnetic stimulation.

In general, this thesis clearly shows that EEG and MEG are not competing modalities but they complement each other especially in situations with low SNRs, and in particular if they are coupled with individual and advanced head models that consider the different sensitivity profiles of EEG and MEG in a source analysis framework. Furthermore, although the main focus of this thesis was the reconstruction of the epilepsy characteristic signals, the methods and results covered here will be of interest not only to clinical researchers but also to other neuroscientists who perform methodological and experimental research and interested in using the combination of EEG, MEG and MRI.

1.3 Scope of the Thesis

In **Chapter 2** the reader is introduced to the fundamental and theoretical knowledge of the issues covered in this thesis. In the beginning of this chapter, the basics of epilepsy and anatomy of the head and the brain are shortly explained. In the later sections, the EEG/MEG and their sensitivity differences are explained. In the next section, the widely used techniques to solve the forward problem are listed and the steps to obtain the formulation of the Venant finite element approach, based on the general Maxwell's equations, are provided. Following the forward problem, the formulation for signal-to-noise-ratio (SNR) based whitening process is explained and the SNR based EEG/MEG problem is defined. After a short literature survey on some of the most widely known inverse solution algorithms, in the end of the chapter source analysis in presurgical epilepsy is discussed.

Chapter 3 begins with the methods section that explains the head modeling pipeline starting from the raw MRI data, skull conductivity calibration steps, and source reconstruction procedure. Afterwards, in the results and discussion sections, the volume conduction effects in source analysis of epileptic activity and somatosensory evoked responses for EEG, MEG and EMEG are investigated.

Chapter 4 focuses on the ability of EEG, MEG and EMEG to estimate the center and the extent of the irritative zone accurately at different phases of epileptic spikes.

Chapter 5 describes a case study, in which the potential of non-invasive EEG/MEG to measure the signals from the whole head is investigated in order to decide on the pre-surgical operation. Here a new MRI sequence that benefits from a parallel transmit technology is used to obtain high resolution MRI images within a region of interest (ROI). The described approach coupled with source analysis might be very relevant to future studies aiming to detect the cortical malformations that cannot be seen in low resolution MRI images.

Chapter 6 describes the source analysis results obtained with somatosensory (SER) and auditory (AER) evoked responses for two healthy subjects. The study with the first subject demonstrates the common responses in general population and the study with a second subject illustrates the auditory evoked responses in the case of exceptional brain formation.

Chapter 7 is dedicated to the studies of non-invasive brain stimulation techniques such as transcranial direct current stimulation and transcranial magnetic stimulation using finite element head models.

Chapter 8 provides general conclusions and the outlook.

2 Fundamentals and Theory

2.1 Epilepsy

According to the World Health Organization (WHO) epilepsy is one of the most common neurological diseases in the world [20]. As of 2005, there were 8.23 and 8.93 people with epilepsy per 1000 population in Europe and in the world, respectively (Figure 2.1) [20]. The main indication of epilepsy is seizures, but since approximately 10 % of the general population has at least one seizure during the lifetime, the diagnosis of epilepsy requires at least two unprovoked seizures. Until the middle of the 19th century, epilepsy was widely assumed to be a vascular disease, but in 1849 Robert Bentley Todd, who was influenced by Michael Faraday's contemporary work on electromagnetism, came up with a new explanation to epilepsy that is based on the electric theory [21, 22]. Today it is known that epileptic seizures are due to abnormal, synchronous and excessive electrical activity in the brain [22].

The first line treatment of epilepsy is administration of anti-epileptic drugs. Although about 60 % of the patients become seizure free after the treatment with the first drug, the number of recovered epilepsy patients can be increased only up to 70 % with additional medication. Thus, still 30 % remains with uncontrolled seizures and are candidates for the epilepsy surgery [23]. The first epilepsy surgery was performed by William Macewen in 1879 and until the invention of electroencephalography (EEG) in 1929 by Hans Berger, the main source of information for the surgery was the seizure semiology observed by the physician [24, 25, 26]. The seizure semiology, however, cannot be used as a reliable method in the diagnosis of epileptogenic brain areas that are away from the motor areas as in the case of temporal lobe epilepsy. Only after 1951, when 25 patients were operated based on the EEG, EEG has gained a wide acceptance as a powerful diagnostic method for the epilepsy surgery [26, 27]. In recent years, the number of epilepsy surgeries is increasing especially in the developed countries due to the advancements in presurgical epilepsy diagnosis. Despite some studies showing that many patients still do not receive surgical evaluation because of the lack of interdisciplinary teams that include neurologists, neurosurgeons, radiologists and engineers or

mathematicians [20].

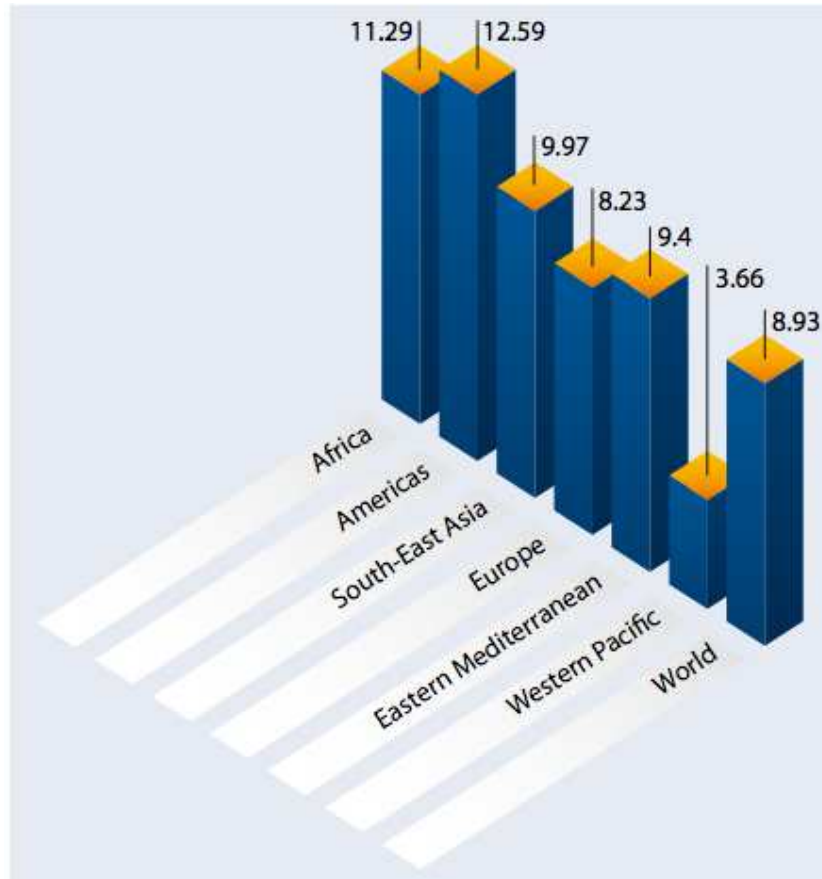


Figure 2.1: Mean number of people with epilepsy per 1000 population in WHO regions and in the world (adapted from [20])

The mechanisms underlying epilepsy are complex and include: (i) changes at the cell membrane (especially ion channels) and neuron, (ii) molecular defects (especially in inherited epilepsy), (iii) abnormalities in neurotransmitter systems (especially gamma-aminobutyric acid (GABA)), (iv) alterations in neuronal architecture or populations, (v) alterations in neuronal networks within cortex or between the cortex and subcortical structures, and (vi) abnormalities in connections between neurons [26].

2.1.1 Zones in presurgical epilepsy diagnosis

There are different zones identified in presurgical evaluation of pharmaco-resistant epilepsy and all of them represent a part of the puzzle that needs to be solved for a seizure free outcome. These zones are:

Epileptogenic zone: This is defined as "the minimum amount of cortex that must

be resected (inactivated or completely disconnected) to produce seizure freedom” [1]. It is the most important zone in presurgical epilepsy due to its definition but it is also only conceptual. All other zones that will later be described are contributing to the determination of this zone.

Seizure onset zone: This zone is defined as the area of cortex from which the seizure activity originates. Even though in many cases this zone gives the most relevant information for obtaining a seizure free outcome, still the removal of just the seizure onset zone might not be sufficient for seizure freedom. This zone is usually determined via invasive and/or non-invasive EEG because, in contrast to magnetoencephalography (MEG) and functional magnetic resonance imaging (fMRI), the electrode positions are fixed to the head, thus not affected by the seizure related movements. Although in some cases, e.g., for patients with focal seizures not involving motor areas, MEG [28] and fMRI [29] can also be used to determine seizure onset zone, their usage is far less common than EEG [30, 31]. In addition, single-photon emission computed tomography (SPECT) is also used in some cases but the need of injection of the radioactive elements just after the start of the seizure and the requirement to bring the patient within one hour to the scanner limit its usage [32].

Irritative zone: Irritative zone is defined as the amount of the cortex that produces synchronous interictal (between the seizures) epileptic activity. It has two main indications. First, it has been shown that the success of the operation for patients with multifocal or contralateral irritative zones is significantly lower than for other patients. Secondly, in cases where the resected area and the irritative zone correspond well the probability of seizure freedom after the surgery is higher than in the cases where only the seizure onset was operated. The irritative zone is usually measured via invasive EEG, non-invasive EEG and MEG, and fMRI [1].

Functional deficit zone: Functional deficit zone is the area of cortex where a functional anomaly is observed. This area is usually larger than the seizure onset and the irritative zone. The hyper- or hypo-activity observed in positron emission tomography (PET) can be used to assess this area [33]. In addition to neuroimaging methods, neuropsychological examinations and seizure semiology are also used for evaluation of this zone.

Lesional zone: Lesional zone is the area where an anatomical anomaly is seen on the cortex. These anomalies might be cortical development problems like focal cortical dysplasia (FCD) and hippocampal atrophy or other lesions caused by trauma or calcification of hippocampus. To detect these regions, usually MRI sequences that are sensitive to lesions like FLAIR (Fluid-attenuated inversion recovery) are used. It

is important to note that for the seizure freedom it might not be needed or sometimes it is not sufficient to resect the whole lesion because usually the seizures start from the borders of the lesion. Moreover, the whole extent of the lesion might not be visible in MRI. Also having a lesion does not always mean that the epileptogenic zone is in this area, but some types of lesions such as FCD type IIB are shown to be highly epileptogenic [34].

All these zones usually intersect with each other but this might not always be the case. For example, for some patients with bi-temporal spikes (with irritative zones in both right and left hemispheres) seizure freedom was achieved after performing operation in just one of the temporal lobes [1]. Also the phenomenon of secondary epileptogenesis has been demonstrated in animals: when seizures are induced to one hemisphere using sub-convulsive electrical stimulation to amygdala or hippocampus after a couple of weeks seizures arising from the contralateral side can be measured [26]. All this data supports the idea of epilepsy as a complicated brain network disease [35, 36], and thus the precise evaluation of these zones in presurgical epilepsy diagnosis has important implications on the success of the surgery.

2.2 Anatomy and Physiology of the Head and Brain

Tissues between electrodes measuring EEG and brain can be roughly divided into three tissue types: scalp, skull and cerebrospinal fluid (CSF).

The outer part of the head is called scalp. The scalp is made up of five layers: skin, cutaneous tissue (fat and connective tissue), aponeurosis (a tough sheet of dense connective tissue), loose areolar tissue (most of the major scalp vessels are situated there) and pericranium (which covers the outside of the skull and supplies nutrition to the bone).

Inside the scalp lies the skull with bony structure. It has a three layer composition with the cancellous bone (skull spongiosa) found between two layers of compact bone (skull compacta) [37].

CSF is found in the subarachnoidal space between the skull and the brain with a volume of approximately 150 milliliters (for the average cerebral cavity volume of ~ 1650 milliliters) [38].

Brain consists of two types of cells: neurons and glial cells. Neurons are responsible for the transmission of the nerve impulses and the main function of glial cells is to support them. A neuron has three parts, which are dendrites, soma and axon. The signals are received from other neurons via dendrites and passed to other neurons via

axons. The soma is the main cell body, which contains the necessary cell structures for protein synthesis and energy production.

Brain is mainly divided into three parts. These are the cerebrum, cerebellum and the brainstem.

The cerebrum is the largest part of the brain and is the most relevant component for presurgical epilepsy diagnosis. It is divided into five lobes: frontal, parietal, temporal, occipital, and limbic lobe (some sources also define insular as a sixth lobe) [39]. It consists of approximately three mm thick gray matter (GM) which surrounds the white matter (WM) except for the limbic system, in which GM structures exist deeply inside the WM. The main functions of these lobes are [40]:

1. The frontal lobe is involved in complicated cognitive tasks such as reasoning, problem solving, decision making and emotions as well as the control of movement (primary motor cortex) and speech (Broca's area).
2. The parietal lobe is associated with somatosensory information (primary somatosensory cortex), integration of auditory visual and somatosensory information and spatial orientation.
3. The temporal lobe is involved in hearing (primary auditory cortex), language comprehension (Wernicke's area in dominant hemisphere) as well as emotion regulation.
4. The occipital lobe differs from other lobes in the sense that it's only main function is controlling the vision processing and this shows the importance of visual processing in humans.
5. Limbic system is mainly related to emotions, learning and memory. It plays an important role in epilepsy since mesio-temporal epilepsy in which the epileptogenic origin is usually within the limbic system (hippocampus and amygdala) accounts for approximately 41 % of adult epilepsies and is the most common one [41].

In the cerebellum, gray matter cortex covers the white matter in a uniform way. However still deep gray matter nuclei also exist inside the white matter. Cerebellum is mainly involved in coordination of movements.

The brain stem connects the brain to other parts of the body and regulates crucial functions such as heart rate, blood pressure, body temperature, breathing, hunger and thirst.

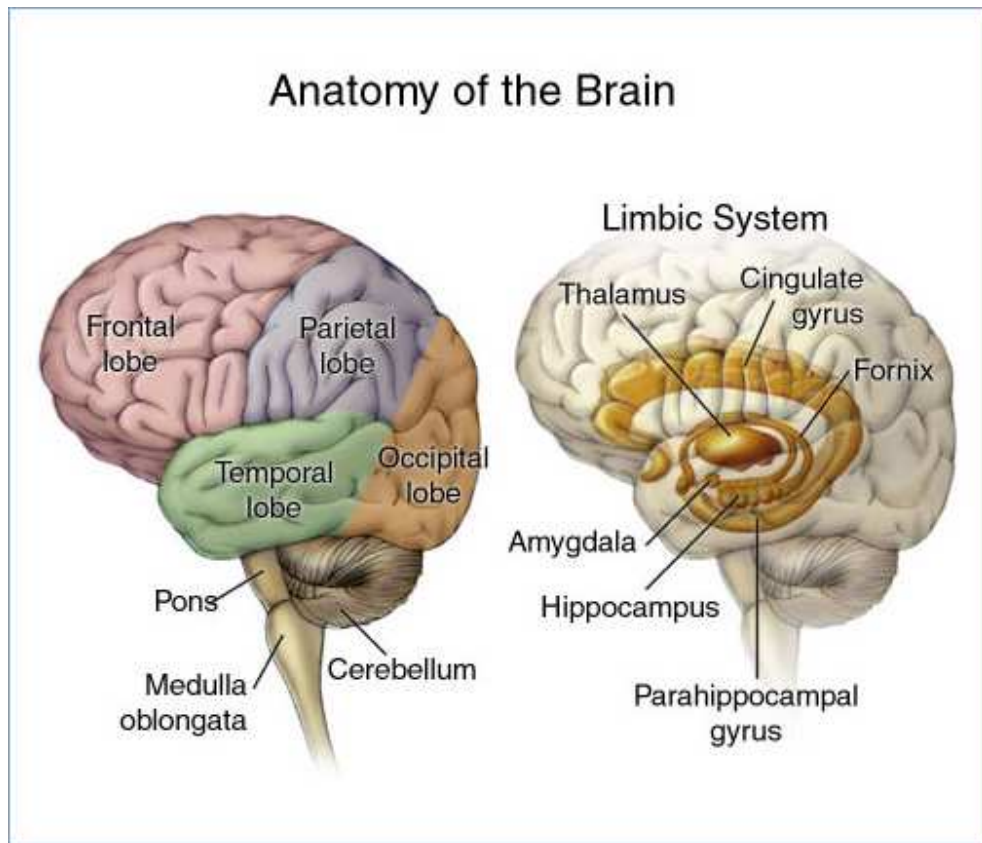


Figure 2.2: Structure of the brain. (adapted from wikicommons).

2.3 Electroencephalography and Magnetoencephalography

EEG and MEG are two widely used techniques to measure the electrical activity of the brain. In surface EEG electrodes pasted to the scalp are used to measure the electrical activity (see Figure 2.4 for the schematic representation of the electrode cap used in this thesis). In contrast to EEG, in MEG there is no direct contact between the scalp and the superconducting quantum interference devices (squid), which reside inside the Dewar flask filled with liquid helium [42] (see Figure 2.5 for the illustration of the MEG sensors used in this thesis). The main advantage of EEG and MEG over other functional neuroimaging methods like fMRI or PET is their high temporal resolution in the range of milliseconds (ms) and their ability to measure the electrical activity directly without using indirect phenomena like hemodynamics or metabolism. However, their spatial resolution is usually lower than fMRI and their sensitivities decrease for sources that are far away from the sensors (e.g., sources in deep structures)

[43]. The EEG and MEG signals are produced by the pyramidal cells (see layers II, III and V in Figure 2.3) that are perpendicular to the cortex surfaces [42, 44, 45]. It is usually regarded that the sources generated by the cortex should be on the order of 10 nAm to produce signals measurable by EEG or MEG [42]. According to the calculations in [45] this corresponds to 50,000 cells. The electrical activity measured with EEG and MEG is due to movement of the ions when the neuron is excited. This electrical activity of a neuron includes two phenomena: action potentials and post-synaptic potentials. With noninvasive EEG and MEG mainly the contributions of the post-synaptic currents are measured because unlike action potentials, which occur very fast and have a quadrupole term, the postsynaptic currents are slower. This slower current increases the chances of a synchronized activity that results in signals that are measurable from far field.

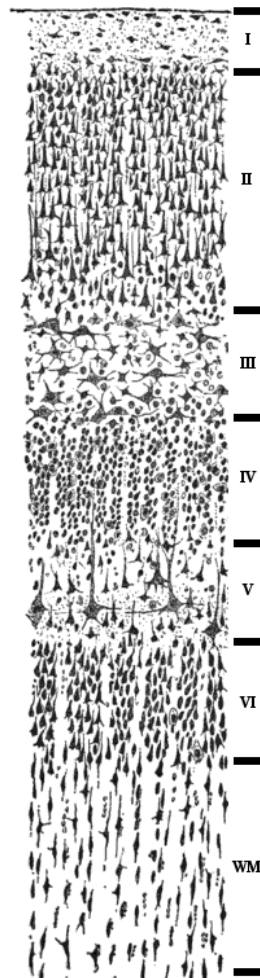


Figure 2.3: Layered structure of visual cortex layers 1 to 6 and the white matter (WM). (adapted from wikicommons).

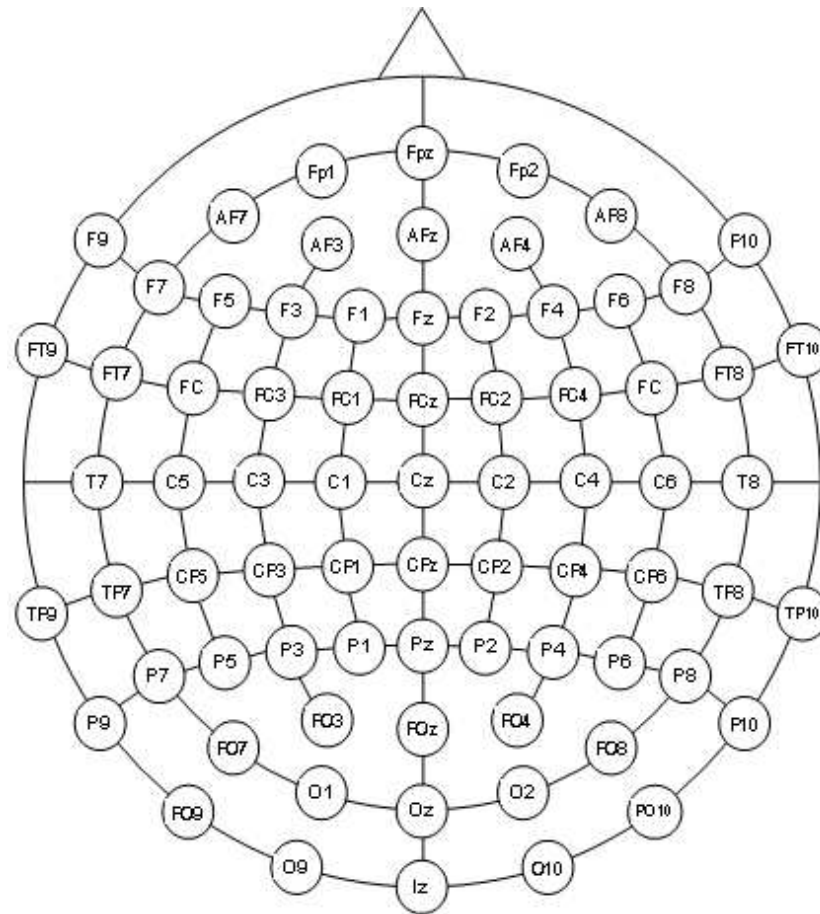


Figure 2.4: EASYCAP EEG cap with 74 equidistant electrode positions (10/10-System). (adapted from www.easycap.de).

2.3.1 Sensitivity differences between EEG and MEG

Although the sources that produce EEG and MEG recordings are the same, the distinct properties of EEG and MEG cause them to produce different sensor signals. Unlike MEG, which measures almost only quasi-tangential sources, EEG can measure both quasi-tangential and quasi-radial sources [6, 42, 46, 47, 48, 49, 50, 51]. When compared to the EEG, MEG is thus less sensitive to all deeper sources, not only because the signal decays with the square of the distance from the source to the measurement sensors (MEG shares this drawback with the EEG), but also because deeper sources become more quasi-radial. In contrast to EEG, MEG achieves higher SNRs (signal-to-noise-ratios) for more lateral quasi-tangential sources, also because the measured signals are nearly not contaminated with mainly quasi-radial biological noise [52]. The signal topographies of EEG and MEG are almost orthogonal to each other, and because the low skull conductivity smears out the EEG, the distance between the poles of dipolar

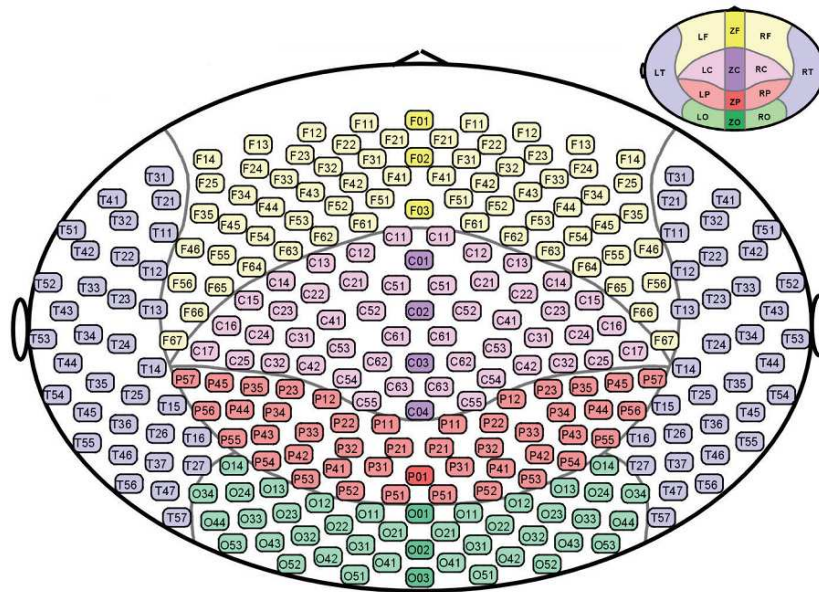


Figure 2.5: The schematic representation of the sensors of the MEG system used in this thesis. Each sensor is named with 5 digits and the first is always M for MEG. The small figure on the upper right corner shows the second and the third digits and the bigger figure shows the last three digits of the sensor name. (adapted from the user manual of CTF, VSM MedTech Ltd.).

EEG topographies is in practice greater than for MEG. Therefore, the simultaneous acquisition of EEG and MEG increases the probability of measuring the important aspects of the signal topographies by at least one of the two modalities, thus stabilizing the source reconstructions.

With regard to the detection of epileptic discharges, studies that show patients with detectable epileptic activity only in EEG or MEG illustrate the importance of simultaneous measurements for epileptic spike detection [53, 54, 55]. In [54] 19 % of the epileptic spikes was only detectable with MEG while 2 % was detectable only with EEG. In a similar study it was found that 13 % of the epileptic spikes was detectable only with MEG while 2 % was detectable only with EEG [55]. The percentage of spikes that was detectable with both EEG and MEG was 72 % in [54] and 59 % in [55]. In frontal lobe epilepsy it was reported that MEG was more successful for screening and localizing than EEG [56].

2.3.2 Forward problem of bioelectromagnetism

2.3.2.1 Maxwell's equations and quasi-static assumption

The forward problem of EEG or MEG is the calculation of the electric potentials at the head surface or the magnetic fields at a small distance to the head surface for a given current source in the brain. The Maxwell's equations form the basis of electromagnetism and thus the forward problem of bioelectromagnetism:

$$\nabla \times \mathbf{E} = -\frac{\partial \mathbf{B}}{\partial t} \quad (2.1)$$

$$\nabla \times \mathbf{H} = \mathbf{J} + \frac{\partial \mathbf{D}}{\partial t} \quad (2.2)$$

$$\nabla \cdot \mathbf{B} = 0 \quad (2.3)$$

$$\nabla \cdot \mathbf{D} = \rho \quad (2.4)$$

with:

E: Electric field (volt per meter (V/m))

H: Magnetic field (ampere per meter (A/m))

B: Magnetic flux density ($T = kg/(s^2A)$)

D: Electric displacement field (C/m^2)

J: Current density (A/m^2)

ρ : Volume charge density (C/m^3)

with units: V =volt, m =meter, A =ampere, T =tesla, kg =kilogram, s =second, C =coulomb.

The material equations listed below supplement Maxwell's equations :

$$\mathbf{D} = \epsilon \mathbf{E} \quad (2.5)$$

$$\mathbf{B} = \mu \mathbf{H} \quad (2.6)$$

where ϵ (F/m) is the permittivity and μ (H/m) is the permeability.

The properties at the interfaces of different media are given by the boundary conditions:

$$\mathbf{n} \times (\mathbf{E}_2 - \mathbf{E}_1) = 0 \quad (2.7)$$

$$\mathbf{n} \times (\mathbf{H}_2 - \mathbf{H}_1) = 0 \quad (2.8)$$

$$(\mathbf{D}_2 - \mathbf{D}_1) \cdot \mathbf{n} = \rho_s \quad (2.9)$$

$$(\mathbf{J}_2 - \mathbf{J}_1) \cdot \mathbf{n} = -\frac{\partial \rho_s}{\partial t} \quad (2.10)$$

with ρ_s representing the surface charge density at the interface and \mathbf{n} being the normal direction from material 1 to 2. The equations 2.7, 2.8 indicate the continuity in the tangential direction and 2.9, 2.10 represent the discontinuity in the medium.

For EEG/MEG forward problem the quasi-static approximation of the Maxwell's equations are used. Quasi-static approximation refers to treating the electrical and magnetic fields as in steady-state for any time instant, which means neglecting the secondary effects of the time variation. In order to use the quasi-static approximation for Maxwell's equations, four assumptions should be satisfied (detailed derivations can be found in [57]):

1. **Capacitive effects:** The fields are assumed to be in synchrony in the quasi-static assumptions and this can only be satisfied if the medium is purely resistive. Considering the electrical properties of biological materials for frequencies below 1 kHz the capacitive effects are very small and thus negligible.
2. **Propagation effects:** The propagation effects should be in a negligible range to satisfy the quasi-static approximation because this determines the time required for the phase changes in the source to be observed in the field point. Since biological materials are non-magnetic and the frequencies are below 1 kHz, the phase delay is negligible and thus this condition is satisfied.
3. **Inductive effects:** The inductive effects are crucial because they represent the amount of electric field that arises from the magnetic induction. As for the propagation effects it is shown that due to non-magnetic behavior and frequencies below 1 kHz for biological materials the inductive effects are also very small and can be ignored.
4. **Boundary conditions:** Boundary conditions are satisfied because for frequencies below 1 kHz the displacement currents ($\partial \mathbf{D} / \partial t$) can be ignored.

After showing that the quasi-static assumption is valid for biological tissues, Maxwell's

equations reduce to:

$$\nabla \times \mathbf{E} = 0 \quad (2.11)$$

$$\nabla \times \mathbf{H} = \mathbf{J} \quad (2.12)$$

$$\nabla \cdot \mathbf{B} = 0 \quad (2.13)$$

$$\nabla \cdot \mathbf{D} = \rho \quad (2.14)$$

The electric field can thus be represented by a potential (u):

$$\mathbf{E} = -\nabla u \quad (2.15)$$

In the case of the EEG/MEG forward problem, the total current density \mathbf{J} can be assumed to be composed of conduction current density $\sigma\mathbf{E}$ and impressed (source) current density J_s

$$\mathbf{J} = \sigma\mathbf{E} + J_s \quad (2.16)$$

and 2.16 becomes the Poisson equation for the electric potential in the head domain Ω :

$$\nabla \cdot (\sigma \nabla u) = -\nabla \cdot \mathbf{J}_s \quad (2.17)$$

with boundary condition

$$\mathbf{n} \cdot (\sigma \cdot \nabla u) = 0 \quad \text{on} \quad \Gamma = \partial\Omega. \quad (2.18)$$

The Poisson equation for the magnetic field can be obtained by substituting the magnetic field (\mathbf{B}), which is equal to $\mu\mathbf{H}$, with the curl of the magnetic potential (\mathbf{A}) in equation 2.12:

$$\nabla^2 \mathbf{A} = -\mu\mathbf{J} \quad (2.19)$$

This leads to the representation:

$$\mathbf{A}(\mathbf{x}) = \frac{\mu}{4\pi} \int_{\Omega} \frac{\mathbf{J}_s(\mathbf{x}') - \sigma(\mathbf{x}') \nabla u(\mathbf{x}')}{|\mathbf{x} - \mathbf{x}'|} d\mathbf{x}' \quad (2.20)$$

A widely used concept in EEG/MEG forward problem is to represent the source with the mathematical point dipole. The mathematical point dipole can be represented as:

$$\mathbf{J}_s(\mathbf{x}) = \mathbf{m}_0 \delta(\mathbf{x} - \mathbf{x}_0) \quad (2.21)$$

where \mathbf{m}_0 is the dipole moment, \mathbf{x}_0 is the dipole position and δ is the Dirac delta distribution.

Using Stokes theorem the magnetic flux Ψ measured with a magnetometer with surface area S and circumference l can be written as:

$$\Psi = \int_S \mathbf{B} dS = \oint_l \mathbf{A}(\mathbf{x}) d\mathbf{x} \quad (2.22)$$

$$\Psi = \underbrace{\frac{\mu}{4\pi} \oint_l \int_{\Omega} \frac{\mathbf{J}_s(\mathbf{x}')}{|\mathbf{x} - \mathbf{x}'|} d\mathbf{x}' \cdot d\mathbf{x}}_{\text{primary magnetic flux}} + \underbrace{\frac{\mu}{4\pi} \oint_l \int_{\Omega} \frac{-\sigma(\mathbf{x}') \nabla u(\mathbf{x}')}{|\mathbf{x} - \mathbf{x}'|} d\mathbf{x}' \cdot d\mathbf{x}}_{\text{secondary magnetic flux}} \quad (2.23)$$

2.3.2.2 Literature survey on the tissue sensitivities of EEG and MEG

The existence and uniqueness of the solution for dipole sources can be proven for the EEG/MEG forward problem [58, 59]. Still in order to solve the forward problem as formulated above a decent head volume conductor model that specifies different tissues is needed and its accuracy is very crucial for noninvasive EEG and MEG source reconstruction. EEG and MEG have different sensitivities to different tissues in the volume conductor. Since EEG is sensitive to volume currents on the scalp, modeling all tissues between the measurement electrodes and the sources inside the brain is very important. In contrast to EEG, MEG is mainly sensitive to the currents inside the inner skull surface (as long as the skull compartment is closed) that do not reach scalp thus it is less sensitive to wrong assumptions on skull and scalp compartments. In the remainder of this section, the sensitivities of EEG and MEG to different tissues in the volume conductor model will be discussed.

Skull: Skull can be assumed as the most important compartment for EEG source analysis. Due to its low conductivity, it smoothens and attenuates the EEG signals before they reach the electrodes on the scalp. Most studies approximate skull as a closed surface but in reality it has holes which might induce errors especially in the close vicinity if not modeled [60, 61]. The skull structure of infants differs significantly from adults, and in these cases, the fontanels should also be included into the model [62]. Although computed tomography (CT) is a more appropriate method to segment the skull than MRI, due to radiation risks its usage for only this purpose is not justified. Even when CT is measured for other purposes (e.g., for localizing the invasive electrodes) not whole but only parts of the head are measured in order to limit the radiation exposure of the patient. The human skull has a three-layer structure, where the relatively high conductive skull spongiosa tissue is found between two layers of low

conductive skull compacta. In EEG source analysis and tDCS (transcranial direct-current stimulation) studies this three layer structure is shown to have an influence on the results [63, 64, 65, 66, 67, 68, 69]. In earlier studies the three layer skull structure was included into the head models by modeling the skull as anisotropic because of the difficulties related to the segmentation of these thin layers from low resolution MRI and because of the limited computational resources that limited the element resolution in the skull compartment [51, 64, 65, 70]. Nowadays most advanced studies use T2 weighted images with higher resolutions (~ 1 mm) whereby it is possible to differentiate skull spongiosa and compacta. The advancements in MRI technology enabled researchers to model the anatomy of the skull more accurately, however for an accurate head model not only the anatomical but also the conductivity information of the tissues is needed. In addition to that, it has been shown that the skull conductivity values show a very high inter-individual variation and for EEG source reconstruction mislocalizations in centimeter range might occur [68, 71]. Although different approaches have been suggested to estimate the skull conductivity such as electrical impedance tomography (EIT) or MR-EIT, the need for injecting current inside the scalp and the need for additional equipment limited their usage so far. In contrast, the effects of skull conductivity on magnetic fields are almost negligible. Thus, EEG is shown to be very sensitive to conductivities of the skull whereas MEG is not very sensitive to it [42, 50, 51, 62, 63, 64, 72, 73, 74]. In addition to the EEG forward and inverse problem, correct modeling of the anatomy and the conductivity of the skull is also important in combined EEG/MEG (EMEG) source analysis. Therefore, inspired by the studies of [62, 75, 76] the calibration of the conductivity of the skull is performed noninvasively by benefiting from the sensitivity differences of EEG and MEG in this thesis.

Cerebrospinal fluid (CSF): Most EEG/MEG source reconstruction studies use three compartment head models that distinguish inner skull, outer skull and the scalp surfaces. Three compartment head models constructed from individual MRIs are shown to increase the accuracies in comparison to multi-sphere models especially for sources located in temporal lobes, where the spherical assumption is far from reality. However, these models still exclude the significant influence of the highly conductive CSF compartment inside the skull. Its conductivity does not show high inter-individual differences and was measured to be 1.79 S/m, averaged over 7 subjects ranging in age from 4.5 months to 70 years, with a standard deviation of less than 2.4 % between subjects and for frequencies between 10 and 10,000 Hz [77]. The stable conductivity of the CSF compartment reduces the modeling problem to just segmenting its complicated geometry. In T1 weighted MRI it is not possible to distinguish CSF from the skull or

the holes (i.e., sinus cavities) but in order to overcome this problem usually T2 weighted MRI, in which CSF appears as white, is used. Another important reason for including the CSF into volume conductor models is the fact that unlike skull, which has far lower influence on MEG than EEG or EMEG, the changes in CSF compartment have a high impact on all three methods (EEG, MEG and EMEG) [50, 51, 70, 74, 77, 78, 79]. As an example in [80] it was shown that when the lying position of the subject is changed from prone to supine, the CSF thickness decreases by approximately 30 % and this causes the occipital signal power measured by EEG to increase on average 80 %.

White and Gray Matter: Another simplification of three compartment models is ignoring the distinction between white and gray matter and representing them and CSF as a single homogeneous compartment with an isotropic conductivity of 0.33 S/m. Recent studies using the finite element method (FEM) showed that the distinction of white and gray matter with their individual conductivities (WM (0.14 S/m) and GM (0.33 S/m)) is important [50, 81]. Furthermore, the main sources measured with EEG or MEG are known to reside within the GM but not in the WM and thus the GM can be used to limit the source space of the model [42, 45].

Conductivity anisotropy of WM and GM: Both gray and white matter have anisotropic conductivities. This anisotropy can be very high especially at pyramidal tracts inside the WM. Previous studies investigated the impact of anisotropic conductivities on EEG/MEG source analysis and found non-negligible effects especially for deeper sources [51, 65, 82, 83, 84, 85]. Earlier studies used a fixed ratio for parallel and orthogonal directions to the fibers, but now with the advancements in diffusion tensor imaging and after the introduction of the relationship between diffusion and conductivity tensors [86], newer studies use the eigenvalues of the diffusion tensors for this purpose [70]. The GM anisotropy is considerably lower in comparison to WM and its measurement with 3T scanners (accurate measurements with 7T scanners were described in the literature [87]) might be prone to errors especially due to partial volume effects of CSF compartments. In this thesis, the gray matter anisotropy was included to the model described in the Section 3 and based on the findings of performed investigations it was decided to include only WM anisotropy for other studies described in this work.

2.3.2.3 Numerical techniques to solve the forward problem of EEG/MEG

Once a decent volume conductor that considers the sensitivity differences explained in the previous section is constructed, the forward solution can be calculated. Although analytical solutions exist for certain geometries as in the case of multisphere models

[88], for realistically shaped head models numerical techniques are needed. The most widely used techniques in EEG/MEG forward solution are boundary element method (BEM), finite element method (FEM) and finite difference method (FDM) [59, 89, 90]. In this section FEM and BEM will be compared and information on FDM can be found in [73] and [89].

In BEM the forward problem is reformulated to a boundary integral equation. This means that, under the assumption of homogeneous and isotropic tissue compartments, modeling and triangulation of just the tissue surfaces is sufficient to calculate the solution [91]. In the EEG/MEG forward problem, these surfaces are usually modeled as scalp, inner skull and outer skull. Since the elements are only placed on the surfaces, the matrices that need to be solved have smaller dimensions in comparison to FEM. However, these matrices are not sparse and their inversion is computationally expensive, especially for more complex geometries (the increase of the computational costs is not linear [90]). The minimum distance of the sources to the boundaries (widely accepted as at least half the triangle side length) and the resolution of boundary discretization also need to be selected carefully to avoid numerical instabilities [92].

Unlike in BEM, in FEM 3D elements such as hexahedra or tetrahedra are used to model the head volume. The advantage of hexahedra is that it is easier and faster to obtain the mesh out of the labeled MRI. For hexahedral meshes, the voxels in the labeled volume can be directly converted to mesh elements, in contrast to tetrahedral meshes, for which this direct conversion is not possible (i.e., hexahedra are divided into tetrahedra or the non-intersecting surfaces are extracted and used for meshing). Usage of hexahedral meshes was shown to result in not smooth and less-realistic edges, which are known as staircase effects. This disadvantage can be largely compensated by shifting the nodes to the material interfaces [93]. This approach was validated for EEG source analysis in multi-layer sphere models, leading to significant error reductions compared to regular hexahedral approaches [94]. It was also shown in this study that the numerical errors introduced due to the deformed node-shifted elements are smaller than the improvements due to higher conformance to the real geometry achieved by geometry adaptation.

Another important decision that has to be made in FEM is choosing a proper method to treat the singularity introduced by the mathematical dipole. Proposed approaches are the partial integration direct potential approach, the subtraction approach and the Venant direct approach [59, 90]. In this thesis the Venant approach was used due to its high accuracy and computational efficiency as shown in [81]. In FEM the need for modeling the whole volume results in increased number of elements (e.g., 100 times

more elements than in BEM) but the matrices are sparse and by using this property the computational costs can be reduced significantly [59, 90]. The computational costs increase almost linearly with the number of elements and using efficient solvers like parallel algebraic multigrid solvers [95] and especially fast FEM transfer matrix approaches [96], it is possible to solve the EEG/MEG forward problem with millions of elements in a reasonable time as also shown in this thesis.

The FEM was selected for numerical solution of EEG and MEG forward problem mainly for two reasons.

1. The anisotropic regions like the pyramidal tracts in white matter can be modeled using FEM.
2. The computational costs of BEM increases significantly when the head model has more than three compartments. Especially because of the complex geometry of CSF and the skull spongiosa, it is very computationally expensive to add and solve these head compartments with BEM.

In the remainder of this section the finite element method formulation will be derived following [59].

The first step is to obtain the weak formulation. For this purpose equation 2.17 is multiplied by a piecewise differentiable function $h(\mathbf{x})$ (basis function) and integrated over the conductor volume V .

$$\iiint_V (\nabla \cdot \mathbf{J}_s) h(\mathbf{x}) d\mathbf{x} = \iiint_V (\nabla \cdot (\sigma \cdot \nabla u)) h(\mathbf{x}) d\mathbf{x} \quad (2.24)$$

After performing integration by parts on the right hand side and exploiting the boundary condition given in equation 2.18, equation 2.24 reduces to

$$\iiint_V (\nabla \cdot \mathbf{J}_s) h(\mathbf{x}) d\mathbf{x} = - \iiint_V (\sigma \cdot \nabla u) \cdot \nabla h(\mathbf{x}) d\mathbf{x} \quad (2.25)$$

Using the approximation:

$$u(\mathbf{x}) \approx \sum_{n=1}^N u_n h_n(\mathbf{x}) \quad (2.26)$$

in equation 2.25 the problem takes the form in equation 2.27.

$$-\sum_{n=1}^N u_n \iiint_V (\sigma \nabla h_n(\mathbf{x})) \cdot \nabla h_m(\mathbf{x}) d\mathbf{x} = \iiint_V \nabla \cdot \mathbf{J}_s h_m(\mathbf{x}) d\mathbf{x} \quad \text{for } m = 1, \dots, N \quad (2.27)$$

Then this equation is arranged as a matrix equation

$$\mathbf{A}\mathbf{u} = \mathbf{b} \quad (2.28)$$

where

$$A_{mn} = - \iiint_V (\sigma \nabla h_n(\mathbf{x})) \cdot \nabla h_m(\mathbf{x}) d\mathbf{x} \quad (2.29)$$

$$b_m = \iiint_V \nabla \cdot \mathbf{J}_s h_m(\mathbf{x}) d\mathbf{x} \quad (2.30)$$

The flux in MEG sensor i ($\psi_M(\mathbf{x}_i)$) can be written as the sum of primary dipolar and secondary source fluxes

$$\psi_M(\mathbf{x}_i) = \Psi_{prim}(\mathbf{x}_i) + \Psi_{sec}(\mathbf{x}_i) = \oint_{\Gamma_i} \mathbf{A}_\infty(\mathbf{x}) \cdot d\boldsymbol{\sigma} - \iiint_\Omega (\boldsymbol{\sigma} \nabla' u(\mathbf{x}')) \mathbf{c}_i(\mathbf{x}') d\mathbf{x}' \quad (2.31)$$

where Γ_i is the loop of the i 'th sensor, $\mathbf{c}_i(\mathbf{x}')$ is

$$\mathbf{c}_i(\mathbf{x}') \equiv \frac{\mu_0}{4\pi} \oint_{\Gamma_i} \frac{1}{|\mathbf{x} - \mathbf{x}'|} d\boldsymbol{\sigma} \quad (2.32)$$

and $\mathbf{A}_\infty(\mathbf{x})$ (the vector potential in an infinite medium with homogeneous conductivity) is

$$\mathbf{A}_\infty(\mathbf{x}) = \frac{\mu}{4\pi} \frac{\mathbf{m}_0}{|\mathbf{x} - \mathbf{x}_0|} \quad (2.33)$$

For the magnetic field, the primary flux in equation 2.31 can be calculated using $\mathbf{A}_\infty(\mathbf{x})$ (equation 2.33).

The secondary flux (Ψ_{sec}) shown in equation 2.31 is arranged in a matrix-vector product form as

$$\Psi_{sec} = \mathbf{S}\mathbf{u} \quad (2.34)$$

When I_{MEG} is assumed as the number of sensors, the elements of \mathbf{S} are written as

$$\mathbf{S}_{in} = - \iiint_{\Omega} (\boldsymbol{\sigma} \nabla' \mathbf{h}_n(\mathbf{x}')) \mathbf{c}_i(\mathbf{x}') d\mathbf{x}' \quad i = 1, \dots, I_{MEG}; n = 1, \dots, N \quad (2.35)$$

In this thesis we used the Venant approach, in which the mathematical dipole is approximated by distribution of monopolar sources and sinks on the FE mesh node closest to the source position and the $C - 1$ neighboring FE mesh nodes [94]. Therefore, the right-hand side vector J^{Venant} has only C nonzero entries at the neighboring FE nodes to the considered dipole location.

$$\mathbf{J}_i^{\text{Venant}} = \begin{cases} \mathbf{j}_c^l & \text{if } \exists c \in \{1, \dots, C\} : i = \text{GLOB}(c) \\ 0 & \text{otherwise} \end{cases} \quad (2.36)$$

In equation 2.36 \mathbf{j}^l is a monopolar source vector with entries \mathbf{j}_c^l at the location x_l . For a source at location x_l , the function *GLOB* determines the global index i to each of the local indices c .

Since for the inverse solution we are only interested in values of the potential at the electrode positions, one can compute transfer matrices that map right-hand side entries \mathbf{b} in equation 2.28 directly to EEG or MEG sensor values. This can be done efficiently by introducing restriction matrices \mathbf{R} $(I_{EEG} - 1) \times N$ and \mathbf{S} $(I_{MEG}) \times N$ with N being the number of nodes used in the inverse solution (source space points) [96, 97, 98]. This way the transfer matrices for EEG and MEG can be written as

$$\mathbf{T}_{EEG} = \mathbf{R}\mathbf{A}^{-1} \quad (2.37)$$

$$\mathbf{T}_{MEG} = \mathbf{S}\mathbf{A}^{-1} \quad (2.38)$$

Thus the direct mapping of \mathbf{b} to the unknowns \mathbf{u} takes the form in equation 2.37 for EEG and equation 2.38 for MEG secondary flux.

$$\mathbf{R}\mathbf{A}^{-1}\mathbf{b} = \mathbf{R}\mathbf{u} \quad (2.39)$$

$$\mathbf{S}\mathbf{A}^{-1}\mathbf{b} = \mathbf{S}\mathbf{u} \quad (2.40)$$

Finally in order to avoid calculating \mathbf{A}^{-1} , which will no longer be sparse after inversion, equations 2.37 and 2.38 can be multiplied with \mathbf{A} from the right side, transposed and the resulting sparse problem can be solved with iterative methods.

Due to fast computation times achieved in [95] we used an algebraic multigrid precon-

ditioned conjugate gradient (AMG-CG) method to solve the linear equation systems in FEM.

2.3.3 Inverse problem of bioelectromagnetism

Since some decades efforts have been made to reconstruct the electrical activity in the human brain that is underlying the measured EEG and/or MEG signals. The reconstruction of the so-called primary currents is called the inverse problem of EEG/MEG. The solution of this problem usually requires estimating the source parameters, calculating the sensor signals these source estimates can produce (solving the forward problem), and minimizing the residual between measured and estimated signals. As a model for the primary current, most of the studies use the mathematical current dipole model, although multipoles have also been studied [99]. Due to the limited number of sensors (in this thesis, 275 for MEG and 80 for EEG) and especially because a 3D reconstruction is aimed from 2D measurements, the inverse problem of EEG/MEG is non-unique. It means that there is an infinite number of source configurations that can produce the same EEG/MEG measurements [42]. This non-uniqueness leads to a variety of inverse reconstruction algorithms that are based on different a priori assumptions. The relationship between EEG and MEG measurements and the sources inside the brain can be represented by the following equations.

$$\mathbf{Y}_{EEG} = \mathbf{L}_{EEG} \mathbf{j} \quad (2.41)$$

$$\mathbf{Y}_{MEG} = \mathbf{L}_{MEG} \mathbf{j} \quad (2.42)$$

If we account for only one time instant, \mathbf{Y}_{EEG} (\mathbf{Y}_{MEG}) is the $I_{EEG} \times 1$ ($I_{MEG} \times 1$) measurement vector, \mathbf{j} is the $3N \times 1$ source vector and \mathbf{L}_{EEG} (\mathbf{L}_{MEG}) is the $I_{EEG} \times 3N$ ($I_{MEG} \times 3N$) leadfield matrix. Where I_{EEG} (I_{MEG}) is the number of EEG (MEG) sensors and N is the number of source space points.

2.3.3.1 Combined EEG/MEG source analysis

EEG and MEG are complementary to each other and it is shown that for a continuously distributed neuronal current, information missing in EEG is precisely the information that is available in MEG, and vice versa [100]. The findings on different sensitivity profiles of EEG and MEG as given in Sections 2.3.1 and 2.3.2.2 encourage researchers to increase the synergy of these two methods by using and evaluating them simultaneously [6, 46, 47, 48, 54, 76, 101]. However, EEG and MEG measure different quantities

so that the units of the measurements are different. Thus, in order to perform a combined analysis both modalities need to be transferred to a common space. Mainly two approaches were suggested for this purpose in [102], [46] and [103] the lead field matrices are normalized by using their norms. In [6], the approach selected here the SNR based transformation is used. In this method the data was whitened according to the noise level (calculated from the pretrigger interval where only spontaneous activity occurs) of each channel so that unitless measures for EEG and MEG were obtained to be used in a combined procedure as explained in detail in the remainder of this section.

2.3.3.1.1 Calculation of SNRs for whitening

The first step is the calculation of the noise statistics for each channel. In this thesis the noise is calculated as the standard deviation of the signal over the pre-trigger interval (time interval preceding evoked responses or spike activity) as given with the formula below [6]:

$$N_I = \sqrt{\frac{\sum_{t=1}^{t_n} (Y_I(t) - \bar{Y}_I)^2}{t_n - 1}} \quad (2.43)$$

where N_I is the noise of channel I between time instants $t = 1, \dots, t_n$, $Y_I(t)$ is the measurement at channel I for time instant t and \bar{Y}_I is the mean of the signal at given time interval $t = 1, \dots, t_n$.

The whitened signal for a channel I at a certain time instant t' ($SNR_I(t')$) is then calculated by:

$$SNR_I(t') = \frac{Y_i(t')}{N_I} \quad (2.44)$$

with this procedure the EEG and MEG signals are represented in the common SNR space.

2.3.3.1.2 Formulation of combined EEG/MEG (EMEG) problem

Afterward equations 2.41 and 2.42 are combined to obtain the EMEG formulation. For this purpose the EEG and MEG leadfield matrices and measurements (all converted to SNR space as explained in Section 2.3.3.1.1) are stacked row wise and the equation takes the form in equation 2.45.

$$\begin{pmatrix} \mathbf{Y}_{EEG_1} \\ \vdots \\ \mathbf{Y}_{EEG_{I_{EEG}}} \\ \vdots \\ \mathbf{Y}_{MEG_1} \\ \vdots \\ \mathbf{Y}_{MEG_{I_{MEG}}} \end{pmatrix} = \begin{pmatrix} \mathbf{L}_{EEG_1} \\ \vdots \\ \mathbf{L}_{EEG_{I_{EEG}}} \\ \vdots \\ \mathbf{L}_{MEG_1} \\ \vdots \\ \mathbf{L}_{MEG_{I_{MEG}}} \end{pmatrix} \begin{pmatrix} \mathbf{j}_1 \\ \vdots \\ \mathbf{j}_N \end{pmatrix} \rightarrow \underbrace{\begin{pmatrix} \mathbf{Y}_{EEG} \\ \mathbf{Y}_{MEG} \end{pmatrix}}_{\mathbf{Y}_{EMEG}} = \underbrace{\begin{pmatrix} \mathbf{L}_{EEG} \\ \mathbf{L}_{MEG} \end{pmatrix}}_{\mathbf{L}_{EMEG}} \mathbf{j} \quad (2.45)$$

In the inverse problem the \mathbf{Y}_{EMEG} and \mathbf{L}_{EMEG} can then be used as the measurement \mathbf{Y} and leadfield \mathbf{L} matrices as for EEG or MEG alone.

2.3.3.2 Inverse algorithms

EEG/MEG inverse algorithms are usually divided into two categories known as equivalent dipole approaches and current density approaches. Here only a short description of the inverse solution approaches will be presented. Detailed reviews with mathematical emphasis can be found in [42, 43], and more practical aspects of the inverse solution approaches are discussed in the reviews [104, 105]

Beamformer approaches are spatial filters that are on data from a sensor array to discriminate between signals arriving from a location of interest and those originating elsewhere.

2.3.3.2.1 Equivalent dipole approaches

In equivalent dipole approaches as the name suggests the sources inside the brain are represented by a couple of dipoles (usually not more than five). Therefore, activities investigated with equivalent dipole approaches should satisfy the assumption of focality. A dipole is represented by three location and three moment parameters, thus only six parameters need to be estimated for each dipole. In so-called moving dipole, these six parameters are calculated separately at each time instant. However, it is also possible to keep the location (rotating dipole) or both location and orientation (fixed dipole) constant for a certain period of time. In classical dipole fit algorithms, the three location parameters are calculated using nonlinear optimization techniques and dipole moments are calculated with a simple linear fit [106, 107]. One problem related to dipole fit algorithms is that the optimization algorithm might get trapped in a local

minimum instead of finding the global minimum [104].

In this thesis, single dipole deviation scans (DSs) (also known as goal function scans) [108] were used for inverse calculations of somatosensory evoked responses and for estimation of the origins of epileptic spikes as described in Chapters 3 and 4. The reason for this was because these signals were shown to be arising from relatively focal sources inside the brain [12, 109]. For auditory evoked responses, two dipole DSs were used because previous studies [110, 111] and our recent findings with hierarchical Bayesian methods [112] show that the two focal dipole source model, one dipole in each hemisphere, is an appropriate model for the rising flank of the N1. Unlike dipole fit algorithms in which the coordinates of the best fitting dipole is determined via nonlinear optimization, the DSs are calculated on a predefined source space, which is also a more natural approach when used in combination with multi-compartment FEM forward modeling. The residual variance (RV), i.e. the squared deviation, of the best fitting dipole to the measurement data is calculated for all source space locations. By this way the risk of trapping in local minimum, as it might be the case for dipole fits, is avoided and the dipole is located at the global minimum. Furthermore, the calculated residual map can be used for estimating the confidence of the results. The RV in dipole scan is calculated with the equation below with proper regularization parameter (λ^2), measurement (\mathbf{Y}) and leadfield (\mathbf{L}) matrices for EEG ($\mathbf{Y}_{I_{EEG} \times 1}$, $\mathbf{L}_{I_{EEG} \times 3N}$), MEG ($\mathbf{Y}_{I_{MEG} \times 1}$, $\mathbf{L}_{I_{MEG} \times 3N}$) or EMEG ($\mathbf{Y}_{(I_{EEG}+I_{MEG}) \times 1}$, $\mathbf{L}_{(I_{EEG}+I_{MEG}) \times 3N}$) [6, 108]:

$$RV = \|(\mathbf{1} - \mathbf{L}(\mathbf{L}^T\mathbf{L} + \lambda^2)^{-1}\mathbf{L}^T)\mathbf{Y}\|^2 \quad (2.46)$$

The goodness of fit (GOF) is then calculated as $GOF = 1 - RV$ and, in the upcoming chapters, both RV and GOF values are given as percentages. The goal of the DS procedure was to determine the source space location with minimal RV and thus maximal GOF value.

The obvious drawback of dipole scans is their higher computational costs especially when the underlying activity is assumed with more than two dipoles. It is also possible to reduce the unknown parameters by imposing further constraints such as constructing the source space only in gray matter (as it is performed in this thesis, see Section 3.1.11) and allowing the orientations of the dipoles to be only perpendicular to the surface of the gray matter. This simplification is justified by the fact that the EEG and MEG signals are produced by the pyramidal cells that are perpendicular to the cortex surface [42, 44, 45]. However, possible errors due to inaccurate segmentation of the gray matter should be considered before imposing these kinds of constraints, This is why in this thesis, the normal-constraint was not used. The common problem with

all dipole models is that the number of dipoles has to be determined a priori to avoid spurious results. An advantage of recently proposed new inverse approaches is that this number parameter is also estimated from the data [112, 113, 114].

Another method in this direction is the multiple signal classification (MUSIC) which can be used to locate multiple asynchronous dipolar sources from the measurements[107]. The algorithm scans a single-dipole model in the source space instead of the multiple-dipole directed search. Furthermore, an eigenvalue decomposition of the data can be used to identify the orientation which saves considerable time and many modifications on the original MUSIC algorithm exist in the literature [115, 116].

2.3.3.2.2 Current density approaches

In current density approaches usually first a source space is constructed and then one (with normal constraint) or three (without normal constraint) dipoles are calculated per source node. The advantage of these methods is that the user does not have to specify the number of dipoles a priori and as in DSs the source space can be limited to gray matter and possibly also with orientation perpendicular to the local surface of the gray matter if a very accurate surface segmentation is available. However, the system in current density approaches is underdetermined because the number of sources (usually about 10,000) is significantly higher than the number of measurements (usually less than 350). Solutions differ for different a priori assumptions and some of the most used approaches are listed below:

1. **Minimum norm estimates (MNE):** Among many solutions with low residuals the one with the smallest L2 norm of the overall current density is selected [117]. The algorithm punishes deep sources with high amplitudes and favors superficial sources which causes the so-called depth bias problem [118].
2. **Weighted MNE:** An additional term to alleviate the depth bias in MNE is introduced to the formulation [119].
3. **Low-resolution electromagnetic tomography (LORETA):** Calculates the solution which minimizes the laplacian of the weighted sources, and thus favors spatially smooth results [120].
4. **Standardized low-resolution brain electromagnetic tomography (sLORETA):** The minimum norm reconstructions are normalized by the posterior covariance and the output is a statistical map [121]. The reconstructions

are shown to be artificially dispersed (the extent is overestimated) and it does not perform well for more than one source with small distances between [118].

5. **Exact low-resolution brain electromagnetic tomography (eLORETA):** It is similar to sLORETA, but unlike the sLORETA it calculates the current distribution [122].
6. **sLORETA-weighted accurate minimum norm (SWARM):** It is designed to calculate current distribution using sLORETA statistical maps. It is similar to weighted minimum norm solutions but the weights are calculated from the sLORETA solution [123].
7. **Beamformer approaches:** In beamformer approaches the activity in a region of interest is estimated by minimizing the contributions of other simultaneous sources [66, 124, 125]. As can be understood from the previous sentence, this approach is not appropriate to estimate time correlated activity [66, 124, 125].
8. **Hierarchical Bayesian approaches:** In these methods uncertainties are allowed in the prior model and the data itself is used to approximate the model by using hyperparameters that are introduced with a priori distributions in a hierarchical way [113, 118, 126, 127].
9. **State space models:** These approaches use not only the spatial information, but also temporal information. Among the state space models, Kalman filter appears as a promising model for solving the inverse problem of bioelectromagnetism [128, 129, 130].

2.3.3.3 Source analysis in presurgical epilepsy diagnosis

The invasive EEG recordings are widely accepted as the current gold standard in presurgical epilepsy diagnosis. As compared to non-invasive techniques, invasive EEG has two key advantages: the electrodes are closer to the sources and the skull layer between sources and electrodes is eliminated. Nevertheless, invasive EEG suffers from serious shortcomings such as the risk of harming the patient due to the invasive procedure and the low spatial coverage (can only cover a part of the brain) due to the limited number of invasive electrodes [1]. Therefore, in addition to invasive EEG, noninvasive EEG and MEG are considered as important tools for presurgical epilepsy diagnosis, too. Especially with increasing use of realistic and individual head models, improved MRI co-registration approaches and high sensor numbers, the accuracy and precision

of noninvasive source reconstructions have increased notably [14, 131, 132, 133, 134]. Noninvasive EEG and MEG not only detect epileptogenic lesions and point out intrinsic epileptogenicity of malformations of cortical development [135, 136], but they can also guide the placement of invasive electrodes. Moreover, in some cases they can even supply sufficient information for a surgical intervention without invasive recordings [10, 16, 131, 137, 138, 139, 140, 141, 142, 143, 144, 145, 146], and also can identify epileptogenic temporal subregions [147]. Furthermore, today it is widely accepted that epilepsy is a network disease, in which different parts of the brain are involved [35, 36], and thus, understanding the networks causing epilepsy requires the evaluation of the information from the whole brain, which is only possible with noninvasive methods like EEG/MEG, EEG/fMRI, etc. It has also been recently shown that there is a good agreement between noninvasive EEG and MEG source reconstructions and fMRI responses [135].

2.3.3.3.1 Location and extent of the epileptogenic zone

Determination of the location and the extent of the epileptogenic tissue are of great importance for successful surgery and seizure freedom. Köhling et al. [12] and Speckmann et al. [15] employed optical imaging to study epileptogenic human neocortical slices removed during epilepsy surgery, and found that the activated cortical areas during sharp waves are focal, with diameters as small as $750\ \mu\text{m}$, and their spatial positions change in a dynamic manner within the epileptogenic tissue. Based on these findings, it can be assumed that the single spike localizations are from very focal sources, in which spatial position changes within the irritative zone in a stochastic way. In line with these results, many studies used the size of the area producing interictal epileptic spikes, the so-called irritative zone, as an indication of the focality and for the prediction of the chance of seizure freedom after the surgery [10, 11, 13, 14, 148]. For this purpose, usually each single spike is localized separately and then the scatter is calculated from the distances between positions of individual spikes and the centroid location. Even though not all sharp waves can be detected with extracranial recordings [149], this approach is appealing because the spreading of the localizations might give an estimation of the focality of the irritative zone [150, 151]. While this approach seems reasonable for high SNRs, the SNRs of single spikes are not always enough to obtain reliable source reconstructions, especially for deeper sources. Furthermore, it was shown in Bast et al. [16] that the scatter size depends highly on the SNR for EEG single spike localizations. Alternatively, it is possible to average the spikes that

belong to the same class (i.e., they have a sufficiently similar EEG/MEG topography) in sensor space and then perform source reconstruction to improve SNR and to achieve more reliable source reconstructions [16, 145]. The latter approach, however, no longer provides much information on the actual size of the underlying irritative zone, because it often uses a single dipole that only represents the center of gravity of a larger activated cortical patch (it is also possible to get a sense of the volume of the irritative zone using confidence ellipsoids [10]). Therefore, the sources obtained in this way from the averaged spikes are a collection of the underlying focal sources and represent a considerable portion of the irritative zone.

Figure 2.6 is an illustration of the epileptogenic tissue. In this figure, the epileptogenic tissue was represented with a black rectangle and the black dots inside this area represent the origins of epileptic activity. Köhling et al. [12] and Speckmann et al. [15] showed that the origin of an epileptic signal might be any of these dots and this origin changes stochastically for each epileptiform signal within the black rectangle (a different point within the irritative zone). Thus, if the effects of noise on single spike localizations could be avoided, the single spike localizations should end up as points inside the epileptogenic tissue (black rectangle), while averaging all spikes would just give the position illustrated with a magenta star (the center of activity).

At first glance, distributed source models and current density approaches might seem more appropriate, but the reconstructed extent in commonly used current density approaches mainly depends on the chosen approach/norm and huge differences in spatial dispersion have been shown for one and the same underlying source [118]. Still among current density approaches, hierarchical Bayesian methods [112, 118] and maximum entropy on the mean method [135, 152] seem promising for future studies.

2.3.3.3.2 Propagation/SNR balance in source reconstruction of epileptic activity

There is a continuous discussion on the selection of the interval for the localization of the spikes. On one hand, the peak of the spike indicates the highest degree of synchrony in the neurons and thus better signal to noise ratios. But on the other hand, this location might not be the origin of the spikes due to the propagation of the activity. Many studies use the middle of the rising flank of the averaged spikes for source localization based on previous studies, which favor it in comparison to the calculation of the peak of the spike [153, 154, 155]. This is a good compromise between the low SNR at the beginning of the spike and the propagation, which might be faced at

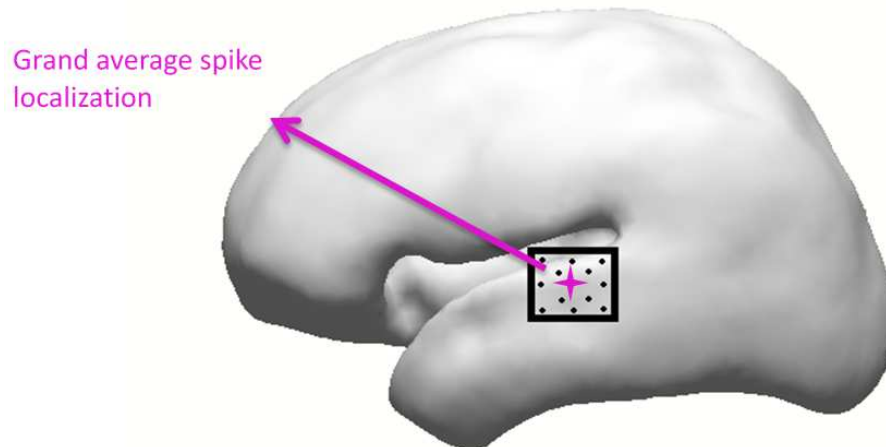


Figure 2.6: Illustration of epileptogenic tissue (black rectangle), the origins of different spikes following the measurements in [12] and [15] (black dots), and the position that is obtained if all spikes are first averaged and then localized (magenta star).

the peak of the spike. In this thesis, in Section 3 the middle of the rising flank was used to investigate the effects of volume conduction with reasonable SNRs. Additionally, in Section 4 the localizations at different phases of epileptic spikes were tested to broaden our knowledge on the propagation phenomenon and in order to compare EEG, MEG and EMEG.

2.4 Magnetic Resonance Imaging

As stated in previous sections accurate modeling of the head and brain is crucial to solve the forward and inverse problems of bioelectromagnetism. In this thesis magnetic resonance imaging (MRI) was used to obtain the geometries of different tissue compartments inside the head as well as the brain conductivity anisotropy. In this section a short overview of the principles of MRI is given. This summary is written using [156, 157, 158] as the main references and detailed explanations on MRI principles can be found in these books. The details on how the MRIs were used to obtain the head models are explained in Chapter 3.

MRI benefits from the nuclear magnetic resonance phenomenon (NMR) to construct the images. NMR theory explains the phenomenon that materials placed in a strong magnetic field absorb or emit signals at specific frequencies, and the first NMR signals were measured by Felix Bloch [159] and Edward Purcell [160] independently in 1946. Each proton and neutron in nucleus has a spin (angular momentum) and normally these

nuclei are randomly oriented and, thus, achieve zero net spin. However, some materials have non zero spins due to odd number of protons and neutrons they have, which results in a nonzero net magnetic moment. These magnetic moments are normally randomly oriented. However, when a strong external magnetic field is applied (by the main magnet in MRI), the nuclei align along the direction of the external magnetic field (parallel or antiparallel). The number of nuclei aligned parallel to the main magnetic field are slightly more than the antiparallel ones and this creates a magnetic vector along the main magnetic field (longitudinal axis). These nuclei precess around this main magnetic field and the rate of this precession is proportional to the strength of the external magnetic field. This means, if the magnetic field is modified so that its strength vary with respect to spatial position, also the precessing frequencies of the protons will differ in this way. In MR scanners the three gradient coils (in x, y and z directions) are used to induce these spatially varying magnetic fields and this is how the spatial information is encoded in MRI.

When a proton is aligned along the main magnetic field, it will be in equilibrium and will not emit any signal unless its orientation is changed by another external field resulting in an angle with the direction of the main magnetic field. These nuclei are sensitive to signals with frequencies equal to their precessing frequencies. In MRI using the radio-frequency (RF) coils these specific signals with matching frequencies are produced and used to excite nuclei. The excited nuclei then change its orientation to the transverse plane and emit an RF signal which is later received and processed to obtain an image.

The excited nuclei are tend to realign themselves by emitting their energy. This phenomenon is called relaxation and the times associated with this are called relaxation times. The three important relaxation times are: 1) T1 or longitudinal relaxation time which is the time needed for the nuclei to return to its equilibrium in longitudinal (along the main magnetic field) direction; 2) T2 or the transverse relaxation time which is the time needed for the spinning moments to become out of phase due to the effects of nearby nuclei (spin-spin interaction); 3) T2* which is due to local inhomogeneities of the magnetic field.

These relaxation times differ for different tissue types and MRI sequences can be designed to focus on certain relaxation times when acquiring the data. For example a T1 weighted image as the name suggests focuses on the differences of T1 relaxation time of different tissues, and can be obtained using short repetition (TR) and echo (TE) times (9.2 ms TR and 4.4 ms TE for T1 MRI in Section 3.1.2). In T1 MRI the tissues from brighter to darker can be sorted as WM (short T1 relaxation time), GM (longer

T1) and CSF (longest T1). In T2 weighted images the focus is on the differences of T2 relaxation time and for this purpose long TR and TE (2000 ms TR and 378 ms TE for T2 MRI in Section 3.1.2) are used. In T2 MRI the tissues from brighter to darker are CSF (long T2 relaxation time), GM (shorter T2) and WM (shortest T2) (see Figure 3.3).

In diffusion weighted MRI the diffusion of the water molecules are measured. For this purpose, two consecutive gradient pulses are sent; the first one to dephase and the second one to rephase the spins. This results in almost no attenuation at the received signals if the spins (protons) do not move between the two pulses. However, if the spins move after the dephasing pulse then the perfect rephasing cannot occur (because the rephasing signal differs with spatial position) and measured signals are attenuated. This is the basic idea behind diffusion weighted imaging. If multiple diffusion weighted images with varying directions are measured (as it is done in this thesis, see Section 3.1.2) then they can be combined to obtain the diffusion tensors (see Figure 3.7). This imaging is then called diffusion tensor imaging (see Figure 3.7).

In this thesis as explained in detail in Chapter 3, T1 and T2 MRIs were used to segment different tissue compartments, and the DTI was used to calculate the water diffusion tensors which are later used to calculate conductivity tensors with the approach suggested in [86].

3 Study I: Volume Conduction Effects on EEG, MEG and EMEG in Presurgical Epilepsy Diagnosis

In this chapter, the volume conduction effects in source reconstruction of the epileptic activity and somatosensory evoked responses were investigated using the data measured from an epilepsy patient. In order to assess the impact of including different tissues and brain conductivity anisotropy to the head model on the outcome of source reconstruction, a six compartment finite element head model was built with 1 mm resolution using the individual T1, T2 and DT MRIs. Furthermore, the conductivity of the skull compartment was calibrated using the measured somatosensory evoked responses. After explaining this new pipeline in detail, this chapter will mainly focus on the effects of the skull conductivity and will compare six and three compartment head models and brain anisotropy. The results and methods explained in this chapter were recently published in [71].

3.1 Patient and Methods

3.1.1 Patient information

The data used in this study was measured from a 17-year-old female suffering from pharmaco-resistant focal epilepsy since 11 years. The patient has a history of epilepsy in her family and her sister also had focal epilepsy. Several 3 Tesla MR acquisitions, following protocols sensitive to epileptogenic lesions, were negative. An FDG-PET scan showed a diffuse and extended left fronto-temporal hypometabolism (see Figure 3.1). According to the clinical assessments she had 4 different seizure types:

- Seizures with aura and a strange feeling in the stomach.
- Hypermotor seizure during sleep with sweating, shaking, standing, stark motor

movements and teeth chattering.

- Tonic hypermotoric seizure with hyperventilation, pull of shoulder, tonic contractions of the arms and disorientation.
- Dissociative seizures

Interictal discharges were recorded in EEG and MEG, with most of them over the left temporal regions and only few over the left frontal region. Resective epilepsy surgery was refused after the invasive work-up due to multifocal activity and an unfavorable risk-benefit ratio of any resective surgical intervention.

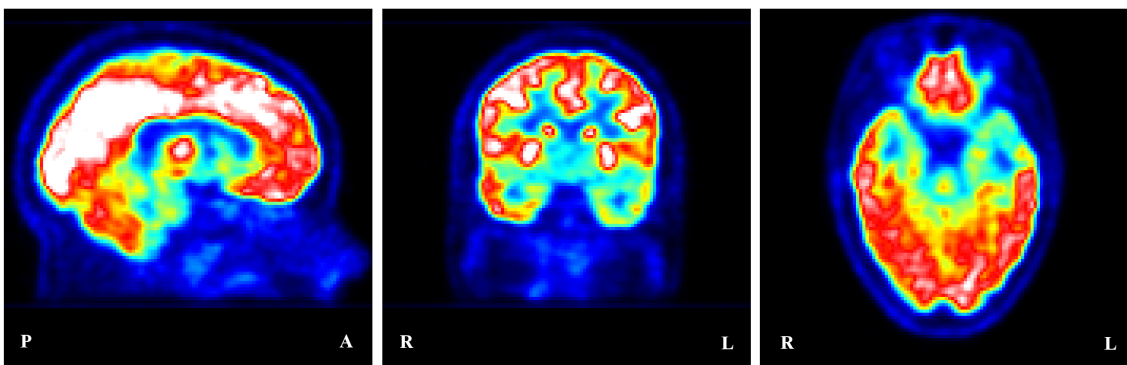


Figure 3.1: FDG-PET showing left fronto-temporal hypometabolism. Red and white regions show higher glucose consumption in comparison to blue regions.

3.1.2 MRI measurements

T1-weighted (which will be abbreviated as just T1 in the rest of the thesis), T2-weighted (T2) and diffusion-tensor (DT) MRI scans were acquired with a 3T scanner (Gyrosan Intera/Achieva 3.0T, System Release 2.5 (Philips, Best, NL)). The details of the sequences were as given below:

- 3D-T1 gradient-echo pulse sequence with inversion prepulses, $TR/TE/TI/FA = 9.2 \text{ ms}/4.4 \text{ ms}/1014 \text{ ms}/9^\circ$, with water selective excitation and voxels with $1.04 \times 1.04 \times 1.17 \text{ mm}$.
- 3D-T2 TSE pulse sequence, $TR/TE = 2000 \text{ ms}/378 \text{ ms}$, cubic voxels, 1.17 mm edge length
- DT-MRIs (DTI) were acquired using a Stejskal-Tanner spin-echo EPI sequence, $TR/TE = 7546 \text{ ms}/67 \text{ ms}$. Geometry parameters were: FOV $240 \times 240 \text{ mm}$ for

70 transverse slices, 1.875 mm thick without gap, square matrix of 128, i.e. cubic voxels with 1.875 mm edge length. One volume was acquired with diffusion sensitivity $b=0 \text{ s/mm}^2$ (i.e. blip-up data with flat diffusion gradient) and 20 volumes with $b=1000 \text{ s/mm}^2$ for diffusion weighting gradients in 20 directions, equally distributed on a sphere.

- Geometry distortion due to susceptibility gradients was maximal in phase encoding direction (anterior-posterior), bandwidth 20.3 Hz/pixel. An additional data set with only flat diffusion gradients (blip-down data) and reversed spatial encoding gradients was acquired for distortion correction according to [161].
- In addition, a T1 dataset with gadolinium markers in nasion, left ear canal and right ear canal was also acquired. In order to distinguish left and right hemispheres two markers were placed on the right hemisphere as shown in Figure 3.2. These fiducials were later used to coregister EEG and MEG sensors to the individual MRI.

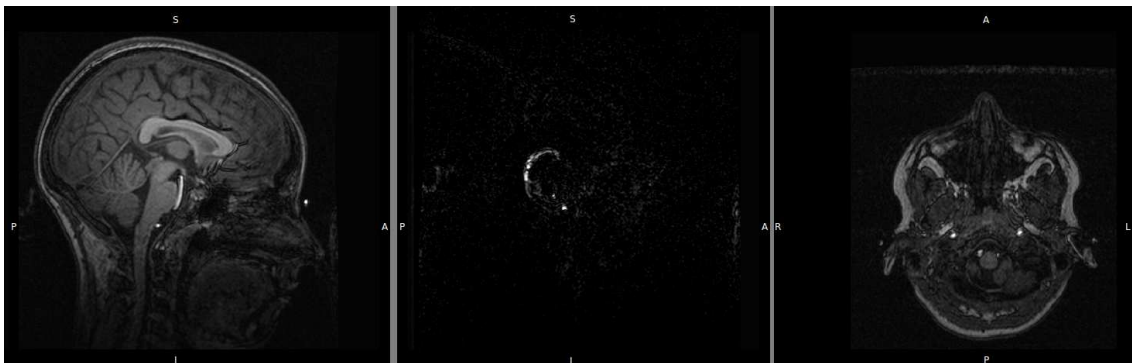


Figure 3.2: Fiducials on T1 MRI. The sagittal image on the left shows the nasion, the sagittal view in the middle shows two gadolinium markers on the right ear, and the coronal view on the right shows one left and one right marker.

3.1.3 Post-processing of structural MRIs

For registration and segmentation purposes mainly the FSL software¹ was used. The first step in the pipeline was resampling of the water selective T1 MRI to 1 mm^3 isotropic voxels with *FSL – FLIRT* algorithm. This data was used as the reference space in the rest of the process. Then T1 MRI with the fiducials and the T2 MRI were

¹<http://www.fmrib.ox.ac.uk/fsl>

registered to the reference water selective T1 with a rigid registration scheme, which uses mutual information as the cost function and splines for interpolation. Water selective T1 MRI and T2 MRI were used in *FSL – BET* to get the estimates of brain, inner skull, outer skull and extracranial tissues (summarized as scalp in the rest of the thesis) [162, 163]. The brain extraction process used in this study depends on one vertex at a time deformation of the triangular tessellation of a sphere surface, in which the center and diameter (half of the estimated brain diameter) are obtained after a rough thresholding, until it reaches the borders of the brain [163].

Special attention was given to skull layer, and inner and outer skull masks were corrected manually using the CURRY 7 software². The scalp segmentations produced with FSL are mainly intended to be used with BEM, and thus its surface was too smooth, another scalp segmentation was calculated via CURRY and used for the head model. The skull spongiosa segmentation pipeline started with the erosion/dilation of the outer/inner skull masks and was followed by masking of the T2 MRI with the eroded skull. Then, a threshold-based segmentation was used to label the voxels as skull spongiosa and compacta. The skull was eroded before masking in order to avoid leakage effects that might happen if elements labeled as skull spongiosa were not always residing between two skull compacta layers. In practice this might happen due to limited resolution and segmentation errors.

The segmentation of white matter (WM), gray matter (GM) and cerebrospinal fluid (CSF) were done using a hidden Markov random field model, which benefits from an iterative approach along with expectation maximization to estimate the bias field and to determine the tissue classes and probabilities (*FSL – FAST*) [164]. Another gray matter mask was calculated with Freesurfer³ and used to correct wrong classification of dura mater as gray matter.

In this study, dura matter, CSF and meninges were not distinguished and thus everything inside the subarachnoid region was assigned as CSF. This might have led to a slight overmodeling of the CSF space but it was decided not to model meninges explicitly in this study due to its thin structure, which makes it very hard to obtain an accurate segmentation, and unknown conductivity [165]. Even though the effects of dura mater for EEG were shown before [166], because of its small average thickness that is just 0.36 mm [167] (the regions where it is thicker consists of mainly blood), it was decided not to distinguish the dura mater in this study (a rough dura mater compartment is included to the head model used in Chapter 5). Thus, meninges

²<http://www.neuroscan.com/curry.cfm>

³<http://surfer.nmr.mgh.harvard.edu>

and dura mater were not included to the head model because they were very thin in comparison to CSF, which has an average thickness of 3.1 mm [167], and because unlike CSF [77] their conductivities are not well known and inter-individually stable. The resulting segmentation is shown in Figure 3.3 along with T1 and T2 images used for segmentation.

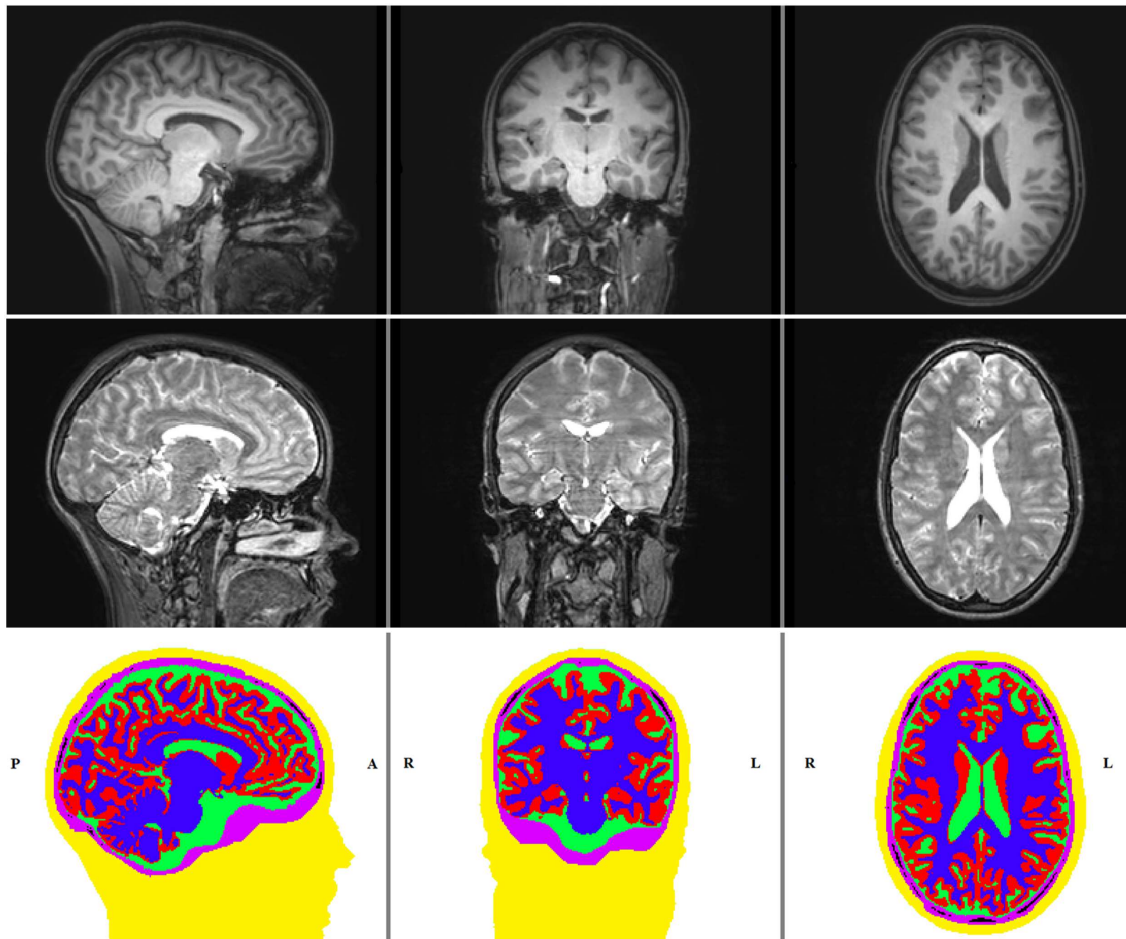


Figure 3.3: T1 (upper row), T2 (middle row) and the segmented (lower row) MRIs. Sagittal (left column), coronal (middle column) and axial (right column) slices. The color codes for the tissues are scalp (yellow), skull compacta (purple), skull spongiosa (black), CSF (green), gray matter (red) and white matter (blue).

3.1.4 Generation of the geometry-adapted hexahedral finite element mesh

A geometry-adapted hexahedral finite element mesh with 1 mm resolution was constructed out of the labeled volume. When constructing the geometry-adapted mesh it was ensured that all interior angles at element vertices are convex and the Jacobian determinant in the FEM computations remains positive by selecting the node-shift factor as 0.33. The final geometry adapted hexahedral FE mesh was generated with *SimBio_VGRID* ⁴ and had 3,993,881 vertices and 3,895,971 elements (see Figure 3.4 visualized with SCIRun ⁵). The overall construction of the head model took about two days, most of the time was used for the manual correction and optimization of the automatic segmentation results. Figure 3.5 shows the regular and geometry adapted hexahedral meshes for frontal regions and the staircase effects in the regular mesh.

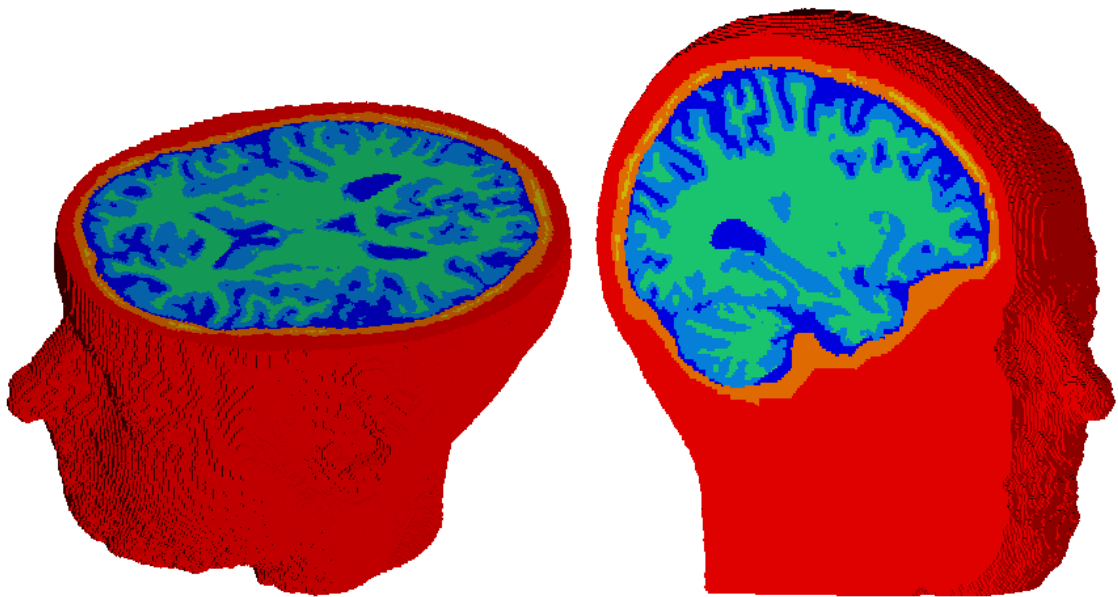


Figure 3.4: Head model visualized with SCIRun. The color codes for the tissues are scalp (red), skull compacta (orange), skull spongiosa (yellow), CSF (dark blue), gray matter (light blue) and white matter (green).

⁴<http://www.rheinahrcampus.de/~medsim/vgrid>

⁵SCIRun: A Scientific Computing Problem Solving Environment, Scientific Computing and Imaging Institute (SCI), downloaded from: <http://www.scirun.org>

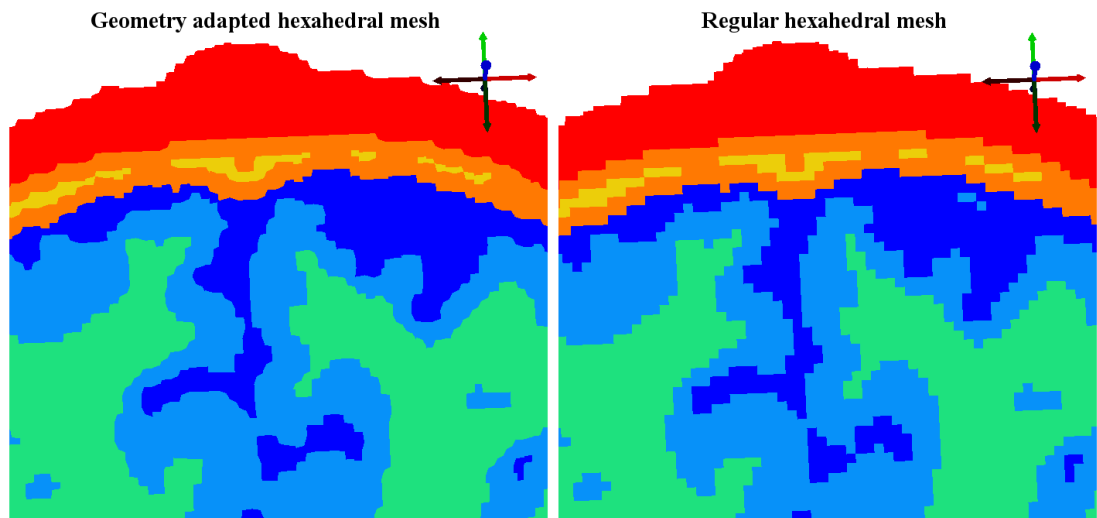


Figure 3.5: Geometry adapted (left) and regular (right) hexahedral meshes (visualized with SCIRun). The color codes for the tissues are scalp (red), skull compacta (orange), skull spongiosa (yellow), CSF (dark blue), gray matter (light blue) and white matter (green).

3.1.5 Inclusion of gray and white matter conductivity tensors

The DTI was corrected for eddy current (EC) artifacts by affinely registering directional images to the image with flat diffusion gradients (blip-up data) using the FSL routine FLIRT. Subsequently, the gradient directions were reoriented using the rotational part of the transformation matrices obtained during the EC correction scheme. Then, a diffeomorphic approach was applied for nonlinear correction of susceptibility artifacts in the DTI dataset according to [161]. For this purpose, first a diffeomorphic warp field, which allows transformations only in the phase encoding direction, was calculated with flat diffusion gradients and reversed spatial encoding gradients (blip-up and blip-down data) and then it was applied to directional images. For this patient the observed displacements on the calculated warp field were ranging from -4.4 mm to 6.2 mm. A sample slice of blip-up data, blip-down data and their difference before (upper row) and after (lower row) susceptibility correction are shown in Figure 3.6. This approach was implemented in the freely-available SPM ⁶ and FAIR ⁷ software packages. Following susceptibility correction, the DT-MRIs were registered to the structural MRIs by registering the susceptibility corrected blip-up data with flat diffusion gradients to the T2 MRI. The rigid transformation matrix obtained in this

⁶<http://www.diffusiontools.com/documentation/hysco.html>

⁷<http://www.mic.uni-luebeck.de/people/jan-modersitzki/software/fair.html>

step was then combined with the T2 to T1 transformation matrix and applied to the directional images. In this step corresponding gradient directions were reoriented once more to ensure conformance to the directional images [161]. After obtaining diffusion tensors an effective medium approach was used to estimate electrical conductivity tensors from water diffusion tensors [70, 86] (see Section 3.1.6 for details). The scaling factor for this dataset was calculated as $0.25 \text{ S} \cdot \text{sec}/\text{mm}^3$ and the resulting mean conductivity values for GM and WM were 0.24 S/m and 0.20 S/m, respectively.

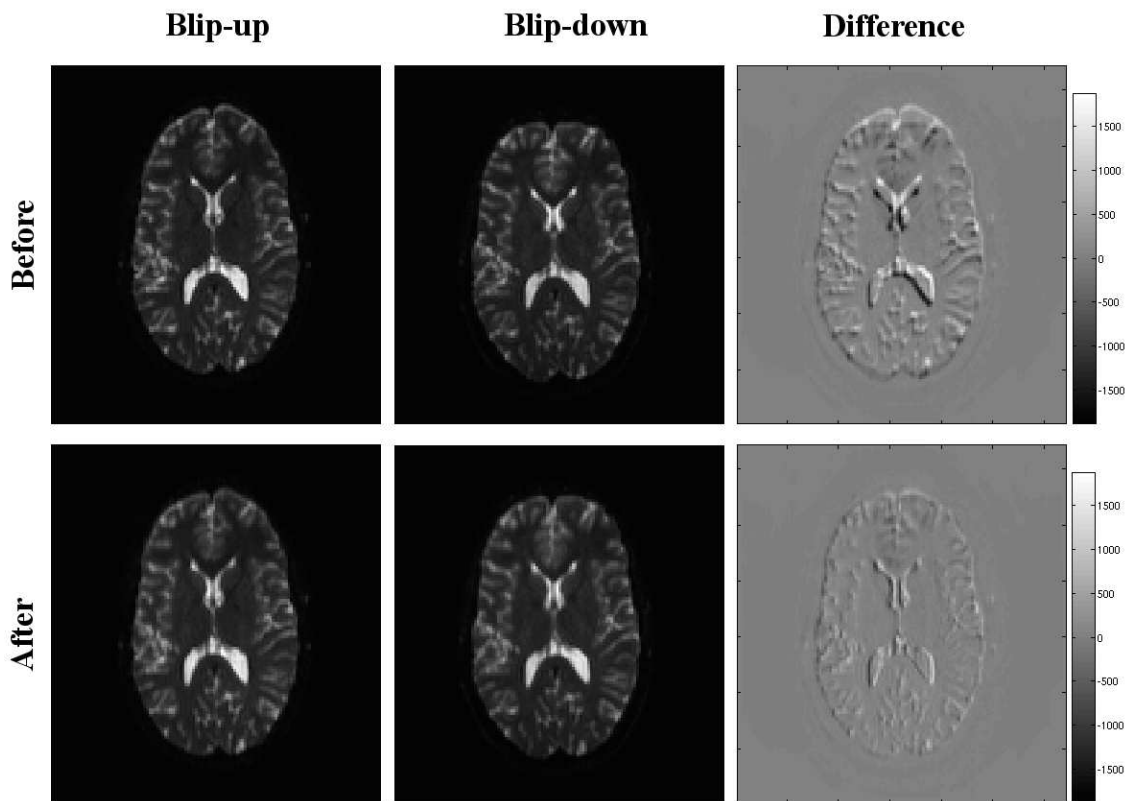


Figure 3.6: A sample slice from the blip-up data (left column), blip-down data (middle column) and their difference (right column) before (upper row) and after (lower row) susceptibility correction.

The artifact corrected and registered DTI data was then used to calculate the diffusion tensors with the FSL routine DTIFIT [168]. In this approach, diffusion tensors are calculated for each voxel [168] and the parameters of the diffusion tensors are estimated in a probabilistic sense relying on the local probability density functions. The main fiber directions obtained with this approach are shown in Figure 3.7.

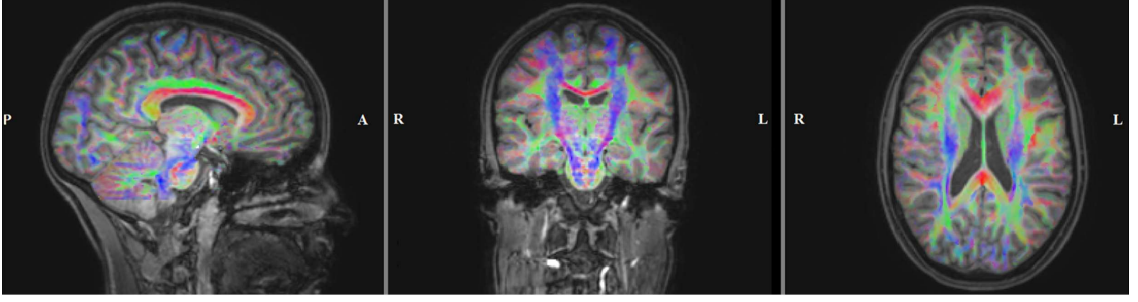


Figure 3.7: Main fiber directions (largest eigenvalues of diffusion tensors) weighted according to the fractional anisotropy (FA) values for sagittal (left), coronal (middle) and axial (right) slices. The maps are registered and plotted on the T1-MRI. The colors indicate the main fiber orientations: red is left-right, green is anterior-posterior and blue is superior-inferior.

3.1.6 Effective medium approach

The water diffusion tensors obtained via diffusion tensor imaging are required to be converted to conductivity tensors before they are included to the head model. For this purpose, following the studies in literature [70, 86] an effective medium approach was used. This approach assumes a linear relationship between the conductivity σ and the water diffusion tensor \mathbf{D} as shown below:

$$\sigma = \frac{\sigma_e}{d_e} \mathbf{D} \quad (3.1)$$

In this equation the ratio of effective extracellular conductivity (σ_e) and diffusivity (d_e) can be represented by a scaling factor (s). Instead of using an empirical scaling like in [84, 86] here it was calculated following [70]. In this approach the assumption is that the arithmetic mean of the anisotropic conductivity tensor volume is the same as the tensor volume when the isotropic conductivity is assumed. Thus, s was calculated with a least squares fit, which ensures the conductivity tensor volumes in the interested tissue match the volume of the corresponding tensor with isotropic conductivity [70].

$$\frac{4\pi}{3} (\sigma_{comp}^{iso})^3 = \frac{\sum_{i=1}^{N_{comp}} \frac{4\pi}{3} \prod_{j=1}^3 \sigma_i^j}{N_{comp}} \quad (3.2)$$

where σ_{comp}^{iso} is the isotropic conductivity for compartment $comp$ which is assigned either white matter (wm) or gray matter (gm), and N_{comp} is the number of conductivity tensors. By replacing the j th eigenvalue of the i th conductivity tensor σ_i^j with $s d_i^j$ (j th eigenvalue of the i th diffusion tensor) and $\frac{\sum_{i=1}^{N_{comp}} \prod_{j=1}^3 s d_i^j}{N_{comp}}$ with d_{comp} , equation 3.2

reduces to:

$$\frac{4\pi}{3}(s \cdot d_{comp})^3 \quad (3.3)$$

Finally s can be calculated with the formula below.

$$s = \frac{d_{wm}\sigma_{wm}^{iso} + d_{gm}\sigma_{gm}^{iso}}{d_{wm}^2 + d_{gm}^2} \quad (3.4)$$

3.1.7 Head models used in this study

The properties of head models used in this work are summarized in Table 3.1.

The most realistic head models contain six compartments (models $6C$ in Table 3.1) scalp, skull compacta, skull spongiosa, CSF, and brain gray and white matter. The conductivity values of 0.43 S/m were used for the scalp compartment [78] and 1.79 S/m for the highly conductive CSF [77]. Conductivity modeling of gray and white matter was described in Section 3.1.5. In this study, the main focus was on the effects of different skull conductivities on EEG, MEG and EMEG source reconstructions due to high interindividual variance of these values and distinct sensitivities of EEG and MEG to it. The only varying parameters in the five head models were the skull spongiosa and compacta conductivities. In order to limit the number of parameters that need to be estimated, a fixed ratio of spongiosa:compacta of about 3.6:1, which was the average of the measurement in [68], was used. The naming convention was the number of compartments followed by an underscore and then the skull compacta conductivity 10^{-4} S/m. For example for the six compartment head model with skull compacta conductivity 0.0041 S/m the name of the model was $6C_{41}$. The references from the literature citing these conductivity values are provided below for each head model.

Model $6C_{41}$: In [169] current dipoles were introduced via subdural strip electrodes and they were localized from the scalp potentials for varying brain to skull ratios. This study concluded that most accurate solutions were obtained for the brain to skull ratio of 80. This conductivity value is also used as a standard skull conductivity in most commercial source analysis packages [6] (to be precise 0.0042 S/m was used in[6]).

Model $6C_{70}$: The values used in this model were the average of the skull spongiosa and compacta conductivities in [68]. The measurements were from live skull samples of four patients who underwent intracranial surgery.

Model $6C_{132}$: Calculated from the simultaneous measurements of intra- and extra-cranial potentials of five epilepsy patients [170]. In their study, the main focus was

on the determination of the brain to skull ratio and an intersubject average of 24.8 was found, which corresponds to 0.0132 S/m in three compartment head models. It is important to mention that all measurements used in this study were from pediatric patients aged 8 to 12 years and younger age is associated with higher skull conductivities in the literature[171].

Model *6C_330*: Measured during intracranial surgeries of five epilepsy patients and all measurements were from the temporal part of the skull [171]. They found skull conductivity values ranging from 0.0320 to 0.0801 S/m.

The standard low-parametric three compartment (*3C*) isotropic volume conductor model (scalp, skull, brain) is still frequently used in source analysis (see recent review in [59]). It is, therefore, instructive to compare results obtained with *6C* and *3C* head models. For the homogenized brain compartment in the *3C* models, a conductivity value of 0.33 S/m was chosen [6, 169]. The skull conductivity value of 0.01 S/m in model *3C_100* was found as an optimal choice to approximate the skull's layeredness in compacta and spongiosa, in a globally isotropic skull modeling approach (in [67], average over four subjects). Finally, the skull conductivities used in the calibrated head models *6C_Cal* and *3C_Cal* were calculated using the somatosensory evoked potentials and fields measured from the patient and this procedure is explained in detail in 3.1.13.

3.1.8 EEG and MEG acquisition and preprocessing

The patient was measured with EEG and MEG simultaneously. The EEG cap had 74 AgCl sintered ring electrodes placed equidistantly according to the 10/10 system (EASYCAP GmbH, Herrsching, Germany). In addition to those 74 electrodes, six additional channels were available and were used to detect eye movements. The MEG system used in this chapter (and throughout the thesis) was a whole head system with 275 axial gradiometers and 29 reference coils (CTF, VSM MedTech Ltd.). The reference coils were used to calculate 3rd order synthetic gradiometers in order to reduce the interference of magnetic fields originating from distant locations (i.e., magnetocardiogram). These measurements were done in a magnetically shielded room to limit the magnetic interference from outside the chamber.

The measurements were performed in the supine position, which not only increases the comfort of the patient but also reduces the movement. Prior measurements showed that the position of the head inside the MEG dewar tends to get lower towards the end of the measurements due to changes in the posture caused by fatigue and measuring in supine position was especially valuable to reduce this movement in superior-inferior

Table 3.1: Head models used in this chapter. The first column indicates the name of the head model and the remaining columns show the conductivities for the respective tissue compartments. The compartments that were and were not distinguished are indicated by a slash (/) and by a dash (.) signs, respectively. Isotropic conductivity values were taken from the literature [6, 67, 68, 77, 78, 169, 170, 171] or were determined in the SEP/SEF skull conductivity calibration procedure described in this work (**_Cal* models; see Sections 3.1.13 and 3.2.1). The sign # indicates that conductivity tensors were determined as described in Section 3.1.5. In all 6C models, the ratio of skull spongiosa to compacta was kept constant to the mean of the ratio measured by [68].

Head Model	Scalp	Skull Compacta	Skull Spongiosa	Skull	CSF	Gray Matter	White Matter	Brain
<i>6C_Cal</i>	0.43 [78]	0.0024	0.0084	/	1.79 [77]	#	#	/
<i>6C_41</i>	0.43	0.0041 [6, 170]	0.0147	/	1.79	#	#	/
<i>6C_70</i>	0.43	0.0070 [68]	0.0251 [68]	/	1.79	#	#	/
<i>6C_132</i>	0.43	0.0132 [170]	0.0471	/	1.79	#	#	/
<i>6C_330</i>	0.43	0.0330 [171]	0.1179	/	1.79	#	#	/
<i>3C_Cal</i>	0.43	-	-	0.0024	-	-	-	0.33 [6, 170]
<i>3C_100</i>	0.43	-	-	0.0100 [67]	-	-	-	0.33

plane. Keeping the same measurement position between the EEG/MEG and MRI measurements also helped to prevent the brain shift. In [80] it was shown that brain shift results in changes in CSF thickness and even these small changes affect EEG signals with power differences up to 600 % and on average 80 % due to CSF's high conductivity value. A problem related to combined EEG/MEG measurements in supine position was the additional pressure induced due to lying on occipital electrodes. In order to avoid possible discomfort of the patients, a cotton wool layer was placed between the electrodes and the dewar.

Electrode locations were digitized with a Polhemus device (FASTRAK©, Polhemus Incorporated, Colchester, Vermont, U.S.A.) prior to measurement. During the measurement the position of the head inside the MEG scanner was constantly measured via three coils that are placed on nasion, left ear and right ear canal. Each coil was driven by sinusoidal currents with different frequencies and they were used to detect head movement. By selecting the frequencies as 1425, 1475 and 1525 Hz it was ensured that they did not interfere with the measurements and were not integer multiples of 50 Hz (line voltage frequency in Germany) [172]. During the measurements, head movement was continuously tracked with three head localization coils and only the runs with maximum head movement lower than 8 mm were accepted for further analysis.

3.1.8.1 Somatosensory evoked potentials (SEP) and fields (SEF)

In order to measure somatosensory evoked potentials and fields the right and the left median nerve of the patient were stimulated in a randomized order. Square electrical pulses with 0.5 ms, produced by an S88 dual output square pulse stimulator (Natus Neurology Incorporated, Middleton, WI, USA), were used for this purpose. The constant voltage output of the s88 stimulator, which was outside the MEG chamber, was fed into two battery powered SIU7 stimulus isolation units inside the chamber to achieve constant current stimulation and photoelectric isolation. The SEP/SEF measurement run was divided into two parts with equal lengths and the direction of the current was reversed between the first and the second part to reduce stimulation artifacts. The stimulus strengths were adjusted to the lowest values, which achieved clear twitching of the thumb. The values used for this patient were 4.5 mA for the right and 5.7 mA for the left nerve during the first part, and 6 mA for the right and 6.5 mA for the left nerve during the second part. The total acquisition time required for both hands was 800 s and 950 events per hand were acquired with a stimulus onset asynchrony of 350 to 450 ms to avoid habituation and to avoid any synchronous activity at the prestimulus interval. The data was acquired with a sampling rate of

1200 Hz and an online lowpass filter of 300 Hz was applied to avoid aliasing.

After the acquisition, data was filtered with a notch filter for line voltage frequency (50 Hz and its harmonics) and a 20 to 250 Hz zero phase bandpass filter in order to increase the signal to noise ratio as suggested in [109]. The continuous run was divided into epochs that span 100 ms before and 200 ms after stimuli. Following visual inspection bad channels were deselected and epochs with artifacts in EEG and/or MEG were detected and excluded with a threshold based semi-automatic approach. The last step before source reconstruction was averaging the remaining epochs, which resulted in SNRs of 11.3 for SEP and 14.4 for SEF for the N20 and corresponding MEG component of the left median nerve stimulation.

3.1.8.2 Spontaneous measurements

Five runs with 480 seconds each were acquired with a 2400 Hz sampling rate and an online low pass filter of 600 Hz. No specific kind of stimulus was applied during the measurements and the patient was advised to relax and close her eyes to prevent blinking and eye movement artifacts.

Afterwards the acquired runs were filtered with the notch filter for the line voltage frequency and its harmonics. Then data was filtered with a zero phase bandpass filter from 1 to 100 Hz. Prior to any further evaluation, the runs were subsampled to 300 Hz because investigation of high frequency oscillations is not in the scope of this thesis and subsampling reduces the computational costs.

All preprocessing steps except the subsampling procedure, which was done with the CTF software (VSM MedTech Ltd.), were performed with the CURRY software.

3.1.9 Marking and clustering of interictal spikes

The epileptic spikes analyzed in this chapter were marked by three experienced clinical reviewers using the CURRY 7 software. All reviewers were supplied with health care records of the patient and with all prior knowledge available on patient's seizures before they marked the epileptic spikes according to their best clinical practice. The reviewers examined and marked the EEG signals recorded during the spontaneous runs and they were allowed to use different electrode montages as they do in clinical practice. The reviewers were asked to mark the negative peak of the spike because in the presence of noise distinguishing of other phases such as spike onset or middle of the rising flank in single spikes is not feasible. The initial clustering was done by the reviewers and it was according to the name of the electrode in which the reviewer observed the maximum

negativity.

Even with this procedure, not all spikes were marked right at the tip and the initial clustering of some of the spikes was not correct. The main reasons were that reviewers used different montages investigating the data, especially bipolar electrode montages that are widely used among epileptologists, and mistakes arose due to decreased attention, especially for data sets from patients who produce hundreds of spikes, as in this case. It is also important to mention that in usual clinical practice, which does not include source reconstruction and EEG is only used to obtain a rough estimation (usually on lobar level) of the epileptic region, marking the spikes exactly on the peak and achieving of a precise clustering are not as crucial. Although in this study clinical reviewers were marking the spikes very carefully by taking into account the above mentioned issues, most of the epileptologists do not have much experience on marking the spikes in a specific manner needed for this and similar studies. Thus, the corrections are often required. In order to address this issue, a Matlab program that semi-automatically corrects these errors was written and tested as part of a master thesis [173]. The program accepts the data after preprocessing and the markings exported from CURRY in ASCII format, checks all channels, which are direct neighbors to the channel selected by the reviewer and renames and moves the marker to the correct time and correct electrode. Details of this procedure and the improvements are explained in detail in [173]. The resulting spike clusters are given in Table 3.2 for each reviewer. As can be seen from this table, the number of temporal lobe spikes (FT9, F9) was much greater than the number of frontal spikes (AFz, Fz) and thus the temporal lobe spikes were analyzed in details in the rest of this section.

Table 3.2: The number of spikes marked by each reviewer. The spike types were named and produced by the semi-automatic clustering algorithm.

Spike type	Reviewer 1	Reviewer 2	Reviewer 3
FT9	208	10	132
F9	111	50	57
AFz	3	5	1
Fz	11	6	7

3.1.10 Forward approach

As explained in detail in Section 2.3.2.3, a Venant direct approach was used to solve the forward problem of EEG and MEG. In order to increase the computational efficiency, the FE transfer matrix approach and the Algebraic MultiGrid preconditioned

Conjugate Gradient (AMG-CG) solver were used along with standard piecewise trilinear basis functions [59]. The SimBio ⁸ software was used for these calculations. The calculation of the leadfield matrix for 74 channel EEG and 275 channel MEG took about one hour and six hours, respectively, on a standard workstation (Intel® Core i7-860 Processor, 2.80 GHz and 16 GB RAM).

3.1.11 Construction of the source space

The source space used in this chapter was calculated inside the gray matter without any orientation constraints. As it was explained in Section 2.3.2.3, the mathematical dipole was approximated by monopolar sources and sinks on neighboring FE mesh nodes in Venant approach, which was used in this thesis. This however, leads to numerical problems and unrealistic results if not all monopolar sources and sinks, used to model the dipole, reside inside the gray matter [81]. To avoid this problem, a custom written Matlab code was used that checks for each source space point if the closest node of the FE mesh belongs only to gray matter elements [113]. The final source space constructed with this code had 13,468 source space points with 2 mm average resolution (See Figure 3.8).

3.1.12 Source reconstruction of interictal spikes

The CURRY 7 software was used for source reconstructions after importing the source space (see Section 3.1.11) and the leadfield matrices (see Section 3.1.10) with approaches described in this chapter. The inverse approach of choice was the single dipole deviation scans, which will be abbreviated as DS in the rest of the thesis. As also explained in Section 2.3.3.2.1 DS result is a function that gives the residual variance (RV) (or $GOF=1-RV$) for each source space point and it is called DS map. In this thesis, the peak of each map was selected and only this peak was represented by a single dipole. Here a separate DS was calculated for each epileptic spike. This allowed to analyze the resulting spike clusters with regard to their centroids and focality as described in the next section. This choice was based on [12, 15], which showed the activated cortical areas during sharp waves to be very focal with their spatial positions changing in a dynamic manner. The appeal of the DS was, that the spread of the localizations might give an estimate on the focality of the irritative zone as also proposed by [150, 151]. The DS map (GOF for each source space point) obtained for an

⁸please see <https://www.mrt.uni-jena.de/simbio> and the integration into Fieldtrip: <http://fieldtrip.fcdonders.nl/development/simbio>

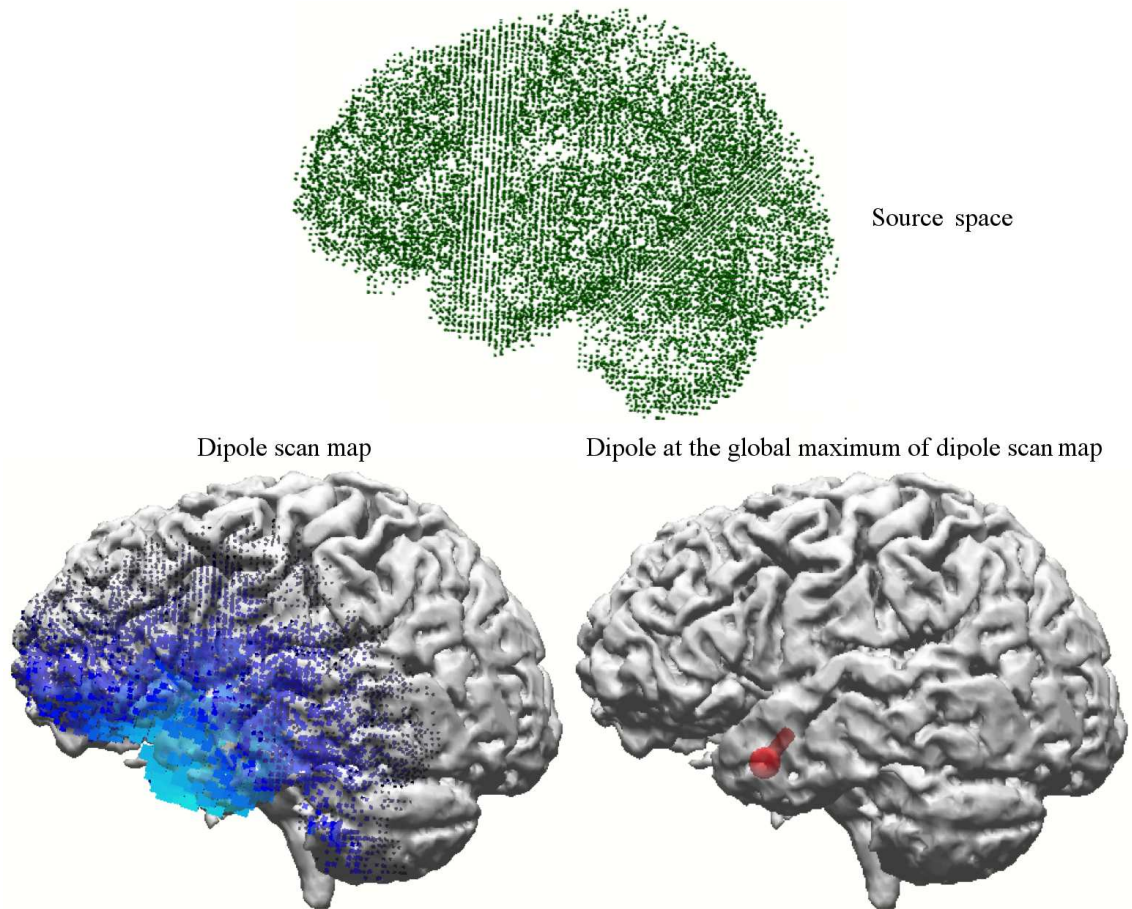


Figure 3.8: An example source space with 2 mm resolution limited to gray matter (top), the dipole scan map obtained for an epileptic spike (bottom left) and the final dipole when only visualizing the dipole that corresponds to the peak of the dipole scan map (bottom right). Note that bigger and brighter squares mean better metrics in these points and the metrics are shown only for points with GOF higher than 50 %.

epileptic spike (bottom left) and the single dipole at the peak of the DS map (bottom right) are shown in Figure 3.8. For epileptic spikes, the peak of the EEG spike was chosen as 0 ms. The time of interest in Figure 3.8 was -13 ms, which corresponds to the middle of the rising flank, and the noise was calculated using the time samples spanning from -200 ms to -70 ms.

In this chapter, EEG and EMEG DSs were not regularized, whereas MEG DSs were regularized according to [6] in order to suppress the influence of spatially high frequent data noise that might otherwise be strongly amplified in high amplitudes of reconstructed radial source orientations [174]. In order to perform combined source reconstruction, EEG and MEG signals were transferred to a unitless common space

(see Section 2.3.3.1) [6].

Most of the results of this study are provided in terms of centroid dipoles, which were used to represent and compare the results of groups of DS dipoles calculated from different spikes. The position of a centroid dipole was calculated as the point, which minimizes the sum of the Euclidian distances of all included individual DS dipoles. In addition to the centroid dipole, spread spheres were also calculated to get a rough estimation on the extent of the spread of DS dipoles that are represented by the centroid dipole. In Chapter 4 the focus will be more on the extent of the spread and each DS dipole will be shown separately instead of using a spread sphere. The details of this procedure are given *Algorithm 1*.

***Algorithm 1* (Computation of centroid dipole and spread sphere):**

1. Perform DS for all spikes which satisfy $\text{SNR} > 3$ within one spike cluster in a predefined head model.
 2. Determine DS dipoles with $\text{GOF} > 91\%$ and use only these in further steps.
 3. Calculate the centroid dipole and save the distances of each DS dipole to the centroid dipole.
 4. Using the distances saved in step three calculate the mean m_{dist} and standard deviation std_{dist} of these distances.
 5. Exclude the DS dipoles in step three in which the distance to the centroid dipole exceeds $m_{dist} + 2(std_{dist})$.
 6. Use the DS dipoles that satisfy the condition in step five to calculate the final centroid dipole, m_{dist} and std_{dist} .
 7. Use the position of the centroid dipole as the center and $m_{dist} + std_{dist}$ as the radius to calculate spread spheres.
-

The step by step representation of *Algorithm 1* is shown in Figure 3.9.

3.1.13 Skull conductivity calibration procedure using SEP and SEF data

As indicated in Section 3.1.7, the skull conductivity value, especially due to its high inter-individual variance, is quite controversial in the literature. However, an appropriate choice of it is crucial for successful source analysis of EEG and combined EEG/MEG data. While EEG source reconstructions are strongly influenced by changes in skull

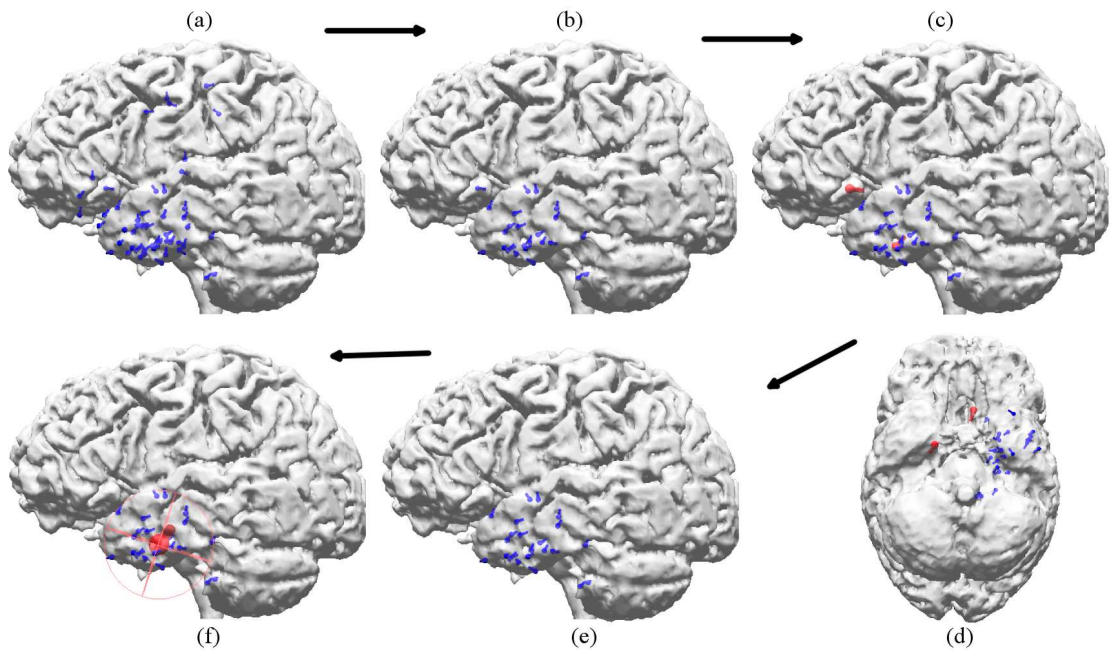


Figure 3.9: Steps of *Algorithm 1*: (a) DS dipoles (in blue) for $\text{SNR} > 3$ (step 1); (b) Spikes $\text{GOF} > 91\%$ (step 2); (c) and (d) Spikes excluded at step five (red dipoles); (e) Dipoles used to calculate the centroid dipole in step six; (f) Final centroid dipole and corresponding spread sphere from step seven (red dipole).

conductivity, the MEG is shown to be far less susceptible to it [42, 51]. In this section, a calibration procedure, which benefits from the different sensitivity profiles of the EEG and MEG, is explained in order to determine skull conductivity individually using the SEP and SEF data of the patient. Results of computer simulation studies for validating the approach and the first application to somatosensory evoked responses from a healthy subject were presented in [175] for single modality EEG and in [176] for combined EEG and MEG. In this chapter, the peak of the mean global field power in the SEP/SEF N20(m) component was used for calibrating the skull conductivity of the individual head model. The SEP/SEF N20 component was chosen for calibration procedure because of the four important properties listed below:

1. The position of this component, in 3b area of the primary somatosensory cortex in the postcentral sulcal wall, is well known from the literature [6, 42] and its central location allows both EEG and MEG to measure both poles. For example, if the underlying source was in temporal lobe, depending on the orientation of the source, one of the modalities might not be able to measure both poles, which would limit the accuracy of the source reconstructions significantly.

2. It is a relatively focal source and it can be represented with just a single dipole as also evidenced by hierarchical Bayesian method results which showed only a single source even though the number of sources was not limited [113]. This results in simpler EEG and MEG maps and simplifies the source reconstruction. This makes SEP/SEF more favorable to auditory evoked responses (N100m), in which the source reconstruction would be more complicated because two dipoles would be needed, again as also supported by the HBM results [113], to model the simultaneous activity in left and right planum temporale. Furthermore, for AEF, MEG can measure all four poles but for AEP in EEG two negative poles over frontal lobe merge into just one negative pole (due to interaction of the dipolar sources) and positive poles cannot be measured completely due to limited coverage of the EEG cap in inferior regions (see the AEP and AEF signals and topographies measured from a healthy subject in Chapter 6, Figure 6.3).
3. It is a quasi-tangential component so it can be assumed that both EEG and MEG can measure it well. Otherwise the MEG would not be able to measure most of the quasi-radial components that EEG measures and this would lead to errors in the calibration process (see the P14 component in Chapter 6, Figure 6.1. This component is clearly visible in EEG but not in MEG due to its quasi-radial orientation and deep location).
4. It is a quite stable component that can be measured in almost all subjects and patients. It is not influenced by factors such as attention or fatigue and N20 is even present in anesthetized patients [177].

The 100 ms pre-trigger interval was used for noise estimation for both SEP and SEF datasets. The calibration procedure used in this work can be summarized by means of *Algorithm 2*. In step 2.a) of *Algorithm 2*, the procedure uses the strength of the MEG in order to appropriately localize the primary somatosensory cortex even for less suitable skull conductivity parameters. Step 2.b) is necessary since o_1 and m_1 might be spurious in the case when the source is not optimally quasi-tangential. It uses the strength of the EEG to appropriately determine the source orientation. However, in case of inappropriate skull conductivity, m_2 will be spurious so that the SEF data is needed to determine the source magnitude in step 2.c).

Algorithm 2 (Conductivity calibration of the skull using SEP/SEF):

1. Define a discrete set of skull conductivity parameters: $\Sigma = \{\sigma_1, \sigma_2, \dots, \sigma_n\}$
 2. For each head model with skull conductivity parameter $\sigma_i, i = 1, \dots, n$:
 - a) Perform DS on SEF, calculate: location x , orientation o_1 and magnitude m_1 of the dipole.
 - b) Keep location x fixed and calculate o_2 and m_2 using a least squares fit to the SEP data.
 - c) Keep x and o_2 fixed, calculate m_3 using a least squares fit to the SEF data.
 - d) Calculate the RV of SEP for the dipole with location x , orientation o_2 and magnitude m_3 .
 - 3.) Output the conductivity in Σ that gives the lowest RV in step 2.d).
-

3.2 Results

The results section is divided into two subsections. In the first subsection, the skull conductivity calibration procedure based on the somatosensory evoked responses is carried out to determine individually optimized head models. The head models are then used in source analysis scenarios for the somatosensory evoked responses as well as, in subsection two, for the evaluation of the epileptic activity using single modality EEG or MEG or combined EEG/MEG source analysis scenarios.

3.2.1 Skull conductivity calibration and source analysis of the somatosensory evoked responses

Table 3.1 and Figure 3.10 show the results of *Algorithm 2* for the six compartment (head model *6C-Cal* in Table 3.1) and the three compartment (*3C-Cal* in Table 3.1) head models. In step 1 of *Algorithm 2*, a set of 11 different conductivity parameters were used in the range between 0.0016 S/m [37] and 0.033 S/m [171] (x-axis in Figure 3.10). In Figure 3.10, the differences in source reconstruction to the calibrated head models (indicated by the bar) when using other skull conductivity parameters are indicated by boxes with dashed frames. Differences are shown in source location x (top row, in mm), orientation o_2 (middle row, in degree) and strength m_2 (bottom row, in %). As expected, the source location x (from SEF in step 2.a)) and the orientation o_2 (from SEP in step 2.b)) of *Algorithm 2* are hardly depending on the skull conductivity

parameter, whereas skull conductivity, RV, and source strength m_2 are closely related to each other.

The value of the calibration procedure presented in this work can be further appreciated by studying the sensitivity of single modality SEP or SEF source analysis to changes in volume conductor modeling. Therefore the $6C_Cal$ DS results were used as reference, and they were compared to the reconstructions with other head models from Table 3.1. First, the data was examined for the $6C_70$ head model. As illustrated by a source localization difference of 7.2 mm (into the depth), an orientation change of 24 degrees and a magnitude reduction by 35 %, SEP source analysis depends significantly on skull conductivity, whereas SEF reconstructions were hardly affected (differences: 0 mm, 3.7 degrees, 2 %). Using of head model $3C_100$ led to source reconstruction differences of 7.2 mm, 8.9 degrees and a magnitude reduction by 60 % for the SEP, and to 4.9 mm, 25.3 degrees and a magnitude reduction by 23 % for the SEF. When head model $3C_Cal$ was used, these differences for the SEP data fell to 0 mm, 6.9 degrees and 21 % magnitude reduction, while the differences for the SEF data remained at a similar level with 4.9 mm, 25.8 degrees and 12 % magnitude reduction.

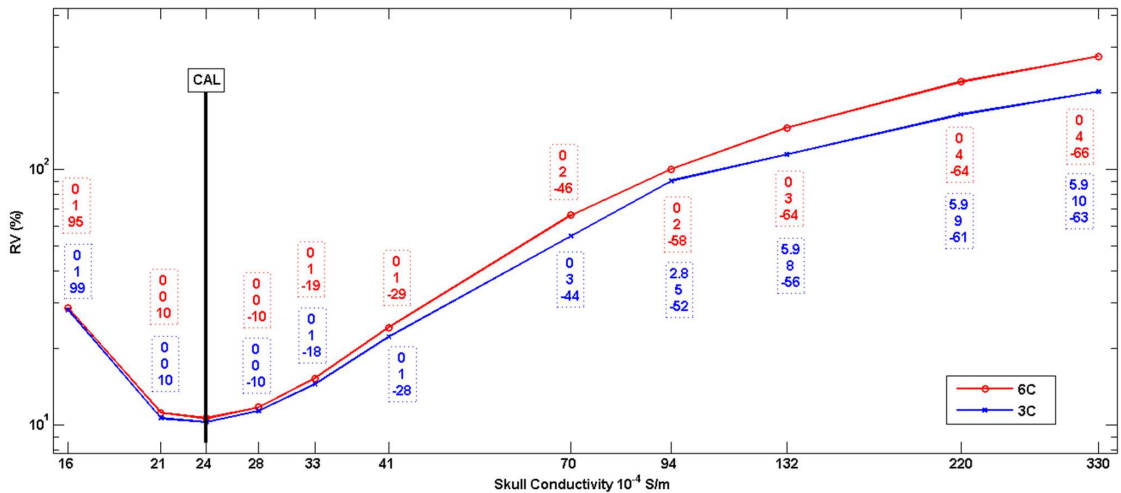


Figure 3.10: RV (in %) obtained from *Algorithm 2* in step 2.d. for different skull conductivity parameters for 6C (red) and 3C (blue) head models. The differences to the calibrated head models $6C_Cal$ and $3C_Cal$ (indicated by the black bar, see also Table 3.1) in source reconstruction are indicated by boxes with dashed frames: difference in source location x (top row, in mm), orientation o_2 (middle row, in degree) and strength m_2 (bottom row, in %).

3.2.2 Evaluation of interictal epileptic activity

3.2.2.1 Interictal spike marking, clustering and SNR improvement

The following investigations with regard to the evaluation of the epileptic activity focus on two left temporal spike types, with a maximum negativity at either FT9 or F9 electrodes, because of their high incidence. The three evaluators marked a total of 568 spikes and the clustering algorithm from Section 3.1.9 determined 350 FT9 and 218 F9 spikes.

A typical FT9 spike and its corresponding topographies for EEG and MEG can be seen in Figure 3.11. For EEG all electrodes, which were not assigned as bad channels, were used for source reconstruction. In the case of MEG and EMEG only the MEG signals measured by the sensors over the left hemisphere (129 channels) were included to calculations in DSs. This subselection resulted in improvements in SNRs and GOFs because the spontaneous brain activity, measured by the sensors over the right hemisphere, was no longer included in calculations. In EEG, it was not possible to make any subselection because the positive pole of the interictal spike was measured by the electrodes on the right hemisphere. In the case of MEG, both poles were covered by the chosen subset of sensors due to orthogonality of EEG and MEG poles and more focal topography in MEG (see Figure 3.11).

3.2.2.2 Effects of varying skull conductivity on source reconstruction for the epileptic activity

In this section the effects of varying skull conductivity on EEG or MEG source reconstruction of FT9 and F9 spikes were investigated. For this purpose, the *Algorithm 1* was used to compute the centroid dipoles and spread spheres for these two spike clusters using the six compartment head models from Table 3.1. In order to focus on skull modeling effects, the GOF selection criterion was used (step 2 in *Algorithm 1*) for the reference head model *6C_Cal* and the same spikes were used for the other head models.

In Figure 3.12, the resulting centroid dipoles and spread spheres for the FT9 cluster are plotted on the T1-MRI. Results for the F9 cluster are very similar (see Table 3.3) and therefore not shown in Figure 3.12. The *6C_Cal* centroid location was used for the selection of sagittal, coronal and axial MRI slices and the color-coded results were projected for the different head models on the chosen slices.

Table 3.3 complements Figure 3.12 in quantifying the differences in FT9 and F9

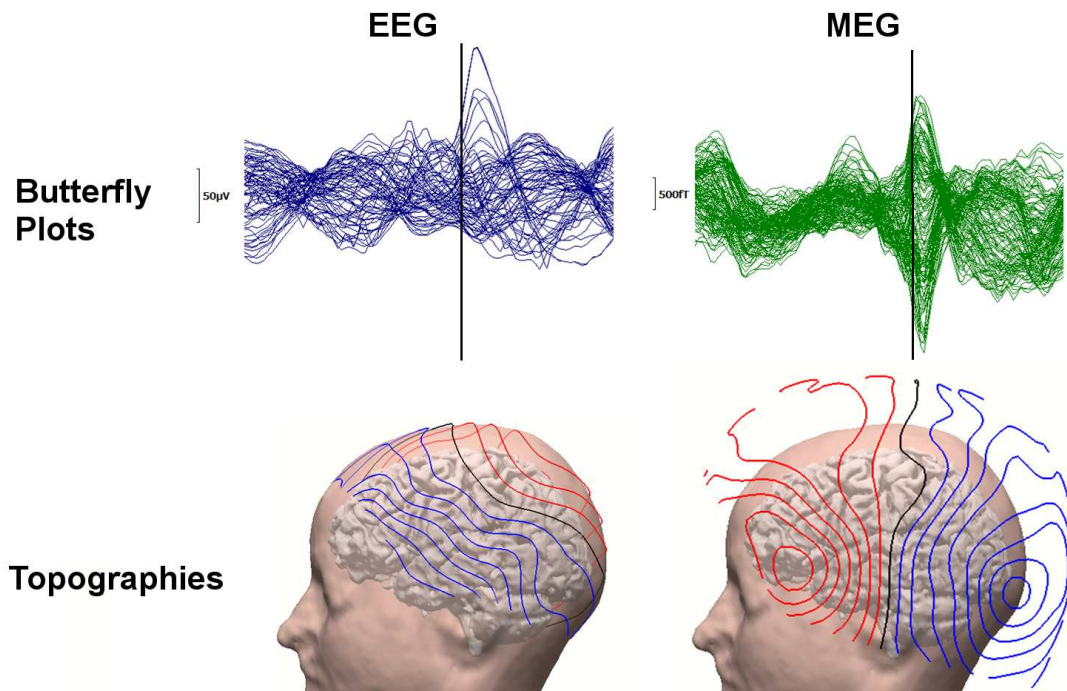


Figure 3.11: The waveform and topography of a representative FT9 spike. 71 channel EEG (left column) and 129 channel MEG (right column) butterfly plots (upper row, time-point -13 ms marked with a black line) and corresponding topographies from left view at time-point -13 ms plotted on individual brain and skin (bottom row).

spike cluster centroid results in terms of location, orientation and strength. In Table 3.3, results in head model *6C_Cal* are used as the reference and they are compared to the results of the other six compartment head models.

For the EEG, as Figure 3.12 and Table 3.3 show, the clear and systematic trend was observed: with increasing conductivity, the spike cluster centroids are localized deeper (here more mesial and superior) in the brain, while their strengths decrease. For the model with the highest conductivity *6C_330*, the centroid locations are deeper by 23.8 mm and 21.1 mm, and the strengths decrease by 66 % and 61 % for the FT9 and F9 spike clusters, respectively. The changes in orientations are moderate. The mean GOF (higher than 93 %) is similar for all these head models.

For the MEG, the centroid location changes for FT9 and F9 spike clusters are very moderate compared to the EEG, and the maximal changes in orientation and strength are 23 degrees and 13 %, respectively (Figure 3.12 and Table 3.3). The MEG results do not point to any systematic sensitivity of MEG localization to skull conductivity. Even if with 8 mm maximal location change, model *6C_132* points towards a slightly more

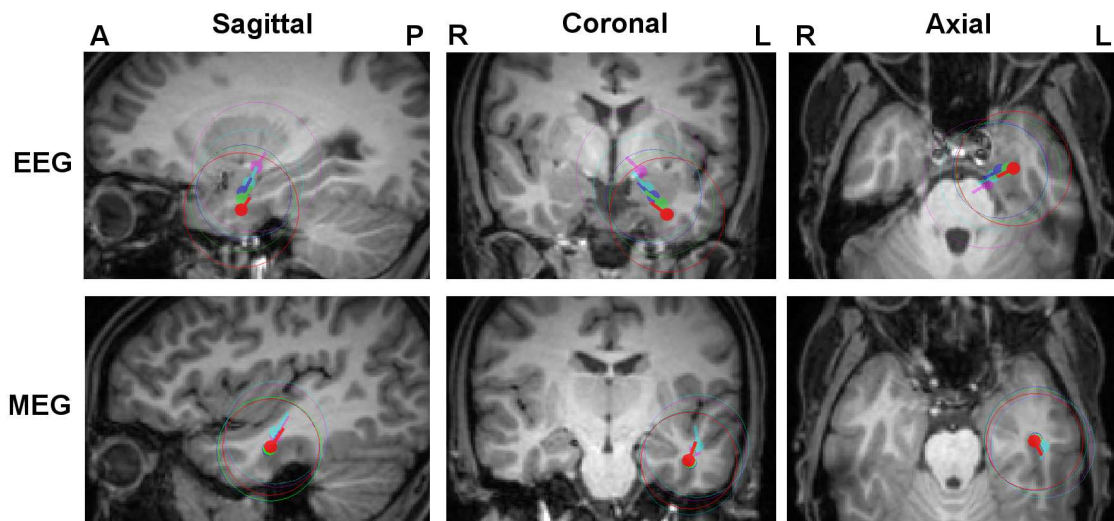


Figure 3.12: Influence of skull conductivity on EEG and MEG localizations. FT9 centroids and spread spheres plotted on T1-MRI for head models *6C_Cal* (red), *6C_41* (green), *6C_70* (blue), *6C_132* (cyan) and *6C_330* (magenta). The centroid dipole locations of *6C_Cal* were used for the selection of MRI slices and all results were projected on these slices.

Table 3.3: Sensitivity of EEG and MEG spike source reconstruction with regard to skull conductivity: Differences in centroid location, orientation and strength for FT9 and F9 spike clusters for different head models from Table 3.1 when compared to the results achieved for the reference head model *6C_Cal*.

Spike Type	Head Model	EEG			MEG		
		Location Diff. (mm)	Orientation Diff. (degree)	Strength Diff. (%)	Location Diff. (mm)	Orientation Diff. (degree)	Strength Diff. (%)
FT9	<i>6C_41</i>	5.7	2	-33	1.2	2	1
	<i>6C_70</i>	10.1	4	-45	2.0	4	0
	<i>6C_132</i>	15.5	11	-57	8.0	23	-10
	<i>6C_330</i>	23.8	8	-66	6.2	15	-13
F9	<i>6C_41</i>	6.0	3	-20	1.2	5	-4
	<i>6C_70</i>	9.9	4	-36	1.6	12	-8
	<i>6C_132</i>	14.5	6	-49	5.3	19	-1
	<i>6C_330</i>	21.1	5	-61	5.4	15	-3

superior and posterior centroid location, no trend can be observed since the change reduces to 6.2 mm for the head model with highest conductivity (*6C_330*). Again, no indicative changes are observed in terms of mean GOF (higher than 94 %) for varying conductivities.

In both EEG and MEG no clear trend in spread sphere diameters can be reported. The Euclidian distances between EEG and MEG centroids, as well as the ratio of

intersection of spread sphere volumes to their union are given in Table 3.4 for the six compartment head models with varying skull conductivities. For both spike types, it is clearly visible that the lower the skull conductivity, the smaller the Euclidean distance between EEG and MEG centroids (from 28.3 mm to 16.6 mm for FT9 and from 29.4 mm to 24.2 mm for F9) and the larger the ratio of intersecting spread sphere volume (from 24 % to 44 % for FT9 and from 13 % to 30 % for F9). It can thus be observed that the calibrated head model *6C_Cal* not only brings SEP and SEF data together as presented in Section 3.2.1, but also reduces the gap (especially in depth) between the EEG and the MEG spike cluster source reconstructions. However, it is also important to note that even after calibration, the EEG centroid is still considerably more anterior than the MEG centroid (see Chapter 4 for further explanations with regard to this important aspect).

Table 3.4: Euclidean distance between the EEG and MEG centroids (in mm) and, in parenthesis, the ratio of intersecting spread sphere volumes of EEG and MEG to their union (in percent) for FT9 and F9 spike clusters and for the different head models.

Spike Type	Head Models				
	<i>6C_Cal</i>	<i>6C_41</i>	<i>6C_70</i>	<i>6C_132</i>	<i>6C_330</i>
FT9	16.6 (44)	17.1 (40)	20.1 (28)	26.1 (19)	28.3 (24)
F9	24.2 (30)	24.2 (31)	26.3 (25)	29.9 (16)	29.4 (13)

In Figure 3.13, the DS dipole reconstructions of single spikes (that passed the GOF criterion, i.e., step 2 in *Algorithm 1*) (left column) as well as the corresponding centroid and spread spheres (right column) are presented. It is clearly visible that, on the one hand, the EEG and MEG centroids fall inside the intersecting part of their spread spheres for the calibrated head model *6C_Cal* (optimized volume conduction can thus reduce the distance between the modalities). However, on the other hand, due to the different sensitivity profiles, a remaining distance between EEG and MEG reconstructions, especially in anterior-posterior direction, persists (see Chapter 4 for further explanations in this regard).

3.2.2.3 Effects of six versus three compartment head modeling on EEG and MEG spike source reconstruction

In this section, the EEG and MEG source reconstructions using the individually calibrated six compartment head model *6C_Cal* are compared to the reconstructions using

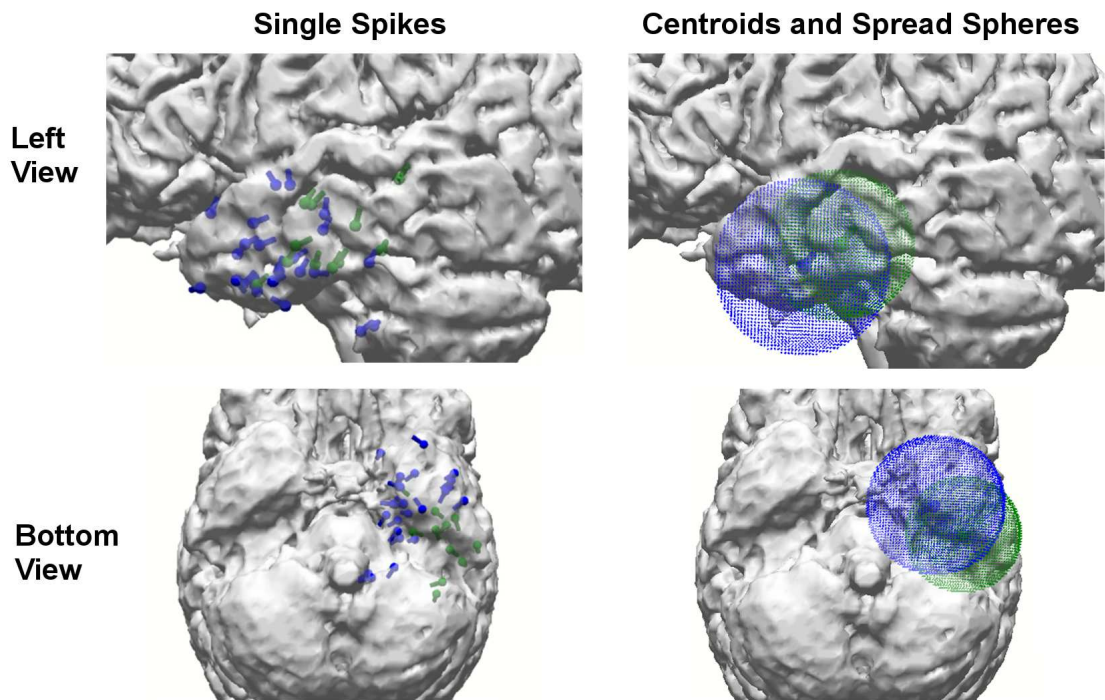


Figure 3.13: Single spike localizations and corresponding centroid and spread sphere. FT9 spike DS reconstructions for EEG (blue) and MEG (green) using the calibrated head model $6C_Cal$ at time-point -13ms: DS dipole reconstruction results of all single spikes that passed step two of *Algorithm 1* (left) and corresponding cluster centroids and spread spheres (right).

three compartment (3C) isotropic head models. Two 3C models, presented in Table 3.1, were considered for this comparison, namely the current standard head model in source analysis, model $3C_100$, as well as the calibrated model $3C_Cal$ as determined in Section 3.2.1.

Figure 3.14 shows the resulting centroid dipoles and spread spheres for the FT9 cluster plotted on the T1 MRI. Results for the F9 cluster are very similar (see Table 3.5) and are therefore not shown in Figure 3.14. Again the $6C_Cal$ centroid location was used for the selection of sagittal, coronal and axial MRI slices and the color-coded results for the different head models were projected on the chosen slices.

Table 3.5 complements Figure 3.14 in quantifying the differences in centroid results in terms of location, orientation and strength. In Table 3.5, results in head model $6C_Cal$ were used as the reference and were compared to the results of the 3C head models.

For the EEG, for FT9 and F9 spikes the differences in centroid locations between $3C_100$ and $6C_Cal$ correspond to 16.2 and 14.6 mm, respectively. Additionally, considerable

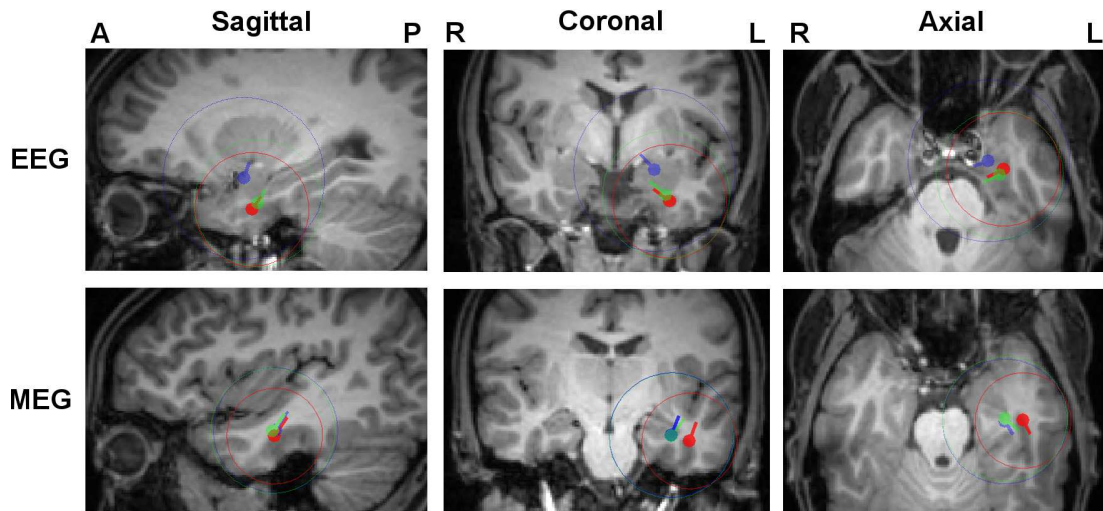


Figure 3.14: Comparison of three and six compartment head models. FT9 centroids and spread spheres plotted on T1-MRI for head models $6C_Cal$ (red), $3C_Cal$ (green) and $3C_100$ (blue). The centroid locations of $6C_Cal$ were used for the selection of MRI slices and all results were projected on these slices.

Table 3.5: Sensitivity of EEG and MEG spike source reconstruction with regard to three compartment (3C) or six compartment (6C) head modeling: Differences in centroid location, orientation and strength for FT9 and F9 spike clusters for the two 3C head models from Table 1 when compared to the results achieved with the reference head model $6C_Cal$.

Spike Type	Head Model	EEG			MEG		
		Location Diff. (mm)	Orientation Diff. (degree)	Strength Diff. (%)	Location Diff. (mm)	Orientation Diff. (degree)	Strength Diff. (%)
FT9	$3C_100$	16.2	13.1	-79	8.7	2.2	43
	$3C_Cal$	4.4	3.8	-36	8.6	15.0	67
F9	$3C_100$	14.6	17.8	-77	8.6	4.1	40
	$3C_Cal$	3.2	12.5	-28	9.1	7.0	72

differences in centroid dipole orientations, much reduced strengths, and strongly increased spread spheres can be reported for head model $3C_100$. Skull conductivity calibration (head model $3C_Cal$) was found to reduce these differences significantly, for centroid locations to 4.4 and 3.2 mm and orientations to 3.8 and 12.5 degrees for FT9 and F9 spike clusters, respectively. Even though the differences in centroid strengths were also reduced by 36 % and 28 % magnitude, differences remain at a significant level.

The situation is different for the MEG, where skull conductivity calibration had

hardly any effect on the localization of the sources. Figure 3.14 and Table 3.5 show that centroids and spread spheres were nearly identical for models $3C_{100}$ and $3C_{Cal}$. However, in comparison to $6C_{Cal}$ they showed about 9 mm and more than 40 %, differences in location and strength, respectively, for both FT9 and F9 spike clusters. Please also note for the MEG the higher strength and orientation differences for $3C_{Cal}$ in comparison to $3C_{100}$. This only shows the weakness of MEG to accurately reconstruct radial source orientation and strength components in the presence of noise. Additionally, significantly larger spread sphere diameters in 3C than in 6C models can be reported here.

3.2.2.4 Comparison of EMEG to single modality EEG or MEG source reconstruction

In previous sections, a deep insight was gained about the factors that influence EEG and MEG source analysis with a special focus on volume conduction effects due to geometry and/or conductivity modeling changes as well as effects, which were mainly due to limited SNR in measurements. The gained knowledge can now be used to study combined EEG/MEG source analysis in comparison to single modality EEG or MEG reconstructions of the epileptic spike activity. In the further analysis, for this comparison, the most advanced head model $6C_{Cal}$ from Table 3.1 was used.

Figure 3.15 and Table 3.6 show the results of *Algorithm 1* for FT9 and F9 spike cluster centroid dipole and spread sphere computations for EMEG and for the single modalities EEG and MEG. In Table 3.6, the EMEG results serve as the reference and differences in centroid dipole locations, orientations and strengths are presented for each of the single modalities, EEG and MEG.

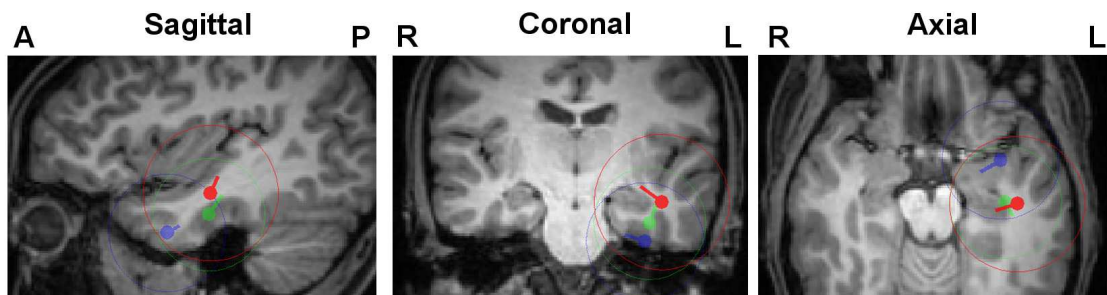


Figure 3.15: Differences of EEG, MEG and EMEG localizations. FT9 centroids and spread spheres plotted on T1-MRI for EMEG (red), MEG (green) and EEG (blue) using head model $6C_{Cal}$. The centroid location of the combined reconstruction was used for the selection of MRI slices and all results were projected on these slices.

Table 3.6: Comparison of EEG and MEG spike cluster centroid results with the results of EMEG using the reference head model *6C_Cal*: Differences in centroid dipole location, orientation and strength for FT9 and F9 spike clusters.

Spike Type	Modality	Difference from EMEG		
		Location Diff. (mm)	Orientation Diff. (degree)	Strength Diff. (%)
FT9	EEG	24.2	26	-7
	MEG	9.8	70	-74
F9	EEG	30.9	21	63
	MEG	9.2	79	-78

Figure 3.15 and Table 3.6 show that the EMEG centroid dipoles are localized about a factor of 2.5 (FT9) and even about 3.4 (F9) closer to the MEG than to the EEG centroid locations. However, with 9.8 mm for FT9 and 9.2 mm for F9, there is still a considerable distance between the EMEG and the MEG centroid localizations. The localization was thus not just totally dominated by the MEG, but was rather a complicated interplay of a main MEG and still a considerable EEG part, pointing to a considerable radial source component as also clearly visible in Figure 3.15. EMEG source orientation and strength results are influenced more by the EEG part, as Figure 3.15 and Table 3.6 clearly show, while with orientation differences of 70 degrees and more, it gets clear that the MEG is mainly missing the radial source component.

As Figure 3.15 shows, the spread sphere diameters of EMEG (29 mm) were slightly larger than those of EEG (25 mm) and MEG (24 mm).

As a final result, Table 3.7 shows the differences in centroid reconstructions in combined EEG/MEG scenarios, using the six compartment models of Table 3.1 instead of the reference head model *6C_Cal*. This table shows a clear trend of increasing source location differences with increasing skull conductivity. A more detailed analysis showed that higher skull conductivity led to deeper source localizations, i.e., similar to the EEG centroid results in Figure 3.12, quasi-radially into the deeper brain regions. However, with maximal differences of 7.8 mm (FT9) and 13.9 mm (F9) for the head model with highest skull conductivity (*6C_330*), the differences are considerably lower than for the EEG (23.8 mm for FT9 and 21.1 mm for F9, see Table 3.3). Table 3.7 shows decreasing source strength with increasing skull conductivity, but with 62 % (FT9) and 52 % (F9) for model *6C_330*, the reductions are smaller than for the EEG (66 % for FT9 and 61 % for F9, see Table 3.3). Interestingly, Table 3.7 now additionally shows a clear and systematic trend of increasing orientation differences with

maximums as 17 degrees (FT9) and 13 degrees (F9) for model *6C_330*, while such a trend could not be observed for the EEG in Table 3.3. A more detailed analysis (using the singular value decomposition of the MEG lead field matrix to determine the quasi-radial orientation component) revealed a decreasing quasi-radial and a constant quasi-tangential centroid component with increasing skull conductivity. The GOF for model *6C_Cal* for combined EEG/MEG is 95 % (FT9) and 93 % (F9). As Table 3.7 shows, for FT9 spikes, the GOF stays mainly on this high level for all 6C head models, while for the F9 spike cluster, a trend towards decreasing GOF with increasing skull conductivity can be noted with a 6 % reduction, i.e., only 87 % GOF, for model *6C_330*.

Table 3.7: Sensitivity of EMEG spike source reconstruction with regard to skull conductivity: Differences in centroid location, orientation, strength and GOF for FT9 and F9 spike clusters for different head models from Table 3.1 when compared to the results achieved for the reference head model *6C_Cal*.

Spike Type	Head Model	EMEG			
		Location Diff. (mm)	Orientation Diff. (degree)	Strength Diff. (%)	GOF Diff. (%)
FT9	<i>6C_41</i>	1.8	3	-26	0
	<i>6C_70</i>	1.7	8	-55	0
	<i>6C_132</i>	3.2	13	-56	0
	<i>6C_330</i>	7.8	17	-62	-1
F9	<i>6C_41</i>	3.3	1	-24	0
	<i>6C_70</i>	6.1	9	-40	-1
	<i>6C_132</i>	11.6	11	-42	-4
	<i>6C_330</i>	13.9	13	-52	-6

3.3 Discussion

In this chapter a new analysis pipeline for combined EEG/MEG as well as single modality EEG or MEG source reconstruction based on a calibrated realistic head model generated from T1, T2 and DT MRI data was presented. Inspired by [29,30,72,73], an algorithm (*Algorithm 2* in Section 3.1.13) was developed and applied for skull conductivity calibration using simultaneously acquired SEP/SEF data. The measurement

time, which was divided as one block for EEG/MEG and one for MRI, was easily manageable for the patient. As input, this procedure needs an accurately segmented model of the head, and in particular, a geometrically correct version of the skull. Whereas computer tomography provides better definition of hard tissues such as bones due to high radiation exposure, its use on humans is not justified with the only purpose of an improved skull modeling for EEG and MEG source analysis [60, 67, 142]. In this chapter, a combination of T1 MRI, which suits to the identification of soft tissues (scalp, brain), and T2 MRI, enabling the segmentation of the inner skull surface and the distinction between skull compacta and spongiosa, was used. The methodology was then applied in a case study to source analysis of interictal epileptic activity of a patient suffering from medically-intractable epilepsy, but could as well be used for any other simultaneous EEG/MEG study in the neuroscientific field (the seven minutes additional measurement time, which was easily manageable even for the patient of this study, should not form an obstacle in a group study with healthy subjects). In investigations presented here, a variety of head models were used, which differed in terms of skull conductivity or in the number of distinguished tissue types (Table 3.1). The most advanced head model, the six compartment (6C) calibrated model *6C-Cal*, consists of the tissues scalp, skull compacta, skull spongiosa, CSF, gray and white matter, uses the individually-optimized skull conductivity parameters from the calibration procedure, and accounts for the anisotropy of the brain tissues. The method presented in this study considers the different sensitivity profiles of the EEG and MEG to properties of the volume conductor and source components (see also [6, 46]). Therefore, before investigating combined EEG/MEG scenarios, the important parameters that influence EEG and/or MEG source reconstruction were studied.

The first investigation focused on a comparison of EEG and MEG with regard to a parameter to which they have the most distinct sensitivity and which, as shown in Table 3.1, has considerable interindividual variability: the skull conductivity. For the same underlying source, due to different sensitivity profiles in volume conduction, the differences between EEG and MEG source reconstructions could increase in case of an erroneously modeled skull compartment. Therefore, a multimodal MRI procedure for skull geometry modeling and *Algorithm 2* based on SEP/SEF data to individually estimate skull conductivity was proposed. The new methodology was then applied to the reconstruction of the SEP and SEF N20 component (Section 3.2.1) and to the detection of spontaneous interictal epileptic activity (Section 3.2.2.2). It was found that for the MEG, skull conductivity changes had no effect in terms of N20 localization, but had non-negligible effects on source orientation and strength. This can be explained with

the well-known instability of MEG in reconstructing quasi-radial source magnitude. In contrast, EEG results differed significantly in terms of N20 location, orientation and strength: the higher the skull conductivity, the deeper the localization and the smaller the source magnitude. Besides the differences (6C versus 3C) discussed further below, these results are therefore mainly in agreement with former 3C head modeling approaches [6, 42, 76]. For the epileptic activity, EEG and MEG were compared, and the effects of varying skull conductivities were investigated in Section 3.2.2.2. For the EEG, a clear trend of deeper source localizations and reduced source amplitudes can be reported with increasing skull conductivity. Table 3.3 showed that location differences of more than 21 mm can result in case of erroneously chosen skull conductivity. MEG source reconstructions of the epileptic activity did not show a trend similar to EEG and the reconstruction differences with changing conductivity were significantly smaller. A closer look at the largest MEG centroid localization change in Table 3.3 (model *6C_132*) confirmed that this difference is not a consequence of a systematic sensitivity of MEG to skull conductivity changes, but mainly is due to the interplay of the high noise in spike data with the chosen procedure of centroid calculation, namely preselecting single spikes with regard to their SNR and GOF, performing single spike and single dipole deviation scans (DSs), and averaging the global peak of the resulting GOF function for computing spike cluster centroids. Figure 3.16 illustrates this problem well. In this figure the positions of three source space points with very similar (best three) GOF values for MEG and head model *6C_132* are shown. The 0.03 % GOF difference between the red and the blue cubes results in 9.8 mm difference in the position of the global maximum and thus the resulting dipole. Since the number of spikes that passed the *Algorithm 1* were limited, even one or two spike localizations like this might result in a considerable shift in the final centroid location (see change in the MEG centroid for *6C_132* in Table 3.3). This point might be especially important for advanced head models presented in this work, in which unlike three compartment BEM the brain is not modeled as a homogeneous compartment but has a complicated structure that includes WM, GM and even conductivity anisotropy. As explained above, MEG orientation and strength components should also be interpreted with caution because of the poor sensitivity of MEG to radial source components.

Regarding the distance between EEG and MEG localizations, Table 3.4 demonstrates that the skull conductivity calibrated model *6C_Cal* reduces the distance (especially the difference in depth) between EEG and MEG localizations and maximizes the ratio of the intersecting spread spheres. However, localization differences might still resist like in the case of this study, and these discrepancies can be explained by

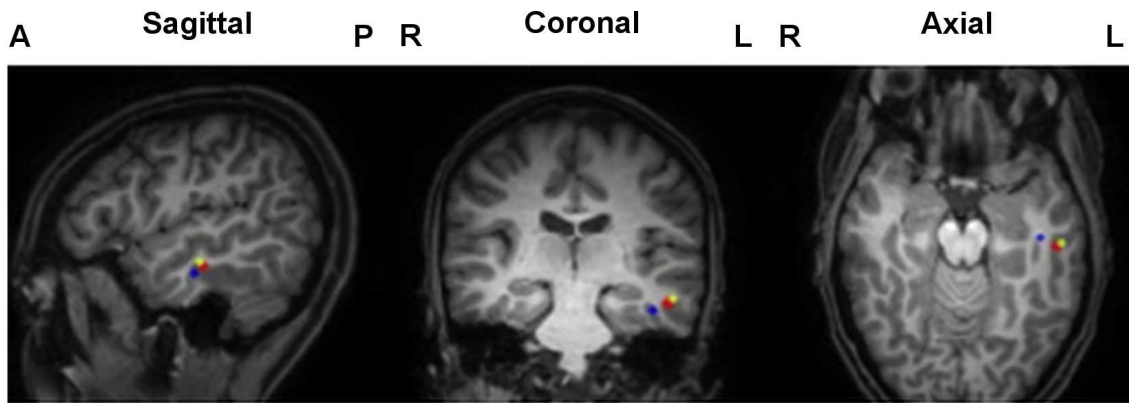


Figure 3.16: Best three DS locations in terms of metrics (cubes with color) for an exemplary MEG dipole scan for head model *6C_132* plotted on T1 MRI. The GOF values for these three locations are very close to each other (95.79 % (red), 95.76 % (blue) and 95.33 % (yellow)) but this small difference of (0.03 %) results in 9.8 mm difference (distance between the red and blue cubes) in the final dipole.

the different sensitivity profiles of EEG and MEG, where MEG mainly sees the more tangential parts of an extended cortical patch (the more posterior localization in results of this study) and EEG detects more the radial parts (the more anterior polar localization in results of this study), as discussed further in Chapter 4 and by [178] and [18].

Another goal of this study was to make a comparison between 6C and 3C head modeling. The *3C_100* head model can be considered as the current standard in source analysis [59, 67]. For the reconstruction of the N20 component in the SEP and SEF scenarios in Section 3.2.1, the significant differences between *3C_100* and *6C_Cal* reconstructions for both EEG and MEG were found. While skull conductivity calibration (model *3C_Cal*) brought no significant change for the MEG (i.e., the MEG differences between *6C_Cal* and *3C_Cal* remained at a significant level), it enabled the reduction of depth localization differences for EEG considerably, while differences in source orientation and strength persisted. In the case of epileptic activity a similar behavior was observed (Section 3.2.2.3). For MEG, significant differences can be reported between *6C_Cal* and *3C_100*, which could again not be reduced by means of skull conductivity calibration. Even if, for the EEG, up to 16 mm differences in centroid locations between *6C_Cal* and *3C_100* could be reduced to less than 5 mm between *6C_Cal* and *3C_Cal*, considerable differences in centroid orientations and strengths persisted. It can be therefore summarize that, for EEG localization, skull conductivity is the dominating parameter, while the highly conducting CSF and brain anisotropy contribute

significantly to EEG and MEG source orientation and strength components (see also [51, 70, 78, 79, 85, 179]). If the sources have a considerable radial orientation component like in case of spike data presented in this study, CSF and brain conductivities can additionally influence MEG localization (about 9 mm in Table 3.5), but the more quasi-tangential the source is, the less MEG is influenced by these parameters (less than 5 mm for the N20 SEF reconstruction). While the modeling of skull inhomogeneity by means of a distinction between skull compacta and spongiosa might be important for EEG in other situations [67], it was not a crucial factor here (see Figure 3.10 and Section 3.2.2.3), because the major spongiosa areas were far from the central and temporal source space areas for this patient (see coronal slice in Figure 3.3).

The effects of using different head models were found to be significantly higher for the epileptic activity in the temporal area in comparison to the somatosensory evoked responses. In the light of the existing literature (see, e.g. [6, 51, 67, 91, 133]), this is not too astonishing. For example, in [91], the comparison of a spherical with a 3C realistically-shaped head model clearly showed larger MEG volume conduction effects for fronto-temporal and deep sources. Huiskamp et al. [133] showed that EEG sources arising from temporal regions are especially susceptible to geometrically inaccurate skull models. Possible explanations are: a) the skull in the temporal area has a higher concavity than in the area of the central sulcus, leading to larger volume conduction effects; b) the underlying source of the SEP/SEF N20 component is mainly a single superficial dipole with quasi-tangential orientation where especially MEG is very sensitive to and therefore less prone to errors due to simplifications in volume conduction (see Figure 3.10). In contrast, both FT9 and F9 temporal spike sources were deeper and had a considerable radial orientation component, rendering especially the MEG more susceptible to volume conduction effects; c) the EEG and MEG sensor coverage is much better above the central sulcus, where both poles are clearly visible in the SEP/SEF data. For the spikes in temporal lobe, some of the activity, which was supposed to appear at inferior regions, could not be measured due to the limited coverage of basal brain regions with the used EEG cap.

The results in Sections 3.2.1 and 3.2.2.4 clearly show that the combined EEG/MEG centroid results profit from the MEG which contains important localizational information for the tangential source components, an information which is even not depending much on the accuracy of skull (and skin) modeling. In contrast, the combined EEG/MEG centroid results profit from the EEG, which could add the information that was mainly missing in the MEG, namely the localizational information about the radial source components, and the full information on source orientation and strength

components (see also [6, 42, 46, 47, 48, 51, 76]). However, the latter statement has the constraint of an underlying accurate and individually-calibrated head volume conductor model, since with more than 21 mm localization differences (see Table 3.3) it was found that EEG localizations highly depend on skull conductivity parameters in accordance with the literature [67, 180].

Source localization techniques have error margins that are proportional to the inverse of the SNR. Since single spike activity has a significantly lower SNR than averaged somatosensory responses, its localization is less reliable and therefore not always sufficient for precise localization of the epileptic tissue. It has, however, been reported that also the orientation of the dipole possesses localizational information regarding the epileptic tissue [142, 144]. In [142] the importance of dipole orientation for temporal spikes was stressed, where the authors showed different seizure freedom ratios for patients with horizontally and vertically oriented dipoles. In [144] all central and interhemispheric, and 73 % of the temporal spike dipoles (positive part) were observed to be oriented towards the epileptogenic side. The MEG source orientations in Section 3.2.2.4 were almost orthogonal to the combined EEG/MEG orientations, because MEG could hardly measure the quasi-radial orientation components of the underlying sources. Combined EEG/MEG thus contains information which is missing in single modality EEG or MEG and this information can be exploited to achieve improved source reconstructions not only with regard to localization, but also with regard to source orientation [142, 144]. However, as it was shown in comparisons in this study, especially source orientation and strength components are susceptible to simplifications or modeling errors with regard to the CSF and brain compartments and in many situations, the distinction between skull spongiosa and compacta might be of high importance [67], too. These arguments underline the need to further validate and evaluate the accuracy of anisotropic 6C volume conductor modeling in future investigations.

The results of combined EEG/MEG in the presence of erroneously chosen skull conductivity (Table 3.7) can be interpreted in the following way: the MEG part of the combined EEG/MEG dataset stabilized especially the depth localization. Localizations quasi-radially into the depth of the brain could be much reduced (e.g., for the FT9 spike cluster centroid from 23.8 mm for EEG in Table 3.3 down to 7.8 mm for combined EEG/MEG in Table 3.7). In order to simultaneously achieve a high GOF to both datasets, the strength of the radial centroid component was reduced for higher skull conductivities (by means of a significant reduction of overall centroid strength and an orientation change towards more quasi-tangential orientation). In this way, high GOF to the EEG data could still be achieved, while keeping the magnitude of

the tangential source component mainly unchanged in order not to change GOF to the MEG data (Table 3.7). Because of the distinct quasi-tangential orientation component of the FT9 spikes, this procedure worked out nearly without any loss in GOF to the combined EEG/MEG data, even in case of highly erroneous skull conductivity. However, GOF reduced by 6 % for the F9 spikes because of their more distinct quasi-radial orientation component. The comparison of the results presented in Table 3.7 with those in Table 3.3 thus represents an advantage of combined EEG/MEG versus single modality EEG or MEG in practical situations. In case of a moderate error in skull conductivity modeling, combined EEG/MEG source analysis can still profit from the strength of the MEG to accurately localize the tangential source component, while the EEG can still contribute much to better localize radial source components and determine source orientation and strength (see also Figure 3.15 and Table 3.6). However, significant errors in skull modeling will be reflected by a complicated interplay of errors in location (especially in depth), orientation and strength of EEG sources, and in the worst case a significantly reduced GOF to the combined EEG/MEG datasets. Therefore it is highly recommended to calibrate skull conductivity using additionally acquired SEP/SEF data.

As described in detail in Section 3.2.2.4, in a first step, three epileptologists used a subset of electrodes to mark the epileptic activity based on the current clinical agreement. In a second step, and using the complete set of sensors, the spikes were then clustered according to the electrode where the maximum negativity in referential montage (common average) occurred. In this way, two different spike types were found, FT9 and F9, which mainly differed with regard to their orientation components. This shows that it might not be sufficient to use the subset of sensors in step one also for step two, the clustering. For example, if the clustering montage did not have an FT9 but just an F9 electrode, FT9 spikes would have been clustered as F9 because the evaluator would have seen the maximum negativity at this electrode. Such issues in clustering process might cause errors in centroid as well as in spread sphere computations. When using spike averaging, it would lead to smeared peaks and SNR reductions. For the purpose of this study, the clustering procedure used in this work led to satisfying results. However, in Section 4.1.1, other concepts such as source montages were also evaluated[181].

In order to avoid effects that are just due to insufficient SNR, here only the spikes with minimal SNR of 3 and GOF of 91 % (*Algorithm 1*) were considered. In this way, still despite low SNR in the single spike data and the resulting lower reliability of source reconstruction results, the effects of EEG, MEG as well as combined EEG/MEG

volume conduction on the reconstruction of the spike clusters could be worked out. These volume conduction effects thus dominate over higher noise and need to be taken into account even in single spike source analysis, while they should appear in an even purer form and accordingly be taken into account when working with averaged spike data. Motivated by the results of [16], in future studies, it would be very interesting to investigate volume conduction effects in EEG, MEG and combined EEG/MEG studies using single spike versus averaged spike reconstructions.

A further important choice when reconstructing epileptic spike activity is the selection of the time-point or time-interval for the localization of the spikes. The peak of the spike indicates the highest degree of neuronal synchronicity and thus better SNRs, but this location might already have been subject to propagation. Therefore, here the middle of the rising flank was selected from the averaged spikes as a time-point for later single spike reconstructions because it was shown to be favorable when compared to the reconstruction at the peak of the spike [154]. Due to higher SNR at the peak of the spike, the presented volume conduction effects could probably be presented in even a clearer form, e.g., the presented effects on MEG in Table 3.3 and 4 were found to be at least partly due to the high noise level and not only due to MEG volume conduction effects. Since reconstructions will be dominated more and more by noise when approaching the area of low SNR at the beginning of the spike, at such early time-points, a combination of the here presented methodology with spike averaging strategies seems to be mandatory and the effects of spike averaging will be deeply investigated in Chapter 4.

It was shown in this study that by means of using a calibrated six compartment head model, it was possible to significantly reduce the distance in localization, orientation and strength between EEG and MEG centroids as well as increasing the intersection of their spread spheres (see Table 3.4 and Section 3.2.2.4). Reasons for the remaining distance between EEG and MEG reconstructions are the following: none of the single modality EEG or MEG contains the full information about the sources, MEG mainly misses the quasi-radial source components and for low SNRs EEG is rather weak in reconstructing the quasi-tangential ones. A remaining difference thus should be expected even with the best head modeling. This problem can be reduced when fusing both modalities in combined EEG/MEG source analysis, as described in Section 3.2.2.4.

Although the results of this study show major effects of skull conductivity calibration as proposed here, not all institutes have access to MEG. In these cases, for estimating skull conductivity, it would be suggested either to use a similar procedure based on

only good quality SEP data as proposed in [175] or to use an electrical impedance tomography (EIT) based approach as described by [182].

4 Study II: Comparison of EEG, MEG and EMEG Localizations of Epileptic Activity at Different Propagation Phases via Sub-Averages

After investigating the effects of volume conduction in the previous chapter, here the focus was on improving the accuracy of epilepsy source analysis by means of averaging and combination of EEG and MEG. A special attention was given to the onset phase of the spike because in later phases the epileptic activity might have already been subject to propagation. The main difficulty with source reconstruction at the spike onset is obtaining accurate results at these low SNR time-instants. The obvious solution to this problem is averaging the spikes with similar topography but unlike evoked responses epileptic spikes do not origin from exactly the same location [12, 15] and this might lead to suboptimal results.

The decision between localizing each single epileptic spike separately and averaging spikes with similar topographies before source reconstruction is a highly disputed issue in presurgical epilepsy diagnosis, and both approaches have their merits and drawbacks. Single spike localizations might be used to estimate the size of the irritative zone [10, 11, 12, 13, 14, 15]. However, these localizations suffer from low SNRs, as also will be shown in Section 4.2.1. Alternatively, averaging similar spikes might increase the SNR and thus, the reliability of the localizations remarkably [16], but information on the extent might get lost. In this thesis, motivated by the findings of Bast et al. [16] and Wennberg and Cheney [17] for EEG, and Wennberg and Cheney [18] for MEG, multiple sub-averages were calculated in order to investigate the effects of SNR and averaging on EEG, MEG and EMEG source reconstructions. This approach allowed comparing the effects of averaging and the resulting SNR in a step-by-step fashion.

The results and methods explained in this chapter were recently published in [183].

4.1 Methods

4.1.1 Detection of the epileptic spikes

As a first step the three runs with minimal head movement were filtered with an 80 Hz low pass filter, resampled to 250 Hz, concatenated and corrected for ECG artifacts using BESA software (BESA GmbH, Gräfelfing, Germany). For this purpose, the ECG channel was selected for detection and averaging, and principal component analysis was used for minimizing the artifacts. The measurements were then examined and epileptic spikes were marked by three clinical reviewers. From these markings, ten clear left temporal spikes, which belong to the most frequent spike type, were selected using source montage (temporal) and averaged. The averaged spike was used in BESA template search in order to find further spike candidates [181]. Selecting left temporal polar, basal and lateral channels from the temporal source montage for template search ensured the detection of spikes with similar location and orientation. After visual inspection, 200 left temporal spikes without any clear artifacts (e.g., eye-blinks), were selected for further analysis. The butterfly plots of the grand-averaged (all 200 spikes) EEG and MEG signals, 4 solid vertical lines with different colors indicating the important instants in time, namely -33, -23, -13 and -3 ms, and the respective topographies at 0 ms (signal peak in EEG shown with dashed vertical line) after averaging are visualized in Figure 4.1. The results shown in this figure will be discussed later in this chapter.

4.1.2 Sub-averaging

Ten sub-average groups each with 200 realizations were constructed from the 200 single spikes detected in the previous section. Each realization in each sub-average group was an averaged signal that was calculated using the same number of single spikes and the name of the sub-average group was determined by this number. For example, in the Av10 sub-average group there were 200 Av10 realizations, each of them was obtained by random drawing and averaging of 10 single spikes. The random drawing was performed with Matlab (The Mathworks, Inc.) and it was ensured that none of the spikes was chosen more than once in the same realization. The sub-average groups that were constructed with this procedure were from Av5 to Av50 with increments of

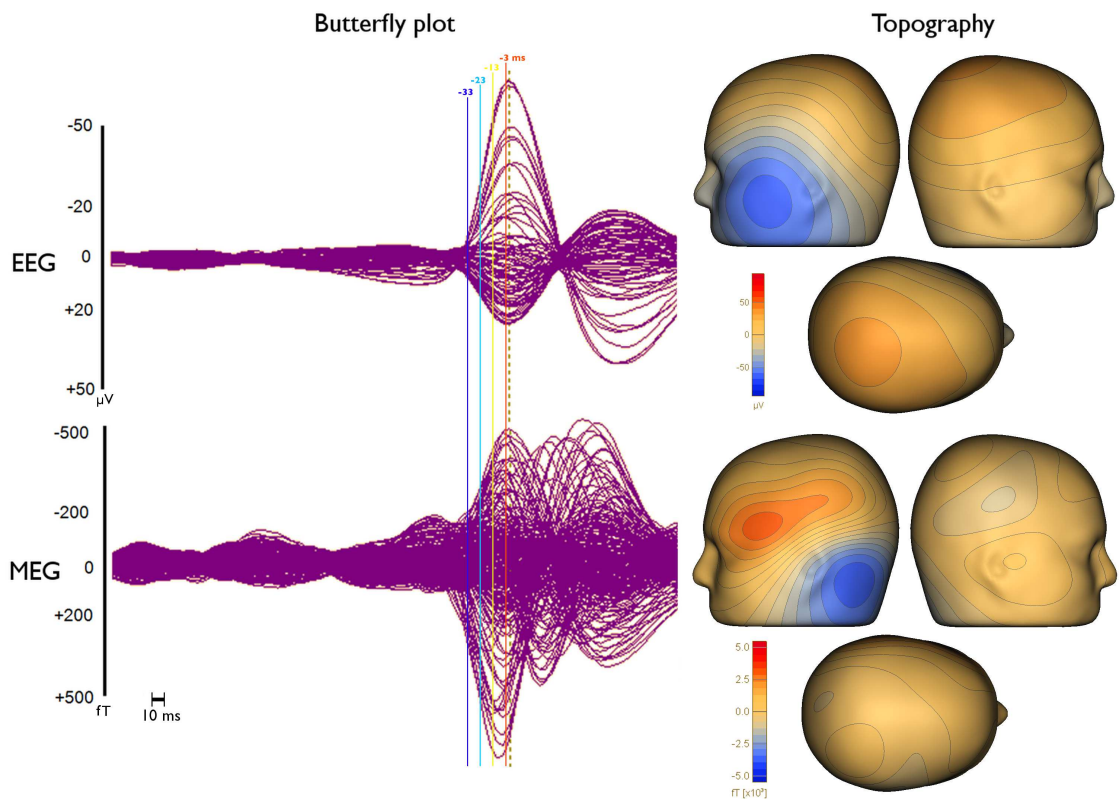


Figure 4.1: Butterfly plots (left) and topographies (right) of EEG (upper row) and MEG (lower row) for the grand-average (average over all 200 single epileptic spikes). The time-points that will be discussed in this chapter, namely -33 ms (dark blue), -23 ms (light blue), -13 ms (yellow) and -3 ms (orange), are indicated by solid vertical lines with different colors. Topographies are shown for the EEG spike peak (time-point 0 ms) as indicated by the dashed vertical line in the butterfly plots.

five. Additionally, the group containing all 200 single spikes was denoted Av1.

The continuous EEG and MEG data were imported into CURRY, filtered from 1 to 100 Hz and divided into 400 ms long epochs (200 ms before and 200 ms after each EEG spike peak). The SNRs were calculated by dividing the signal power at a certain time-point, which was used for the source reconstruction, by the variance of the noise, determined from the interval from -200 to -70 ms. The SNRs of EEG, MEG and EMEG signals were calculated separately for each time-instant (from -33ms to 0 ms) and only the signals with SNRs higher than three in the corresponding modality and sub-average at the time-point of interest were included in the further analysis.

4.1.3 Source reconstruction procedure

A cortically-constrained deviation scan (DS) inverse approach was used for source reconstruction [107, 108]. For this purpose, a source space with 2 mm resolution was calculated as described in Section 3.1.11. The SimBio software was then used to calculate EEG and MEG leadfield matrices for the given source space, FE head model and sensor configurations (See Section 3.1.10). The leadfield matrices were then imported into CURRY and single dipole DSs were calculated from -33 to 0 ms with 0 corresponding to the peak of the EEG signal. Unlike classical dipole fit algorithms, the cortically-constrained deviation scan provides goodness-of-fit (GOF) values for all source space points and the location with the highest GOF was then used as the final deviation scan result.

As in Section 3.1.12, in MEG source reconstructions regularization was used to avoid implausible results, which might occur due to MEG's insensitivity to radial components, for EEG and EMEG we did not use any regularization. Furthermore, only the MEG sensors over the left hemisphere were used for MEG and EMEG source reconstructions to improve SNR and GOF.

In the results section sometimes, instead of spike clusters, so-called centroid dipoles, defined by the mean location and orientation of all deviation scan result dipoles belonging to the corresponding cluster were used (see Section 3.1.12 for details).

4.1.4 Stereo-EEG Measurements

sEEG relying on 14 intracerebral depth electrodes with 167 contacts in total, showed independent epileptic activity with left frontal and temporal origins from three different seizure onset zones: i) left fronto-basal mesial, ii) left temporal and iii) left frontal parasagittal (see Figure 4.2 which summarizes the sEEG findings in the clinical report). In this figure, contacts were represented with squares and they show either the interictal (left) or ictal activity (right). The active contacts during interictal activity were separated into frequent (dark blue) and rare (light blue) and the seizure activity was divided into seizure onset (red) and early propagation (orange color) with some contacts showing both and represented with both colors. The inactive contacts were white. As in the previous chapter the focus was only on the left temporal spikes due to their high occurrence rate (see F9 and FT9 spikes in Table 3.2). For this purpose, TA, E, A, HA, and HP sEEG electrodes all of which were marked as measuring ictal or frequent interictal activity were selected along with TSM, TSP and IM sEEG electrodes, which were non-active at seizure onset or during interictal spikes in Figure 4.2.

Examples of an averaged spike and a single spike measured simultaneously with sEEG and low density scalp EEG (ldEEG) (21 electrodes) are shown in Figure 4.3. Based on the information from the clinical report (Figure 4.2), the sEEG contacts were represented with three different colors: the green spheres represent the sEEG contacts that measured only interictal activity, red spheres represent the sEEG contacts active during the seizure onset and the blue spheres represent the contacts near the left temporal lobe that neither measured the interictal nor seizure onset activity. All contacts that were active during seizure onset were also measuring interictal spikes and were thus within the irritative zone (Figure 4.2). The locations of the sEEG contacts were marked manually using the post-operative T1-MRI and computed tomography images that had been registered to the pre-operative T1 MRI using an affine registration scheme.

4.1.5 Square distance index (SDI)

In order to quantify the amount of agreement between noninvasive source reconstructions and sEEG, a formula, which weights each dipole by the inverse of its square distance to each active sEEG contact, was used.

$$SDI_i = \frac{\sum_{j=1}^N \frac{1}{d_j^2+1}}{N} \times 100$$

Where i is a specific sEEG contact, e.g., A1, which measures frequent interictal activity, N is the number of dipoles that passes the SNR criterion ($SNR > 3$) for the respective modality, and d_j is the Euclidian distance between the j 'th dipole and the sEEG contact i . The addition of 1 ensures the appropriate weighting for perfect localizations ($d_j = 0$). A high value of this index at a certain sEEG contact indicates concentrated dipole localizations near this contact. Alternatively, high differences in SDIs for different sEEG contacts indicate that the localizations highlight only a certain area within the irritative zone and not the whole. Thus, the mean of SDIs over all sEEG contacts should be high, whereas its standard deviation over different contacts should be low for an accurate and complete depiction of the irritative zone.

4.2 Results

The result section is divided into two subsections. In the first subsection, the epileptic spike sub-averaging was investigated with the aim of finding the sub-average number

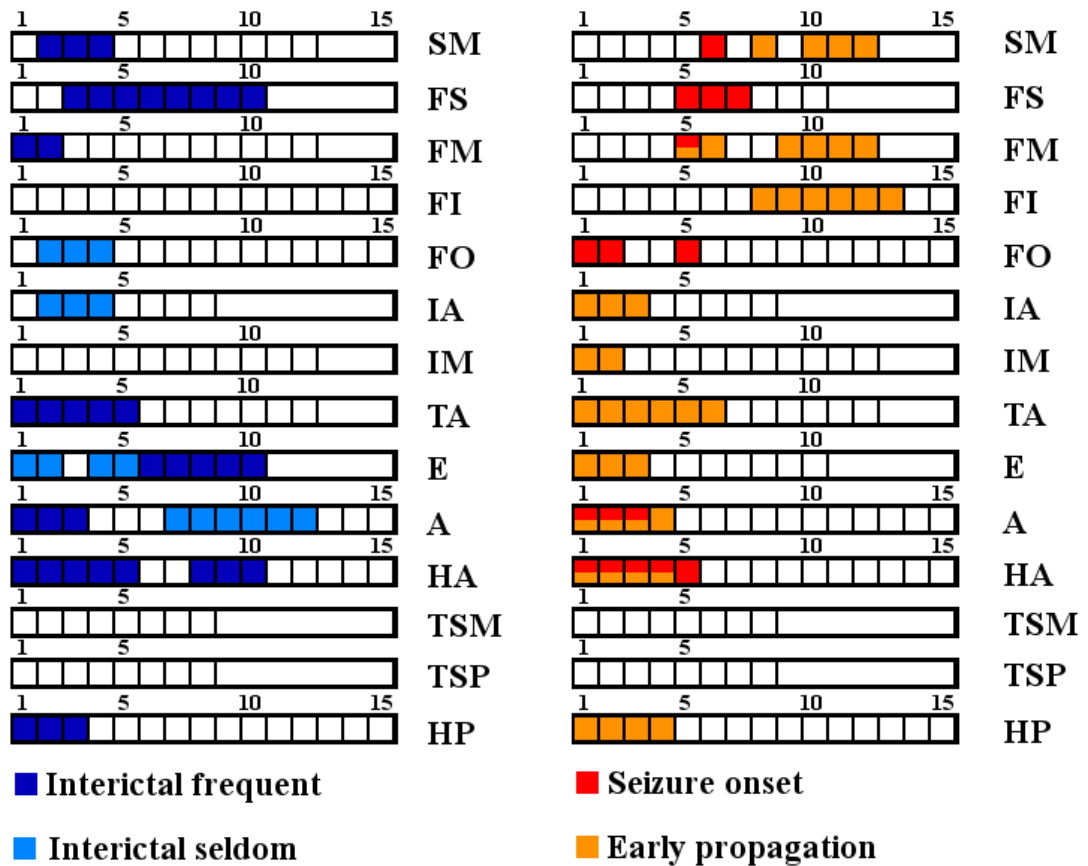


Figure 4.2: The summary of the sEEG findings for all contacts. Each rectangle represents a sEEG electrode (e.g., SM) and these rectangles are divided into squares that represent the contacts on this electrode. The colors of squares show the interictal (left) or ictal activity (right). Interictal activity was divided into frequent (dark blue) and rare (light blue) spikes. The seizure activity is marked as the seizure onset (red) or early propagation (orange color) with some contacts showing both and represented with both colors.

that allows both an appropriate reconstruction of the center of gravity and an estimation of the size of the irritative zone. The determined optimal sub-average number is then used in subsection two to investigate sensitivity differences of EEG and MEG, and especially to evaluate the contribution of combined EEG/MEG in comparison to single modality EEG or MEG source analysis of the epileptic activity.

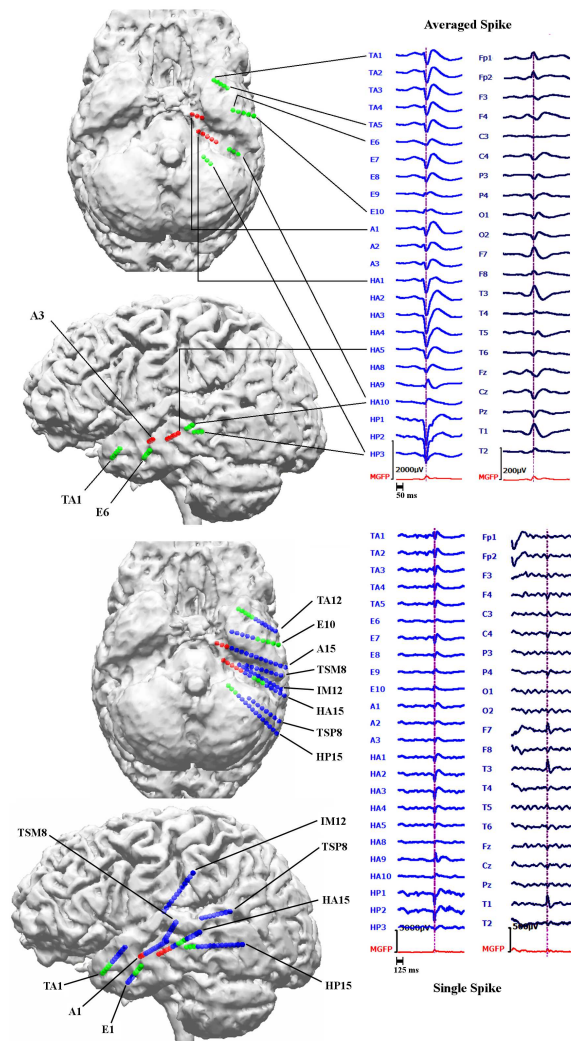


Figure 4.3: Locations of sEEG contacts inside the brain and epileptic activity measured with sEEG and ldEEG. Examples for an averaged (top right block) and a single epileptic spike (bottom right block) measured simultaneously with sEEG (left column in each block) and 21-electrode low density scalp EEG (ldEEG) (right column in each block). Maximum of sEEG is at the HP2 contact, as shown by the vertical lines at the peak of this contact. In the upper two brain figures (left block), only the active (that measures interictal or ictal signals) sEEG contacts are indicated while the two images at the bottom indicate the positions of both active and non-active sEEG contacts close to the left temporal lobe. The union of green and red spheres shows the sEEG contacts measuring frequent interictal activity, red spheres alone show the contacts measuring seizure onset and blue contacts do not measure interictal or seizure activity.

4.2.1 Effects of epileptic spike averaging on source reconstruction

Figure 4.1 (left column) shows butterfly plots of the grand-averaged (all 200 spikes) signals in EEG (upper row) and MEG (lower row). As the dashed vertical line in this

figure clearly shows, the MEG signal peak (time-point -7 ms) precedes the EEG signal peak (time-point 0 ms) by 7 ms. Furthermore, the time-instants that are discussed in the following sections are indicated in Figure 4.1 by solid vertical lines with different colors (-33 ms in dark blue, -23 ms in light blue, -13 ms in yellow and -3 ms in orange).

Next, the SNRs of the different modalities, sub-averages and time-points were investigated. Figure 4.4 shows the SNR results (average values with error bars indicating the standard deviations) for EEG (blue), MEG (green) and EMEG (red). In this figure it seems like for EMEG, the standard deviation indicates SNRs below three but this is only because the error bar was plotted symmetric around the mean and the standard deviation was influenced by the higher variation of values above three while the SNRs below three were not allowed. The upper row presents the results for time-point -23ms at the rising flank of the averaged spike (see light blue vertical line in Figure 4.1) for different average numbers. It shows only single spikes with a minimal SNR of 3 (Av1) or sub-averages (Av5 to Av50) made up of spikes with possibly lower SNRs than three, but which then reach the threshold of three within the averaging procedure. As a result of this, and because the amplitudes of the single spikes vary, the SNR does not increase with the square-root of the average number of spikes as it would be expected for example in an analysis of evoked responses. However, it still clearly increases with increasing average number and for all three modalities. Figure 4.4 (lower row) shows the results for sub-averages of 10 (Av10) for different time-points. A different behavior of EEG and MEG over time can be observed in this subfigure. At spike onset (time-point -33 ms, see dark blue vertical line in Figure 4.1), EEG and MEG SNRs are almost identical. However, in later instants in time at the rising flank of the epileptic spike (time-points -30 ms to -3 ms) the SNR of the EEG increases faster than the SNR of the MEG, which leads to considerable differences in SNRs at the EEG spike peak (time-point 0 ms). Finally, it is also clearly visible that the standard deviations (error bars) increase with increasing SNR.

Then, the centroid dipoles were calculated for different sub-averages at -23 ms (see light blue vertical line in Figure 4.1) and the results were visualized in Figure 4.5. This figure shows large differences in source reconstructions between single and sub-averaged epileptic spikes. The single spike source reconstructions (Av1) are considerably more superior and deeper than the sub-averages for EEG, MEG and EMEG indicating a systematic noise bias of Av1. The noise bias in Av5 has a similar tendency, but it is already much smaller than for Av1, and no more bias can be observed for sub-averages with more spikes, especially for MEG and EMEG. Starting from Av10 and further increasing the number of averaged spikes results in only minor changes to the centroid

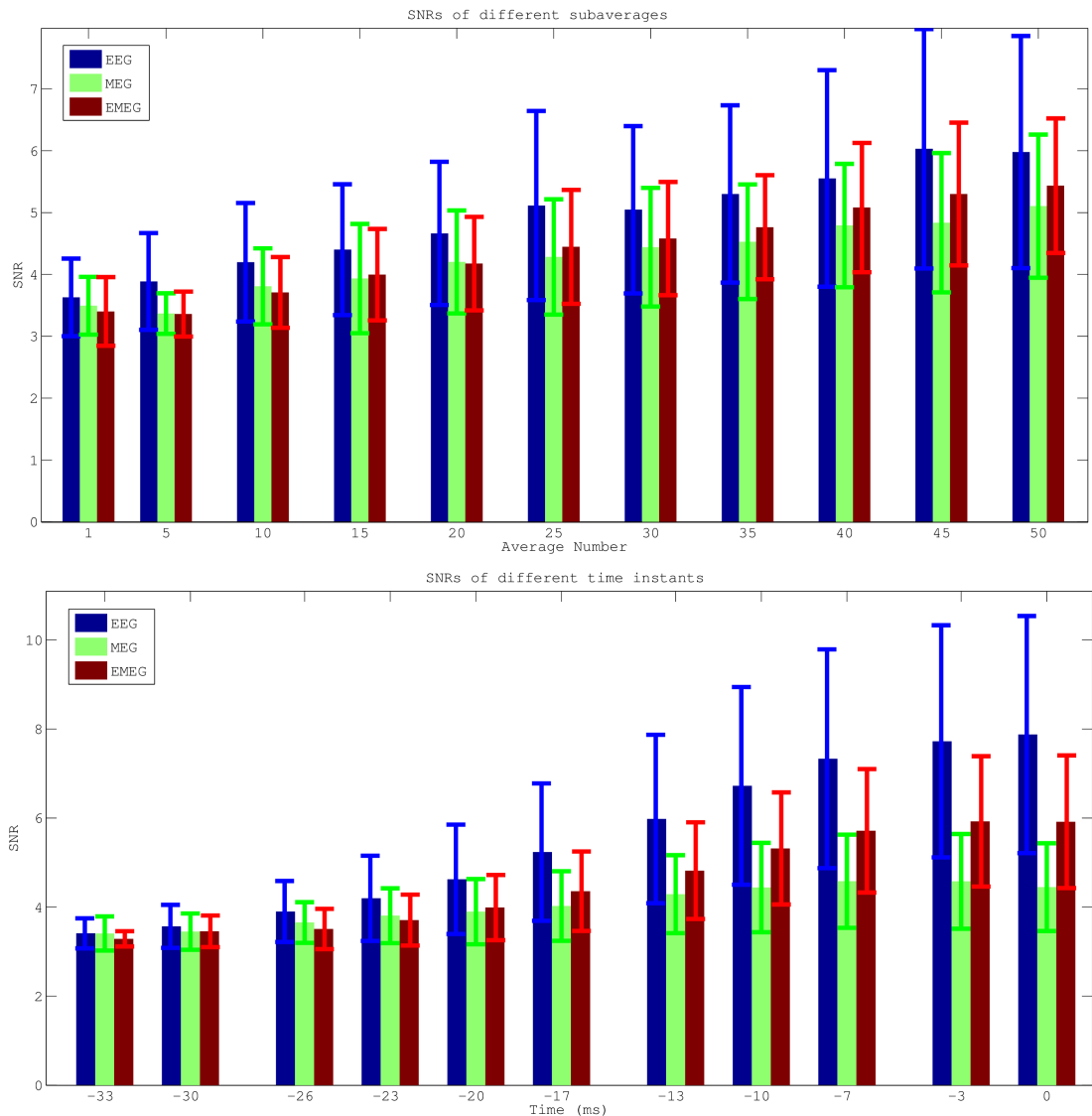


Figure 4.4: Average SNRs (with error bars indicating the standard deviations) for EEG (blue), MEG (green) and EMEG (red). Only single epileptic spikes (Av1) or sub-averages (Av5-Av50) with SNRs higher than three were taken into account in these figures. The upper row shows the results for different average numbers for time-point -23 ms at the rising flank of the averaged epileptic spike and the lower row for different time-points from -33ms (spike onset) to 0ms (spike peak in EEG) for sub-average 10 (Av10).

dipoles. Figure 4.5 thus shows that a minimal average number of 10 should be used for this patient to avoid a noise bias in the reconstruction of the center of gravity of the irritative zone.

Figure 4.6, which shows, visualized with blue dipoles, the deviation scan peaks for Av1, Av5, Av10, Av 25 and Av50 at -23 ms, further strengthens and complements

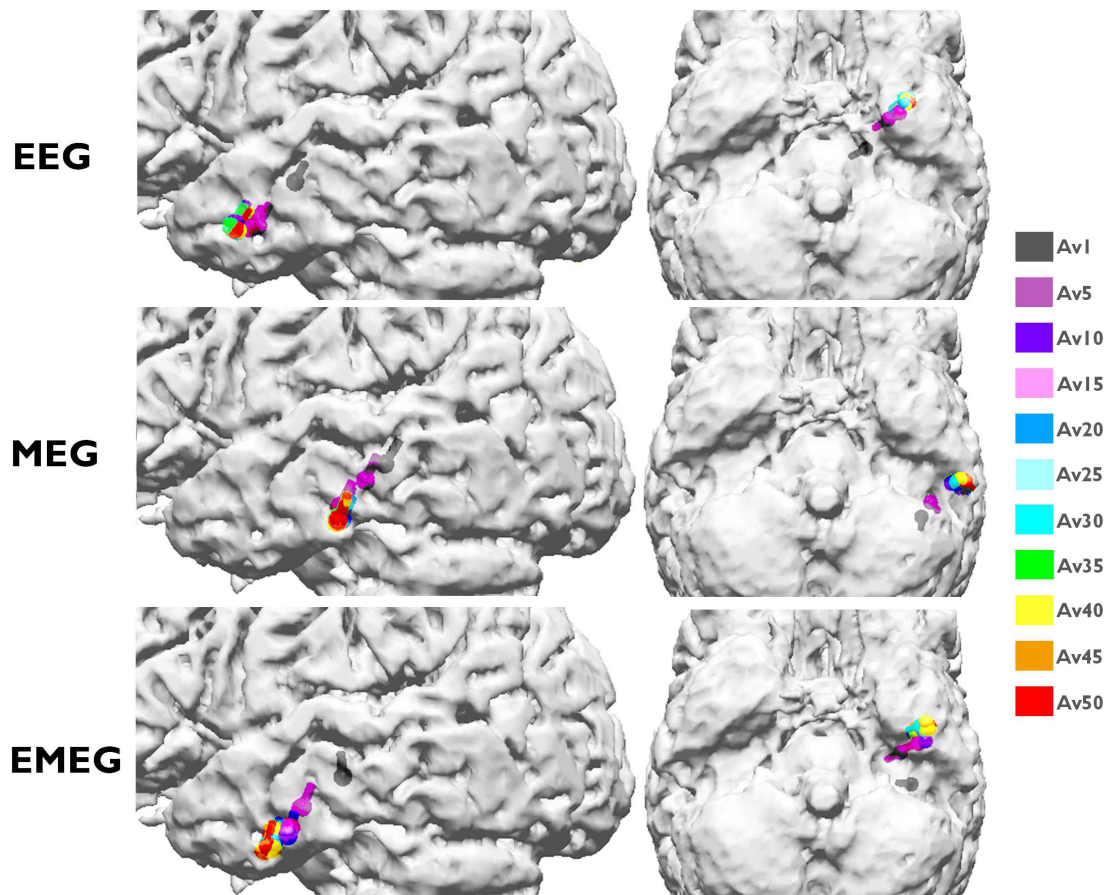


Figure 4.5: Centroid dipoles determined from the dipole scan peaks of EEG (upper row), MEG (middle row) and EMEG (lower row) for different sub-averages at 23 ms before the EEG spike peak. Each color shows centroids for different sub-averages and Av1 is the centroid for single spike reconstructions. The centroid dipoles were computed from those random realizations out of 200 random realizations for each group, which satisfied the $SNR > 3$ criterion.

the results of Figure 4.5. Green and red spheres in Figure 4.6 represent the sEEG contacts, which measured frequent interictal epileptic activity, thus giving an impression of the minimal size of the irritative zone, and red spheres are the sEEG contacts that additionally measured ictal activity. Most of the observations in this figure are similar for EEG, MEG and EMEG, and as long as the modality name is not explicitly mentioned in the following description, these observations are valid for all three of them. It is clear from Figure 4.6 that very few single spikes (Av1) pass the SNR criterion ($SNR > 3$) and even among them spurious dipoles (outliers) persist. When the sub-average number is increased to five, although the localizations become more stable

and dipole clusters start to emerge, still many outliers can be observed. For Av10 the clusters become more distinguishable with only few outliers. These results thus support the argumentation from the previous paragraph (Figure 4.5) to use a minimal average number of 10 for this patient. The following argumentation now delivers the complementary information that, from the chosen sub-average numbers, Av10 even seems to be optimal: Av25 results again differ from Av10, especially with regard to a further decrease in the scatter of dipoles. When increasing the sub-average number to 50 the scatter of the dipoles further decreases and MEG epileptic spikes are localized more lateral than for Av10 and Av25. Now the dipole scatters can be evaluated with the information from the sEEG. Figure 4.6 shows that for Av10 the dipole scatter covers almost all active sEEG contacts, i.e., it covers the minimal size of the irritative zone. For Av25 the clusters are already too focal, missing the active HA8-10 and all HP contacts. Av50 is even more focal, missing even more of the active sEEG contacts (additionally to HA8-10 and all HP, also HA1-5 contacts are outside the estimated irritative zone) and thus they are strongly underestimating the size of the irritative zone.

4.2.2 Comparison of EEG, MEG and EMEG source reconstructions

For comparing EEG, MEG and EMEG localizations, based on the results of the previous subsection, the focus will be on Av10 results. This choice is based on Figures 4.5 and 4.6, which show that a minimal average number of 10 is needed to sufficiently reduce noise bias and appropriately reconstruct the center of gravity of the irritative zone and that higher average numbers result in too focal dipole clusters that lead to an underestimation of the extent of the irritative zone.

The Av10 EEG reconstructions in Figure 4.6 are mainly localized in an area close to the pole of the temporal lobe and close to sEEG TA contacts (Temporal Anterior, see Figure 4.3). In contrast, no activity is localized near HP1-3 and HA1-5 (the hippocampus posterior and anterior contacts). In MEG the localizations are more posterior than in EEG with clusters in the vicinity of HA8-10 (the posterior lateral neocortical contacts that, in contrast to their label, are not located in the hippocampus anterior, see Figure 4.3), and close to HP contacts although no cluster was formed around them. Unlike in EEG, there are no localizations in the vicinity of TA in MEG. In EMEG, noninvasive reconstructions cover all active sEEG contacts. EMEG even shows localizations near the HP contacts, where neither the sensitivity of EEG (see EEG side-view in the second column of Av10 in Figure 4.6) nor of MEG (see MEG

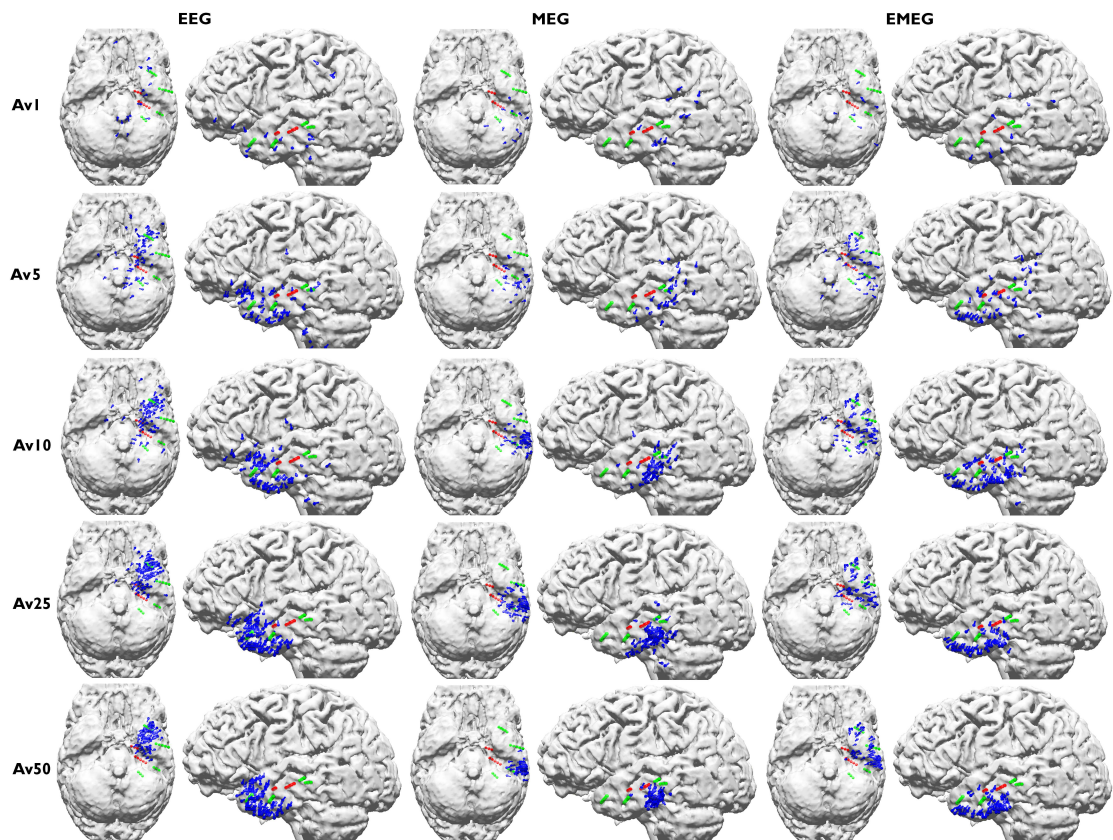


Figure 4.6: Peaks of the deviation scans (illustrated by blue dipoles) of EEG (left two columns), MEG (middle two columns) and EMEG (right two columns) for different sub-averages. The figure shows the results at 23 ms before the peak of the EEG. Both green and red spheres show the sEEG contacts where frequent interictal activity can be measured, thus giving an impression of the minimal size of the irritative zone, and red spheres alone show seizure onset contacts.

bottom-view in the third column of Av10 in Figure 4.6) was sufficient to reconstruct any activity.

The plots in Figure 4.7 add quantitative information to Av10 source reconstructions visualized in Figure 4.6. The plots show the SDIs (upper subfigure) and the percentage of dipoles that are closer than 10 mm to each sEEG contact measuring frequent interictal activity (lower subfigure). In these plots, the contacts that are also part of the seizure onset zone (amygdala contacts A1-3, and hippocampus anterior contacts HA1-5) are enclosed within rectangles with dotted lines. The upper subfigure clearly shows that most of the EEG localizations are clustered near the TA contacts and the lower subfigure shows that there are dipoles within 10 mm at only 6 out of overall 24 interictal and 1 out of 8 ictal contacts. MEG values for the same measures are 10

out of 24 interictal and 2 out of 8 ictal, and the localizations are clustered especially near the posterior lateral neocortical contacts HA8-10 and HP contacts. In contrast, for EMEG 23 out of 24 interictal and 7 out of 8 ictal contacts have at least one non-invasive localization within 10 mm. In the SDI plot the EEG SDIs for TA contacts are considerably higher than for other contacts, while for MEG the SDIs at contacts HA8-10 are larger. For EMEG the SDI index is almost equally distributed over the sEEG contacts and it does not show a huge variation as in EEG and MEG. The means and standard deviations of SDIs for EEG, MEG and EMEG demonstrate this behavior well. The average SDIs for EEG and MEG are 0.22 ± 0.15 and 0.18 ± 0.11 , respectively, and with 0.24 the average SDI for EMEG is higher and, most importantly, with 0.05 its standard deviation is considerably lower than for EEG or MEG.

In Figure 4.6 the signals that passed the SNR criterion were determined separately for each modality and thus the spikes that satisfy the criterion in EEG might differ from the ones that satisfy it in MEG or EMEG. This means that by applying the selection criterion based on the SNR at each modality separately, it was selectively focused on the signals arising from sources that a certain modality is more sensitive to. Since EEG and MEG have different sensitivities depending on the source location and orientation this may increase discrepancy between their localizations. In order to investigate the influence of this selection in Figure 4.8, the spikes that pass the SNR criterion in EMEG for Av10 at -23 ms were localized regardless of their SNRs in EEG or MEG. This procedure reveals some localizations near TA and E electrodes for MEG in Figure 4.6 for Av10, but they were few and the main clusters were still around HA and HP contacts. This result also supports the idea that the main reason behind varying EEG and MEG localizations is their different sensitivity profiles.

As already noted, the MEG signal peak precedes the EEG maximum by approximately 7 ms (Figure 4.1). In order to investigate which sources are dominating the EEG and MEG signals, the timings of epileptic spikes in sEEG and the simultaneously measured ldEEG were compared (Figure 4.9). In this figure, different colors for sEEG contact groups were used in order to see the peaking times clearly in the butterfly plot. It was observed that simultaneously with the ldEEG peak, sEEG contact TA4 (green) is also at its peak value. In contrast, the peak of the HP2 contact (blue), the contact, which measures the highest amplitude in sEEG, is occurring 7.5 ms before the ldEEG and TA4 peaks. Moreover, the peaks of A1-3 and HA1-5 (red signals), i.e., the seizure onset contacts, are also preceding the TA contacts and are almost simultaneous with the HP contacts (especially contacts A1-3). The peaking times of the E contacts (pink) were in general earlier than TA but later than HP. The peaks of contacts HA8-10 were

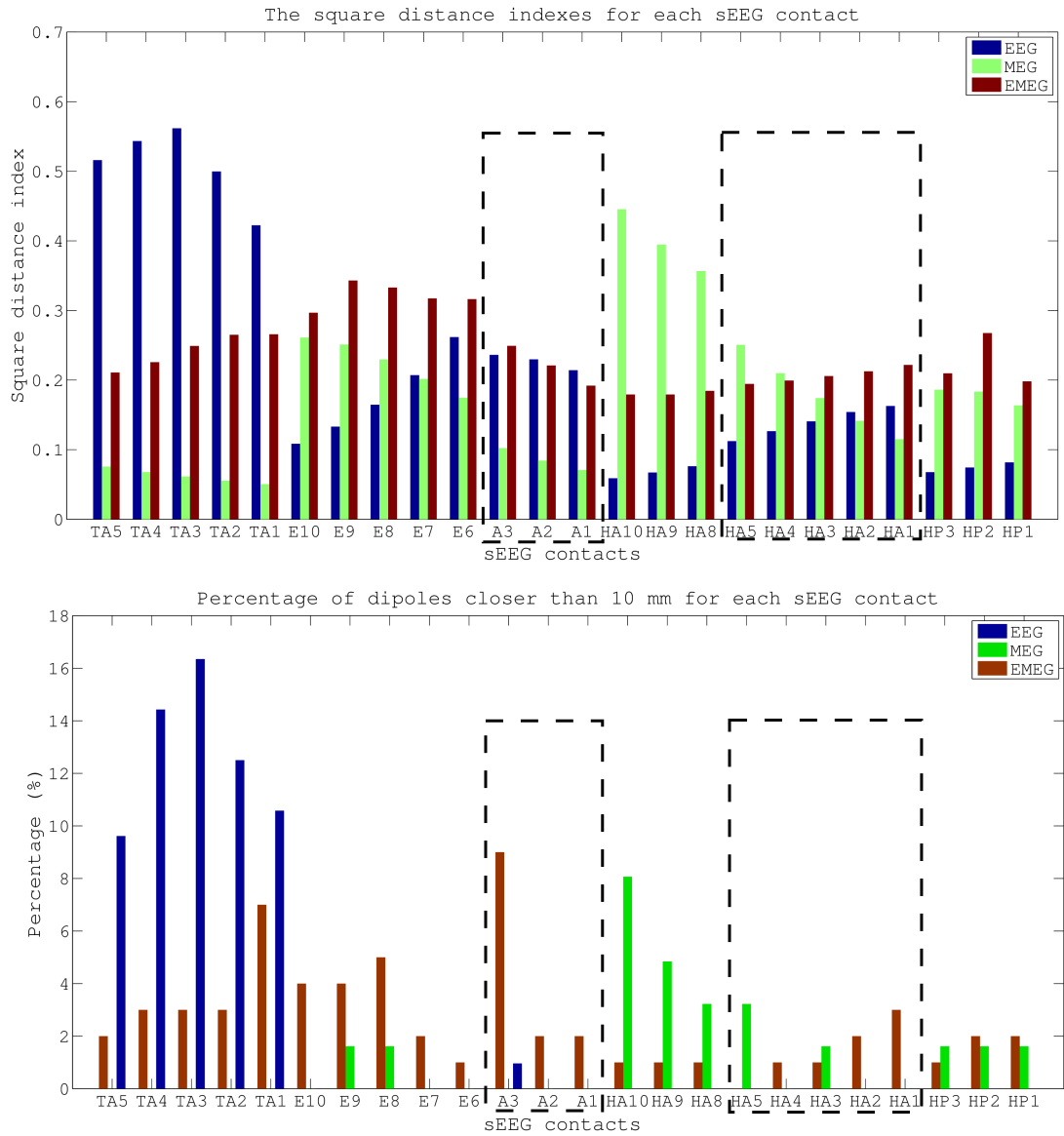


Figure 4.7: Square distance index and the percentage of dipoles closer than 10 mm for each sEEG contact. The values are given for EEG, MEG and EMEG for sub-averages of 10 at -23 ms. The sEEG contacts enclosed by dashed lines are within the seizure onset zone.

different. While the HA8 peaks almost simultaneous to HP1-2, the HA9 and HA10 contacts were peaking later.

Figure 4.10 shows the pathways from spike onset to late propagation determined from EEG (upper two rows), MEG (middle two rows) and EMEG (lower two rows). Av10 deviation scan reconstructions for 4 different time-points are visualized from -33 ms (spike onset, left column, see also dark blue vertical line in Figure 4.1) to -3 ms

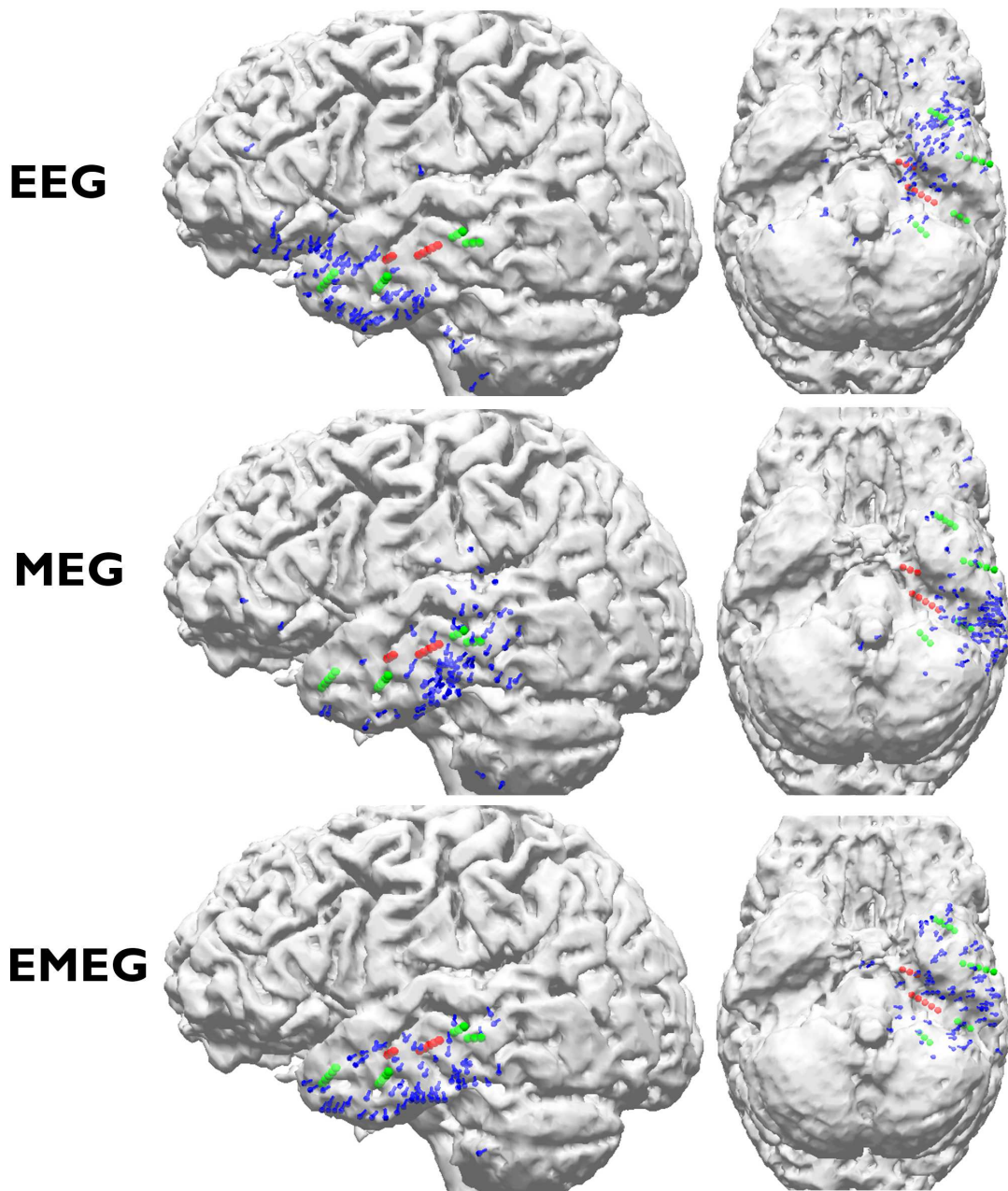


Figure 4.8: Dipole localizations of EEG, MEG and EMEG for sub-averages of 10. The figure shows the results at 23 ms before the peak of the EEG. The signals with SNRs higher than 3 in EMEG were selected and these spikes were used for calculations in EEG, MEG and EMEG regardless of whether EEG or MEG SNRs were higher than 3 or not. Blue dipoles illustrate the noninvasive localizations, the union of green and red spheres shows the sEEG leads measuring interictal activity, and red spheres show the leads measuring seizure onset.

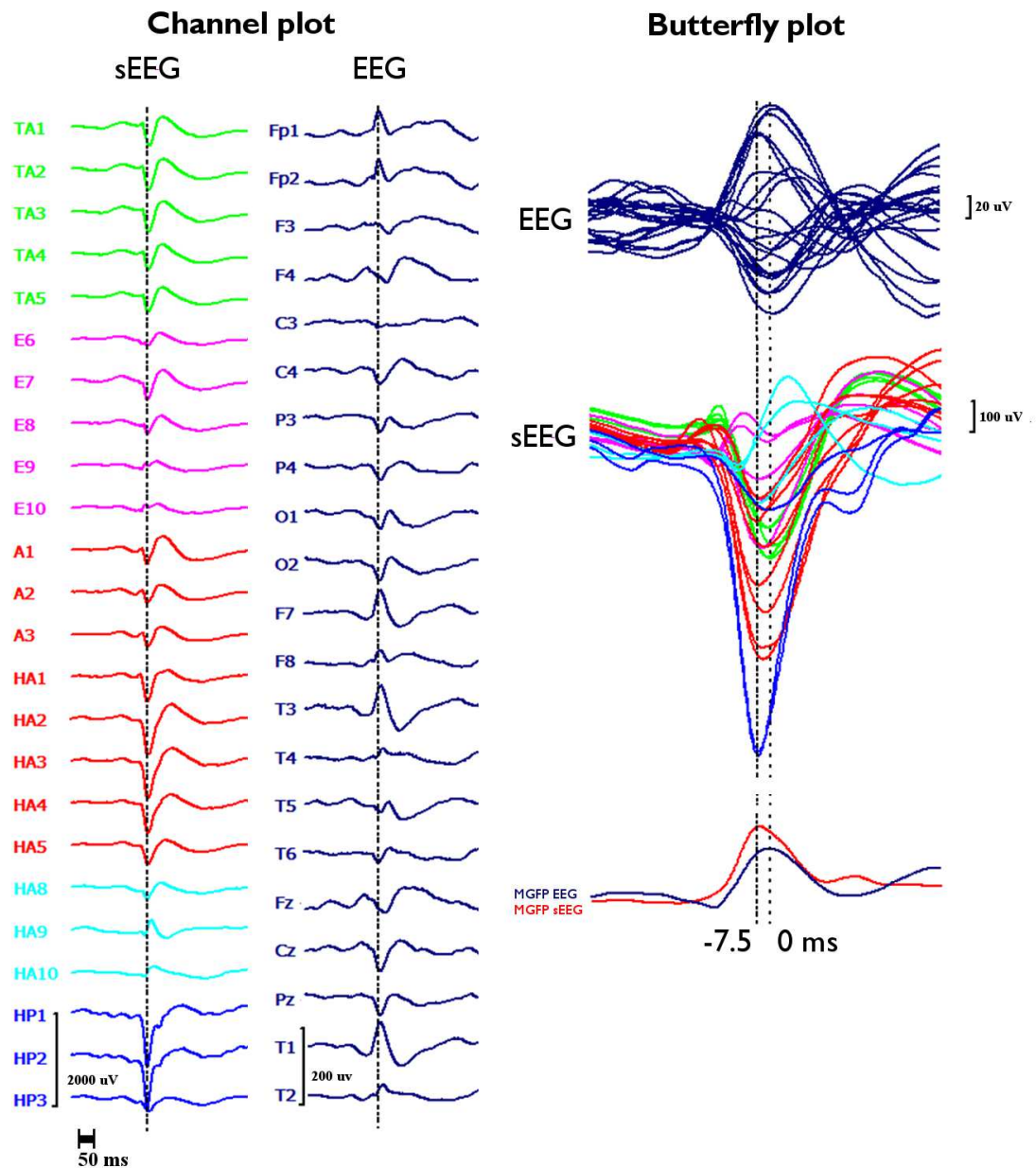


Figure 4.9: Average waveform of the spikes measured simultaneously with sEEG (left column in channel plot; middle row in butterfly plot) and 21 electrodes low density scalp EEG (ldEEG) (right column in channel plot; upper row in butterfly plot). Maximum of sEEG is at the HP2 contact as shown by the vertical line at the peak of this contact in the channel plot. In butterfly plot, the vertical line at 0 ms shows the EEG peak and the vertical line at -7.5 ms shows the sEEG peak. The lower row in butterfly plot shows the mean global field power. The same color code is used for sEEG in channel and butterfly plots.

(late propagation phase close to EEG peak, right column, also see orange vertical line in Figure 4.1) in steps of 10 ms. The first striking observation in this figure is the considerably higher stability of EMEG source reconstructions at spike onset, in comparison to single modality EEG and MEG. The EMEG source reconstructions at time-point -33 ms are correctly clustered close to the seizure onset zone (red spheres at A1-3 and HA1-5 contacts). In contrast, EEG is strongly dominated by noise with source reconstructions spreading over a wide region. Although MEG reconstructions at spike onset are already better than EEG, they are still too lateral and are spread over a too large region and the low SNR still leads to many spurious reconstructions. The results for EEG, MEG and EMEG at the propagation phase also differ. EMEG source reconstructions show that during the 10 ms period from spike onset to time-point -23 ms, at the rising flank of the signal, the reconstructed activity spreads from amygdala and hippocampus to a wider area over the temporal lobe, thus covering all active sEEG contacts. At time-points -13 ms and -3 ms, the reconstructed EMEG activity accumulates near the pole of the temporal lobe. The propagation paths shown by single modality EEG and MEG differ quite much from the one of EMEG and, when compared to the sEEG findings and the EMEG reconstructions, they are both incomplete. For EEG, the first stable (by improved SNR) source reconstructions shown in Figure 4.10 are the ones at -23 ms near the pole of the temporal lobe. EEG alone completely misses the more posterior activity close to the HA and HP contacts (see Figure 4.3) in this early propagation phase (see especially the first row and second column in Figure 4.10). At later instants in time, the EEG is only able to reconstruct activity at the tip of the temporal pole. With regard to the MEG, at -23 ms, source reconstructions are at more posterior temporal areas especially covering the HA8-10 contacts (see Figure 4.3 and second row in Figure 4.10) very well. Later on at time-points -13 ms and -3 ms, the reconstructed MEG activity travels to more anterior and temporobasal regions. During the whole propagation phase MEG alone completely misses the temporo-polar activity close to the TA contacts (fourth row in Figure 4.10).

Corresponding to the visualizations of the propagation pathway in Figure 4.10, the plots in Figure 4.11 add quantitative information on Av10 EMEG source reconstructions for the four different time-points. The upper subfigure, presenting the SDIs, shows that at -33 ms (spike onset) the source localizations are mostly clustered near the A and HA1-5 contacts (seizure onset). At later time-points, i.e., closer to the spike peak, the reconstructed activity propagates to E and TA contacts. The lower subfigure, presenting the percentage of dipoles that are closer than 10 mm to each sEEG contact measuring frequent interictal activity, shows that at -33 ms 7 contacts are covered by

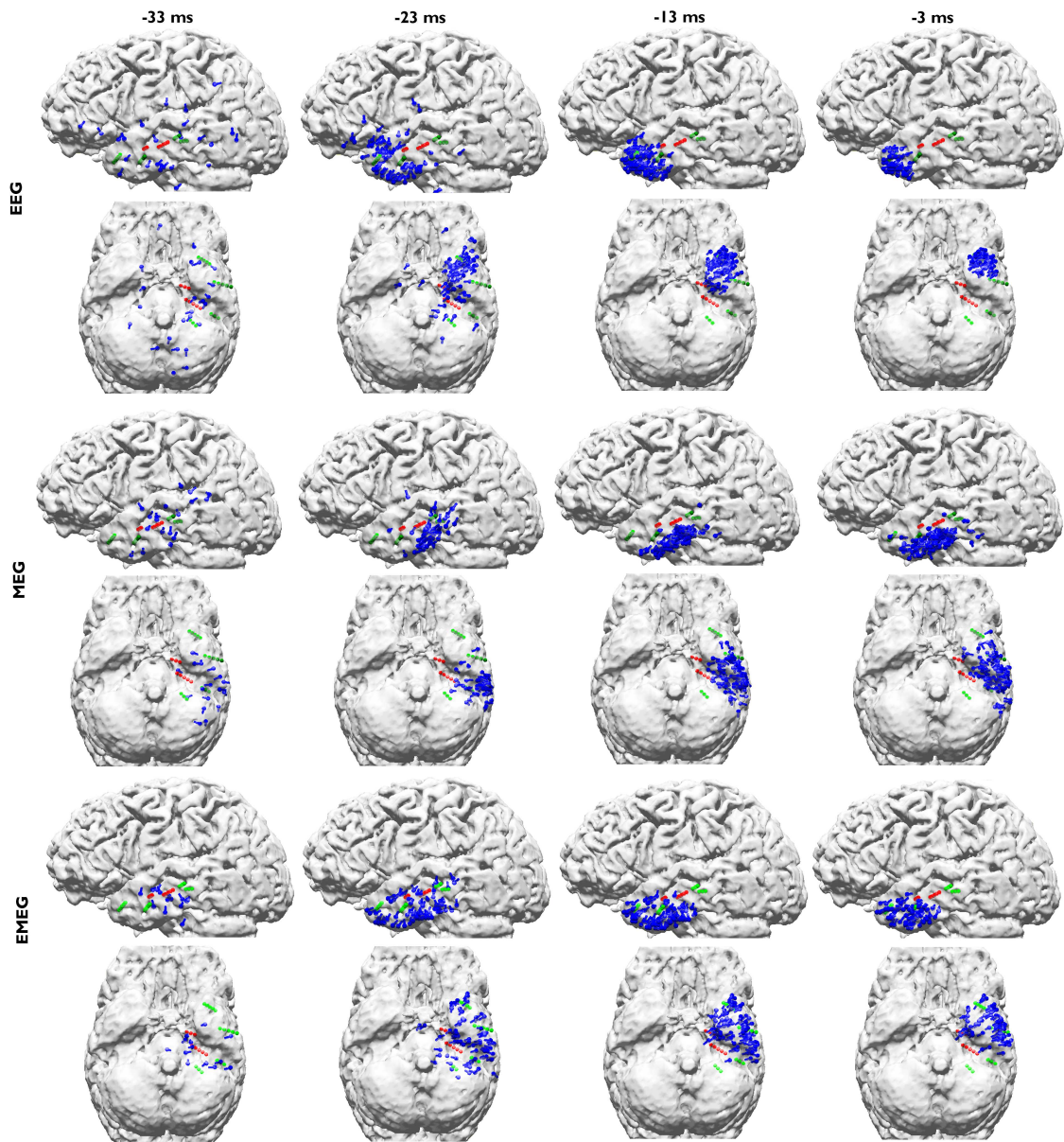


Figure 4.10: EEG (upper two rows), MEG (middle two rows) and EMEG (lower two rows) deviation scan peaks (illustrated by blue dipoles) of Av10 for time-points from -33 ms (spike onset, left column) in steps of 10 ms until time-point -3 ms (late propagation phase close to EEG peak, right column). Both green and red spheres show the sEEG contacts where frequent interictal activity can be measured, thus giving an impression of the minimal size of the irritative zone, and red spheres alone show seizure onset contacts.

the noninvasive EMEG reconstructions. Among them, 6 are ictal contacts (it covers 6 out of 8 ictal contacts) and the other one is the HP1 contact, which peaks earlier

than the TA contacts, as shown in Figure 4.3. While the EMEG reconstructed activity continuously decreases over time at the seizure onset amygdala and hippocampal contacts, it continuously increases at most of the TA and E contacts.

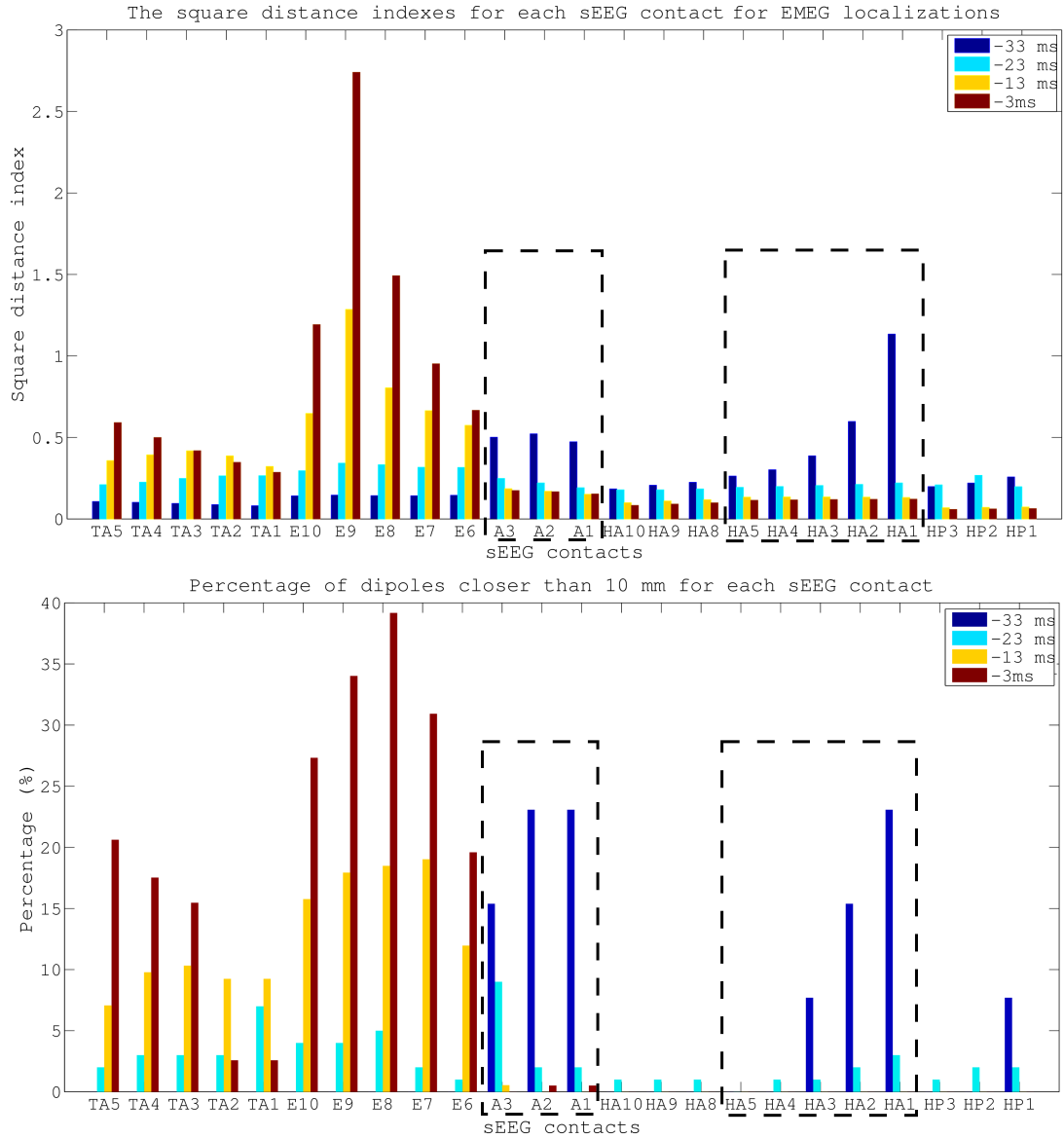


Figure 4.11: Square distance indexes and the percentage of dipoles closer than 10 mm for each sEEG contact. The values are given for Av10 EMEG sub-averages at -33, -23, -13 and -3 ms. The sEEG contacts enclosed by dashed lines were within the seizure onset zone.

In Figures 4.7 and 4.11 the SDI values on active sEEG contacts were compared in order to study the sensitivity of the noninvasive source reconstruction results. For studying specificity, in Figure 4.12, the SDI values for EEG, MEG and EMEG at

-33 ms were plotted, now also including the non-active sEEG contacts. The SDIs were colored according to the measured activity: seizure onset contacts (red), interictal contacts (green) and non-active contacts (blue). The figure shows that not only the sensitivity but also the specificity of EMEG results are superior to EEG and MEG alone. EMEG SDIs of sEEG contacts are gradually decreasing with distance to the seizure onset contacts (see HA6 to HA15 and A4 to A9). EEG and MEG source reconstructions alone not only failed to highlight the seizure onset due to low SNRs but also their specificities were inferior to the EMEG results presented here.

4.3 Discussion

This section starts with the most important results first, thus the order of the sub-chapters was inverted in respect to the order used in the section describing results.

4.3.1 Comparison of EEG, MEG and EMEG source reconstructions

4.3.1.1 Propagation phenomenon: Problems and opportunities for noninvasive source reconstruction

Propagation of interictal epileptic activity is a well-known phenomenon, which might lead to misinterpretations and spurious diagnosis if not taken into account. In order to cope with it, many studies suggested reconstructing sources at the middle of the rising flank instead of the peak of the epileptic spike (see [154] and references therein). Although this might seem to be a good compromise between low SNRs at the spike onset and propagation at the spike peak, the activity at the middle of the rising flank might have already been subject to propagation, e.g., in mesial temporal lobe epilepsy, as shown in this study. Alternatively, in cases where the propagation pathway is always identical over different spikes, like in the case discussed here, propagation provides also a great opportunity: propagation of activity from low SNR locations (in this study, the deep amygdala and hippocampal structures) to locations with much higher SNRs (in this study, the pole of the temporal lobe, see Figure 4.4 with regard to the increase in SNR) enables the examiner to detect spikes and thus supply the necessary triggers for averaging, which in turn might then enable revealing the preceding activity with lower SNR. This was shown in the study presented here, where it was possible to accurately (with regard to the sEEG validation measure, see further discussion below) reconstruct the complete pathway of the epileptic activity from onset to spike peak using sub-averaging techniques and combined EEG and MEG source analysis. Similar scenarios

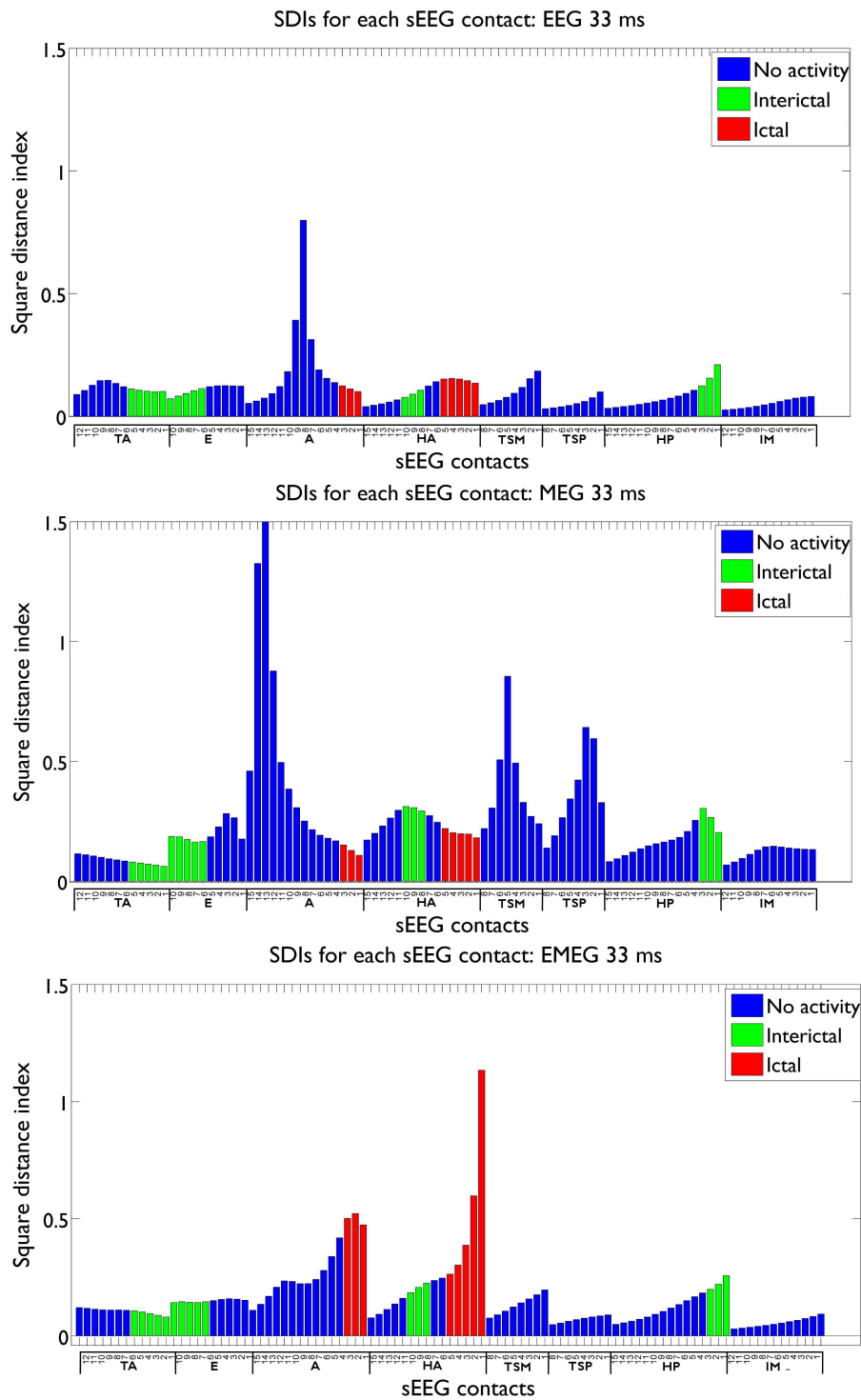


Figure 4.12: SDI values for EEG, MEG and EMEG at -33 ms. The SDI bars are colored according to the measured activity: seizure onset contacts (red), only interictal contacts (green) and non-active contacts (blue).

are discussed in the literature. For example, simultaneous scalp and intracranial EEG studies showed that, while scalp EEG might not directly be able to distinguish the activity from deeper structures from the noise, it might be possible to extract the EEG signal by averaging intracranial epileptic spikes [184, 185].

4.3.1.2 EEG, MEG and EMEG source reconstructions at spike onset

Despite the strategies explained in the previous paragraph, as it was shown in Figures 4.10 and 4.11, at very early instants in time (-33 ms, see dark blue vertical line in Figure 4.1) single modality EEG or MEG source reconstructions might not be reliable enough to draw conclusions on the origin of the epileptic spike. In the results presented here, EEG was strongly dominated by noise and although MEG source reconstructions were more stable, they had a lateral bias with still too many spurious dipole positions. The source reconstructions with single modality EEG or MEG stabilized at later instants in time (see time-point -23 ms in Figure 4.10), but the activity had already been subject to propagation by then. One of the most important and clinically relevant findings of this study is thus the ability of EMEG to benefit from the complementary information of EEG and MEG at especially these very early instants in time, and thereby the ability to stabilize the source reconstructions in cases of low SNR. As shown in Figures 4.10 and 4.11, at -33 ms the source reconstructions of EMEG are mainly clustered near amygdala and hippocampus, i.e., regions within the seizure onset zone as estimated from sEEG.

4.3.1.3 Differences of EEG, MEG and EMEG source reconstructions in revealing the propagation pathway

The EEG, MEG and EMEG source reconstructions differed not only at spike onset but also at later instants in time. At -23 ms (see light blue vertical line in Figure 4.1), although both EEG and MEG source reconstructions were clustered near the spiking sEEG contacts, they highlighted different contacts. EEG localizations were mainly clustered near TA contacts, while MEG results were close to the posterior lateral neocortical contacts HA8-10 and, partially, to HP. In agreement with the findings of this study, in temporal lobe epilepsy, posterior MEG source reconstructions in comparison to EEG were also observed in other studies [18, 178]. The main reason for this difference might be the increased size of the active patch at this time-point due to propagation. Considering the wide extent of active cortex measured with sEEG in this study, the proposed hypothesis is that the peak of the EEG deviation scan was found

at the temporal pole because of its considerable radial source orientation component. As a result, this activation did not contribute much to the MEG signals. In contrast, the activity arising from especially the posterior lateral neocortical contacts HA8-10 and from the HP contacts was more tangentially oriented, leading to higher SNRs in MEG, and thus MEG was mainly focusing on this part of the cortex. Furthermore, the averaged MEG signal peak was not synchronous with the EEG peak, it preceded the EEG by approximately 7 ms (see dashed vertical line in Figure 4.1). In order to determine the sources dominating the EEG and MEG signals, the time relationship between the peaks of the simultaneously measured sEEG and low-density EEG (ldEEG) epileptic spikes was investigated. It was observed that the peaks of the ldEEG and the TA4 contact were simultaneous, and the EEG localizations were clustered around TA4. Although MEG and sEEG were not measured simultaneously, the results of the simultaneous ldEEG-sEEG to the simultaneous EEG-MEG measurements might be extrapolated and commented on the timings of the measured signals. Considering the fact that the MEG peak is also approximately 7 ms before the EEG it can be stated that the MEG maximum is concurrent in time with the HP2 contact. This means, the peaks of the MEG and the HP2 contact are almost simultaneous and might explain why MEG was also localized closer to HP2. All these results fit well to the proposed hypotheses that a larger activated cortical patch is underlying the measured activity and that EEG and MEG focus on only parts and, due to their distinct sensitivities, to non-identical parts of this activity. Although EEG and MEG source reconstructions were able to highlight just a subset of spiking sEEG contacts, EMEG results were covering almost all relevant sEEG contacts with only a few spurious localizations. EMEG localizations were not simply the union of EEG and MEG results but a rather complicated interplay of both modalities compensating their relative shortcomings. For example at -23 ms, in Figures 4.7 (especially the lower subfigure) and 4.10, no major dipole cluster was noticeable neither with EEG nor with MEG around the E contacts in sEEG, while there were clear clusters around these active contacts in EMEG. This also supports the idea that combining EEG and MEG can supply important additional information that cannot be achieved by localizing EEG and MEG alone, and then comparing their results. Therefore, whenever it is technically feasible to measure EEG and MEG simultaneously, it might be important to not only analyze single modality EEG and MEG but also to compare with combined EMEG reconstructions to obtain accurate localization results. Furthermore, the asynchronous EEG and MEG peaks along with the more complete overview on the propagation pathways provided only by EMEG, as shown here, might also help distinguishing between the primary

and secondary interictal areas as reported by [186].

Close to the spike peak (-3 ms) the source reconstructions were more anterior in comparison to earlier instants in time and were clustered close to the pole of the temporal lobe. The SNR values shown in the lower subfigure of Figure 4.4 support the findings that epileptic activity had started at deeper areas and then propagated to the pole of the temporal lobe at the spike peak. The SNRs of EEG and MEG at spike onset were almost identical, but later on, the increase in EEG SNR was higher than in MEG due to the mainly radial source orientation in the area of the temporal pole.

4.3.2 Effects of epileptic spike averaging on source reconstruction

The results of this study show that the centroid dipoles obtained from epileptic spike clusters differ considerably between different sub-averages. It was observed that spikes with lower number of sub-averages and thus lower SNRs were localized more mesial and superior in comparison to those with higher number of averages (and higher SNRs) at -23 ms (Figure 4.5). The reason for this localization bias might be due to background activity, which can be considered as noise in our case. Since at this time-instant the propagation had already occurred, the noise bias shifted the localizations from lateral parts of the temporal lobe into deeper regions in the brain. The data of this study support this hypothesis by showing higher localization differences in the left-right (LR) and superior-inferior (SI) than in the anterior-posterior (AP) axis. The lateral regions of the left temporal lobe are situated farther away from the center of the brain in LR and SI axes, while in AP axis they are close to the center. Therefore, it was expected that the difference in localizations would be higher for axes' that were farther away from the center of the brain. For example, if the patient had frontal spikes then this shift would have been probably higher in AP axis. In agreement to the results of this study and the proposed hypothesis, Plummer et al. [187] studied EEG spike localizations for single and averaged spikes and although they did not explicitly stress it in their paper, their results for patients with benign focal epilepsy with centro-temporal spikes showed a similar shift between single and averaged spikes. They obtained more superficial localizations for averaged spikes in comparison to single spikes in 11 out of 12 localizations (4 patients, 3 time-points for each). Furthermore, the studies of Wennberg and Cheney [17, 18] also showed similar shifts to the center of the brain.

4.3.3 Preselection criteria to improve single and sub-averaged spike source reconstructions

Different preselection criteria for epileptic spikes have been suggested to avoid errors in single spike localizations [10, 13, 145]. Following these criteria, only the spikes with SNR higher than three were localized in this study. This preselection strategy resulted in more reasonable localizations but the number of single spikes that satisfied this condition also got smaller. From the 200 measured single spikes, only 20 EMEG spikes passed the criterion at 0 ms (spike peak with highest SNR). At -23 ms this number was even reduced to only 7 for EMEG and even among them spurious localizations persisted (see EMEG results for Av1 in Figure 4.6). Therefore, it is highly recommended (1) to use sub-averages and (2) to observe the changes in centroid dipoles and scatter size with increasing averages.

4.3.4 Estimation of the optimal sub-average number

For the estimation of the optimal sub-average number, the following procedure is recommended: a sub-average should be selected that averages enough spikes (in our case Av10) so that its centroid dipole no longer differs much from the centroids of the sub-averages with more spikes (in our case Av25 and Av50). Since even for an extended source the center of gravity would always result in the same position in noise free set-up, the changes in the centroid dipole for different sub-averages are mainly due to insufficient SNR. By selecting Av10 in which the location of the centroid dipole does not differ much from Av50, the effects of noise on dipole scatter can be reduced [188, 189]. Averaging more spikes may not be favorable, as this may artificially reduce the scatter size leading to an underestimation of the extent of the irritative zone. Nevertheless, even for the optimal sub-average number estimated with this procedure, the effects of spatial averaging on scatter size will persist and possibly lead to a slight underestimation of the size of the irritative zone. However, the negative influence will be much smaller than localizing single spikes with insufficient SNRs. In this study, Av10 was a good compromise, but this number might surely be different for other patients. The better performance of Av10 in comparison to Av50 might be surprising since the higher SNRs of Av50 might be expected to result in better localizations. However, in the light of the results presented here and the relevant literature, this expectation can be questioned at least for localization of interictal spikes: in [190], among 19 patients with Engel I or II outcomes, the resected areas in four cases were concordant to only single spikes, in two to only averaged spikes, and in five to both single and

averaged spike localizations. A possible explanation for the latter results can be sought in the light of the publications of [12] and [15], in which using optical imaging they showed that the origins of the epileptic activity change in a stochastic way within a certain region. This questions the assumption that spikes from the same irritative zone have exactly the same origin and waveform, and can be used as an argument against averaging.

4.3.5 Topology of the irritative zone

Another important aspect is the topology of the irritative zone. In this study, the irritative zone had a convex shape so that the center of gravity was part of the zone. However, in case of a concave shape, this might change. As an example, the center of gravity of a half-moon-shaped concave topology might be outside the structure (see, e.g., the half-moon-shaped single spike localizations in Figure 4.13 which was adapted from Figure 1B in the study of [190]). However, even in the latter case, using the centroid localization change between different sub-averages is still an important measure, because a centroid shift between single spike and sub-averaged spike localizations will still indicate a systematic shift of single spike localizations due to noise.

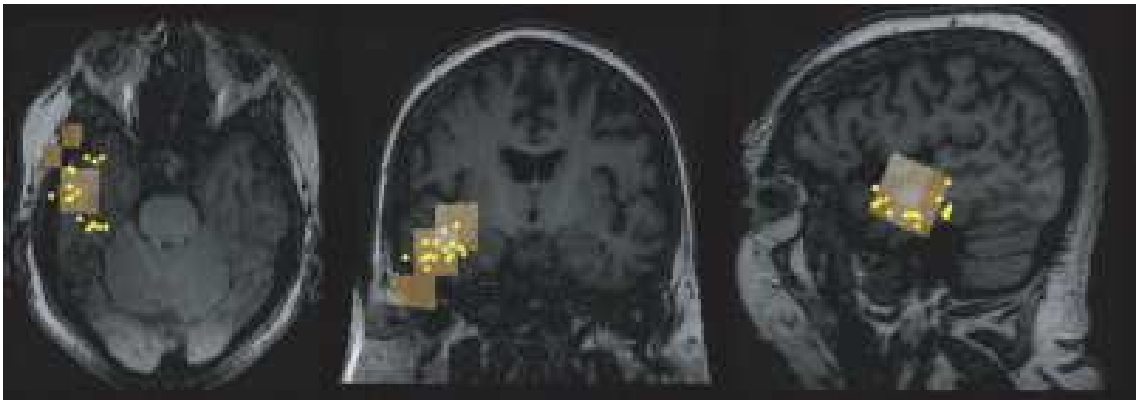


Figure 4.13: An example concave topology for single spike localizations with MEG. Single spike dipole localizations (yellow dots) and spike-locked beta/gamma activity localizations (squares) shown on individual MRI of a patient. Figure adapted from [190].

4.3.6 Relationship between size of dipole scatter, SNR and extent of the irritative zone

Oishi et al. [13] showed in an MEG study that 8 out of 9 patients, in which the spike cluster coincided entirely with the ictal onset zone determined by subdural EEG (and resected afterwards), became seizure free, whereas the ratio was just 3 out of 11 for the cases where spike cluster and ictal onset zone either only coincided partly or did not coincide at all. In agreement with the studies of [10, 11, 14, 191], this shows the potential benefit of single spike localizations. In contrast, the results of this study show that the amount of scatter is highly correlated with the number of sub-averages and the SNR, especially for relatively low SNRs. Here presented results on scatter size are mainly in line with Bast et al. [16] and Wennberg and Cheney [17, 18]. However, it was additionally shown here that the effects of sub-averaging and SNR on scatter size are valid for all investigated modalities, i.e., EEG, MEG and EMEG. Furthermore, while the other studies rely on simpler volume conduction modeling such as spherical shell models used in Bast et al. [16], the high-resolution six-compartment head model with calibrated skull conductivity and anisotropic representation of the white matter compartment as proposed in this study does not only enable simultaneous analysis of EEG and MEG, but also has the potential to improve localization accuracy for single modality EEG or MEG or in combined EMEG analysis. The latter is especially important in the temporal lobe, where a sphere approximation of the skull can result in significant errors for both EEG (e.g., [133]) and MEG (e.g., [91, 192]). The results of this study are also in a good agreement with EEG simulations of Kobayashi et al. (2005) showing dipole clusters to become less erroneously distributed with increasing SNR. However, in summary, the identification of the exact size of the irritative zone still remains a difficult problem because, as also shown in this study, scatter varies significantly with SNR, spike selection criterion and sub-average number.

Reconstructing slightly distributed activity using a single dipole model might lead to a depth-bias (sources that are localized too deep). Here, three measures were taken in order to alleviate such depth-bias and to accurately (as validated by the sEEG) reconstruct the center of the underlying activity: 1) a cortically-constrained source space, which prevents erroneous localizations inside white matter was used. 2) a head model that distinguishes CSF, gray matter, and anisotropic white matter was constructed instead of a homogeneous brain, in which the topographies for dipoles with different depths and locations might have been more similar and homogeneous. 3) a dipole scan instead of a dipole fit is preferred to ensure the finding of the global optimum of the

GOF cost function over the cortically-constrained source space.

It is important to state that in this study the aim was not to estimate the extent of a patch in which all neurons are active simultaneously and always in the same way but to estimate the extent of a patch in which the origin of the activity is different for each spike. Using optical imaging on epileptic human neocortical slices removed during epilepsy surgery, Köhling et al. [12] and Speckmann et al. [15] showed that the activated cortical areas during epileptic waves are focal and their spatial positions change in a dynamic manner within the epileptic tissue. This finding was the main reason why a subaveraging procedure was selected instead of averaging all spikes. Therefore, in this study the aim with investigating the dipole scatter was not to determine the extent of a patch that always follows exactly the same activation pattern but to benefit from the small differences on the activation pattern within the epileptogenic zone due to the dynamic and stochastic behavior of each spike as shown in [12, 15].

With regard to the chosen inverse approach, besides the cortically-constrained deviation scan as employed here (see, e.g., [70, 107, 108]), promising results were also achieved with current density approaches [70], with hierarchical Bayesian modeling frameworks [112, 113, 118] and with spatio-temporal current density approaches [130, 193] in non-invasively reconstructing networks of (epileptic) activity from EEG and/or MEG. However, also those methods need to embed correct prior knowledge in some form into the inverse approach and it still needs to be shown that the methodology is stable even in the presence of low SNR in realistic epilepsy datasets [112, 193]. Furthermore, in Bouet et al. [194], using frequency domain beamformers, the determination of the spiking volume was possible in 16 out of 21 patients with sensitivity (76%) and specificity (67%), as also validated through sEEG measurements. However, [66] showed that beamformer approaches are sensitive to head volume conductor properties. Therefore, in a future study, it will be interesting to combine other inverse methods with the sub-averaging, the head modeling and the combined EEG/MEG procedure as presented here and to evaluate their quality by means of the intracranial EEG recordings.

5 Study III: A Three Step MRI-EMEG-MRI Pipeline in Presurgical Epilepsy Diagnosis.

In this section, the EEG/MEG and MRI data measured from a 49-years-old female patient was used to study the importance of the whole head coverage of EEG/MEG for detection of epileptogenic zone. The patient signed the written consent forms and all procedures were approved by the ethics committee of the University of Erlangen, Faculty of Medicine on 10.05.2011 (Ref. No. 4453). Furthermore, in this work, a new pipeline that uses noninvasive source reconstructions and special MRI acquisitions in a three step approach (MRI then EMEG then again MRI) to find the epileptogenic zone was established. The case studied here will show that a focal cortical dysplasia (FCD) found in MRI does not always point to the epileptogenic zone even though it might be coinciding with the results of source localization. Thus, localization of earlier activity and performing of advanced MRI sequences might sometimes be crucial to reveal FCDs that cannot be detected with a standard resolution MRI, but which might be the main trigger responsible for the activation of other FCDs.

5.1 Methods

In this study, the same methods as described in Chapter 3 were used with small modifications, which are explained below. The steps of the pipeline used in this study are the following:

1. Simultaneous measurement of EEG/MEG.
2. Acquisition of a first set of MRI data (T1, T2 and DTI) that was used to construct head models and to check for lesions and cortical malformations using FLAIR MRI.

3. Source analysis of the EEG/MEG signals and comparison of the obtained results with other available sources of information such as seizure semiology and MRI findings.
4. Acquisition of a second set of MRI, which uses the ZOOMit (see Section 5.1.5) in order to obtain high resolution images (cubic voxels with 0.5 mm edge length) of a small region of interest.
5. Evaluation of the ZOOMit MRIs for lesions or cortical malformations that might not be visible in lower resolution whole brain MRIs.

5.1.1 Simultaneous measurement of EEG/MEG

The simultaneous measurements of spontaneous EEG/MEG and somatosensory evoked potentials and fields using electric median nerve stimulation were obtained and pre-processed using the procedure explained in Chapter 3.

5.1.2 Acquisition of the first set of MRI data

The first set of data included T1, T2, DT MRIs as explained in Section 3.1.2 and it was used to construct the FE head model. During this measurement also a 3D-FLAIR with TR/TE 7000 ms/322 ms and inversion time of 2400 ms was measured (cubic voxels with edge length of 1.17 mm). In radiological examinations, a right frontal FCD was detected.

5.1.3 Segmentation, head model construction, conductivity calibration and calculation of leadfield matrix

The head modeling pipeline was the same as described in Chapter 3 except that dura mater was segmented and included to the head model as the seventh compartment. The segmentation of the dura mater was performed using Seg3D¹ and involved manual segmentation as well as basic image processing techniques. Note that because of limited MRI resolution, only the thickest parts of the dura mater were segmented. The conductivity of dura mater was modeled as 0.1 S/m [195]. Other steps in head model construction were the same as described in Chapter 3 and the skull compacta and spongiosa conductivities were estimated to be 0.0033 and 0.0116 S/m, respectively,

¹Seg3D: Volumetric Image Segmentation and Visualization. Scientific Computing and Imaging Institute (SCI), Download from: <http://www.seg3d.org>

with the skull conductivity calibration procedure described previously in this work (see Section 3.1.13 for the procedure). The leadfield matrices were calculated for a source space with 2 mm resolution (see Section 3.1.11) as explained in Section 3.1.10. The head model and the source space are shown in Figure 5.1.

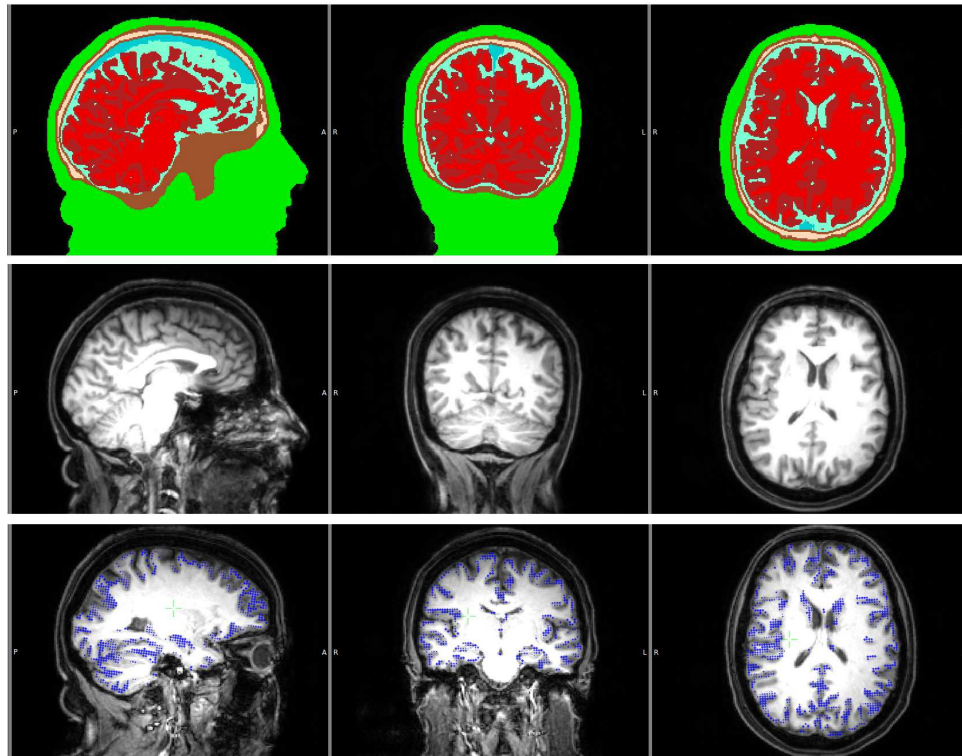


Figure 5.1: Segmented MRI (upper row), T1 MRI (middle row) and the source space points (blue points) shown on T1 (lower row) MRI. Sagittal (left column), coronal (middle column) and axial (right column) slices. Please note that the slices selected in the lower row are different from the top two rows in order to better visualize the source space points. The color codes for the tissues are scalp (green), skull compacta (brown), skull spongiosa (beige), dura mater (dark turquoise), CSF (light turquoise), gray matter (burgundy) and white matter (red).

5.1.4 Marking of the epileptic spikes and source reconstruction procedure

Ten epileptic spikes (maximum negativity at F6 in EEG), marked by a clinical reviewer, were averaged and used for source reconstruction. A current density approach sLORETA was used as the inverse approach [121]. The sLORETA current density approach was used because it is known to perform well in situations where a network of

sources are temporally disentangled so that at each time-point, only a single activation center or multiple activation centers whose leadfields are sufficiently uncorrelated need to be accurately localized [118, 121]. The inverse solutions were calculated using the CURRY 7 software after importing the leadfield matrices calculated with the SimBio (see Chapter 3).

5.1.5 Acquisition of a second set of MRI data

The second set of MRI scans were acquired with another 3T scanner (MAGNETOM Prisma 3.0T, (Siemens Medical Solutions, Erlangen, Germany)). In this set an MRI sequence that benefits from the new advancements in parallel transmission in MRI [19] was used to acquire high resolution images in a restricted area (rectangular prism with a volume $160 \times 82 \times 28 \text{ mm}^3$ spanned with cubic voxels with edge length of 0.5 mm). A 3D sequence with TR/TE 2320 ms/198 ms was used with four averages and the total acquisition time was approximately 12 minutes. This ZOOMit feature was used to acquire detailed MRIs from two restricted regions. The first region was the right frontal FCD, which was also visible in the first set of MRI data, and the second area was the left fronto central region, selected based on the results of EMEG source reconstructions, as explained in the following Section 5.2.

5.1.6 DTI tractography

After performing eddy current and susceptibility correction as explained in Section 3.1.5, the *FSL-BEDPOSTX* routine was used to calculate the distribution of diffusion parameters at each voxel using Markov Chain Monte Carlo sampling. Afterwards, the *FSL-PROBTRACKX* routine was used to perform probabilistic tractography between two regions of interest [196]. These two regions were the same as used in ZOOMit MRIs, selected based on the results of EEG/MEG source reconstructions.

5.2 Results and Discussion

All figures presented here were obtained using the CURRY-SimBio and FSL software and, unless it is stated otherwise, the shown localizations were obtained with combined EEG/MEG.

The butterfly plots of the averaged signals for EEG and MEG are shown at the upper left corner in Figure 5.2 with two vertical dashed lines indicating the spike peak (at 0 ms) and a preceding peak (at -23 ms). In the Figure 5.2, the EEG and MEG

topographies from 0 to -33 ms are shown, too. In these topographies, near the spike peak (from 0 to -7 ms) a clear dipolar pattern over the right frontal lobe is visible. In addition, when the signals were traced back in time other dipolar patterns were present at -23 ms (the preceding peak in butterfly plots).

In Figure 5.3 the sLORETA localizations projected on the FLAIR MRI slices at -7 ms are shown. In the left column of this figure, the localizations point to the right frontal region, where the FCD was detected in the FLAIR MRI (shown in the middle column). The results of ZOOMit MRI are shown in the right column of this figure, where the boundaries of the FCD can be clearly seen. In most cases, these findings would have been sufficient to decide on the resection of the right frontal FCD. In this study, the interictal spikes showed right frontal activity near the peak and a clear FCD was detected with MRI, but the seizure semiology (tingling feeling at the right anterior torso, ascending feeling of nausea, then loss of consciousness, hypermotor movement, tongue bite, enuresis) of the patient was pointing to the left fronto-central regions.

In order to investigate if the mismatch between sLORETA localizations, MRI and seizure semiology was due to propagated activity, the time points prior to the spike peak were investigated. At -23 ms, at the time of the preceding MEG peak in the butterfly plot in Figure 5.2, two main sLORETA source localization clusters were detected: in left fronto-central (see Figure 5.4) and right central (see Figure 5.5) regions. The cluster in the left fronto-central region was especially intriguing, since it was in a good agreement with the seizure semiology and the results of FLAIR MRI at the place of this localization were suspicious (see the middle column in Figure 5.4). When the patient was measured with ZOOMit MRI a small FCD at the place of the left fronto-central localization was found (see the right column in Figure 5.4).

The case studies describing a superior to inferior propagation of the epileptic spikes in frontal gyrus in just 14 ms were recently described in the literature [197]. The propagation of the epileptic activity could also explain the results of the current study. Thus, it was decided to search for an anatomical pathway that might support the hypothesis of propagation. For this purpose, DTI tractography was performed. As shown in Figure 5.6 illustrating the results of DTI tractography, fiber connections (green paths) between the two FCDs (blue spheres) might explain the very fast propagation of epileptic activity from the left fronto-central FCD to the right frontal FCD.

The localizations described in this chapter up to this point, were all obtained with EMEG (Figures 5.3, 5.4, 5.5). In Figure 5.7 the source localizations obtained with EEG, MEG and EMEG were compared. The source localizations at -23 ms (left column) and at -7 ms (right column) are shown on 3D volume rendering of the individual

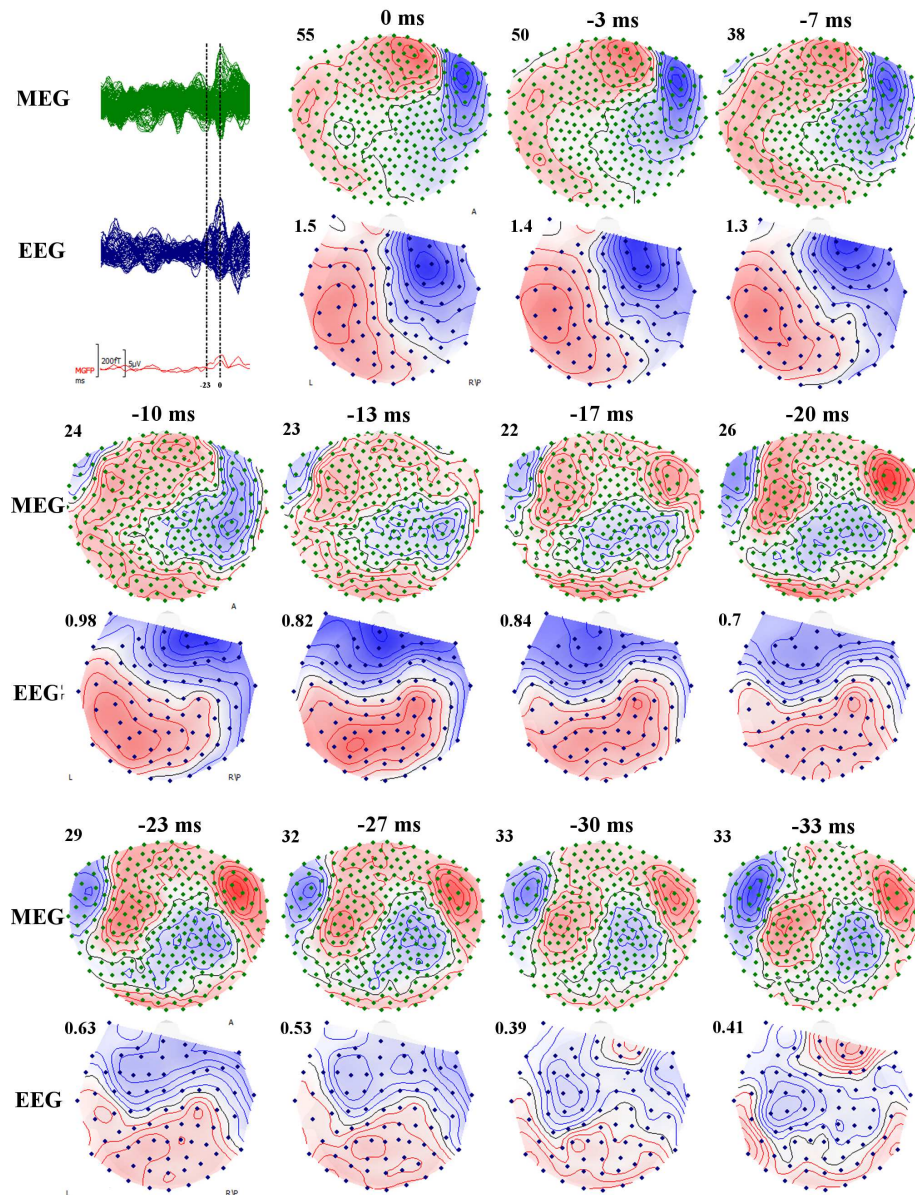


Figure 5.2: Butterfly plots (top left) for MEG (green) and EEG (blue), and topographies of MEG (upper topography) and EEG (bottom topography) for the averaged spike at 11 different time instances. The time points at 0 ms (peak of the spike) and -23 ms (the preceding peak on MEG) are indicated by dashed vertical lines in butterfly plots (top left). The MEG and EEG topographies are shown for every ~ 3.3 ms starting from 0 ms and going backwards until -33 ms. In MEG and EEG topographies, the blue (red) isopotential lines indicate negativity (positivity). The increments between contour lines for each map are shown on upper left corners and the units for EEG and MEG are μV and fT respectively. Letters in topographies indicate the orientation (L: Left, R: Right, A: Anterior, P: Posterior).

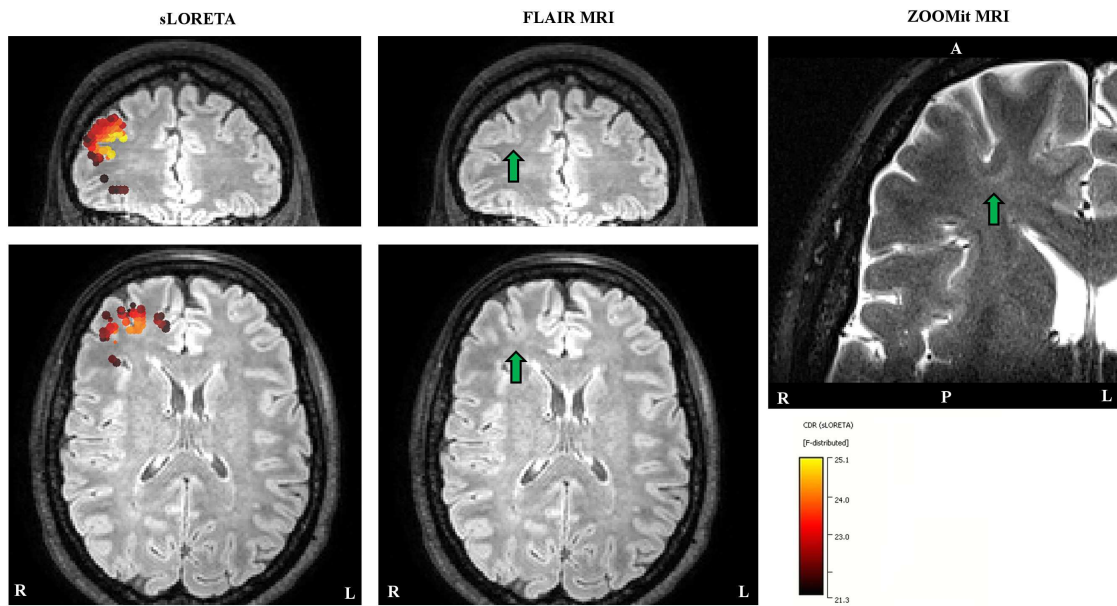


Figure 5.3: Source localizations at -7 ms. In the left column the sLORETA results projected to the FLAIR MRI are shown (only results obtained with a threshold of 85 % for the maximum F-value are shown). In the middle column, the FLAIR image without the localizations is shown. The right column shows the results of ZOOMit MRI. The green arrows indicate the FCD and the white letters on MRIs show the orientation (L: Left, R: Right, A: Anterior, P: Posterior).

brain and the positions of FCDs detected with MRI are indicated with blue spheres. In EMEG (top 2 rows) the localizations were coinciding well with the FCD positions at both time instances. At -7 ms in EEG and MEG the localizations were not as close to the FCDs as in case of EMEG, however, they were still within the close proximity of the FCD. In contrast, at -23 ms both EEG and MEG localizations were far away from the left fronto-central FCD. These results are in a good agreement with the findings described in Chapter 4 indicating that EMEG benefits from the complementary information of EEG and MEG to stabilize the source reconstructions, especially in case of low SNR.

In Chapter 4 it was shown that by using EMEG the epileptic activity and its propagation can be distinguished in a sub-lobal level within the temporal lobe. In that study, the intracranial stereo-EEG (sEEG), which is widely accepted as the "gold standard", was used for the validation purposes. However, intracranial recordings suffer from low spatial sampling due to limited number of invasive electrodes, and the tunnel view effect due to limited coverage [1]. For example, if in this study the intracranial elec-

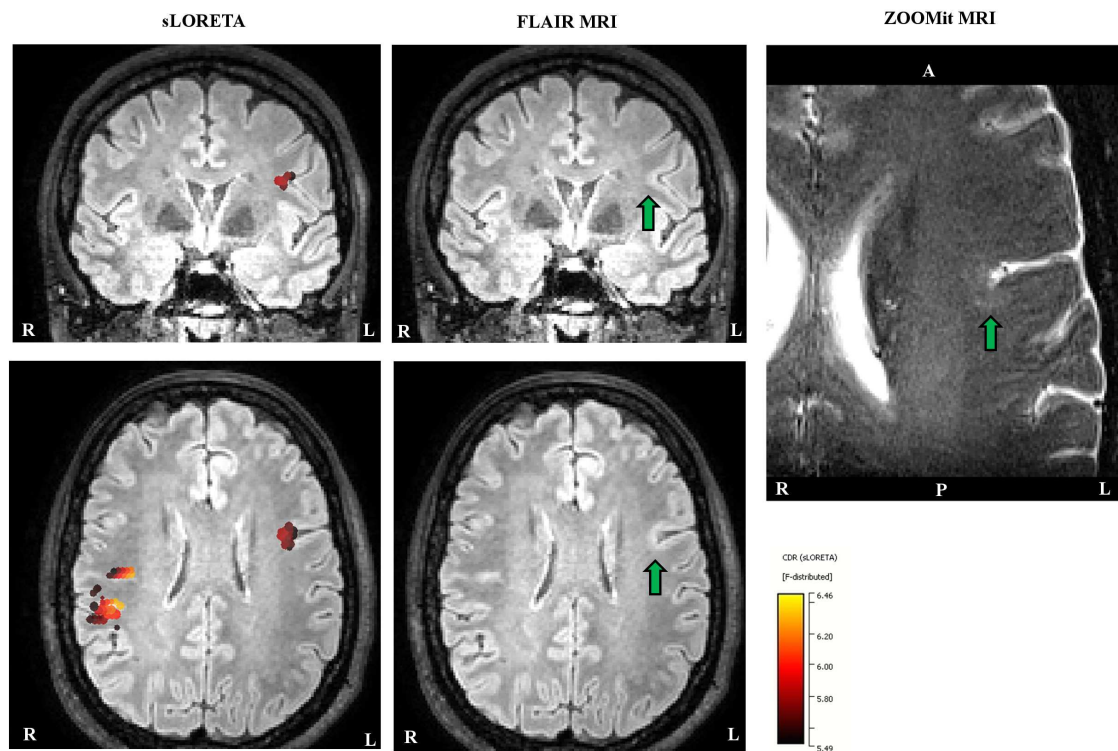


Figure 5.4: Source localizations at -23 ms, slices selected according to the left hemispheric activity. In the left column, the sLORETA results registered to the FLAIR MRI are shown (only results obtained with a threshold of 85 % for the maximum F-value are shown). In the middle column, the FLAIR image without localizations is shown. The right column shows the ZOOMit MRI for the localization cluster (detected with sLORETA) at the left fronto-central region. The green arrows show the FCD and the white letters on MRIs indicate the orientation (L: Left, R: Right, A: Anterior, P: Posterior).

trodes would have been placed near the right frontal FCD they would not have been able to measure the epileptic activity in the left fronto-central FCD. Therefore, it is very important to find the right location for the invasive electrodes by combining the information obtained from noninvasive EEG/MEG, MRI and the seizure semiology.

It is important to note that sLORETA might suffer from artificially dispersed localizations, and it does not perform well in situations with multiple sources and a limited distance between sources [118]. Thus methods that do not have these problems, like hierarchical Bayesian methods [112, 118] and maximum entropy on the mean method [135, 152] might be a better choice for the future studies. A second important point is that the dura mater segmentation used here was not optimal. However, it is still expected that the constructed head model, which includes dura mater as a seventh compartment, to perform better than a head model in which the dura mater is mod-

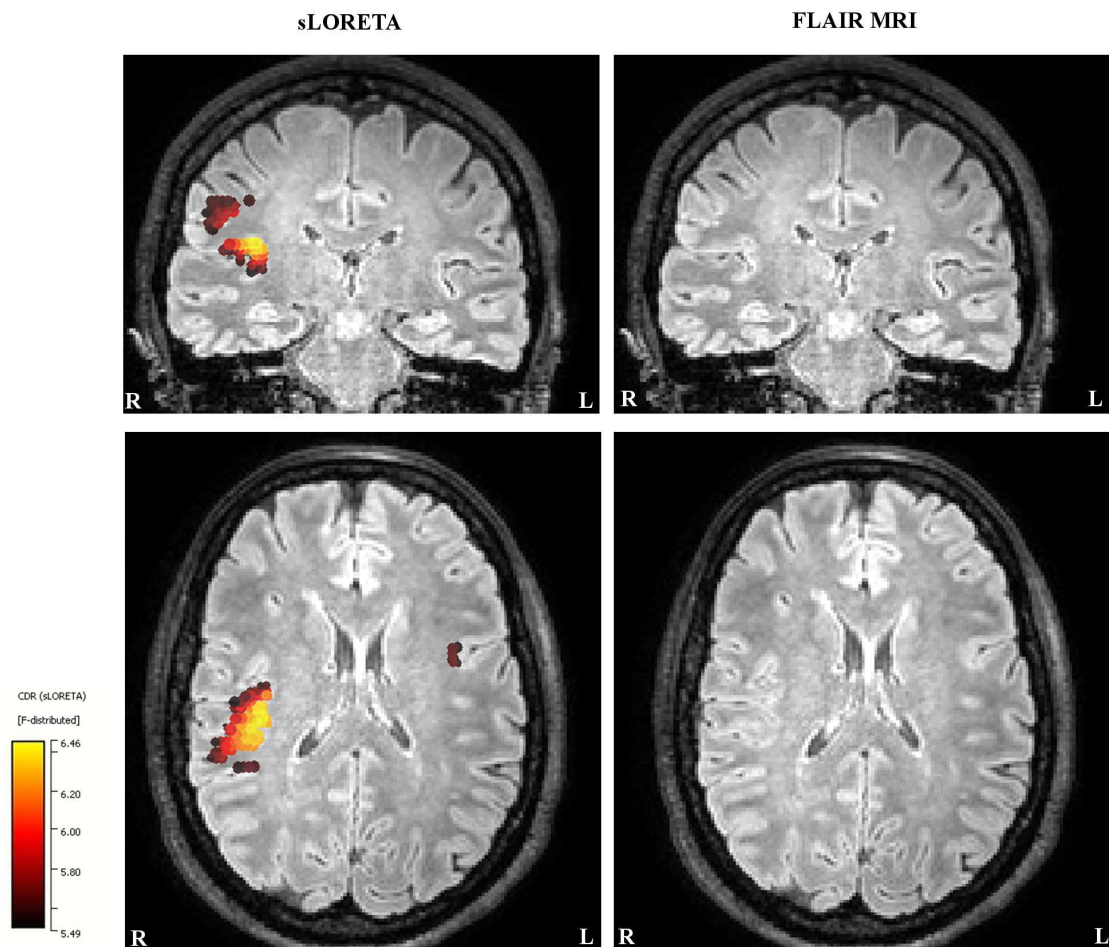


Figure 5.5: Source localizations at -23 ms, slices selected according to the right hemispheric activity. The sLORETA results registered to the FLAIR MRI are shown in the left column (only results obtained with a threshold of 85 % for the maximum F-value are shown). In the right column, the FLAIR image without the localizations is shown. The white letters on MRIs indicate the orientation (L: Left, R: Right, A: Anterior, P: Posterior).

eled as part of the CSF.

To summarize, a short study, which was used to test the feasibility of a pipeline that employs the recent advancements in MRI technology and noninvasive source analysis in presurgical epilepsy diagnostics, was presented in this section. The re-investigation of MRIs using findings of source analysis is not a new idea [198], but the main novelty of the pipeline described in this work is the usage of ZOOMit MRI to obtain high resolution images from a small region of interest, which to the best of the author's knowledge was not reported before. Based on the findings presented in this study, the patient was operated on the left fronto-central FCD and she is seizure free for 4 months

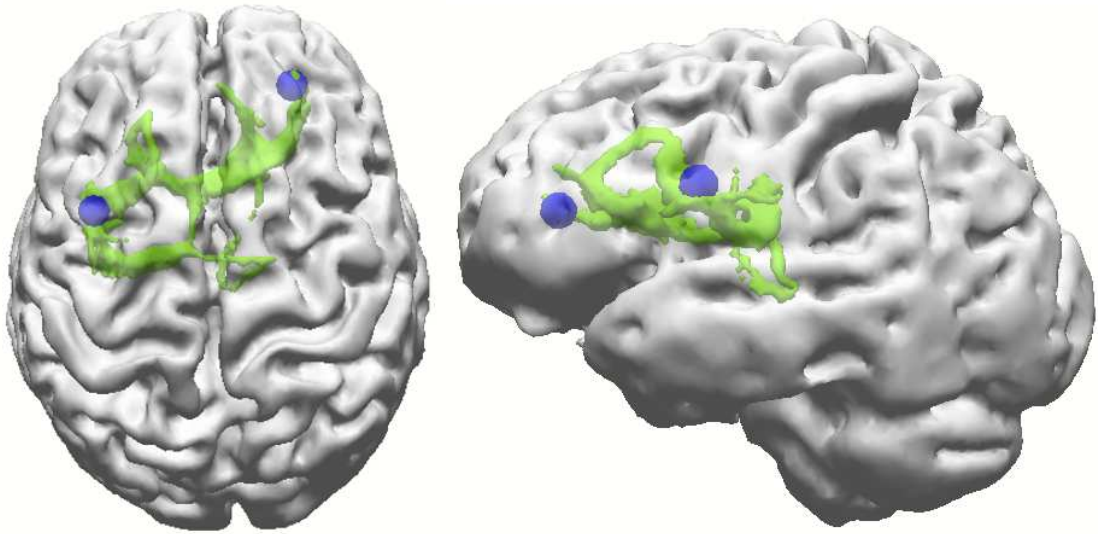


Figure 5.6: The results of DTI tractography. The green paths show the tracts that were found between the two FCDs indicated by blue spheres.

now. Thus, the three step MRI-EMEG source analysis-MRI procedure presented here can be used as a very promising tool to detect small lesions or cortical malformations and in some cases this might help invasive recordings.

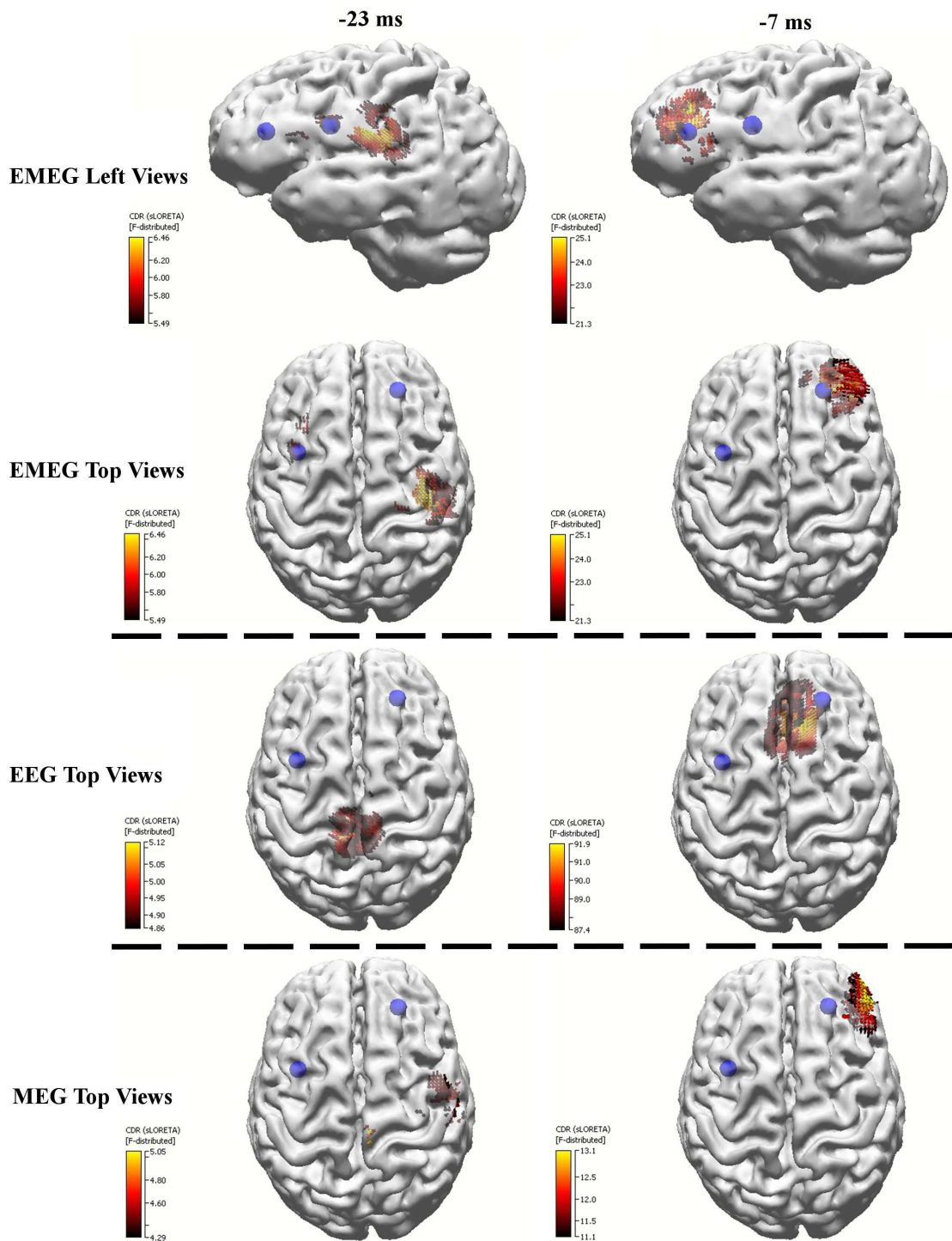


Figure 5.7: The EMEG (top two rows), EEG (third row from the top) and MEG (bottom row) localizations at -23 ms (left column) and -7 ms (right column). Only the results that passed 85 % threshold of the maximum F-value are shown. The FCDs detected with MRI are indicated by the blue spheres. Left and top views of the brain are shown for EMEG and only top view of the brain is shown for EEG and MEG.

6 Study IV: EMEG Source Analysis of Evoked Responses with Finite Element Head Models

Before the EEG/MEG/MRI data from patients with pharmaco-resistant epilepsy was investigated, the performance of EEG, MEG and EMEG in analyzing evoked responses was compared. In this study, the focus was on two kinds of evoked responses: somatosensory evoked responses (SER) and auditory evoked responses (AER).

The post-processing of the signals and construction and calibration of the FE head model was done with the same processing pipeline as described in Chapter 3, thus these methods are not explained here.

The data presented in this section was measured from two different healthy subjects. The subjects, 45 and 25 years old males, signed the written consent forms and all procedures were approved by the ethics committee of the University of Erlangen, Faculty of Medicine on 10.05.2011 (Ref. No. 4453).

In this section, a general convention is used to name evoked potential (in EEG) and evoked field (in MEG) components. In this context if the name N20 is used for the component measured in EEG, then N20m will be used for the MEG counterpart, and N20(m) will be used when both EEG and MEG components are discussed.

6.1 Subject I: General Properties of Somatosensory and Auditory Evoked Responses

6.1.1 Head model

A six-compartment finite element head model with anisotropic brain compartment was constructed and used in this study. The head model was constructed from the individual MRIs as explained in Chapter 3. After performing conductivity calibration,

conductivities for skull compacta (0.0033 S/m) and spongiosa (0.01155 S/m) tissues were obtained. The conductivity values for the other compartments were the same as in those in Section 3.1.7.

6.1.2 Somatosensory evoked potentials and fields

Somatosensory evoked responses were measured for two main purposes. First, the data was required to calibrate the skull conductivity as explained in Section 3.1.13. Secondly, it was aimed to use it for evaluation of the proposed methods, namely EMEG with conductivity calibrated FE head models, since the brain areas for the processing of primary-sensory stimuli are relatively well known. The main interest was the N20(m) component because (as already explained in previous sections) the underlying sources behind this component can be explained with single mainly tangentially oriented dipole. This dipole represents the activation in the primary sensory cortex SI (postcentral sulcal wall, Brodmann area 3b), contralateral to the stimulation side [6, 42, 109].

6.1.2.1 Stimulus properties, signals and topographies

In this study, the stimulation and source reconstruction procedures were identical to the ones used for the patients (see Section 3.1.8.1). The somatosensory evoked potentials (SEP) and fields (SEF) of the subject due to electrical stimulation of the median nerve of the right hand is shown in Figure 6.1. In this figure the MEG (green) and EEG (blue) butterfly plots are given. The first peaks visible in these plots are around 4 ms and they are due to the artifact caused by the electrical stimulation. The extent of this artifact is related to the strength and the duration of the stimulating electric current. In test measurements (data not shown here), it was found that this artifact is observed mainly on the side where the EEG amplifiers are situated, and the strength of this stimulation drops considerably when the cables for the electric stimulation are twisted to avoid possible magnetic induction due to currents they carry. Tactile somatosensory stimulation using an air-pressure driven membrane was also tested for comparison with electric stimulation. The responses generated by the air-puff stimulation were no longer as sharp as in the case of electrical stimulation and their amplitudes were smaller. Similar results were also observed in a previous study [199]. Another interesting characteristic of this stimulation artifact is its sinc style fading, which gives the impression that there is stimulation even before 0 ms. This is mainly due to the two way (backward-forward) filters used to achieve a zero phase difference.

The first real component in Figure 6.1 is the so-called P14 component in the EEG butterfly plot. This component is important because it clearly shows the sensitivity differences between EEG and MEG. In contrast to EEG, this component is not observed in the butterfly plot of MEG. The P14(m) component is thought to occur at the brain-stem [109] and because of the deep location and mainly quasi-radial orientation of the source, the P14m component is hard to detect with MEG (see corresponding topographies in Figure 6.1).

The first component that is visible in both EEG and MEG is the N20(m). As expected, both EEG and MEG topographies have clear dipolar patterns with almost 90 degree shift between the poles. Furthermore, the EEG poles are further away from each other in comparison to the MEG due to effects of low conductive skull (see N20(m) topographies in Figure 6.1).

6.1.2.2 EEG, MEG and EMEG source reconstructions for SER

Figure 6.2 shows the source reconstructions for the N20(m) component based on EEG (blue), MEG (no regularization) (green) and EMEG (red) on the MRI (upper figures) and on a volume rendering of the brain (lower figures). The Brodmann area 3 (depicted in purple in Figure 6.2) was calculated by registering the Talairach atlas to the individual MRI using CURRY7. As can be seen from the Figure 6.2, the positions of the EEG and MEG sources are very close to each other. This supports our hypothesis of a quasi-tangential focal source. In line with the results in Section 3.2.2.4 the EMEG dipole was not located simply between the EEG and MEG dipoles. Furthermore, its location fitted very well to the estimated Brodmann area 3. In terms of orientation, the MEG dipole indicates a quasi-radial direction while the EEG and EMEG shows a quasi-tangential orientation, which is in a good agreement with the findings of other studies [109]. This difference in orientation is observed mainly because MEG is insensitive to quasi-radial components. As also explained in [6] the radial orientation of the MEG dipole is due to low gain components in the MEG leadfield matrix that correspond to quasi-radial components. In order to avoid this, all MEG source reconstructions, except those described in this section, were performed with regularization. The user thus decides with his choice of the regularization parameter about the contribution of the quasi-radial source component to the estimated source orientation. In this section, the results of MEG are shown without regularization in order to emphasize this important point. Another key finding, which is obvious from Figure 6.2 is that the depths of EEG and MEG dipoles fit very well to each other. This is important because it shows that a proper conductivity calibration strategy (described in Section 3.1.13)

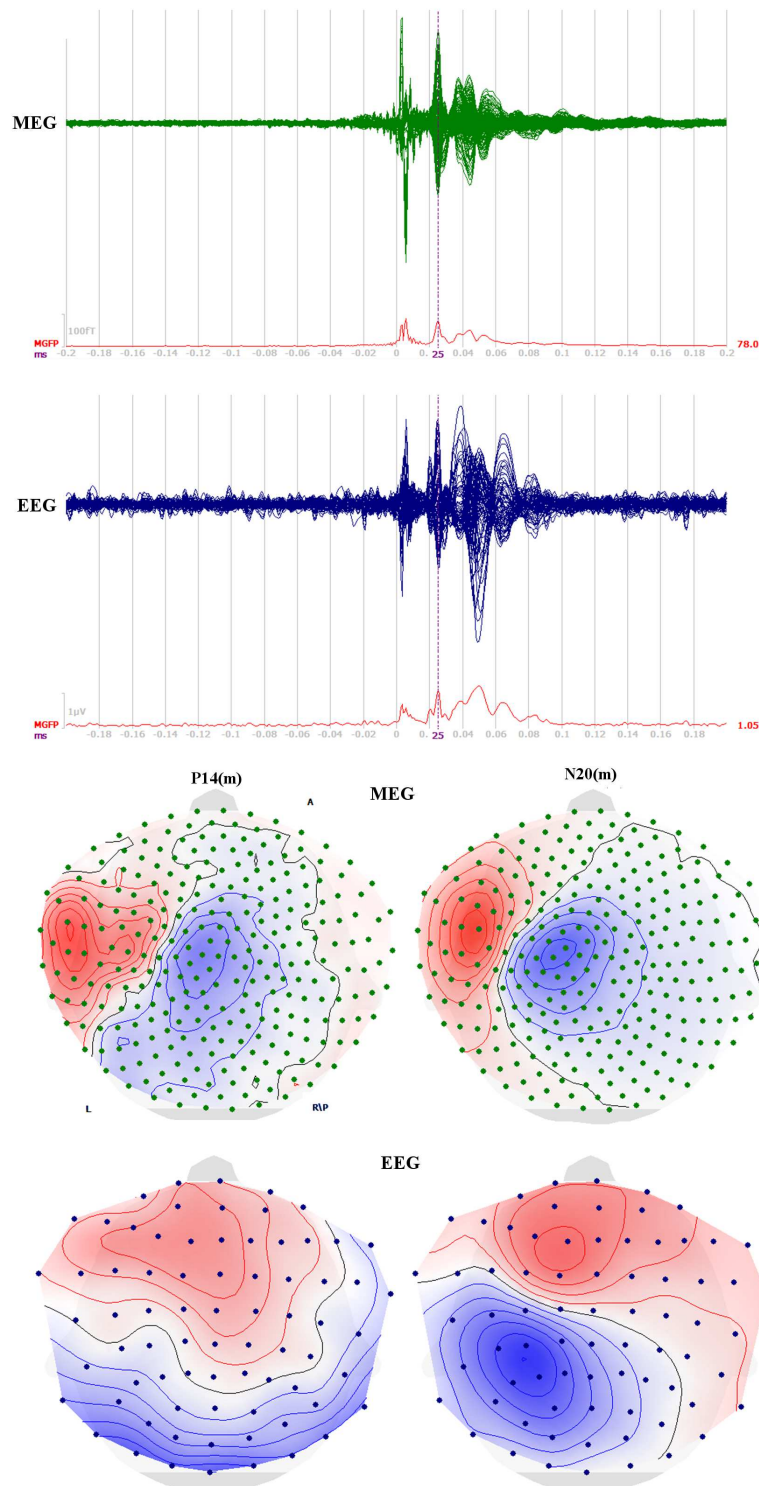


Figure 6.1: Healthy subject SEP(EEG)/SEF(MEG) butterfly plots and topographies for P14(m) and N20(m) components.

was selected.

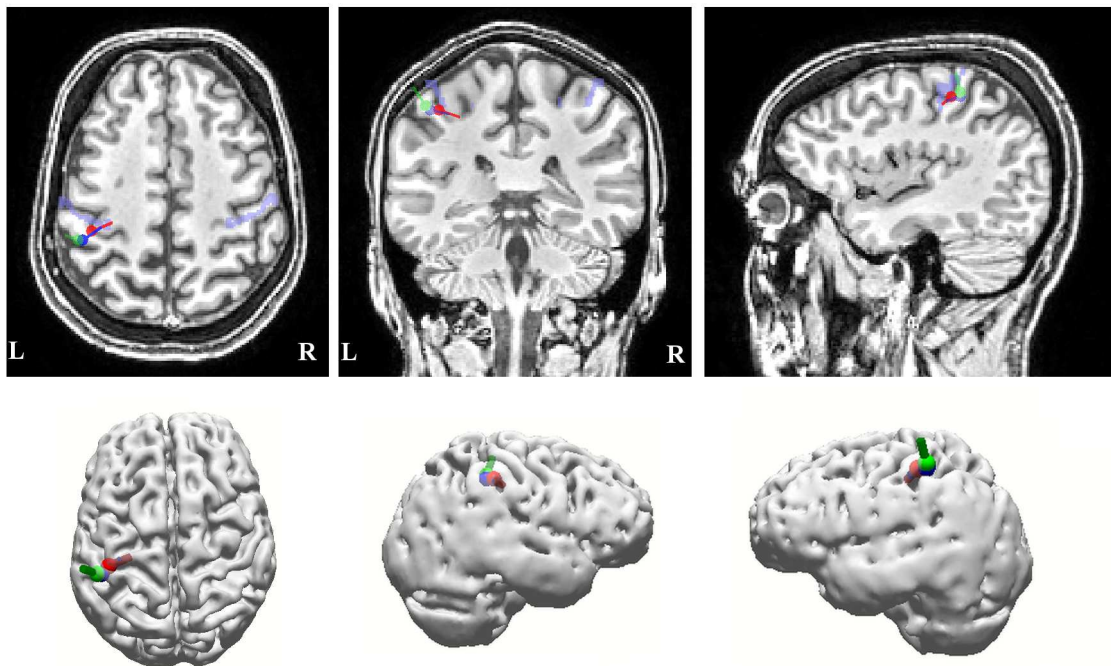


Figure 6.2: Source reconstructions for the N20(m) component for a healthy subject based on EEG (blue), MEG (no regularization) (green) and EMEG (red) shown on the MRI (upper figures) and on a volume rendering of the brain (lower figures). Left and right sides are depicted with L and R, respectively, in the top figures. The Broadmann 3 area is highlighted with purple in MRIs.

6.1.3 Auditory evoked potentials and fields

It is known that human auditory cortex has a tonotopic organization, i.e., different frequencies are processed in different locations in the auditory cortex [200]. The N100(m) component, a component with latency around 100 ms, is a stable and high magnitude component in both auditory evoked potentials (AEP) and auditory evoked fields (AEF) [200]. In previous studies it was shown that the N100(m) response could be used to investigate the tonotopy, and that the tonotopic distance is rather small (8 mm depth difference for stimuli with frequencies between 500 Hz and 4,000 Hz) [201]. Thus, even the smallest errors in the forward or inverse model used for non-invasive source reconstruction might prevent the observation of the tonotopic behavior and this motivates to use realistic FE head models with calibrated skull conductivities to investigate the tonotopic behavior.

6.1.3.1 Stimulus properties, signals and topographies

Pure sinusoidal tones with 500 ms duration and frequencies of 250, 1000 and 4000 Hz (always two octaves in between) were presented bilaterally. The hearing thresholds for each frequency were measured separately inside the MEG chamber, and 55 dB above this level was used for stimulation. Each AER run was eight minutes long, and a total of six runs (each frequency twice) were measured in a session. In each run, only one tone frequency was presented, and the order of the frequencies used in each run was 1000, 4000, 250, 4000, 250 and 1000 Hz. Each run had ~ 110 events with randomized stimulus onset asynchrony (SOA) from 3.5 to 4.5 s. A relatively long SOA was used because according to our initial tests, the mean global field power of the responses can increase up to 60 % when an SOA of 3.5-4.5 s is used instead of 1.7-2.2 s. Similar findings were also reported in the literature [111, 202].

In order to compensate for the delay between the trigger, sent from the computer, and the actual time the signal reaches the ear of the subject, a cosine shaped pulse signal was added to the stimulus signal, and a second trigger was created when this signal was detected in the chamber. The used cosine shaped pulse signal had a carrier frequency of 18 kHz, peak to peak amplitude of 20 % of the peak amplitude of the stimulus signal, and a total duration of 2 ms. The acoustic sound was transmitted through a rubber tube with a length of 90 cm and an inner diameter of 3 mm. The frequency transfer characteristics of the system and the tubes (which are almost linear in a frequency range from 125 Hz up to 6 kHz) ensure sufficient damping of this high frequency trigger, so that it is not audible.

The signals measured for three frequencies (250, 1000 and 4000 Hz) and the topographies at the rising flank of the N100(m) component are shown for EEG (butterfly plot with blue lines and the topography map next to it) and MEG (butterfly plot with green lines and the topography map next to it) in Figure 6.3. As can be seen from the Figure 6.3, in the butterfly plots the highest components were at around 100 ms in all measurements. In MEG topography maps four poles are clearly visible, supporting the two-dipolar structure of the rising flank of the N100m component. Furthermore, hierarchical Bayesian modeling has shown that the two dipole model is an appropriate model for the rising flank of the N100(m) [113]. In contrast, in EEG topography maps the two poles at frontal regions appear as one and the other two poles on the right and left posterior regions are visible only partly, most likely because we used a standard 10-10-system electrode cap that contains deeper electrodes, but still not deep enough for the two positive auditory poles. While it might be possible to measure

these partly visible poles completely with other EEG caps (by sacrificing SNR due to muscle artifacts measured by the electrodes on the neck), the two melted negative poles over the frontal lobe can not be disentangled with any EEG cap. Thus, considering the measured topographies, in this case MEG seems to be the stronger modality to study AER N100(m) component for adults with regard to stable localization, but MEG is still weak with regard to an appropriate reconstruction of source orientations and magnitudes.

6.1.3.2 EEG, MEG and EMEG source reconstructions for AER

EEG and MEG leadfield matrices were calculated with SimBio, the source spaces were constructed as explained in Section 3.1.11 and imported to Curry 7. The signals were filtered with a zero phase bandpass filter (1-20 Hz) [110] and a semi automatic artifact rejection procedure based on the amplitudes was applied.

A two dipole solution was obtained for the rising flank of the N100 signal with a two-step dipole scan approach. First, a source space with a resolution of 4 mm was constructed within the gray matter volume (see Section 3.1.11). Then, a scan was performed for both MEG and EMEG for the measurement results of all frequencies and head models in order to get a rough estimation of the source positions. In the second step, a 1 mm source space was constructed within 8 mm distance of the initial localization results and a new scan was performed using this source space.

The EEG (blue), MEG (green) and EMEG (red) source reconstructions for the rising flank of the N100(m) component for the stimulation with 1000 Hz are shown on the MRI (upper figures) and on a volume rendering of the brain (lower figures) in Figure 6.4. The results for the AER differ from the results for SER, presented in Section 6.1.2.2. The main difference is the distance between EEG and MEG localizations, which is as high as 24 mm for AER. It is assumed that this difference is caused by EEGs inability to measure all poles for the N100(m) as explained in Section 6.1.3.1. In line with the results presented in Table 3.6, in the case of EMEG, the locations are mainly determined by MEG and EEG information mostly contributes to the orientation of the sources (Table 6.1 and Figure 6.4). However, especially for the left hemisphere there is still a considerable distance (8.2 mm) between the EMEG and the MEG centroid localizations (Table 6.1).

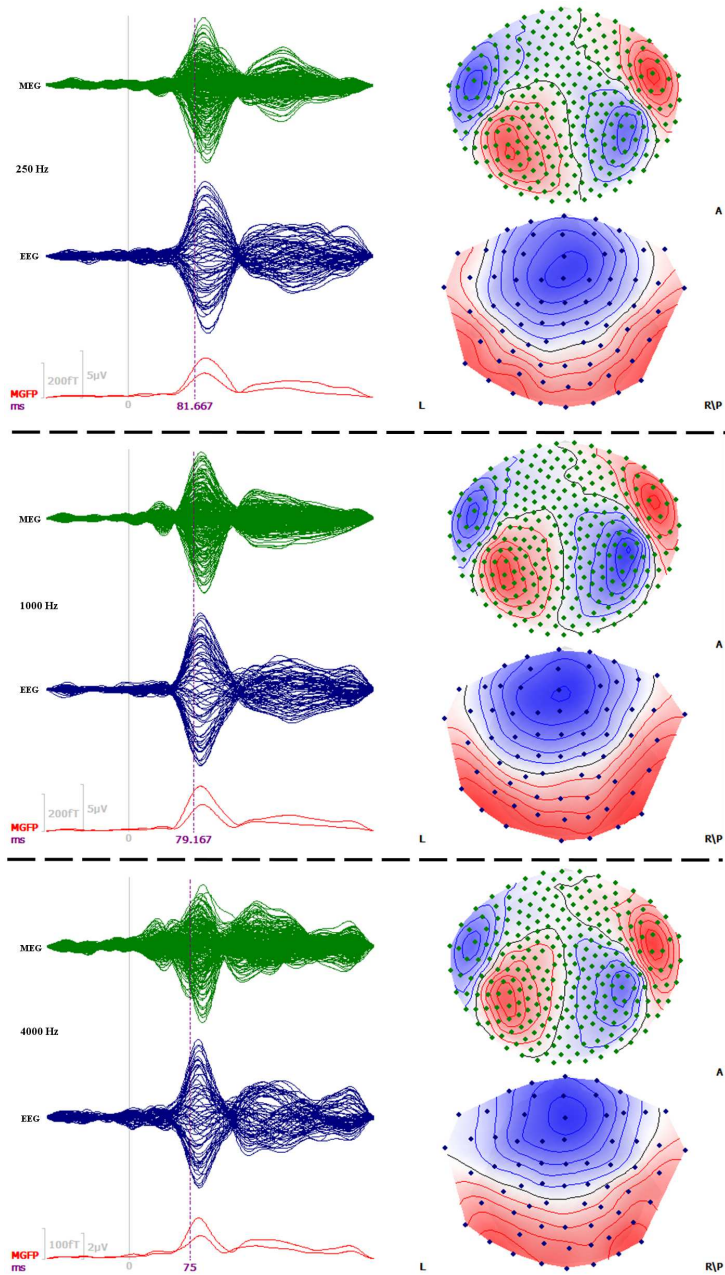


Figure 6.3: AEP/AEF signals and topographies for 250 Hz (upper two rows), 1000 Hz (middle two rows), 4000 Hz (lower two rows) sinusoidal tones. The topographies at the rising flank of the N100(m) component are shown for EEG (butterfly plot with blue lines and the topography map next to it) and MEG (butterfly plot with green lines and the topography map next to it). The dashed vertical lines in butterfly plots indicate the time points for which the topographies are shown.

6.1.3.3 Source reconstructions for AERs for different stimulus frequencies

In Figure 6.5 the EMEG source reconstructions for 250 (red), 1000 (blue) and 4000 (green) Hz stimulus frequencies are shown on the MRI (upper figures) and on a volume

Table 6.1: Comparison of EEG and MEG source reconstructions of the auditory N100(m) with the results of EMEG for the left and right hemisphere: differences in dipole locations and orientations for the left and right hemisphere obtained with 1000 Hz stimulus.

Hemisphere	Modality	Difference from EMEG	
		Location Diff. (mm)	Orientation Diff. (degree)
Right	EEG	9.2	21
	MEG	2.6	45
Left	EEG	19.7	17
	MEG	8.2	36

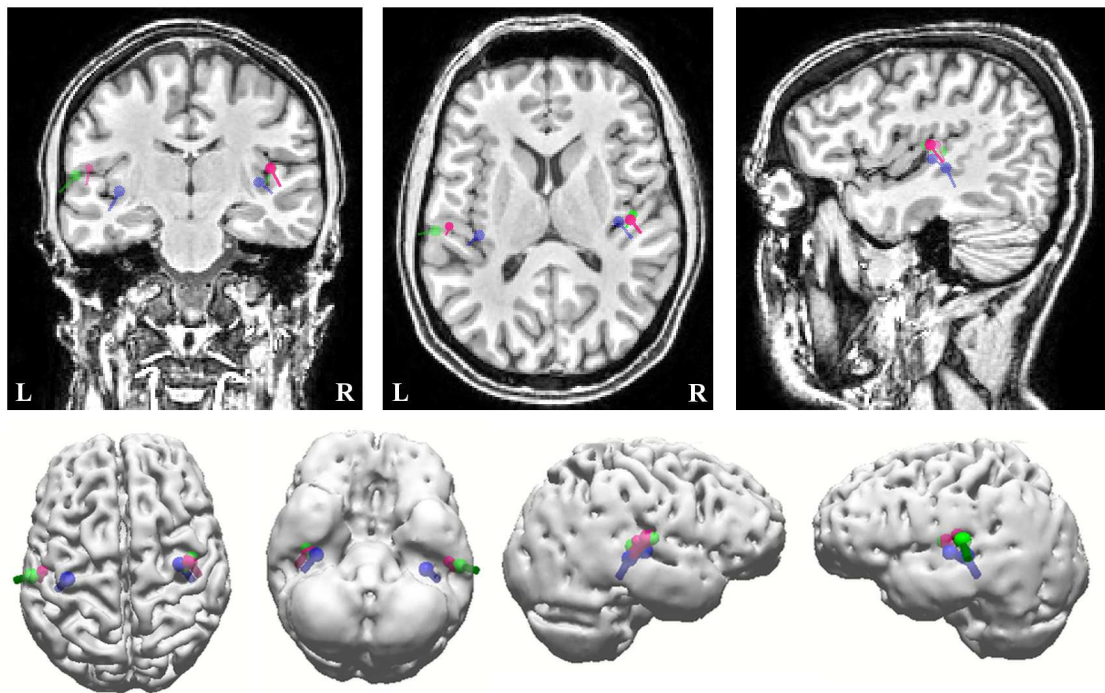


Figure 6.4: The EEG (blue dipoles), MEG (green dipoles) and EMEG (red dipoles) source reconstructions for the rising flank of the N100(m) component for the stimulation with 1000 Hz are shown on the MRI (upper figures) and on a volume rendering of the brain (lower figures).

rendering of the brain (lower figures). In line with the literature, the dipoles in the right hemisphere are localized deeper for higher frequencies [201]. In Table 6.2 the positions of the EMEG dipoles are given for the tested frequencies on the left and right hemisphere. The results in this table are given in the PAN coordinate system, thus, the

coordinates are determined using the left preauricular (PAL), the right preauricular (PAR) and the nasion (NAS) fiducials. With the x-axis from PAL to PAR (lateral-medial direction), y-axis goes through NAS (posterior-anterior direction) and z-axis (inferior-posterior direction) points up from the intersection of x- and y- axes. As expected, the main difference for different frequencies is observed on the lateral-medial (x-axis) direction and the difference between 250 and 1000 Hz is almost the same as the one between 1000 and 4000 Hz. In the left hemisphere the dipole for 250 Hz is localized more lateral than for 1000 and 4000 Hz, however, there is only 0.1 mm difference, which is below the uncertainty level of non-invasive source reconstruction methods. Therefore, between 1000 and 4000 Hz the results are not sufficient to claim the tonotopic scheme for this hemisphere. Small anatomical differences between the right and the left auditory cortices as well as differences on the achieved SNRs [203] could explain these results. Nevertheless, these findings are in a good agreement with the results of [204], which showed that the dipoles are spanning a larger area in right hemisphere for N100m component in comparison to the left hemisphere. As stated in Section 6.1.3.2, in contrast to EEG, the contributions of MEG to the source location are more important for the AER, thus the small changes in the anatomy that lead to more quasi-radial sources might disturb the results.

Table 6.2: The positions of the EMEG dipoles are given for the tested frequencies in the left and right hemisphere. The x coordinates correspond to lateral-medial direction (higher absolute values correspond to more lateral locations), y corresponds to posterior-anterior direction (higher values correspond to more anterior locations) and z corresponds to inferior superior direction (higher values correspond to more superior locations).

Hemisphere	Stimulus Frequency	Coordinates		
		x	y	z
Right	250 Hz	54.1	24.5	65.9
	1000 Hz	47.0	22.8	59.1
	4000 Hz	40.2	17.6	62.5
Left	250 Hz	-47.6	15.9	62.6
	1000 Hz	-45.3	17.1	62.1
	4000 Hz	-45.4	22.3	62.6

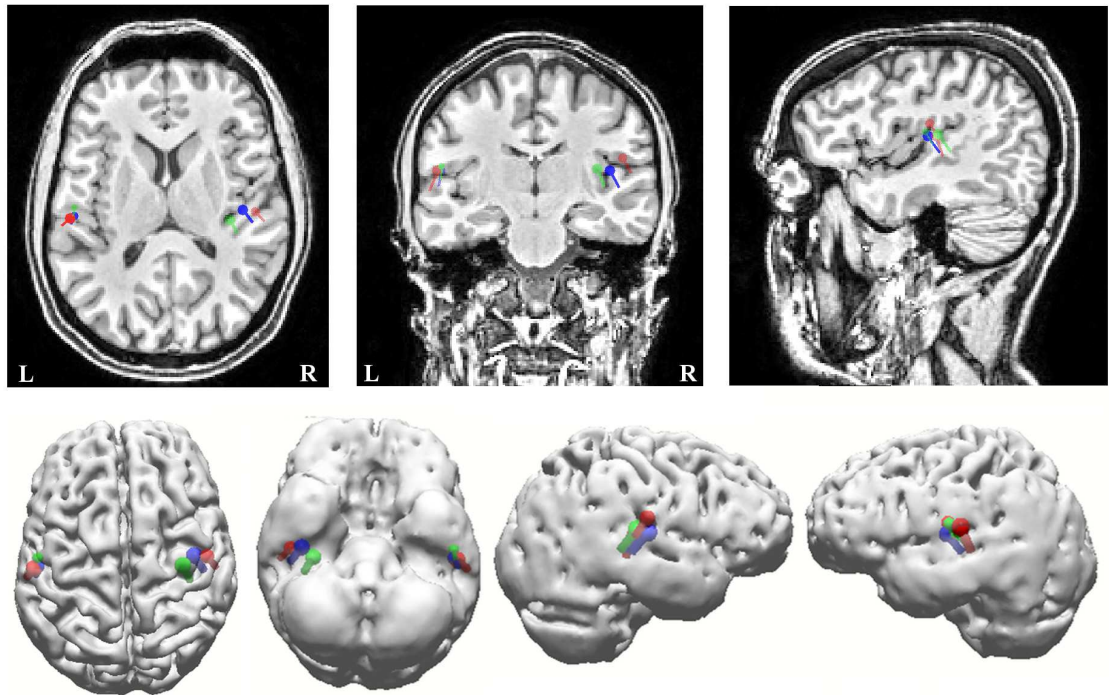


Figure 6.5: EMEG source reconstructions for auditory stimulation with sinusoidal tones with 250 (red), 1000 (blue) and 4000 (green) Hz are shown on the MRI (upper figures) and on a volume rendering of the brain (lower figures)

6.2 Subject II: Comparison Between the Primary and the Secondary Auditory Cortices

In the previous section, data measured from a subject with common auditory evoked responses was investigated. In this section, the special ¹ AERs from another healthy subject, whose audiogram, clinical examination and radiologic examination showed no pathology, were analyzed. The first measurements were done using the same stimuli as described in Section 6.1.3.1 and it was observed that although the subject can hear normally with both ears as evidenced by the audiogram, in the topography maps the N100(m) component mainly only appears over one (the right) hemisphere. In order to investigate the reasons for this unusual observation, two additional experiments were performed and the findings are presented here. The key results point to the importance and extent of the individual variance of the brain activities.

¹Special in the sense that the measured AERs differ from the mean of the AERs of the general population.

6.2.1 Experiment 1: Investigation of the long latency components

6.2.1.1 Properties of the stimulus and pre-processing

In the first experiment a paradigm that is designed to investigate the long latency components, i.e., the N100(m), was used. The conditions of the experiment are listed below:

- Stimulation type: In contrast to the experiment described in Section 6.1.3.1, monaural stimulation was studied in order to better investigate the hemispheric differences.
- Tone duration: 800 ms with 10 ms rise and fall time.
- Tone frequency: 1400 Hz to ensure good SNR.
- Inter stimulus interval (ISI): randomized between 3.5 to 4.5 seconds to ensure high SNR and to avoid habituation.
- Number of epochs: ~ 350 .
- Strength of the stimulus: 60 dB above hearing level.
- Measurement duration: In total ~ 56 minutes, 28 minutes for each ear.

Prior to source reconstruction, the baseline of the data was corrected using the pre-stimulus interval (from -200 to 0 ms) and filtered with zero-phase bandpass (1-100 Hz) and notch (50 Hz) filters. After visual inspection TP9, F2 and FC3 were selected as bad channels. Following the amplitude based semi-automatic artifact rejection process, 320 epochs were averaged for the left ear and 329 for the right ear stimulation.

6.2.1.2 Results

6.2.1.2.1 Signals and topographies

The butterfly plots of the AERs for the left ear stimulation (LES) are shown in Figure 6.6. For MEG (green) the sensor signals over the LH and over the RH are plotted separately. For EEG (blue) only the signals on three electrodes over the LH (T7, FT7, FT9) and over the RH (T8, FT8, FT10) are plotted to enhance comprehension (to minimize the effects of the activity on the other hemisphere). In this figure P50m, N100m and later components, measured with MEG sensors over the right hemisphere, are clearly visible. In contrast, over the left hemisphere, there is little or no signal for

the P50m and the N100m and only the later components components (> 175 ms) are clearly visible. In EEG (in the selected electrodes) also, the N100 component over the RH is significantly higher than over the LH. With the selected electrodes it is hard to comment on the P50 component (in EEG), thus, the hemispheric differences of P50 component will be discussed later in this section with the help of the topography maps.

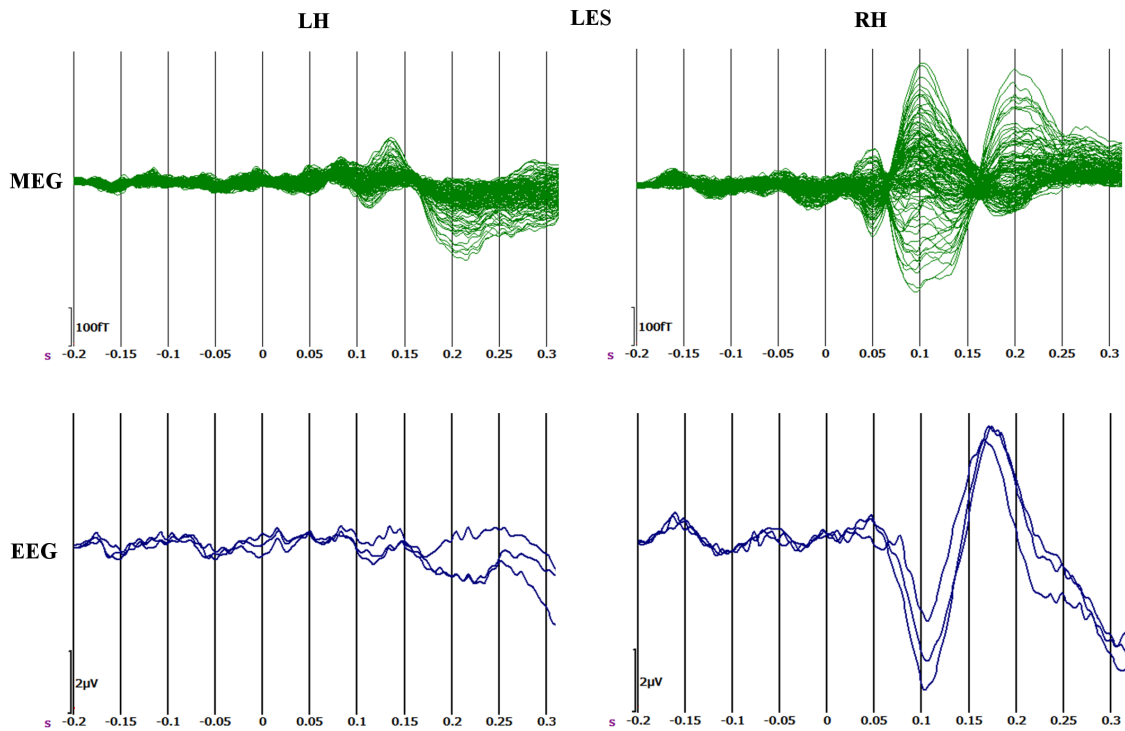


Figure 6.6: Left ear stimulation: Auditory evoked responses for 800 ms long sine tones. For MEG (green) the sensor signals over the LH and over the RH are plotted separately. For EEG (blue) only the signals on three electrodes over the LH (T7, FT7, FT9) and over the RH (T8, FT8, FT10) are plotted to enhance comprehension.

The butterfly plots of the AERs for the right ear stimulation (RES) are shown in Figure 6.7. Again for MEG (green) the sensor signals over the LH and over the RH are plotted separately. For EEG (blue) only the signals on three electrodes over the LH (T7, FT7, FT9) and over the RH (T8, FT8, FT10) are plotted to enhance comprehension. For RES the P50m and N100m are visible over the RH but with smaller amplitudes (especially for N100m) in comparison to LES (see MEG signals in Figures 6.6 and 6.7). Unlike for the LES, very weak P50m and N100m components are detectable also over the LH. The EEG signals for the RES also show higher amplitudes for electrodes over the RH but the hemispheric difference is lower than for LES. With the selected electrodes it is hard to comment on the P50 component (in EEG), thus,

the hemispheric differences of P50 component will be discussed later in this section with the help of the topography maps.

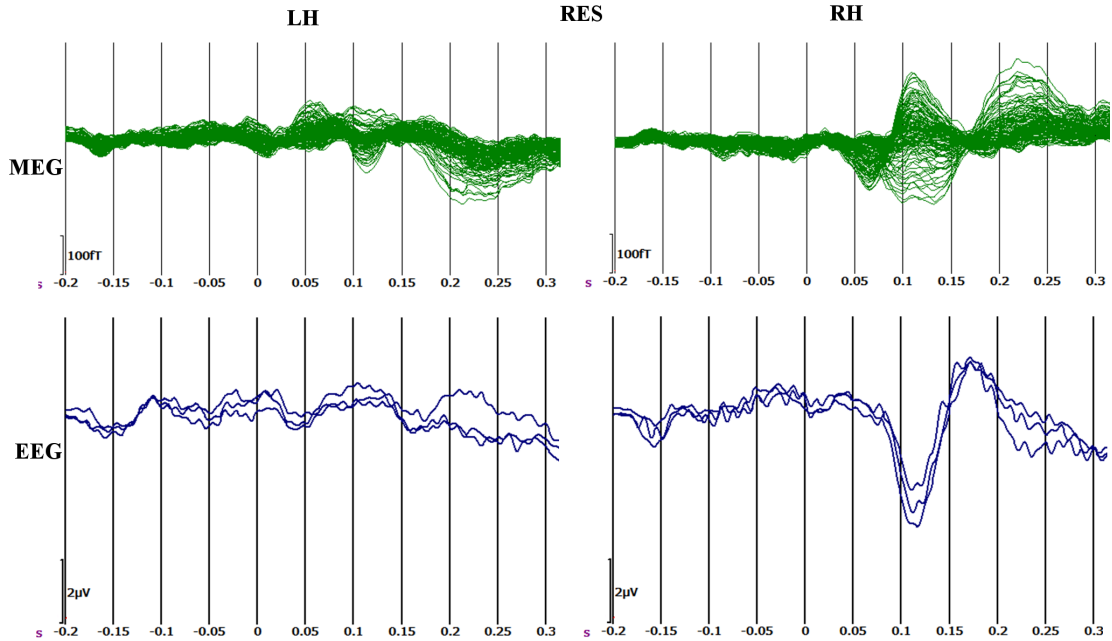


Figure 6.7: Right ear stimulation: Auditory evoked responses for 800 ms long sine tones. For MEG (green) the sensor signals over the LH and the RH are plotted separately. For EEG (blue) only the signals on three electrodes over the LH (T7, FT7, FT9) and over the RH (T8, FT8, FT10) are plotted to enhance comprehension.

The mean global field power (MGFP) values in Table 6.3 indicate higher signals over the RH for both P50(m) and N100(m) with the exception of the P50m in case of RES and MEG. The hemispheric differences are higher for the N100(m) in comparison to the P50(m) and for RES in comparison to LES.

Table 6.3: Mean global field powers of sensors for P50(m) and N100(m) components. (800 ms sine tones)

Components	Hemisphere	Left ear stimulation (LES)		Right ear stimulation (RES)	
		EEG	MEG	EEG	MEG
P50(m)	Left	0.365	14.7	0.206	22
	Right	0.661	36.7	0.336	20.6
N100(m)	Left	1.71	21.4	1.44	24
	Right	2.91	108	1.9	62.9

The topography maps for the LES (Figure 6.8) and the RES (Figure 6.9) at the

peak of the N100(m) component as measured by MEG (first row) and EEG (second row) are shown in upper two rows of Figures 6.8 and 6.9. These maps are in a good agreement with the butterfly plots presented in Figures 6.6 and 6.7. For both RES and LES, there is a clear dipolar pattern on RH, especially in MEG. In Figure 6.9 for RES, over the LH, a dipole like pattern can be seen in MEG, but it is very weak in comparison to the RH. For LES and MEG, it is even weaker and, with the chosen number of isopotential lines, only the peaks of the two poles are visible. In the case of EEG, there is almost no dipolar pattern visible for both LES and RES. Table 6.3 show also high EEG signals over the LH. However, the topography maps show that the observed high amplitudes are mainly due to the orientation of the dipole in the RH (the negative pole (blue lines) in the frontal region in the Figure 6.8). This is also the reason why, only three electrodes (in each hemisphere) are selected and plotted in Figures 6.6 and 6.7.

6.2.1.2.2 Source reconstructions

In order to study the hemispheric differences in detail, the source reconstructions for the P50(m) and the N100(m) components were calculated and examined. Two-dipole scan and SWARM (sLORETA-weighted accurate minimum norm) [123] were used for the inverse solutions. The two-dipole scan was selected because it explains auditory long latency components of the general population very well, as it was demonstrated in the previous section (Section 6.1.3.2) and in [113] (Chapter 5.4.5, Figure 5.35). In order to obtain meaningful dipole solutions, the auditory cortices in the right and left hemispheres were selected from the MRI and the source dipole scan was performed only within 25 mm distance to these locations. This was necessary because in many cases dipole reconstruction for the unusual AERs, measured from the subject, did not produce any dipoles in the LH. In the case of SWARM, this constraint was not used and the source reconstructions were calculated for the whole source space (2 mm resolution), but only the upper 50 % of the currents were visualized. In order to investigate the activity that might arise from regions other than auditory cortex (which would not be detected with the two-dipole scan that is restricted to the area around the auditory cortices), a current density approach (SWARM) was used.

The dipole strengths in the LH and RH of EEG, MEG and EMEG for the left and right ear stimulations are presented in Table 6.4 along with SNRs and GOF values. For P50(m) LES the dipole strength in RH was found to be ~ 2.7 (~ 3.2) times higher than the dipole strength in LH for MEG (EMEG) with GOF > 93 % and SNR > 3.1. In the

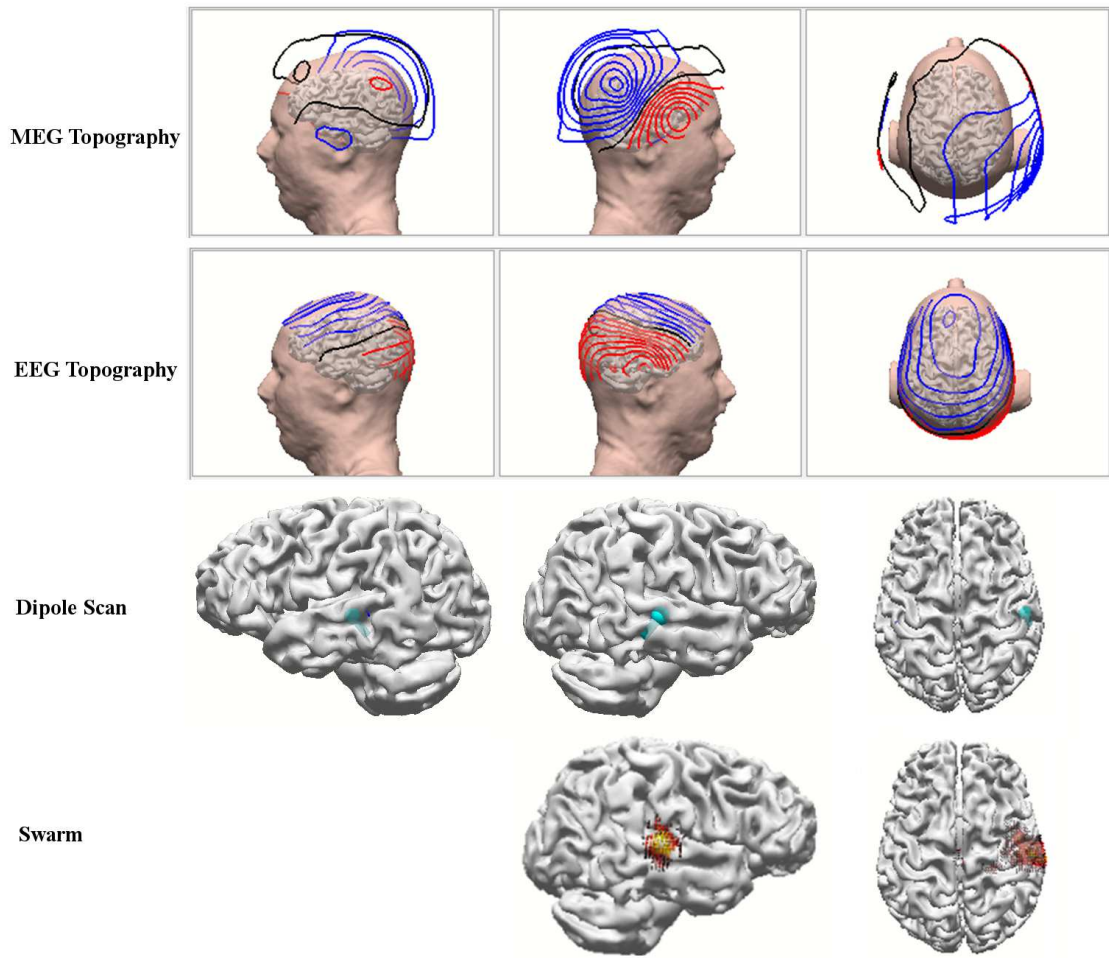


Figure 6.8: Left ear stimulation: MEG (first row from the top) and EEG (second row from the top) topographies along with the segmented cortex and skin recorded for 102 ms after 800 ms sine tones. The dipole scan results for EMEG at this time instant are shown in the third row. Turquoise (blue) dipole indicates the source localization in the contralateral (ipsilateral) hemisphere with respect to the stimulus. Fourth row from the top shows the EMEG SWARM solution and the individual cortex obtained from MRI. The upper view uses the transparent cortex and only the right view is shown because no activity was visible on the left side.

case of EEG, the dipole strength ratio was considerably lower with just ~ 1.3 . However, it should be noted that it was possible to obtain localizations in both hemispheres only after increasing the regularization coefficient to the value that was three times higher than the value estimated from the pre-stimulus interval. Even in this case, the localization in the Table 6.4 only shows insular cortex for LH with a GOF of just 87%. For RES all three methods (EEG, MEG or EMEG) were not able to localize any

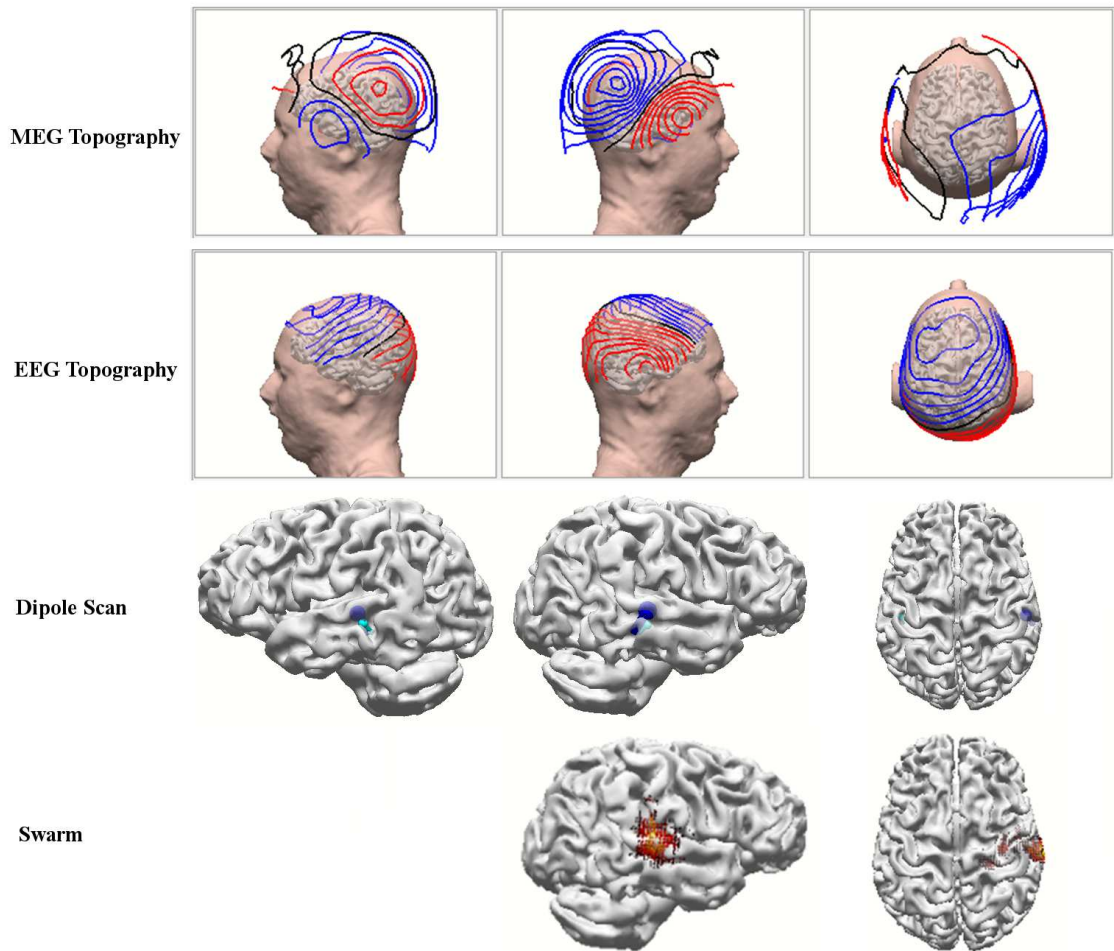


Figure 6.9: Right ear stimulation: MEG (first upper row) and EEG (second upper row) topographies along with the segmented cortex and skin recorded at 107 ms after 800 ms sine tones. The dipole scan results for EMEG at this time instant are shown in the third row. Turquoise (blue) dipole indicates the source localization in the contralateral (ipsilateral) hemisphere with respect to the stimulus. Fourth row shows the EMEG SWARM solution and the individual cortex obtained from MRI. The upper view uses the transparent cortex and only the right view is shown because no activity was visible on the left side.

dipole in the LH. Both dipoles were reconstructed in the RH with GOF values above 93 %.

In case of the N100(m) LES, again the localization in the LH with EEG was only possible with high regularization. As calculated from Table 6.4, the ratios of the RH to LH dipole strengths were ~ 5.6 , ~ 9.1 and ~ 4.9 for EEG, MEG and EMEG, respectively, with GOF > 95 %. The SNR of EEG (12.4) was considerably higher than MEG (8).

The LH dipole reconstruction for RES with EEG was also only possible after high regularization. In this case higher dipole strengths for RH was indicated for the MEG (~ 2.3 times higher) and the EMEG (~ 2 times higher). The LH dipole strength for EEG was higher than for the RH. The SNRs were similar for all modalities for RES but the GOF values for MEG (97 %) and EMEG (96 %) were considerably higher than for the EEG (89 %). The localized dipoles for the peak of the N100(m) for EMEG are shown in the third rows of Figure 6.8 for LES and Figure 6.9 for RES.

The SWARM results for LES and RES N100(m) EMEG can be found at the bottom row in Figures 6.8 and 6.9. When using SWARM, the activity was localized only in the RH with a threshold of 50% for LES and RES. As can be seen from both figures, significant current density was reconstructed over the RH in the auditory cortex, while no activity was reconstructed in the LH.

Table 6.4: Source localization results for N100(m) and P50(m) components. Dipole strengths (μAmm), signal to noise ratio (SNR) and goodness of fit (GOF %) are given for EEG, MEG and EMEG two dipole deviation scan (800 ms sine tones). RH and LH stand for right and left hemisphere, respectively. JRH (just right hemisphere) indicates that both dipoles ended up in the right hemisphere. * indicates localization in insular cortex, which was achieved after increasing the regularization coefficient to a value that was three times its normal value (as explained above) and, thus, these results are not very reliable.

Components	Attribute		LES			RES		
			EEG	MEG	EMEG	EEG	MEG	EMEG
P50(m)	Dipole Strength	LH	*6.83	3.42	1.89	-	JRH	JRH
		RH	8.51	9.05	6.11	-	JRH	JRH
	SNR		2.6	3.2	3.1	-	3.7	3.5
	GOF		87	94	93	-	94	93
N100(m)	Dipole Strength	LH	*9.73	6.48	10.4	*31.2	10.9	10.6
		RH	54.7	58.8	51	25.5	25.5	20.8
	SNR		12.4	8	9.1	7.1	7.3	7.3
	GOF		95	96	95	89	97	96

6.2.2 Experiment 2: Investigation of the middle latency components

6.2.2.1 Properties of the stimulus and pre-processing

A paradigm that is designed to investigate middle latency components, i.e., P30(m) and Pb(m), was used in the second experiment. It was aimed to find a step of the auditory processing in which the uncommon responses start. In this section, the P50 is called Pb complex because, due to convention, P50 or P1 is used to study long latency responses and Pb is used to analyze middle latency responses [205]. Furthermore, the Pb component was divided into Pb1 (latency ~ 52 ms) and Pb2 (latency ~ 76 ms) [205]. The conditions of the experiment were as follows:

- Stimulation type: Monaural.
- Tone duration: 20 ms with 3 ms rise and fall time.
- Tone frequency: 1400 Hz.
- Inter stimulus interval (ISI): randomized between 200 and 400 ms.
- Number of epochs: ~ 5000 .
- Strength of the stimulus: 60 dB above hearing level.
- Duration of the measurement: In total ~ 54 minutes, 27 minutes for each ear.

Prior to source reconstruction, baseline correction was performed using the pre-stimulus interval (-50 to 0 ms) and then data was filtered with zero-phase bandpass (3-150 Hz) and notch (50 Hz) filters [205]. After visual inspection, P7, P5, Pz and F4 were discarded as bad channels. Following the amplitude based semi-automatic artifact rejection process, 4792 and 4779 epochs were averaged for the left and right ear stimulation, respectively.

6.2.2.2 Results

6.2.2.2.1 Signals and topographies

The butterfly plots of the AERs for the LES are shown in Figure 6.10. For MEG (green) the sensor signals over the LH and over the RH are plotted separately. For EEG (blue) only the signals on four electrodes over the LH (FC3, FC5, C5, F5) and

over the RH (FC4, FC6, C6, F6) are plotted to enhance comprehension (to minimize the effects of the activity on the other hemisphere). Since these components have a smaller magnitude than the long latency responses, it is harder to evaluate them just by visual inspection. For the P30m, unlike RH, MEG sensors over the LH showed no signal detectable by the visual inspection (see Figure 6.10). In addition, the MEG MGFP over RH sensors was ~ 4.4 times higher than the MGFP over LH sensors (Table 6.5). The Pb1m was visible over both LH and RH (Figure 6.10), but the signals over the RH were higher than over the LH by ~ 3 times. In EEG the Pb1 (over the selected electrodes) was clearly visible over the RH, but it was very weak over the LH. With the selected electrodes it is hard to comment on the P30 component (in EEG), the hemispheric differences of the P30 component will be discussed later in Section 6.2.2.2.2 using the source reconstructions.

For RES, the P30m was hard to detect over any of the hemispheres (please note that the peak in LH before the Pb1m is at 40 ms in Figure 6.11), but the topography at this time-instant showed a dipolar pattern over the RH (data not shown here). The differences between P30 and Pb1 for EEG were not as high as for MEG but still the signals over the RH were higher than over the LH (Table 6.5). In general, the MGFP values of LES and RES shown in Table 6.5 indicate higher signals over the RH for both P30(m) and Pb1(m), except the P30m for RES (please note with an MGFP of just 3.15, the LH signals for RES are still low).

Table 6.5: Mean global field powers of sensors for P30(m) and Pb1(m) components (20 ms sine tones)

Components	Hemisphere	LES		RES	
		EEG	MEG	EEG	MEG
P30(m)	Left	0.178	2.18	0.079	3.15
	Right	0.216	9.54	0.131	2.81
Pb1(m)	Left	0.278	5.72	0.163	3.08
	Right	0.397	17.4	0.228	11.9

Figure 6.12 (6.13) shows the topography maps for LES (RES) at the peak of the Pb1(m) component at 57 ms (59 ms) as measured by MEG (first row) and EEG (second row). For both LES and RES, there was a clear dipolar pattern over the RH in both EEG and MEG. As Figure 6.13 shows, for RES, although it was weaker in comparison to the RH, a dipolar pattern was also observed by MEG over the LH. In Figure 6.12 for LES, a negative pole is visible in the MEG topography over the LH, which might belong to a dipole, but the positive counterpart pole for such a hypothetical dipole is not visible. In EEG, no pole is visible over the LH for both LES (Figure 6.12) and

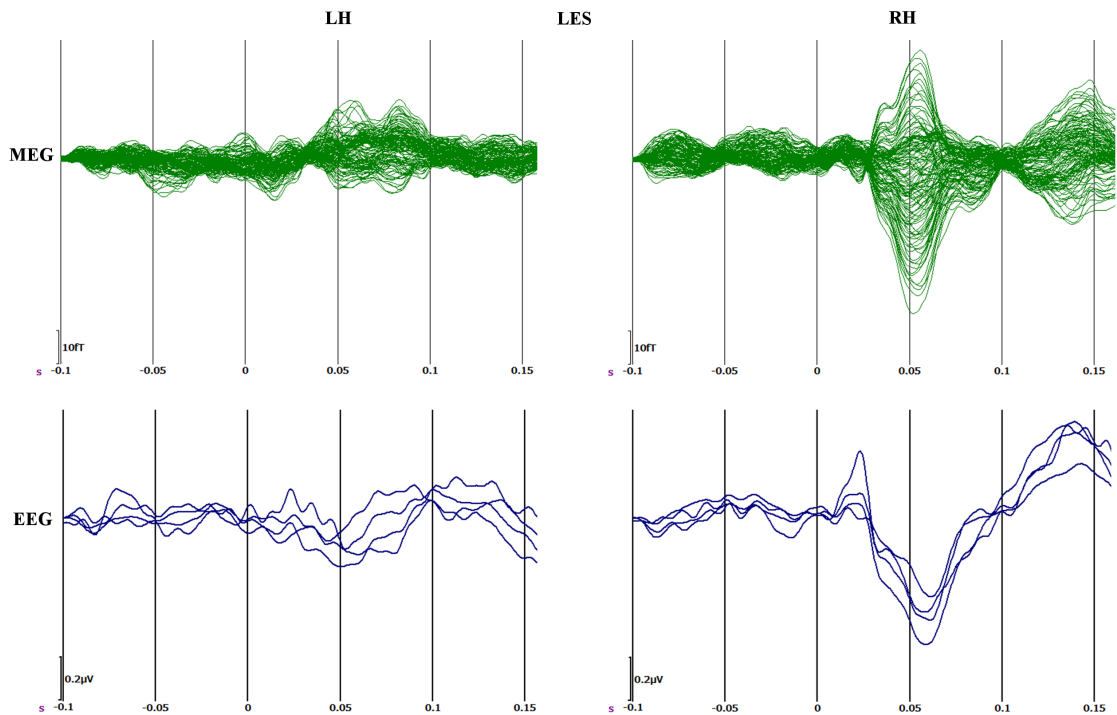


Figure 6.10: Left ear stimulation: Auditory evoked responses for 20 ms long sine tones. For MEG (green) the sensor signals over the LH and the RH are plotted separately. For EEG (blue) only the signals on four electrodes over the LH (FC3, FC5, C5, F5) and over the RH (FC4, FC6, C6, F6) are plotted to enhance comprehension.

RES (Figure 6.13), but the negativity over temporal areas points to a dipole in inferior regions whose poles could not be fully measured due to the limited coverage of the EEG cap.

6.2.2.2.2 Source reconstructions

In this section source reconstructions for P30(m) and Pb1(m) components were investigated. The same procedure as explained in Section 6.2.1.2.2 was used for source reconstruction.

Regarding the P30(m) reconstruction results (upper row in Table 6.6). No two-dipole scan result for EEG had GOF higher than 70 %, as indicated by the empty EEG cells. For LES and for MEG (EMEG), the dipole strength in the RH was ~ 2.9 (~ 2.4) times higher than the dipole strength in LH with GOF > 86 % and SNR > 4.6. For RES neither EEG nor MEG were able to localize any dipole in the LH and also the source reconstructions in the RH were not very stable due to low SNR (<2.1) and

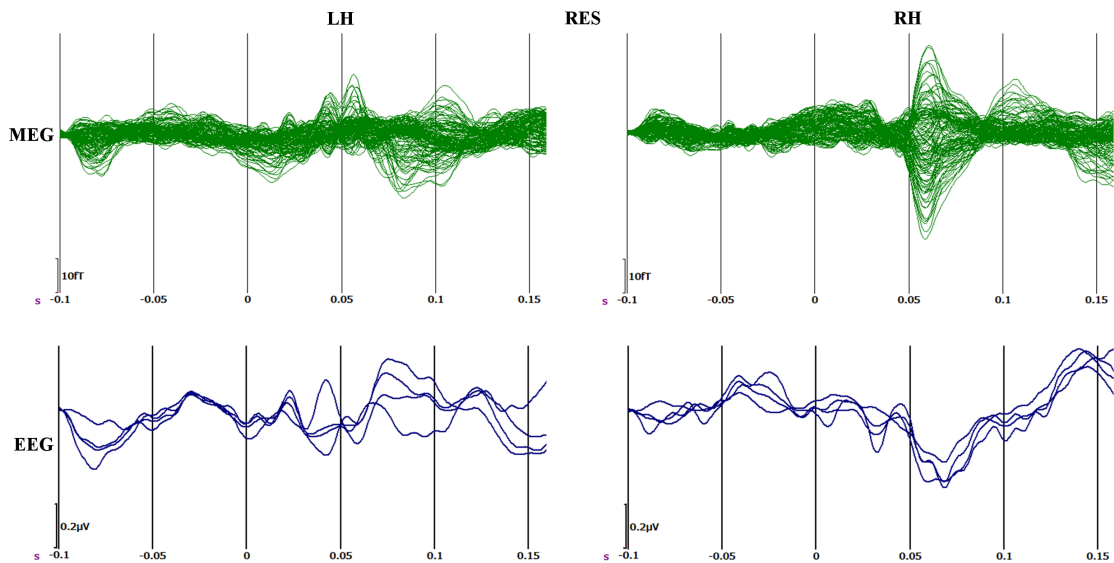


Figure 6.11: Right ear stimulation: Auditory evoked responses for 20 ms long sine tones. For MEG (green) the sensor signals over the LH and the RH are plotted separately. For EEG (blue) only the signals on four electrodes over the LH (FC3, FC5, C5, F5) and over the RH (FC4, FC6, C6, F6) are plotted to enhance comprehension.

GOF (<55 %).

In the case of Pb1(m) (second row in Table 6.6), due to increased SNRs in comparison to P30(m), better GOF values were achieved. For EEG again there was no localization with GOF higher than 70 %. However, for LES, MEG and EMEG source reconstructions showed GOF values of 96 %. For LES, the ratios of the RH to LH dipole strengths were ~ 2.1 and ~ 2.4 for MEG and EMEG, respectively. For RES with MEG, both dipoles were localized in the RH with a GOF of 91 %. The EMEG result for RES achieved 94 % GOF and the ratio of RH to LH dipole strength was 1.83. The localized dipoles at the peak of the Pb1(m) component for EMEG LES and RES are presented in the third row in Figures 6.12 and 6.13, respectively. For LES (Figure 6.12), while the orientation of the dipoles is nearly parallel, the LH dipole seems to be deeper localized than the RH dipole. For RES (Figure 6.13), while the orientation of the dipoles is nearly parallel, the LH dipole seems to be localized slightly more anterior and inferior to the RH dipole.

Similar to N100(m) component, the EMEG SWARM results for Pb1(m) revealed activity only in the RH with a threshold of 50 % for LES and RES as shown at the bottom rows in the Figures 6.12 and 6.13.

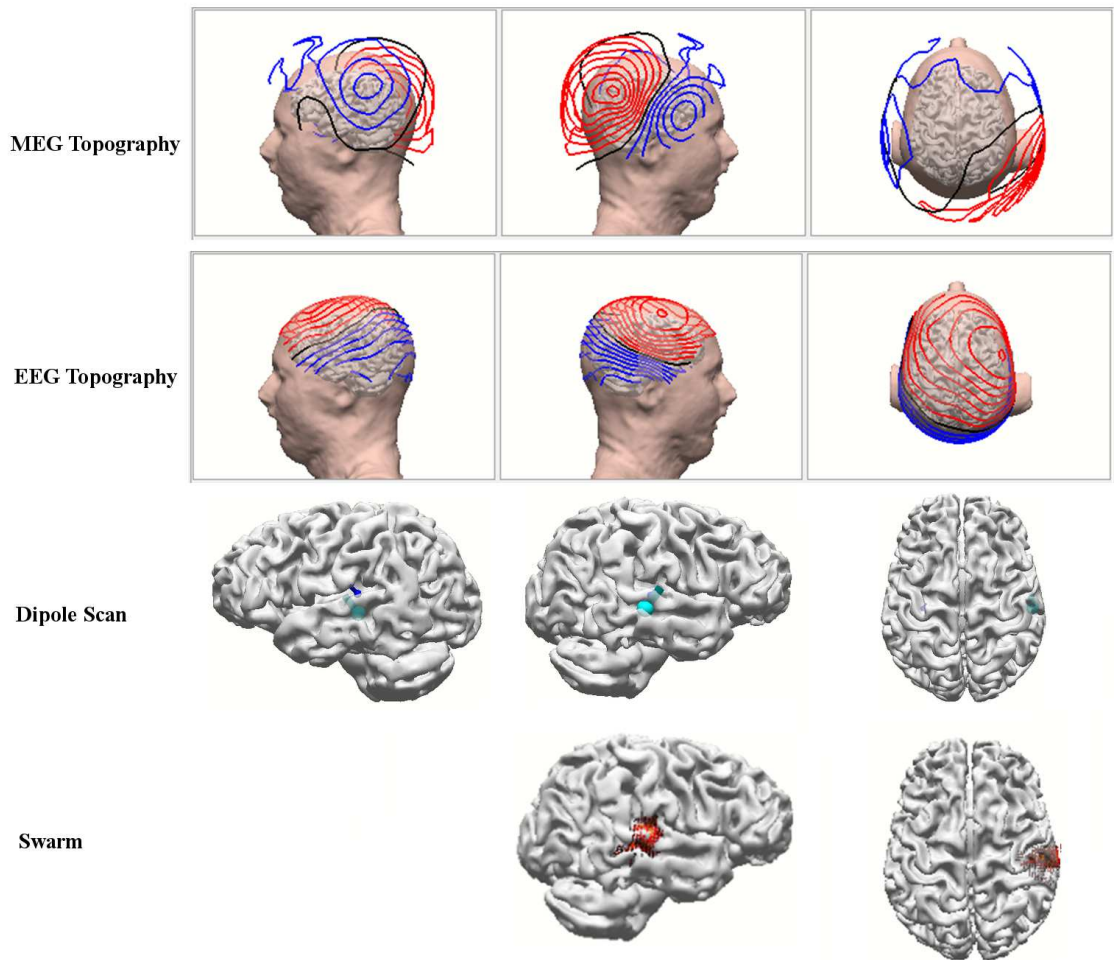


Figure 6.12: Left ear stimulation for 20 ms sine tones: MEG (first row) and EEG (second row) topographies along with the segmented cortex and skin at the peak of the P1b(m) component at 57ms. The dipole scan results for EMEG at this time instant are shown in the third row. Turquoise dipole (blue) indicates the source localization in the contralateral (ipsilateral) hemisphere with respect to the stimulus. Fourth row shows the EMEG SWARM solution and the individual cortex obtained from MRI. The upper view uses the transparent cortex and only the right view is shown because no activity was visible on the left side.

6.2.3 Discussion

The signals, topography maps and source reconstructions presented in this section revealed that in the brain of the subject of this study the LH produces very small if any auditory evoked responses and the RH clearly dominates for both LES and RES. However, the audiogram showed no significant difference between left and right ear and all values were within the normal range.

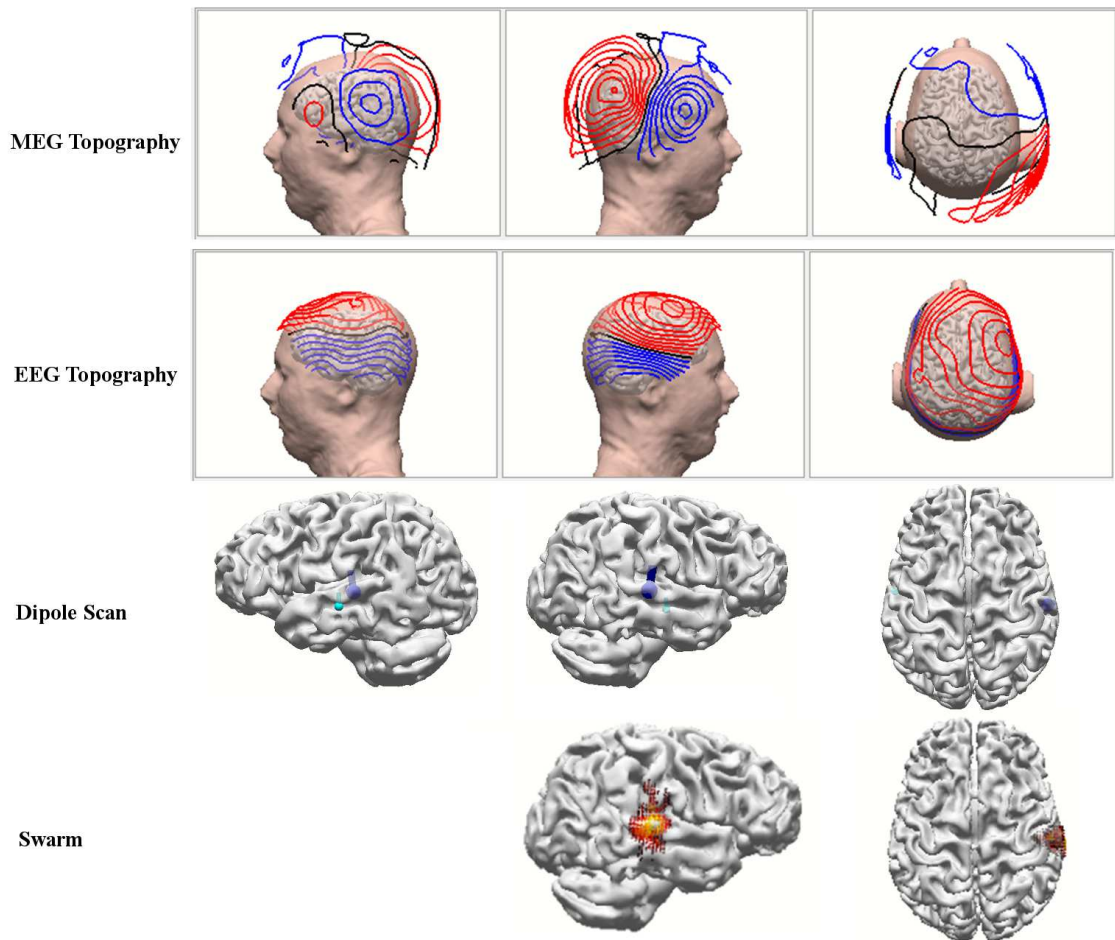


Figure 6.13: Right ear stimulation for 20 ms sine tones: MEG (first row) and EEG (second row) topographies along with the segmented cortex and skin at the peak of the P1b(m) component at 59 ms. The dipole scan results for EMEG at this time instant are shown in the third row. Turquoise dipole (blue) indicates the source localization in the contralateral (ipsilateral) hemisphere with respect to the stimulus. Fourth row shows the EMEG SWARM solution and the individual cortex obtained from MRI. The upper view uses the transparent cortex and only the right view is shown because no activity was visible on the left side.

In the first experiment long latency responses were analyzed and results showed uncommon responses for P50(m) and N100(m). It was previously shown that, the monaural stimulation results in activation of both hemispheres for N100(m) component [111, 206]. In [206] and [111], dipole strengths in the contralateral side were found to be stronger than in the ipsilateral side. In this study, the dipole strength in the RH was found to be significantly higher than in the LH for both LES and RES. Despite

Table 6.6: Source localization results for P30(m) and Pb1(m) components. Dipole strengths (μAmm), signal to noise ratio (SNR) and goodness of fit (GOF %) are given for EEG, MEG and EMEG two-dipole scan. (20 ms Sine tones). For the empty cells, no localization with GOF higher than 70 % was achieved. RH and LH stand for right and left hemisphere, respectively. JRH indicates that the both dipoles ended up in the right hemisphere.

Components	Attribute		LES			RES		
			EEG	MEG	EMEG	EEG	MEG	EMEG
P30(m)	Dipole Strength	LH	-	1.88	1.83	-	JRH	JRH
		RH	-	5.5	4.47	-	JRH	JRH
	SNR		-	4.6	4.9	-	1.5	2.1
	GOF		-	88	86	-	48	55
Pb1(m)	Dipole Strength	LH	-	2.71	2.75	-	JRH	1.15
		RH	-	5.63	6.7	-	JRH	2.11
	SNR		-	8.3	8.6	-	5.2	5
	GOF		-	96	96	-	91	94

that there was a significant difference of dipole strength in RH between LES and RES, smaller dipole strength in the RH for the ipsilateral stimulation (the strength of EMEG dipole in RH for RES was 41 % of the LES in Table 6.4). In contrast, the LH dipole strength was barely changing for ipsilateral and contralateral sides. In [206] authors found this ratio to be 72 % for both LH and RH. Therefore, the activity in the LH is not only weaker, but also its strength does not vary between ipsilateral and contralateral sources. This is also in line with the results of [207], in which it was found that for patients with chronic unilateral ischemic lesions of the auditory cortex, the N100m responses in contralesional side are similar to healthy subjects. It is known that contralateral N100m sources are slightly anterior in comparison to ipsilateral ones [206]. The results of this study also point to a more anterior contralateral dipole (turquoise dipole in Figure 6.8) for LES and the dominant RH in agreement with [206]. However, for RES the ipsilateral source (blue dipole in Figure 6.9) was slightly more anterior, which also points to a special hemispheric asymmetry. The P50(m) component was clearly visible over the RH sensors for LES but over the LH it was either not distinguishable (in EEG) or very weak (in MEG) (Figure 6.6). Source reconstruction results were also showing a RH dominance. These results suggest that the uncommon responses are not only restricted to N100(m) component but also present in earlier time points. However, it should also be considered that the P50(m) component is not as stable as the N100(m) and it cannot be observed in all subjects [208]. Even if it was shown

that, e.g., arousal and attention have an influence on the P50(m) and the N100(m) [209], these phenomena can not explain the absence of the LH response as presented here. In a lesion study, it was shown that large temporo-parietal lesions might cause the disappearance of the N100m from the damaged hemisphere [210]. Furthermore, large but less deep fronto-temporal lesions can cause smaller amplitudes on the damaged hemisphere [210]. For the subject of this study, the MRIs were investigated by a radiologist and no brain lesion was detected. Moreover, frontal lesions and small lesions in supra-temporal plane was shown to not affect the N100(m) component in [210]. Overall, it thus seems very unlikely that the observed absence of LH response could be due to a lesion.

In Section 6.2.2 auditory middle latency responses were investigated to determine if the difference between RH and LH can also be observed in those earlier components, where at least the P30(m) can be assigned to the primary auditory cortex. The experimental set-up with short tone duration and short ISI allowed to collect far more trials (~ 5000 trials in comparison to ~ 350 collected for long latency responses), so that still reasonable SNRs could be obtained. Because there is less synchronization in the primary auditory cortex, many more trials are required for middle latency responses [205, 211]. Due to the middle latency stimulus type, the P50(m) component consists of two distinct peaks, the Pb1(m) and the Pb2(m) [205]. The results for Pb1(m) showed that the RH is dominant for both LES and RES although this dominance is weaker in comparison to the P50(m) results obtained with longer tone stimuli. Although it is still controversial, some studies localize the Pb1(m) component in or around the primary auditory cortex. Therefore, the results presented in this study might support the hypothesis that differences already occur in the primary auditory cortex [208]. The P30(m) component is known to have a bi-hemispheric distribution [208] and this study showed similar hemispheric differences (dominant RH) as in case of Pb1(m). Previous studies that used depth electrodes, localized this component in primary auditory cortex [212]. Therefore, there is strong evidence that the hemispheric differences in our subject, which might be due to deeper source location and/or a weaker synchronization in the LH, is already present in primary auditory cortex.

In order to rule out any uncommon processing at the brainstem level prior to the activation of the primary auditory cortex, a clinical evaluation of the early latency (or brainstem) auditory responses in the first 10 ms after stimulus was performed and a healthy auditory pathway was determined.

It is important to note that since SWARM uses the sLORETA weighting, it might not perform well in situations with multiple sources and a limited distance between

sources, as shown for sLORETA in [118]. In order to confirm the findings, the minimum norm estimates were also obtained and the findings were in agreement with the ones presented here.

In conclusion, based on the findings in this chapter, there is strong evidence that the hemispheric differences in our subject might be due to deeper sources (the EMEG P30(m) source was ~ 1 cm deeper in the LH in comparison to the RH) and/or due to lower levels of synchronicity in the LH. The lower synchronicity probably starts in the primary auditory cortex (P30(m) and Pb1(m) components) and carried to the later components (N100(m)). These findings are an important demonstration of the high variance of the brain activities, even within the healthy population.

7 Other Studies: Simulation of Noninvasive Brain Stimulation Techniques with High Resolution Finite Element Head Models

The EEG/MEG forward problem is closely coupled to brain stimulation techniques such as tDCS (transcranial direct current stimulation) and TMS (transcranial magnetic stimulation) via Helmholtz reciprocity [213, 214]. Therefore, it is possible to use the finite element head models, which are constructed in this work employing the same pipeline as described in Chapter 3, for also in tDCS and TMS simulations. TMS has recently received National Food and Drug Agency approval in US, as a treatment against migraine ¹ and depression [215]. In addition, there is a wide interest in using brain stimulation techniques for the treatment of a broad range of mental diseases and even as a tool for enhancement of cognitive abilities. The use of brain stimulation was described for the treatment of diseases like epilepsy, Alzheimer and Parkinson, and for the recovery of stroke patients (see citations in [216]). tDCS has the potential not only to increase the effects of other therapies but also, as stated by Brunoni et al., it can be used as a safe and cheap option to reduce the risk of pharmacological interaction of different drugs and to treat patients with poor drug tolerance [217].

The current standard in tDCS studies is the injection of 0.5 to 2 mA current via two large patch electrodes at the skin, and investigation of the excitation or the inhibition effects depending on the positions of the cathode and the anode. It is known that the cortical excitability of the area close to the anode increases, whereas stimulation via cathode has an opposite effect [217].

Although there are many different hypotheses for the functioning of tDCS, the process is still not well understood in detail. Most likely the effects are due to the interplay of several mechanisms some of which are listed below (please see [217] for details and

¹<http://www.fda.gov/NewsEvents/Newsroom/PressAnnouncements/ucm378608.htm>

further references therein):

- Induction of changes in the resting membrane potentials.
- Induction of prolonged neurochemical changes.
- Modification of synaptic microenvironment (e.g., synaptic strength of N-methyl-D-aspartate (NMDA) receptor, γ -Aminobutyric acid (GABA)ergic activity).
- Modulation of intracortical and corticospinal neurons.
- Stimulation/repression of the non-neuronal components of the central nervous system.
- Induction of indirect effects via the connectivity between the stimulated area and more distant structures.

In contrast to tDCS, where weak currents (0.5 to 2 mA) are introduced to the surface of the head via electrodes, in TMS, a time varying magnetic field is produced by large (~ 5 kA) and abrupt (less than 1 ms) currents and this way an electric field inside the brain is induced. TMS is shown to be more precise than tDCS or tACS (transcranial alternating current stimulation) and in contrast to tDCS and tACS, it can directly excite neurons [218].

One important question is how large the electrical field should be in order to influence the firing of the neurons. Recent studies performed with rats revealed that an electrical field of ~ 1 mV/m is sufficient to synchronize neural firing for a sinusoidal signal [219].

In the context of this work, contributions were made to three studies [216, 220, 221] that investigated simulation of brain stimulation techniques. The main findings of these three studies are shortly summarized in the following sections (Sections 7.1, 7.2 and 7.3) with a focus on the contributions of the author of this thesis. In the first study the effects of modeling different compartments in tDCS simulations were investigated [216]. In the second study the precision of some of the most widely used tDCS electrode setups in stimulating the target areas was analyzed [220]. In the last study, the influence of sulcus width on the simulated electric fields in TMS was investigated [221].

7.1 Study I: Investigation of tDCS Volume Conduction Effects in a Highly Realistic Head Model

In this section, the effects of head modeling on tDCS simulations were investigated [216]. For the purpose of this study, five different head models were constructed.

Four of these head models were named according to the number of compartments in the model $3C$, $4C$, $5C$, $6C$ and the fifth was named as $6CA$ to emphasize the modeled anisotropic white matter conductivity. The properties of these head models are described in Table 7.1.

Table 7.1: Head models used in this study: The first row indicates the name of the head model and the conductivities for the respective tissue compartments were given in the remaining columns. The compartments that were (were not) distinguished are indicated by a slash (dash) sign. Isotropic conductivity values were taken from the literature (see references in Table 3.1). The # sign indicates that conductivity tensors were determined as described in section 3.1.5.

Compartment	$3C$	$4C$	$5C$	$6C$	$6CA$
Electrodes	1.4	1.4	1.4	1.4	1.4
Scalp	0.43	0.43	0.43	0.43	0.43
Skull Compacta	-	0.007	0.007	0.007	0.007
Skull Spongiosa	-	0.025	0.025	0.025	0.025
Skull	0.01	/	/	/	/
CSF	-	-	1.79	1.79	1.79
Gray Matter	-	-	-	0.33	0.33
White Matter	-	-	-	0.14	#
Brain	0.33	0.33	0.33	/	/

In this study, the same head modeling pipeline as described in Chapter 3 was used except that skull conductivity was not calibrated. Instead the conductivity values of 0.007 S/m for skull compacta and 0.025 S/m for skull spongiosa were used [68]. Furthermore, the step with the Freesurfer gray matter mask described in Section 3.1.3 was not performed. Instead, the gray matter segmentation obtained with *FSL-FAST* was used. Different from the head models used for source reconstruction in previous chapters, two rectangular tDCS patch electrodes (7 cm x 5 cm) were included to the FE model [222]. The thicknesses of these patches were 4 mm and their conductivities were set to 1.4 S/m [223]. The sponges were created by dilating the skin by 4 mm and then by carving the patches from them.

The target at the auditory cortex of the subject was determined by localizing the N100m component of the auditory evoked fields measured from the same subject. For this purpose 800 ms long pure sinusoidal tones were presented binaurally (see Chapter 6 for details). The motor cortex was determined by first localizing the N20m component of the somatosensory evoked fields to determine the posterior wall of the central sulcus and then, by defining the motor cortex at the nearby anterior wall of the central sulcus.

The right median nerve of the subject was stimulated with square electric pulses in order to measure the somatosensory evoked fields (similar to the paradigm explained in Section 3.1.8.1). The positions of the electrode patches were then selected based on these localizations. The stimulation paradigms and details on the source reconstruction process can be found in Chapter 6.

The simulated volume currents for different head models were investigated both visually and quantitatively. For quantitative comparisons *Ang* (orientation change in degrees) and *Amp* (magnitude change) metrics were calculated with the formulas given below. By using the *Ang* instead of other commonly used metrics such as the relative difference measurement star (*RDM**), first the emphasis was put on the orientation, and secondly not only the mean but also the the maximum and minimum orientation changes were calculated to detect regional changes.

$$Ang(i) = \arccos \frac{\langle \vec{j}_1(i), \vec{j}_2(i) \rangle}{\|\vec{j}_1(i)\| \|\vec{j}_2(i)\|} \quad (7.1)$$

$$Amp(i) = \frac{\|\vec{j}_1(i)\|}{\|\vec{j}_2(i)\|} \quad (7.2)$$

In the equations above \vec{j}_1 and \vec{j}_2 represent the current densities in the compared head models and i is the element in which this comparison was made.

For construction of different head models, a step by step approach was followed by including one tissue compartment or anisotropy at each stage. For the sake of clarity, the parts of the figures (see, e.g., Figure 7.1) illustrating different head models are named in a systematic order. The numbers and letters before the underscore sign indicate the number of compartments (e.g., *3C* stands for a three compartment head model) and the letters following the underscore depict the visualized attribute in the figure. These attributes are *CD* for current density and *Ang* or *Amp* for orientation and magnitude change in comparison to the previous model. The main figures are not visualized in full resolution in order to avoid overcrowded current density vector fields that reduce the comprehensibility. For this purpose, only the center vector of a 4 by 4 FE block is shown in these figures. The exceptions are the figures labeled as *CDz*, where a zoom of a small area of a brain in a full resolution is shown.

7.1.1 Effects on currents in scalp, skull and CSF

In this section, the current density differences in scalp, skull and CSF were investigated for three, four and five compartment head models. The changes for WM/GM

distinction and WM anisotropy were not covered in this part because they had limited to no effects on currents in scalp, skull and CSF.

Three compartment head model:

For the three compartment head model ($3C_{CD}$) shown in Figure 7.1 the highest currents are seen at the edges of the patches with $1.2 A/m^2$. Most of the currents are channeled through the scalp due to its relatively high conductivity in comparison to the skull and air. These currents are tangential to the skull and only a small fraction of them penetrate inside the skull, where they become radially oriented. Therefore, the current density inside the brain is homogeneous and very small in comparison to skin.

Four compartment head model:

The resulting current density vector field after including the skull spongiosa/compacta distinction is shown in Figure 7.1, $4C_{CD}$. The orientation changes in comparison to the $3C$ model are very small in brain and skin compartments, whereas differences up to 63.5 degree can be seen in the skull compartment ($4C_{Ang}$ in Figure 7.1). The slightly more tangential current density vector field in skull spongiosa tissue become clearer in the figure with zoomed full resolution ($4C_{CDz}$ in Figure 7.1). This is due to the higher conductivity of spongiosa in comparison to compacta. Also, as expected, considerable amplitude reductions and increases at skull compacta and spongiosa region, respectively, and a small amplitude decrease in the whole brain is observed for the current densities in $4C_{Amp}$.

Five compartment head model:

The last head model that was investigated in this section is $5C$, which additionally models the CSF compartment. Due to the high conductivity value of the CSF, clear tunneling effects are visible in Figure 7.1, $5C_{CD}$. The current density vectors in this compartment are mainly tangentially oriented and the current is channeled underneath the anode to more distant areas, as can be seen in detail in the magnified figures $5C_{CDz1}$ and $5C_{CDz2}$ in Figure 7.1. The high orientation (up to 75°) and amplitude (up to 6.1 times) changes indicate the importance of the CSF compartment in simulation studies (see $5C_{Amp}$ and $5C_{Ang}$ in Figure 7.1).

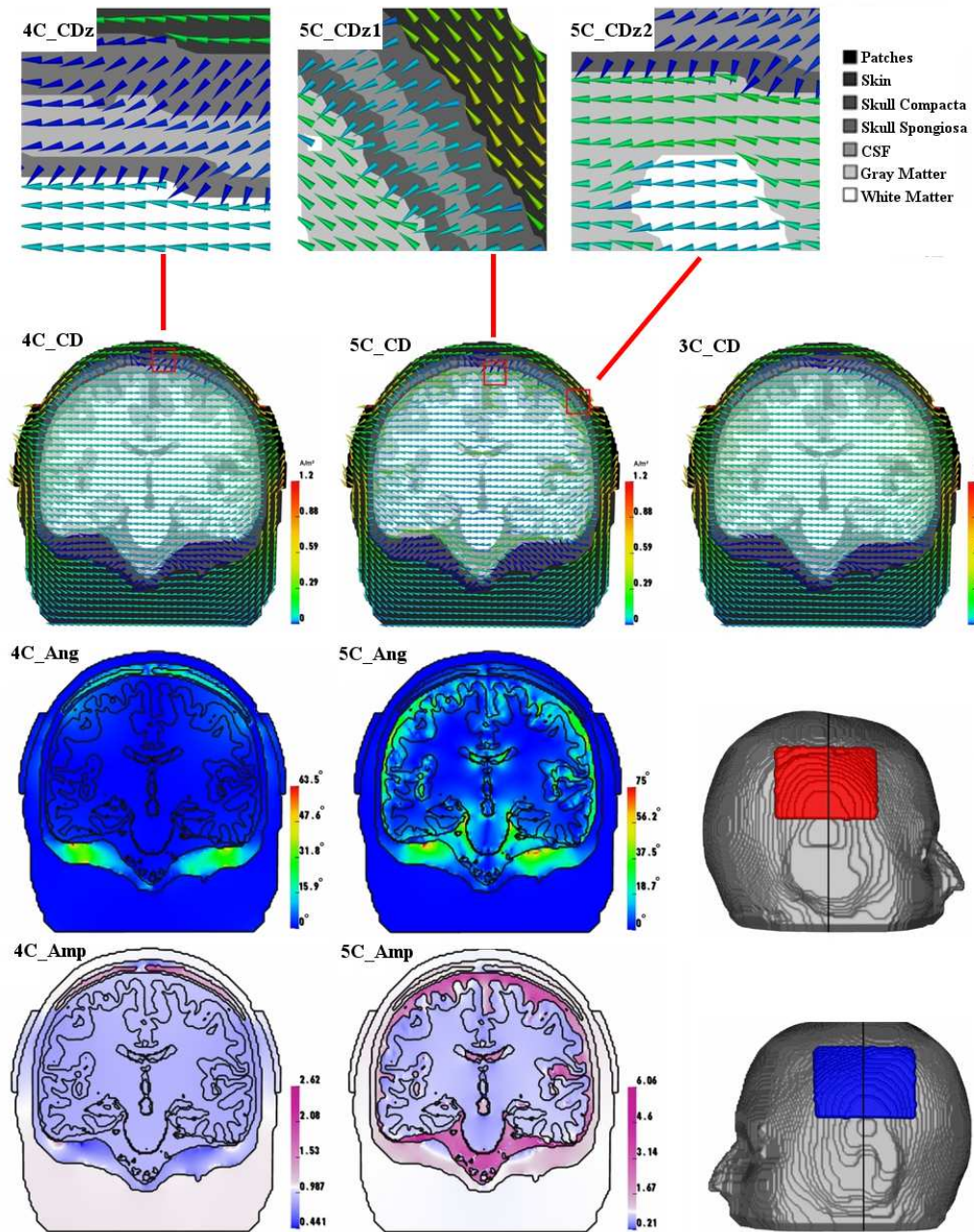


Figure 7.1: Current densities for three, four and five compartment models for a sample slice near auditory cortex. For $4C$ ($5C$) head model the differences relative to $3C$ ($4C$) head model are given in terms of orientation $4C_Ang$ ($5C_Ang$) and magnitude $4C_Amp$ ($5C_Amp$) change. $4C_CDz$, $5C_CDz1$ and $5C_CDz2$ zooms into the areas outlined with red squares in full resolution. The electrode patches (red anode, blue cathode) are shown on the skin surface. (Adapted from [216])

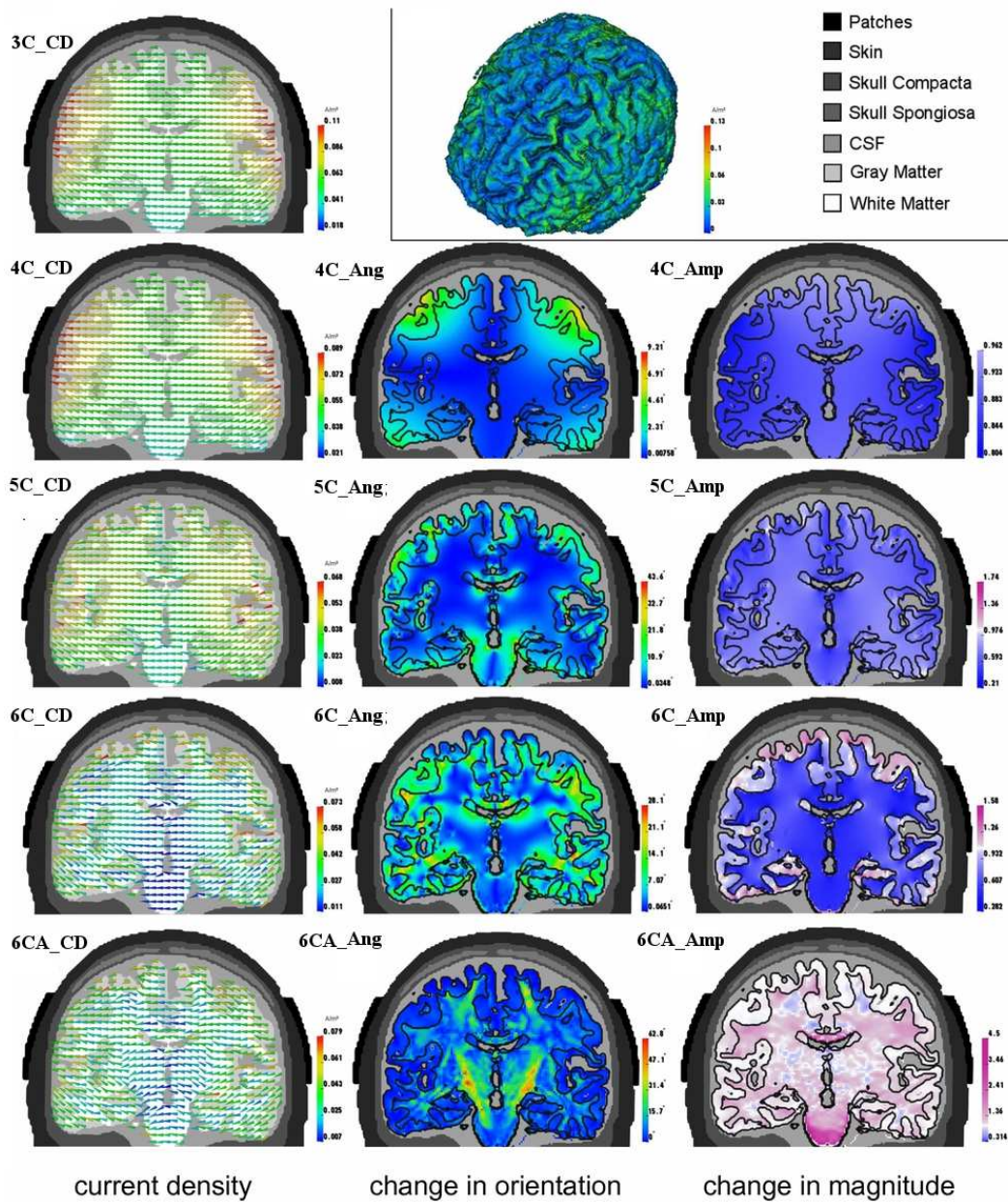


Figure 7.2: Current densities inside WM and GM. Current densities $*C_{CD}$ and changes in orientation ($*C_{Ang}$) and amplitude ($*C_{Amp}$) for the head models used in this study for a sample slice near auditory cortex. The differences are calculated with respect to the adjoint model in terms of complexity, e.g., $4C$ against $3C$. The current density in the cortex is shown at the upper right corner. (Adapted from [216])

7.1.2 Effects on currents inside the brain

Different from the previous section, here mainly the currents in WM and GM were investigated. Unless stated otherwise, the interpretations are based on Figure 7.2. In

Figure 7.1 the values are scaled for the whole head and since the currents penetrating the skull are very low in comparison to scalp currents, and the currents in CSF are very high in comparison to those in WM/GM, a comprehensive analysis of the effects of currents in the brain is difficult to study with just one figure. To overcome this, in Figure 7.2, the currents in scalp, skull and CSF are not shown and the scales are adjusted accordingly so that the currents inside the brain are better visible and easier to analyze.

Three compartment head model:

For the three compartment model, the currents inside the brain are very homogenous and their amplitudes are decreasing gradually as the distance to the tDCS electrodes increases. The highest values are observed just under the tDCS electrodes with a maximum of 0.11 A/m^2 (see $3C_CD$ in Figure 7.2).

Four compartment head model:

Adding the spongiosa/compacta distinction results in amplitude and orientation changes (see $4C_CD$, $4C_Amp$ and $4C_Ang$ in Figure 7.2). Although these orientation changes are up to 9.2° , they are focal and mainly visible in areas underneath the spongiosa tissue, thus, they are not in the target area for auditory cortex stimulation. In contrast, for other target regions these changes might be more important (up to 12° changes within the motor cortex target area in [216]). In terms of amplitude, a general decrease ($MAG < 1$) is observed over the whole brain with some increase in regions underneath large patches of spongiosa. The location with the highest cortical current density is identical to the one in the $3C$ model.

Five compartment head model:

Including the CSF compartment renders the current density distribution considerably more complicated in $5C_CD$ in comparison to $4C_CD$, mainly due to the tunneling effects of the CSF. The orientation changes inside the brain are up to 44° and these changes are observed in almost the whole cortex that is neighboring the CSF. The current densities decrease in WM and most of the GM in $5C_Amp$. The general trend of decreasing current densities with increasing distance to the electrode patches is still obvious, but no longer true for all regions. This is due to the paths from the cortical crown to the bottom of sulci underneath the electrodes supplied by the highly conductive CSF (see also [224]). In the proximity of the electrodes, the current

densities decrease by about a factor of two, whereas the currents in more distant regions (surrounded by the CSF) increased significantly.

Six compartment head model:

Most of the orientation changes due to the modeling of WM and GM separately occur at the WM/GM boundary. These changes are up to 28° and usually the current vectors near the WM/GM border are oriented towards the GM. In general, increased (decreased) current densities are observed in CSF (WM). In GM the amplitudes of current densities close to the electrodes slightly decreased while they increased in more distant regions.

Six compartment head model with anisotropic white matter:

Including the WM anisotropy via DTI causes orientation changes up to 62° in WM and 15° in GM (see *6CA_Ang*). These changes in GM are mainly at deeper regions and they are considerably smaller in superficial areas. The magnitude changes are also similar to orientation changes with the largest effects in WM, some effects in deep GM and small effects in superficial GM (see *6CA_Amp*). In *6CA_CD* the current density vectors in especially the pyramidal tracts are oriented along the main fiber direction and, thus, they are no longer homogeneous (see *6C_CD* in Figure 7.2).

7.1.3 Conclusion

The results presented here demonstrate the importance of using an accurate volume conductor model for tDCS simulation. By starting with the three compartment head model and increasing the complexity gradually, it was possible to provide guidelines for tDCS modeling and to investigate how the inclusion of the different compartments and WM anisotropy into the head model affects the outcome of tDCS simulations. The most important addition to the *3C* head model was the CSF compartment because it significantly changed the magnitudes and the orientations of currents all over the brain in an inhomogeneous way. This investigation also showed that just as the CSF compartment, but to a less extent, inclusion of WM/GM distinction is important for an accurate tDCS or tACS simulation. The effects of skull spongiosa/compacta distinction were mainly limited to regions close to thick skull spongiosa plates, e.g., motor cortex. The effects of white matter anisotropy also depend heavily upon the target area: if the target is deep, it is highly recommended to model the WM anisotropy, but for superficial targets, the effects of white matter anisotropy are less significant.

Therefore, it can be summarized that the degree of complexity needed for an accurate simulation is mainly based on the tissues between the tDCS electrodes and the target area.

7.2 Study II: Assessing the Efficiency of Six Electrode Setups for Transcranial Direct Current Stimulation

Finding the optimal positions for the stimulating electrodes is crucial to achieve the highest currents in and around target areas in tDCS. In many studies, however, the electrode patches are positioned heuristically, and actual stimulation area might be suboptimal with regard to the target site due to suboptimal electrode placement and volume conduction effects. In this section, the electric fields are simulated for six electrode setups, which are often used in clinical and cognitive research [220]. These electrode setups are targeting the primary motor cortex (M1), dorsolateral prefrontal cortex (DLPFC), inferior frontal gyrus (IFG), occipital cortex (Oz), and cerebellum. The electric fields are calculated for the whole brain and for the target area, and the electric field is analyzed in terms of strength and direction. Taking into account the effects of volume conduction, as also described in Section 7.1, a detailed finite element head model with white matter anisotropy is used.

The anisotropic volume conduction model of the head was constructed based on MRIs of a healthy 25-year-old male subject. The T1- and T2-weighted images were used to reconstruct realistic geometries of the scalp, skull compacta, skull spongiosa, CSF, cerebral gray matter (GM), cerebral white matter (WM), cerebellar gray matter (cGM), cerebellar white matter (cWM), brainstem, eyes, and neck muscles (see Table 7.2). The triangular surface meshes for each tissue type were then combined into one tetrahedral volume mesh consisting of 672 thousand nodes and 4.12 million linear tetrahedral elements with an element size restricted to 1 mm in brain. Anisotropic conductivities obtained from DTI were included for all GM, WM, cGM and cWM. The head model construction pipeline was different from the one explained in Chapter 3 due to higher number of segmented compartments and the requirements of the tetrahedral mesh. The details of the pipeline used in this study can be found in [220]. The electrode patches had 3 mm thickness and their sizes were 7 cm x 5 cm and 5 cm x 5 cm for cerebral and cerebellar targets, respectively.

When the effects of electric field strengths on the GM surface are investigated, as it can be partly seen in Figure 7.3, for cerebral targets, the maximums are in between

Table 7.2: Conductivities used in this section. The symbol (#) indicates that conductivity tensors were determined as described in Section 3.1.5 and the symbol (*) indicates that the conductivity of the brainstem is assigned the mean of the conductivities of WM and GM.

Compartment	Conductivity (S/m)
Electrodes	1.4
Scalp	0.465
Skull spongiosa	0.007
Skull compacta	0.025
CSF	1.65
GM, cGM	#
WM, cWM	#
brainstem	*
eyes	1.5
muscle	0.4

the electrodes and 20 to 40 mm away from the targets. Therefore, the here presented simulations point to a sub-optimal electrode setup in terms of obtaining the highest electric fields in the target regions. For the two setups for the stimulation of the dorsolateral PFC (see left and dual DLPFC in Figure 7.3), the strengths of the electric fields are very similar and the only difference is the less focal stimulation achieved by dual-DLPFC in comparison to the left-DLPFC setup.

Unlike the setups for cerebral stimulation, the setup used for cerebellum (shown in Figure 7.3) achieves almost optimal stimulation in our simulations. However, the maximum electric field strength is just 1.1 mV/cm and is considerably smaller than the maximums obtained with configurations for cerebral stimulation (2.4-3.2 mV/cm). This decrease in the strength of electric field might be due to the currents, which do not enter the skull and bypass it by traveling through the scalp.

In addition to the strength, the orientation of the electric field is also very important for the evaluation of the effectiveness of an electrode configuration, i.e., inhibitory/exhibitory effects for cathodal/anodal stimulation [217]. In terms of orientation, it is found that the perpendicular (with respect to GM surface) field strengths are higher under the electrodes than in the areas with overall highest strengths (see the red regions in the volume rendered brain in Figure 7.3). This might explain why no undesirable effects have been reported in studies that use the experimental setups investigated here. This supports the idea that not only the strength, but also the direction of the electric field is very important, and must be investigated carefully in

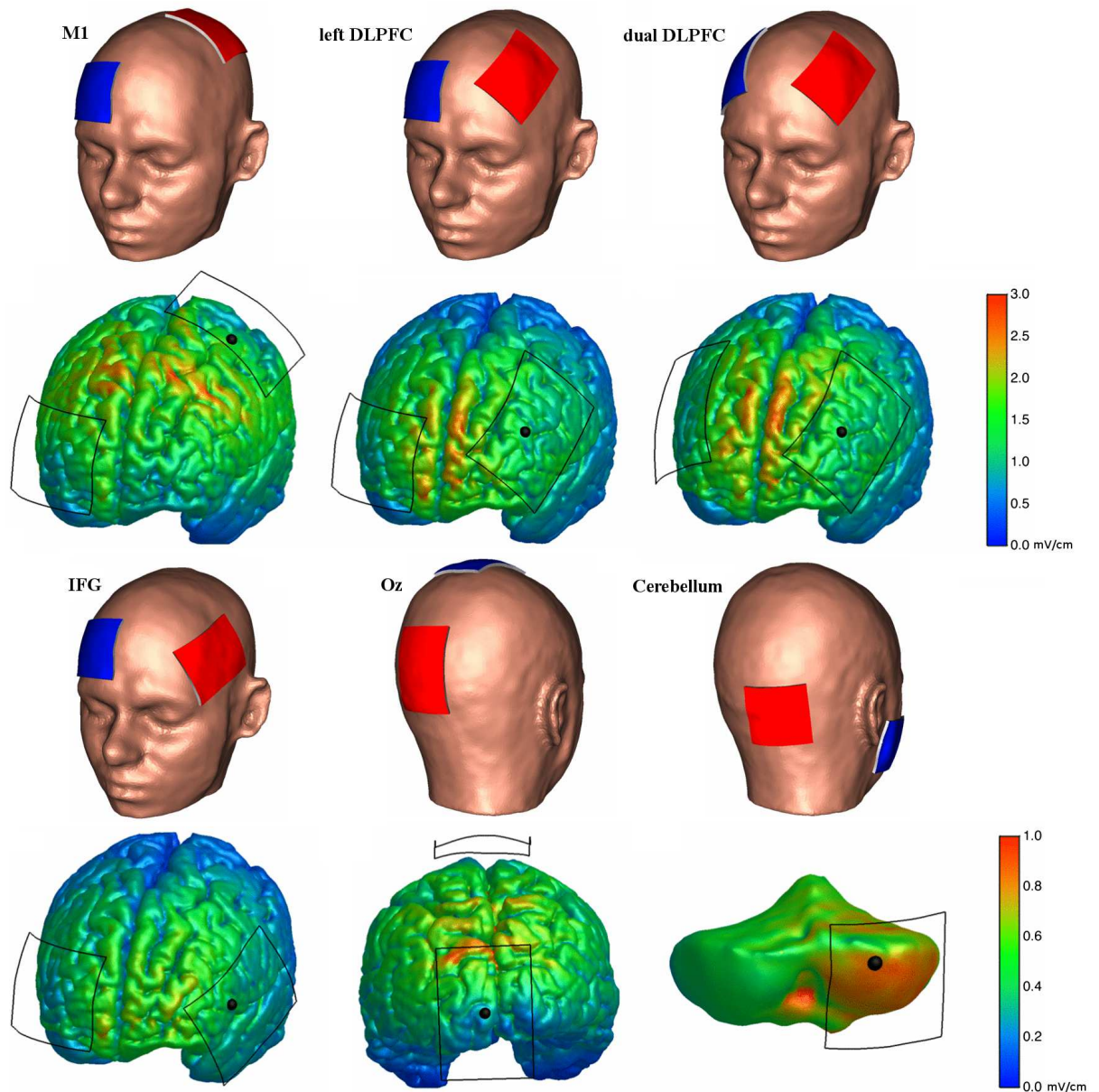


Figure 7.3: Investigation of the efficiencies of six electrode setups for tDSC. The positioning of the electrodes for the six different tDCS setups used are shown in the first and the third rows (volume rendering of the scalp), where the anode and cathode patches are depicted in red and blue color, respectively. The simulated electric field strengths for the stimulation setups are shown on the surface of the GM in the second and fourth rows (volume rendering of the brain), where the electrode-skin interface is outlined with black lines and the target of stimulation is depicted with a black dot. Different scales are used for the cerebral targets (second row) and the cerebellar targets (fourth row). The figure is adapted from [220]

order to find the optimal electrode configurations.

General findings of this study are in a good agreement with the findings described in the first study in this chapter, and thus, they are not explained here in detail and only summarized shortly below (see [220] for details). The general findings of this study are:

- For the scalp, the highest electric field values are found at the rim of the electrodes and especially at the corners closer to the other electrode.
- For the skull, the highest electric field values are more dispersed but still lie under the electrodes.
- Most of the currents are channeled through the skin and, thus, they do not enter the brain.
- The channeling effect of highly conductive CSF carries currents to a wider area.

After showing that in five of the six configurations tested here, the maximum of electric field is far away from the target, two new electrode configurations are designed and tested. These electrode configurations are designed based on the findings of this study that the maximum electric field is approximately in the midway between the stimulating electrodes (Figure 7.4). Using these configurations, the electric field strengths at the target areas, motor and occipital cortex, are increased by 88 and 94 %, respectively.

7.3 Study III: The Influence of Sulcus Width on Simulated Electric Fields Induced by Transcranial Magnetic Stimulation

In recent years, the interest in TMS for noninvasive brain stimulation has dramatically increased. Unlike tDCS and tACS, in which only sub-threshold electric fields can be induced to neurons, with TMS it is possible to create a much stronger electric field that can excite the neuron clusters inside the brain [218]. Simulation studies performed with realistic high resolution finite element head models are very important in TMS because these studies can be used not only to analyze different effects, but also to investigate the biophysical mechanisms underlying these effects [221]. In this study, the effects of the errors in cortical surface geometry modeling on TMS induced brain electric fields are investigated using the high resolution head model described in Section 7.2. Here

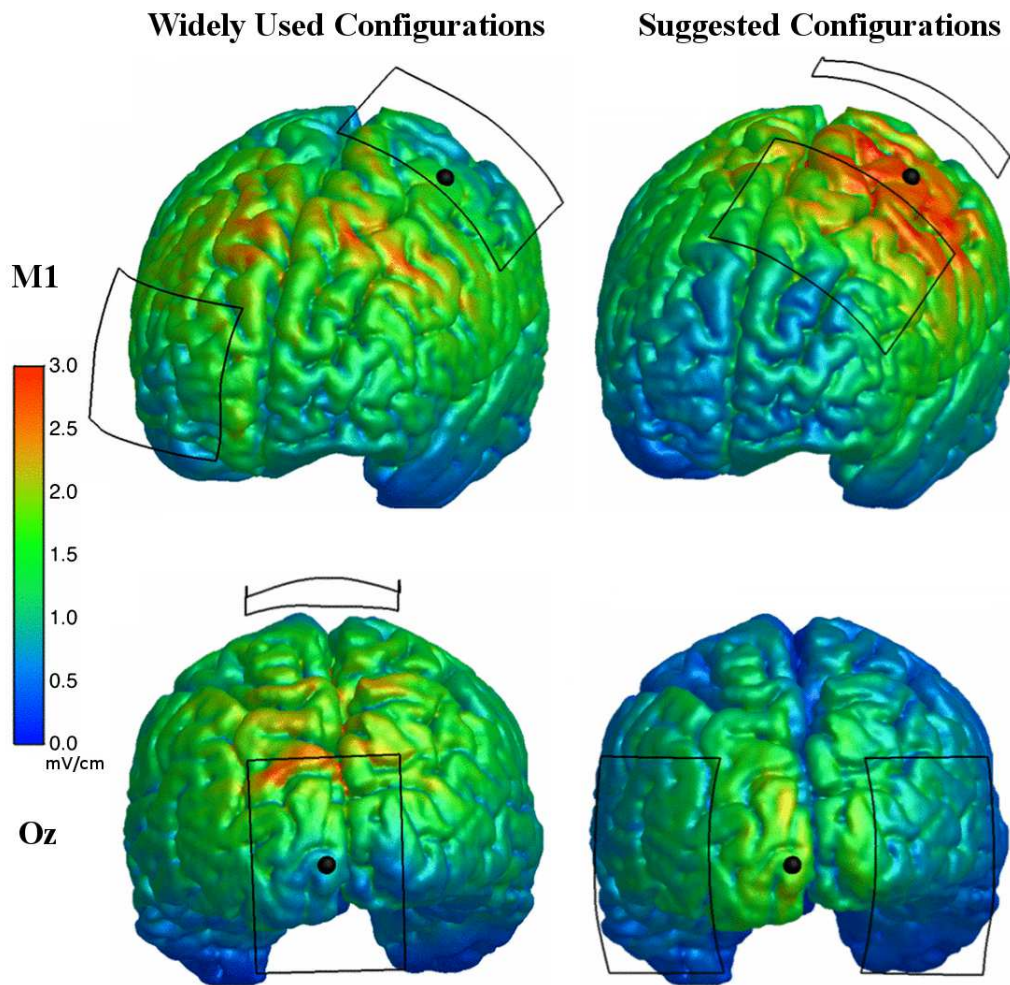


Figure 7.4: The electric field strengths on the surface of the GM for motor (M1) and occipital (Oz) cortex stimulation simulations with different electrode configurations. The common electrode configurations, widely used in other studies, are shown on the left, whereas the new electrode configurations are shown on the right. The target is shown by a black dot. The electrode-skin interface is outlined with black lines. The figure is adapted from [220].

only the main findings of the study are summarized and the details can be found in [221].

In this study, the main interest is on the cortical surface geometry because the GM surfaces obtained with widely used MR post-processing programs show considerable variability when analyzed with different methods (e.g., the specificities (probability that a not GM voxel is classified as not GM) of GM segmentation for Freesurfer, FSL and SPM are found as 0.82, 0.87 and 0.90, respectively in [225]). The differences on the geometry of the cortical surface are introduced by changing the width of the sulcus. In this way, it was possible to keep the coil-target distance constant, which

allows investigating the effects of cortical surface geometry changes while avoiding alterations caused by different coil-target distances. Additionally, changing the sulcus width allows simulating the effects of the CSF close to sulci and this might have important implications on the resulting electric fields due to the high conductivity of the CSF.

The main findings of this study are shortly summarized below:

- The highest electric fields occur at the top and the lips of the gyri, mainly close to thin CSF passages between the gyri and the skull.
- High sulcus width increases the electric field at neighboring gyri and it might change the position, where the maximum electric field occurs.
- Alterations up to 3 mm in sulcus width cause only slight and local differences in the calculated electric fields, thus deeper regions are not affected.

Based on these results, it is suggested that for a global approximation of the electric field potentials, errors that might occur due to wrong estimation of the sulcus width up to 3 mm are not very crucial. However, more attention should be paid in studies, in which the aim is to determine the exact location of the maximum of the electric field or in studies that couples the results with neuron models (see Section 4.2 in [221] for more on this issue).

7.4 Contributions of the Author to the Presented Brain Stimulation Studies

The main contribution of the author of this thesis to the studies described in this chapter was the construction of different head models as specified below:

- The acquisition of the MRI and EEG/MEG data (along with the medical technical assistants) in [216] (see Section 3.1.2).
- All steps required to construct the FE head model from the acquired MRIs in [216] (see Sections 3.1.3, 3.1.4, 3.1.5).
- Processing of the DTI data to model WM/GM anisotropy in [221] and [220].
- Processing and localization of the auditory N100m and somatosensory N20m evoked responses to determine individual target areas in [216] (same processing steps as in Chapter 6).

- Interpretation of the results and writing the related sections in [216, 220, 221].

8 Summary and Outlook

8.1 Summary

The main aim of this work was to evaluate and increase the accuracy of source reconstruction in presurgical epilepsy diagnosis by means of using combined EEG/MEG (EMEG) and advanced finite element head models.

In this work, a new experimental and methodological source analysis pipeline that combines the complementary information in EEG and MEG was introduced and applied to study a patient, suffering from refractory focal epilepsy. The results of this study were published in [71]. In this study, a six compartment finite element head model with brain anisotropy was constructed from individual MRI data and skull conductivity parameters were estimated in a calibration procedure using somatosensory evoked potentials (SEPs) and fields (SEFs). These data were measured in a single run before acquisition of further runs of spontaneous epileptic activity. This study showed that even for single interictal spikes EEG and MEG volume conduction effects dominate over noise and need to be taken into account for an accurate source analysis. EEG and MEG contain complementary information and a simultaneous acquirement of both datasets is highly recommended in order to increase reliability of results not only in presurgical epilepsy diagnosis, but also in other neuroscientific applications. The time needed to acquire the additional data is easily manageable by the patient and should not form an obstacle for the proposed procedure even in clinical group studies. In this work, a proof of concept was presented that skull conductivity calibration in realistic six and three compartment head models is needed to combine EEG and MEG source analysis accurately.

In the second study, described in Chapter 4 and published in [183] a high-resolution realistic six-compartment finite element head model with anisotropic white matter and calibrated skull conductivity was used to evaluate the performances of EEG, MEG and EMEG for different signal-to-noise-ratios (SNRs). In this study, source reconstructions in different phases of the epileptic activity and with different subaverages were investigated. The results were compared with the stereo-EEG (sEEG), which is the current

gold standard in presurgical epilepsy diagnosis. The results of this study revealed that EMEG source analysis can increase accuracy and confidence in source reconstructions significantly, which might have important clinical implications, especially for localizing at spike onset and for depicting propagation pathways as complete as possible. Furthermore, as shown by this study, sub-averaging might provide important and accurate information that neither single nor grand-averaged spike reconstructions can supply. However, the extent of dipole scatter is still correlated to the number of sub-averages and to the SNR.

In Chapters 3 and 4 an advanced head model, which might improve the accuracy of source reconstructions, was used. The significant differences that are found between the three and the six compartment head models in this thesis support the use of highly realistic head models for source modeling and brain stimulation. As concluded in these studies, also the use of more homogenized ways of forward modeling such as the classical three compartment (skin, skull, brain) approach might still benefit from the sub-averaging pipeline and the calibration procedure for combining EEG and MEG.

In the third study on epilepsy (Chapter 5), non-invasive source reconstructions were coupled with new advancements in parallel transmission in MRI [19] to obtain high resolution images within a small predefined region to detect small lesions that otherwise could not be detected. The pipeline was used to investigate the measurements from a patient with a known right frontal focal cortical dysplasia (FCD) and EMEG source analysis was performed. Then, high resolution MRI was acquired within the limited region pointed by the EMEG. In the end, a second FCD, which was not detected with normal MRI sequences was found in the high resolution MRI. The patient was operated from this second FCD (pointed by the EMEG) and became seizure free.

In Chapter 6 the head modeling pipeline explained in Chapter 3 was used to investigate auditory (AER) and somatosensory (SER) evoked responses. In the first part, the AERs and SERs from a subject with common responses were evaluated. The signals and source reconstructions were in line with the literature and, for the calibrated head model, the differences between EMEG and EEG and MEG alone were small for SER (as shown, this changes strongly if the head model is not calibrated), while they were significant for AER even in the calibrated head model. As found in that study, in EMEG, MEG was mainly contributing to the location and EEG was providing the information on orientation because of its ability to measure quasi-radial sources. The AERs measured from a second subject presented an uncommon case in which one hemisphere was mainly silent for components up to 100 ms. Despite this, the audiogram was normal for both ears, and clinical and radiologic examination showed no

pathology. The results obtained in this study are an important demonstration of the high variance of the brain activities even within the healthy population.

In Chapter 7 the focus was on the effects of volume conduction in non-invasive brain stimulation. The chapter shortly demonstrates the results of three published studies [216, 220, 221], for which the author of this thesis provided the whole [216] or parts [220, 221] of the used finite element head models and contributed to the writing of the papers and the work on the revisions. The results showed that, apart from the scalp and the skull, the most important compartments for an accurate simulation of transcranial direct current stimulation are CSF followed by white/gray matter distinction. The influences of other modeling aspects such as distinguishing skull spongiosa/compacta and including brain anisotropy depend on the placement of the electrode patches and target regions. Furthermore, the results of the study with transcranial magnetic stimulation revealed that the highest electric fields occur at the top and the lips of the gyri, mainly close to thin CSF passages between the gyri and the skull, and moderate changes in sulcus width have only local influences in calculated electric fields.

8.2 Outlook

In this thesis, it was shown that EMEG coupled with conductivity calibrated and anisotropic finite element head models can improve source reconstruction of interictal spikes considerably. However, this thesis mainly consists of proof of principle studies with single cases. Therefore, there is a need for further evaluation of the proposed approaches in a group study to determine in a statistical way the improvements through the proposed methodology.

Another important step is the further validation of the procedures in a group study. In Chapter 4, sEEG measurements were used for validation purposes because sEEG is widely accepted as the "gold standard" in presurgical epilepsy diagnosis. However, in that study, EEG/MEG/sEEG were not measured simultaneously. For future studies, simultaneous acquisition of EEG/MEG/sEEG data might be very useful to investigate if epileptic spikes that are visible in sEEG are also visible at the head surface with EEG and MEG. In addition to intracranial recordings, investigation of the measurements from patients with focal cortical dysplasia (especially type IIB) could also be used for validation purposes.

On the inverse problem side, future directions might be hierarchical Bayesian modeling [112, 113, 118] and the maximum entropy on the mean method [135, 152] following the promising results shown in these studies for focal and distributed sources.

In this thesis, interictal spikes are used for estimating the irritative zone. However, EEG data offer other ways of analysis. In [226], e.g., the epileptogenic zone was localized noninvasively from resting state EEG and promising results were achieved. This analysis might be used in patients without any distinguishable seizure or epileptic spike during the time of the measurement.

Another important direction for future studies is the improvement of the Polhemus-procedure for EEG sensor registration. The procedure based on the fiducials for morphing EEG and MEG onto the MRI as well as patient movement during EEG/MEG and MRI data acquisition cause artifacts, which are reflected in persisting differences of EEG and MEG reconstructions and even in some cases resulting in reductions in signal-to-noise-ratios [227]. In this thesis, following [80], as in MRI, all subjects were measured in supine position in EMEG and the space between the MEG dewar and the EEG cap was filled with filter cotton. As the head position measurements showed, on this way, head movements could be reduced to acceptably low rates of a few millimeters. Furthermore, in [228] and [229, 230], new tools were developed for improving MRI and MEG co-registration using optimized point-clouds of the head surface. Finally, a new method for rapid and accurate localization of electrode positions was designed and implemented, based on the "FlyTri" method, developed at the Institute of Optics, Information and Photonics, University of Erlangen-Nuremberg, Germany [231]. In [227], it was shown that the method is more accurate than the frequently applied electromagnetic digitizer technique and that this increased accuracy results in better reconstruction of weak neuronal activity. This method is currently being developed further to support head position localization and tracking for use in MEG. A MEG-compatible prototype has been implemented as part of a master's thesis [232] and is currently being optimized.

In terms of volume conductor model, the next steps should be the modeling of the dura matter and skull holes. Although in Chapter 5 dura mater was modeled in regions where it was the thickest, the thinner regions were not modeled due to the complexity of segmentation and appropriate numerical modeling. However, [166] reported about significant reductions in EEG potentials when ignoring the modeling of dura mater, showing the necessity of more accurately modeling this compartment in future investigations. Skull hole modeling is another difficult aspect. On one hand it was shown that skull holes have significant effects on both EEG [60] and on MEG [61]. However, on the other hand, these studies also showed that for small holes the errors tend to be limited to the close vicinity of the hole. In case of craniotomy, where the hole is near the brain region of interest, it should be modeled for a reliable source

reconstruction [233]. Therefore, larger skull holes definitely need to be modeled, while the modeling or neglect of smaller skull holes might be decided from case to case.

Bibliography

- [1] H. O. Lüders, I. Najm, D. Nair, P. Widdess-Walsh, and W. Bingman, “The epileptogenic zone: general principles,” *Epileptic Disord*, vol. 8 Suppl 2, pp. S1–9, Aug 2006.
- [2] R. Degen, A. Ebner, R. Lahl, S. Bartling, H. W. Pannek, and I. Tuxhorn, “MRI and EEG findings in surgically treated patients with partial seizures due to neuronal migration disorders, their relations to each other and to surgery outcome,” *Acta Neurol Scand*, vol. 108, pp. 309–18, Nov 2003.
- [3] J. Janszky, H. Jokeit, R. Schulz, M. Hoppe, and A. Ebner, “EEG predicts surgical outcome in lesional frontal lobe epilepsy,” *Neurology*, vol. 54, pp. 1470–6, Apr 2000.
- [4] S. K. Lee, S. Y. Lee, K.-K. Kim, K.-S. Hong, D.-S. Lee, and C.-K. Chung, “Surgical outcome and prognostic factors of cryptogenic neocortical epilepsy,” *Ann Neurol*, vol. 58, pp. 525–32, Oct 2005.
- [5] G. Alarcón and Z. Agirre-Arrizubieta, “Magnetoencephalography in epilepsy: is it time for EMEG?,” *Clin Neurophysiol*, vol. 122, pp. 1282–3, Jul 2011.
- [6] M. Fuchs, M. Wagner, H. A. Wischmann, T. Köhler, A. Theissen, R. Drenckhahn, and H. Buchner, “Improving source reconstructions by combining bioelectric and biomagnetic data,” *Electroencephalogr Clin Neurophysiol*, vol. 107, pp. 93–111, Aug 1998.
- [7] W. W. Sutherling, P. H. Crandall, T. M. Darcey, D. P. Becker, M. F. Levesque, and D. S. Barth, “The magnetic and electric fields agree with intracranial localizations of somatosensory cortex,” *Neurology*, vol. 38, pp. 1705–14, Nov 1988.
- [8] D. Sharon, M. S. Hämäläinen, R. B. H. Tootell, E. Halgren, and J. W. Belliveau, “The advantage of combining MEG and EEG: comparison to fMRI in focally stimulated visual cortex,” *Neuroimage*, vol. 36, pp. 1225–35, Jul 2007.

-
- [9] R. E. Greenblatt, M. E. Pflieger, and A. E. Ossadtchi, “Connectivity measures applied to human brain electrophysiological data,” *J Neurosci Methods*, vol. 207, pp. 1–16, May 2012.
- [10] M. J. M. Fischer, G. Scheler, and H. Stefan, “Utilization of magnetoencephalography results to obtain favourable outcomes in epilepsy surgery,” *Brain*, vol. 128, pp. 153–7, Jan 2005.
- [11] A. Genow, C. Hummel, G. Scheler, R. Hopfengärtner, M. Kaltenhäuser, M. Buchfelder, J. Romstöck, and H. Stefan, “Epilepsy surgery, resection volume and msi localization in lesional frontal lobe epilepsy,” *Neuroimage*, vol. 21, pp. 444–9, Jan 2004.
- [12] R. Köhling, J. M. Höhling, H. Straub, D. Kuhlmann, U. Kuhnt, I. Tuxhorn, A. Ebner, P. Wolf, H. W. Pannek, A. Gorji, and E. J. Speckmann, “Optical monitoring of neuronal activity during spontaneous sharp waves in chronically epileptic human neocortical tissue,” *J Neurophysiol*, vol. 84, pp. 2161–5, Oct 2000.
- [13] M. Oishi, S. Kameyama, H. Masuda, J. Tohyama, O. Kanazawa, M. Sasagawa, and H. Otsubo, “Single and multiple clusters of magnetoencephalographic dipoles in neocortical epilepsy: significance in characterizing the epileptogenic zone,” *Epilepsia*, vol. 47, pp. 355–64, Feb 2006.
- [14] G. Scheler, M. J. M. Fischer, A. Genow, C. Hummel, S. Rampp, A. Paulini, R. Hopfengärtner, M. Kaltenhäuser, and H. Stefan, “Spatial relationship of source localizations in patients with focal epilepsy: Comparison of MEG and EEG with a three spherical shells and a boundary element volume conductor model,” *Hum Brain Mapp*, vol. 28, pp. 315–22, Apr 2007.
- [15] E. Speckmann, C. Elger, and A. Gorji, *Neurophysiologic basis of EEG and DC potentials. Niedermeyer’s Electroencephalography: Basic Principles, Clinical Applications and Related Fields*. Lippincott, Williams and Wilkens, 2012.
- [16] T. Bast, T. Boppel, A. Rupp, I. Harting, K. Hoechstetter, S. Fauser, A. Schulze-Bonhage, D. Rating, and M. Scherg, “Noninvasive source localization of interictal EEG spikes: effects of signal-to-noise ratio and averaging,” *J Clin Neurophysiol*, vol. 23, pp. 487–97, Dec 2006.

-
- [17] R. Wennberg and D. Cheyne, “EEG source imaging of anterior temporal lobe spikes: validity and reliability,” *Clin Neurophysiol*, vol. 125, pp. 886–902, May 2014.
- [18] R. Wennberg and D. Cheyne, “Reliability of MEG source imaging of anterior temporal spikes: analysis of an intracranially characterized spike focus,” *Clin Neurophysiol*, vol. 125, pp. 903–18, May 2014.
- [19] M. Blasche, P. Riffel, and M. Lichy, “Timtx trueshape and syngo zoomit technical and practical aspects,” *Magnetom Flash.*, vol. 1, pp. 74–84, 2012.
- [20] W. H. Organization *et al.*, “Atlas: epilepsy care in the world,” 2005.
- [21] R. B. Todd, “On the pathology and treatment of convulsive diseases.,” *London Medical Gazette*, vol. 8, pp. 661–671, 724–729, 766–772, 815–822, 837–846, 1849.
- [22] E. H. Reynolds and M. R. Trimble, “Epilepsy, psychiatry, and neurology,” *Epilepsia*, vol. 50, pp. 50–55, 2009.
- [23] W. H. Organization, “Epilepsy fact sheet no:999,” 2012.
- [24] W. Macewen, “Tumour of the dura mater removed during life in a person affected with epilepsy,” *Glas Med J*, vol. 12, p. 210, 1879.
- [25] H. Berger, “Über das elektrenkephalogramm des menschen,” *European Archives of Psychiatry and Clinical Neuroscience*, vol. 87, no. 1, pp. 527–570, 1929.
- [26] R. I. Kuzniecky, G. D. Jackson, and J. Aicardi, *Magnetic resonance in epilepsy*. Raven Press New York, NY, USA:, 1995.
- [27] P. Bailey and F. A. Gibbs, “The surgical treatment of psychomotor epilepsy,” *Journal of the American Medical Association*, vol. 145, no. 6, pp. 365–370, 1951.
- [28] H. Fujiwara, H. M. Greiner, N. Hemasilpin, K. H. Lee, K. Holland-Bouley, T. Arthur, D. Morita, S. V. Jain, F. T. Mangano, T. Degrauw, and D. F. Rose, “Ictal MEG onset source localization compared to intracranial EEG and outcome: improved epilepsy presurgical evaluation in pediatrics,” *Epilepsy Res*, vol. 99, pp. 214–24, May 2012.
- [29] A. Salek-Haddadi, M. Merschhemke, L. Lemieux, and D. R. Fish, “Simultaneous EEG-correlated ictal fMRI,” *Neuroimage*, vol. 16, pp. 32–40, May 2002.

-
- [30] J. S. Ebersole and S. V. Pacia, "Localization of temporal lobe foci by ictal EEG patterns," *Epilepsia*, vol. 37, pp. 386–99, Apr 1996.
- [31] R. Schulz, H. O. Lüders, M. Hoppe, I. Tuxhorn, T. May, and A. Ebner, "Interictal EEG and ictal scalp EEG propagation are highly predictive of surgical outcome in mesial temporal lobe epilepsy," *Epilepsia*, vol. 41, pp. 564–70, May 2000.
- [32] S. S. Ho, S. F. Berkovic, M. R. Newton, M. C. Austin, W. J. McKay, and P. F. Bladin, "Parietal lobe epilepsy: clinical features and seizure localization by ictal SPECT," *Neurology*, vol. 44, pp. 2277–84, Dec 1994.
- [33] R. C. Knowlton, "The role of FDG-PET, ictal SPECT, and MEG in the epilepsy surgery evaluation," *Epilepsy Behav*, vol. 8, pp. 91–101, Feb 2006.
- [34] J. Wagner, H. Urbach, P. Niehusmann, M. von Lehe, C. E. Elger, and J. Wellmer, "Focal cortical dysplasia type iib: completeness of cortical, not subcortical, resection is necessary for seizure freedom," *Epilepsia*, vol. 52, pp. 1418–24, Aug 2011.
- [35] C. Dansereau, P. Bellec, K. Lee, F. Pittau, J. Gotman, and C. Grova, "Detection of abnormal resting-state networks in individual patients suffering from focal epilepsy: An initial step toward individual connectivity assessment," *Name: Frontiers in Neuroscience*, vol. 8, p. 419, 2014.
- [36] M. A. Kramer and S. S. Cash, "Epilepsy as a disorder of cortical network organization," *Neuroscientist*, vol. 18, pp. 360–72, Aug 2012.
- [37] M. Akhtari, H. C. Bryant, A. N. Mamelak, L. Heller, J. J. Shih, M. Mandelkern, A. Matlachov, D. M. Ranken, E. D. Best, and W. W. Sutherling, "Conductivities of three-layer human skull," *Brain Topogr*, vol. 13, no. 1, pp. 29–42, 2000.
- [38] J. E. Hall, *Guyton and Hall Textbook of Medical Physiology: Enhanced E-book*. Elsevier Health Sciences, 2010.
- [39] K. Miller, *Biomechanics of the Brain*. Springer, 2011.
- [40] M. Patestas and L. P. Gartner, *A textbook of neuroanatomy*. John Wiley & Sons, 2009.
- [41] E. Kobayashi, I. Lopes-Cendes, C. A. Guerreiro, S. C. Sousa, M. M. Guerreiro, and F. Cendes, "Seizure outcome and hippocampal atrophy in familial mesial temporal lobe epilepsy," *Neurology*, vol. 56, pp. 166–72, Jan 2001.

-
- [42] M. Hämäläinen, R. Hari, R. J. Ilmoniemi, J. Knuutila, and O. V. Lounasmaa, “Magnetoencephalography-theory, instrumentation, and applications to noninvasive studies of the working human brain,” *Reviews of Modern Physics*, vol. 65, pp. 413–497, Apr. 1993.
- [43] S. Baillet, J. C. Mosher, and R. M. Leahy, “Electromagnetic brain mapping,” *Signal Processing Magazine, IEEE*, vol. 18, no. 6, pp. 14–30, 2001.
- [44] R. Llinas and C. Nicholson, “Analysis of field potentials in the central nervous system,” *Handbook of electroencephalography and clinical neurophysiology*, vol. 2, no. Part B, pp. 61–85, 1974.
- [45] S. Murakami and Y. Okada, “Contributions of principal neocortical neurons to magnetoencephalography and electroencephalography signals,” *J Physiol*, vol. 575, pp. 925–36, Sep 2006.
- [46] S. Baillet, L. Garnero, G. Marin, and J. P. Hugonin, “Combined MEG and EEG source imaging by minimization of mutual information,” *IEEE Trans Biomed Eng*, vol. 46, pp. 522–34, May 1999.
- [47] D. Cohen and B. N. Cuffin, “A method for combining MEG and EEG to determine the sources,” *Phys Med Biol*, vol. 32, pp. 85–9, Jan 1987.
- [48] A. K. Liu, A. M. Dale, and J. W. Belliveau, “Monte carlo simulation studies of EEG and MEG localization accuracy,” *Hum Brain Mapp*, vol. 16, pp. 47–62, May 2002.
- [49] J. Sarvas, “Basic mathematical and electromagnetic concepts of the biomagnetic inverse problem,” *Phys Med Biol*, vol. 32, pp. 11–22, Jan 1987.
- [50] J. Vorwerk, J.-H. Cho, S. Rampp, H. Hamer, T. R. Knösche, and C. H. Wolters, “A guideline for head volume conductor modeling in EEG and MEG,” *Neuroimage*, vol. 100, pp. 590–607, Oct 2014.
- [51] C. H. Wolters, A. Anwander, X. Tricoche, D. Weinstein, M. A. Koch, and R. S. MacLeod, “Influence of tissue conductivity anisotropy on EEG/MEG field and return current computation in a realistic head model: a simulation and visualization study using high-resolution finite element modeling,” *Neuroimage*, vol. 30, pp. 813–26, Apr 2006.

-
- [52] J. Haueisen, M. Funke, D. Güllmar, and R. Eichardt, “Tangential and radial epileptic spike activity: different sensitivity in EEG and MEG,” *J Clin Neurophysiol*, vol. 29, pp. 327–32, Aug 2012.
- [53] G. L. Barkley and C. Baumgartner, “MEG and EEG in epilepsy,” *J Clin Neurophysiol*, vol. 20, no. 3, pp. 163–78, 2003.
- [54] M. Iwasaki, E. Pestana, R. C. Burgess, H. O. Lüders, H. Shamoto, and N. Nakasato, “Detection of epileptiform activity by human interpreters: blinded comparison between electroencephalography and magnetoencephalography,” *Epilepsia*, vol. 46, pp. 59–68, Jan 2005.
- [55] S. Knake, E. Halgren, H. Shiraishi, K. Hara, H. M. Hamer, P. E. Grant, V. A. Carr, D. Foxe, S. Camposano, E. Busa, T. Witzel, M. S. Hämäläinen, S. P. Ahlfors, E. B. Bromfield, P. M. Black, B. F. Bourgeois, A. J. Cole, G. R. Cosgrove, B. A. Dworetzky, J. R. Madsen, P. G. Larsson, D. L. Schomer, E. A. Thiele, A. M. Dale, B. R. Rosen, and S. M. Stufflebeam, “The value of multi-channel MEG and EEG in the presurgical evaluation of 70 epilepsy patients,” *Epilepsy Res*, vol. 69, pp. 80–6, Apr 2006.
- [56] P. Ossenblok, J. C. de Munck, A. Colon, W. Drolsbach, and P. Boon, “Magnetoencephalography is more successful for screening and localizing frontal lobe epilepsy than electroencephalography,” *Epilepsia*, vol. 48, pp. 2139–49, Nov 2007.
- [57] R. Plonsey and D. B. Heppner, “Considerations of quasi-stationarity in electrophysiological systems,” *Bull Math Biophys*, vol. 29, pp. 657–64, Dec 1967.
- [58] C. H. Wolters, H. Köstler, C. Möller, J. Härdtlein, L. Grasedyck, and W. Hackbusch, “Numerical mathematics of the subtraction method for the modeling of a current dipole in EEG source reconstruction using finite element head models,” *SIAM Journal on Scientific Computing*, vol. 30, no. 1, pp. 24–45, 2007.
- [59] J. C. De Munck, C. H. Wolters, M. Clerc, *et al.*, “EEG and MEG: forward modeling,” *Handbook of neural activity measurement*, pp. 192–256, 2012.
- [60] B. Lanfer, M. Scherg, M. Dannhauer, T. R. Knösche, M. Burger, and C. H. Wolters, “Influences of skull segmentation inaccuracies on EEG source analysis,” *Neuroimage*, vol. 62, pp. 418–31, Aug 2012.
- [61] S. Lau, L. Flemming, and J. Haueisen, “Magnetoencephalography signals are influenced by skull defects,” *Clin Neurophysiol*, vol. 125, pp. 1653–62, Aug 2014.

-
- [62] S. Lew, D. D. Sliva, M.-s. Choe, P. E. Grant, Y. Okada, C. H. Wolters, and M. S. Hämäläinen, “Effects of sutures and fontanels on MEG and EEG source analysis in a realistic infant head model,” *Neuroimage*, vol. 76, pp. 282–93, Aug 2013.
- [63] S. P. van den Broek, F. Reinders, M. Donderwinkel, and M. J. Peters, “Volume conduction effects in EEG and MEG,” *Electroencephalogr Clin Neurophysiol*, vol. 106, pp. 522–34, Jun 1998.
- [64] G. Marin, C. Guerin, S. Baillet, L. Garnero, and G. Meunier, “Influence of skull anisotropy for the forward and inverse problem in EEG: simulation studies using FEM on realistic head models,” *Hum Brain Mapp*, vol. 6, no. 4, pp. 250–69, 1998.
- [65] H. Hallez, B. Vanrumste, P. Van Hese, S. Delputte, and I. Lemahieu, “Dipole estimation errors due to differences in modeling anisotropic conductivities in realistic head models for EEG source analysis,” *Phys Med Biol*, vol. 53, pp. 1877–94, Apr 2008.
- [66] O. Steinsträter, S. Sillekens, M. Junghoefer, M. Burger, and C. H. Wolters, “Sensitivity of beamformer source analysis to deficiencies in forward modeling,” *Hum Brain Mapp*, vol. 31, pp. 1907–27, Dec 2010.
- [67] M. Dannhauer, B. Lanfer, C. H. Wolters, and T. R. Knösche, “Modeling of the human skull in EEG source analysis,” *Hum Brain Mapp*, vol. 32, pp. 1383–99, Sep 2011.
- [68] M. Akhtari, H. C. Bryant, A. N. Mamelak, E. R. Flynn, L. Heller, J. J. Shih, M. Mandelkern, A. Matlachov, D. M. Ranken, E. D. Best, M. A. DiMauro, R. R. Lee, and W. W. Sutherling, “Conductivities of three-layer live human skull,” *Brain Topogr*, vol. 14, no. 3, pp. 151–67, 2002.
- [69] V. Montes-Restrepo, P. van Mierlo, G. Strobbe, S. Staelens, S. Vandenberghe, and H. Hallez, “Influence of skull modeling approaches on EEG source localization,” *Brain Topogr*, vol. 27, pp. 95–111, Jan 2014.
- [70] M. Rullmann, A. Anwander, M. Dannhauer, S. K. Warfield, F. H. Duffy, and C. H. Wolters, “EEG source analysis of epileptiform activity using a 1 mm anisotropic hexahedra finite element head model,” *Neuroimage*, vol. 44, pp. 399–410, Jan 2009.
- [71] Ü. Aydın, J. Vorwerk, P. Küpper, M. Heers, H. Kugel, A. Galka, L. Hamid, J. Wellmer, C. Kellinghaus, S. Rampp, and C. H. Wolters, “Combining EEG

- and MEG for the reconstruction of epileptic activity using a calibrated realistic volume conductor model,” *PLoS One*, vol. 9, no. 3, p. e93154, 2014.
- [72] J. Haueisen, C. Ramon, M. Eiselt, H. Brauer, and H. Nowak, “Influence of tissue resistivities on neuromagnetic fields and electric potentials studied with a finite element model of the head,” *IEEE Trans Biomed Eng*, vol. 44, pp. 727–35, Aug 1997.
- [73] H. Hallez, B. Vanrumste, P. Van Hese, Y. D’Asseler, I. Lemahieu, and R. Van de Walle, “A finite difference method with reciprocity used to incorporate anisotropy in electroencephalogram dipole source localization,” *Phys Med Biol*, vol. 50, pp. 3787–806, Aug 2005.
- [74] S. Vallaghé and M. Clerc, “A global sensitivity analysis of three- and four-layer EEG conductivity models,” *IEEE Trans Biomed Eng*, vol. 56, pp. 988–95, Apr 2009.
- [75] S. Gonçalves, J. C. de Munck, J. P. A. Verbunt, R. M. Heethaar, and F. H. L. da Silva, “In vivo measurement of the brain and skull resistivities using an eit-based method and the combined analysis of sef/sep data,” *IEEE Trans Biomed Eng*, vol. 50, pp. 1124–8, Sep 2003.
- [76] M.-X. Huang, T. Song, D. J. Hagler, Jr, I. Podgorny, V. Jousmaki, L. Cui, K. Gaa, D. L. Harrington, A. M. Dale, R. R. Lee, J. Elman, and E. Halgren, “A novel integrated MEG and EEG analysis method for dipolar sources,” *Neuroimage*, vol. 37, pp. 731–48, Sep 2007.
- [77] S. B. Baumann, D. R. Wozny, S. K. Kelly, and F. M. Meno, “The electrical conductivity of human cerebrospinal fluid at body temperature,” *IEEE Trans Biomed Eng*, vol. 44, pp. 220–3, Mar 1997.
- [78] C. Ramon, P. Schimpf, J. Haueisen, M. Holmes, and A. Ishimaru, “Role of soft bone, CSF and gray matter in EEG simulations,” *Brain Topogr*, vol. 16, no. 4, pp. 245–8, 2004.
- [79] K. Wendel, N. G. Narra, M. Hannula, P. Kauppinen, and J. Malmivuo, “The influence of CSF on EEG sensitivity distributions of multilayered head models,” *IEEE Trans Biomed Eng*, vol. 55, pp. 1454–6, Apr 2008.
- [80] J. K. Rice, C. Rorden, J. S. Little, and L. C. Parra, “Subject position affects EEG magnitudes,” *Neuroimage*, vol. 64, pp. 476–84, Jan 2013.

-
- [81] J. Vorwerk, M. Clerc, M. Burger, and C. H. Wolters, “Comparison of boundary element and finite element approaches to the EEG forward problem,” *Biomed Tech (Berl)*, vol. 57 Suppl 1, 2012.
- [82] P. W. Nicholson, “Specific impedance of cerebral white matter,” *Exp Neurol*, vol. 13, pp. 386–401, Dec 1965.
- [83] C. H. Wolters, A. Anwander, M. A. Koch, S. Reitzinger, M. Kuhn, and M. Sven-sén, “Influence of head tissue conductivity anisotropy on human EEG and MEG using fast high resolution finite element modeling, based on a parallel algebraic multigrid solver,” *Forschung und wissenschaftliches Rechnen*, pp. 111–157, 2001.
- [84] J. Haueisen, D. S. Tuch, C. Ramon, P. H. Schimpf, V. J. Wedeen, J. S. George, and J. W. Belliveau, “The influence of brain tissue anisotropy on human EEG and MEG,” *Neuroimage*, vol. 15, pp. 159–66, Jan 2002.
- [85] D. Güllmar, J. Haueisen, M. Eiselt, F. Giessler, L. Flemming, A. Anwander, T. R. Knösche, C. H. Wolters, M. Dümpelmann, D. S. Tuch, and J. R. Re-ichenbach, “Influence of anisotropic conductivity on EEG source reconstruction: investigations in a rabbit model,” *IEEE Trans Biomed Eng*, vol. 53, pp. 1841–50, Sep 2006.
- [86] D. S. Tuch, V. J. Wedeen, A. M. Dale, J. S. George, and J. W. Belliveau, “Conductivity tensor mapping of the human brain using diffusion tensor MRI,” *Proc Natl Acad Sci U S A*, vol. 98, pp. 11697–701, Sep 2001.
- [87] R. M. Heidemann, A. Anwander, T. Feiweier, T. R. Knösche, and R. Turner, “k-space and q-space: combining ultra-high spatial and angular resolution in diffusion imaging using zooppa at 7 t,” *Neuroimage*, vol. 60, pp. 967–78, Apr 2012.
- [88] J. C. de Munck and M. J. Peters, “A fast method to compute the potential in the multisphere model,” *IEEE Trans Biomed Eng*, vol. 40, pp. 1166–74, Nov 1993.
- [89] H. Hallez, B. Vanrumste, R. Grech, J. Muscat, W. De Clercq, A. Vergult, Y. D’Asseler, K. P. Camilleri, S. G. Fabri, S. Van Huffel, and I. Lemahieu, “Review on solving the forward problem in EEG source analysis,” *J Neuroeng Rehabil*, vol. 4, p. 46, 2007.

-
- [90] J. Haueisen and T. R. Knösche, “Forward modeling and tissue conductivities,” *Magnetoencephalography: From Signals to Dynamic Cortical Networks*, pp. 107–127, 2014.
- [91] M. S. Hämäläinen and J. Sarvas, “Realistic conductivity geometry model of the human head for interpretation of neuromagnetic data,” *IEEE Trans Biomed Eng*, vol. 36, pp. 165–71, Feb 1989.
- [92] J. Haueisen, A. Böttner, M. Funke, H. Brauer, and H. Nowak, “Effect of boundary element discretization on forward calculation and the inverse problem in electroencephalography and magnetoencephalography,” *Biomed Tech (Berl)*, vol. 42, pp. 240–8, Sep 1997.
- [93] D. L. Camacho, R. H. Hopper, G. M. Lin, and B. S. Myers, “An improved method for finite element mesh generation of geometrically complex structures with application to the skullbase,” *J Biomech*, vol. 30, pp. 1067–70, Oct 1997.
- [94] C. H. Wolters, A. Anwander, G. Berti, and U. Hartmann, “Geometry-adapted hexahedral meshes improve accuracy of finite-element-method-based EEG source analysis,” *IEEE Trans Biomed Eng*, vol. 54, pp. 1446–53, Aug 2007.
- [95] C. Wolters, M. Kuhn, A. Anwander, and S. Reitzinger, “A parallel algebraic multigrid solver for finite element method based source localization in the human brain,” *Computing and visualization in science*, vol. 5, no. 3, pp. 165–177, 2002.
- [96] C. H. Wolters, L. Grasedyck, and W. Hackbusch, “Efficient computation of lead field bases and influence matrix for the FEM-based EEG and MEG inverse problem,” *Inverse Problems*, vol. 20, pp. 1099–1116, 2004.
- [97] D. Weinstein, L. Zhukov, and C. Johnson, “Lead-field bases for electroencephalography source imaging,” *Ann Biomed Eng*, vol. 28, pp. 1059–65, Sep 2000.
- [98] N. G. Gençer and C. E. Acar, “Sensitivity of EEG and MEG measurements to tissue conductivity,” *Phys Med Biol*, vol. 49, pp. 701–17, Mar 2004.
- [99] K. Jerbi, S. Baillet, J. C. Mosher, G. Nolte, L. Garnero, and R. M. Leahy, “Localization of realistic cortical activity in MEG using current multipoles,” *Neuroimage*, vol. 22, pp. 779–93, Jun 2004.

-
- [100] G. Dassios, A. Fokas, and D. Hadjiloizi, “On the complementarity of electroencephalography and magnetoencephalography,” *Inverse Problems*, vol. 23, no. 6, p. 2541, 2007.
- [101] F. H. Lopes da Silva, H. J. Wieringa, and M. J. Peters, “Source localization of EEG versus MEG: empirical comparison using visually evoked responses and theoretical considerations,” *Brain Topogr*, vol. 4, no. 2, pp. 133–42, 1991.
- [102] J. W. Phillips, R. M. Leahy, J. C. Mosher, and B. Timsari, “Imaging neural activity using MEG and EEG,” *IEEE Eng Med Biol Mag*, vol. 16, no. 3, pp. 34–42, 1997.
- [103] J. H. Hong, M. Ahn, K. Kim, and S. C. Jun, “Localization of coherent sources by simultaneous MEG and EEG beamformer,” *Med Biol Eng Comput*, vol. 51, pp. 1121–35, Oct 2013.
- [104] C. M. Michel, M. M. Murray, G. Lantz, S. Gonzalez, L. Spinelli, and R. Grave de Peralta, “EEG source imaging,” *Clin Neurophysiol*, vol. 115, pp. 2195–222, Oct 2004.
- [105] D. A. Pizzagalli, “Electroencephalography and high-density electrophysiological source localization,” *Handbook of psychophysiology*, vol. 3, pp. 56–84, 2007.
- [106] M. Huang, C. J. Aine, S. Supek, E. Best, D. Ranken, and E. R. Flynn, “Multi-start downhill simplex method for spatio-temporal source localization in magnetoencephalography,” *Electroencephalogr Clin Neurophysiol*, vol. 108, pp. 32–44, Jan 1998.
- [107] J. C. Mosher, P. S. Lewis, and R. M. Leahy, “Multiple dipole modeling and localization from spatio-temporal MEG data,” *IEEE Trans Biomed Eng*, vol. 39, pp. 541–57, Jun 1992.
- [108] M. Fuchs, H.-A. Wischmann, M. Wagner, R. Drenckhahn, and T. Köhler, “Source reconstructions by spatial deviation scans,” in *Biomag 96*, pp. 213–216, Springer, 1998.
- [109] H. Buchner, M. Fuchs, H. A. Wischmann, O. Dössel, I. Ludwig, A. Knepper, and P. Berg, “Source analysis of median nerve and finger stimulated somatosensory evoked potentials: multichannel simultaneous recording of electric and magnetic fields combined with 3D-MR tomography,” *Brain Topogr*, vol. 6, no. 4, pp. 299–310, 1994.

-
- [110] B. Lütkenhöner and O. Steinsträter, “High-precision neuromagnetic study of the functional organization of the human auditory cortex,” *Audiol Neurootol*, vol. 3, no. 2-3, pp. 191–213, 1998.
- [111] C. Pantev, B. Ross, P. Berg, T. Elbert, and B. Rockstroh, “Study of the human auditory cortices using a whole-head magnetometer: left vs. right hemisphere and ipsilateral vs. contralateral stimulation,” *Audiol Neurootol*, vol. 3, no. 2-3, pp. 183–90, 1998.
- [112] F. Lucka, Ü. Aydın, J. Vorwerk, M. Burger, and C. H. Wolters, “Hierarchical fully-Bayesian inference for combined EEG/MEG source analysis of evoked responses: From simulations to real data,” in *First Int. Conf. on Basic and Clinical multimodal Imaging (BaCI), Sept.5-8, Geneva, Switzerland.*, 2013.
- [113] F. Lucka, *Bayesian Inversion in Biomedical Imaging*. PhD thesis, University of Münster, 2015.
- [114] C. Campi, A. Pascarella, A. Sorrentino, and M. Piana, “Highly automated dipole estimation (HADES),” *Computational intelligence and neuroscience*, vol. 2011, 2011.
- [115] J. C. Mosher and R. M. Leahy, “Recursive MUSIC: a framework for EEG and MEG source localization,” *IEEE Trans Biomed Eng*, vol. 45, pp. 1342–54, Nov 1998.
- [116] J. C. Mosher and R. M. Leahy, “Source localization using recursively applied and projected (RAP) MUSIC,” *Signal Processing, IEEE Transactions on*, vol. 47, no. 2, pp. 332–340, 1999.
- [117] M. S. Hämäläinen and R. J. Ilmoniemi, “Interpreting magnetic fields of the brain: minimum norm estimates,” *Med Biol Eng Comput*, vol. 32, pp. 35–42, Jan 1994.
- [118] F. Lucka, S. Pursiainen, M. Burger, and C. H. Wolters, “Hierarchical Bayesian inference for the EEG inverse problem using realistic FE head models: depth localization and source separation for focal primary currents,” *Neuroimage*, vol. 61, pp. 1364–82, Jul 2012.
- [119] F.-H. Lin, T. Witzel, S. P. Ahlfors, S. M. Stufflebeam, J. W. Belliveau, and M. S. Hämäläinen, “Assessing and improving the spatial accuracy in MEG source localization by depth-weighted minimum-norm estimates,” *Neuroimage*, vol. 31, pp. 160–71, May 2006.

-
- [120] R. D. Pascual-Marqui, C. M. Michel, and D. Lehmann, “Low resolution electromagnetic tomography: a new method for localizing electrical activity in the brain,” *Int J Psychophysiol*, vol. 18, pp. 49–65, Oct 1994.
- [121] R. D. Pascual-Marqui, “Standardized low-resolution brain electromagnetic tomography (sLORETA): technical details,” *Methods Find Exp Clin Pharmacol*, vol. 24 Suppl D, pp. 5–12, 2002.
- [122] R. Pascual-Marqui, “Discrete, 3D distributed, linear imaging methods of electric neuronal activity,” *Part 1: exact, zero error localization. arXiv: 0710.3341 [math-ph]*, <http://arxiv.org/pdf/0710.3341>, 2007.
- [123] M. Wagner, M. Fuchs, and J. Kastner, “SWARM: sLORETA-weighted accurate minimum norm inverse solutions,” in *International Congress Series*, vol. 1300, pp. 185–188, Elsevier, 2007.
- [124] J. Vrba and S. E. Robinson, “Signal processing in magnetoencephalography,” *Methods*, vol. 25, pp. 249–71, Oct 2001.
- [125] K. Sekihara, S. S. Nagarajan, D. Poeppel, A. Marantz, and Y. Miyashita, “Reconstructing spatio-temporal activities of neural sources using an MEG vector beamformer technique,” *IEEE Trans Biomed Eng*, vol. 48, pp. 760–71, Jul 2001.
- [126] D. Wipf and S. Nagarajan, “A unified Bayesian framework for MEG/EEG source imaging,” *Neuroimage*, vol. 44, pp. 947–66, Feb 2009.
- [127] D. Calvetti, H. Hakula, S. Pursiainen, and E. Somersalo, “Conditionally gaussian hypermodels for cerebral source localization,” *SIAM Journal on Imaging Sciences*, vol. 2, no. 3, pp. 879–909, 2009.
- [128] A. Galka, O. Yamashita, T. Ozaki, R. Biscay, and P. Valdés-Sosa, “A solution to the dynamical inverse problem of EEG generation using spatiotemporal Kalman filtering,” *Neuroimage*, vol. 23, pp. 435–53, Oct 2004.
- [129] U. Aydin and Y. S. Dogrusoz, “A Kalman filter-based approach to reduce the effects of geometric errors and the measurement noise in the inverse ECG problem,” *Med Biol Eng Comput*, vol. 49, pp. 1003–13, Sep 2011.
- [130] L. Hamid, Ü. Aydin, C. Wolters, U. Stephani, M. Siniatchkin, and A. Galka, “MEG-EEG fusion by Kalman filtering within a source analysis framework,” *Conf Proc IEEE Eng Med Biol Soc*, vol. 2013, pp. 4819–22, 2013.

-
- [131] V. Brodbeck, L. Spinelli, A. M. Lascano, M. Wissmeier, M.-I. Vargas, S. Vulliemoz, C. Pollo, K. Schaller, C. M. Michel, and M. Seeck, “Electroencephalographic source imaging: a prospective study of 152 operated epileptic patients,” *Brain*, vol. 134, pp. 2887–97, Oct 2011.
- [132] M. Fuchs, M. Wagner, and J. Kastner, “Development of volume conductor and source models to localize epileptic foci,” *J Clin Neurophysiol*, vol. 24, pp. 101–19, Apr 2007.
- [133] G. Huiskamp, M. Vroeiijstijn, R. van Dijk, G. Wieneke, and A. C. van Huffelen, “The need for correct realistic geometry in the inverse EEG problem,” *IEEE Trans Biomed Eng*, vol. 46, pp. 1281–7, Nov 1999.
- [134] B. J. Roth, D. Ko, I. R. von Albertini-Carletti, D. Scaffidi, and S. Sato, “Dipole localization in patients with epilepsy using the realistically shaped head model,” *Electroencephalogr Clin Neurophysiol*, vol. 102, pp. 159–66, Mar 1997.
- [135] M. Heers, T. Hedrich, D. An, F. Dubeau, J. Gotman, C. Grova, and E. Kobayashi, “Spatial correlation of hemodynamic changes related to interictal epileptic discharges with electric and magnetic source imaging,” *Hum Brain Mapp*, vol. 35, pp. 4396–414, Sep 2014.
- [136] T. Bast, O. Oezkan, S. Rona, C. Stippich, A. Seitz, A. Rupp, S. Fauser, J. Zentner, D. Rating, and M. Scherg, “EEG and MEG source analysis of single and averaged interictal spikes reveals intrinsic epileptogenicity in focal cortical dysplasia,” *Epilepsia*, vol. 45, pp. 621–31, Jun 2004.
- [137] Z. Agirre-Arrizubieta, N. J. Thai, A. Valentín, P. L. Furlong, S. Seri, R. P. Selway, R. D. C. Elwes, and G. Alarcón, “The value of magnetoencephalography to guide electrode implantation in epilepsy,” *Brain Topogr*, vol. 27, pp. 197–207, Jan 2014.
- [138] P. Boon, M. D’Havé, B. Vanrumste, G. Van Hoey, K. Vonck, P. Van Wallegghem, J. Caemaert, E. Achten, and J. De Reuck, “Ictal source localization in presurgical patients with refractory epilepsy,” *J Clin Neurophysiol*, vol. 19, pp. 461–8, Oct 2002.
- [139] J. S. Ebersole, “Non-invasive pre-surgical evaluation with EEG/MEG source analysis,” *Electroencephalogr Clin Neurophysiol Suppl*, vol. 50, pp. 167–74, 1999.

-
- [140] M. Gavaret, J.-M. Badier, P. Marquis, F. Bartolomei, and P. Chauvel, “Electric source imaging in temporal lobe epilepsy,” *J Clin Neurophysiol*, vol. 21, no. 4, pp. 267–82, 2004.
- [141] R. C. Knowlton, S. N. Razdan, N. Limdi, R. A. Elgavish, J. Killen, J. Blount, J. G. Burneo, L. Ver Hoef, L. Paige, E. Faught, P. Kankirawatana, A. Bartolucci, K. Riley, and R. Kuzniecky, “Effect of epilepsy magnetic source imaging on intracranial electrode placement,” *Ann Neurol*, vol. 65, pp. 716–23, Jun 2009.
- [142] E. Patarraia, G. Lindinger, L. Deecke, D. Mayer, and C. Baumgartner, “Combined MEG/EEG analysis of the interictal spike complex in mesial temporal lobe epilepsy,” *Neuroimage*, vol. 24, pp. 607–14, Feb 2005.
- [143] S. Rampp and H. Stefan, “Magnetoencephalography in presurgical epilepsy diagnosis,” *Expert Rev Med Devices*, vol. 4, pp. 335–47, May 2007.
- [144] K. A. Salayev, N. Nakasato, M. Ishitobi, H. Shamoto, A. Kanno, and K. Inuma, “Spike orientation may predict epileptogenic side across cerebral sulci containing the estimated equivalent dipole,” *Clin Neurophysiol*, vol. 117, pp. 1836–43, Aug 2006.
- [145] H. Stefan, C. Hummel, G. Scheler, A. Genow, K. Druschky, C. Tilz, M. Kaltenhäuser, R. Hopfengärtner, M. Buchfelder, and J. Romstöck, “Magnetic brain source imaging of focal epileptic activity: a synopsis of 455 cases,” *Brain*, vol. 126, pp. 2396–405, Nov 2003.
- [146] W. W. Sutherling, A. N. Mamelak, D. Thyerlei, T. Maleeva, Y. Minazad, L. Philpott, and N. Lopez, “Influence of magnetic source imaging for planning intracranial EEG in epilepsy,” *Neurology*, vol. 71, pp. 990–6, Sep 2008.
- [147] C. Baumgartner, G. Lindinger, A. Ebner, S. Aull, W. Serles, A. Olbrich, S. Lurger, T. Czech, R. Burgess, and H. Lüders, “Propagation of interictal epileptic activity in temporal lobe epilepsy,” *Neurology*, vol. 45, pp. 118–22, Jan 1995.
- [148] E. Patarraia, P. G. Simos, E. M. Castillo, R. L. Billingsley, S. Sarkari, J. W. Wheless, V. Maggio, W. Maggio, J. E. Baumgartner, P. R. Swank, J. I. Breier, and A. C. Papanicolaou, “Does magnetoencephalography add to scalp video-EEG as a diagnostic tool in epilepsy surgery?,” *Neurology*, vol. 62, pp. 943–8, Mar 2004.

-
- [149] R. Wennberg, T. Valiante, and D. Cheyne, “EEG and MEG in mesial temporal lobe epilepsy: where do the spikes really come from?,” *Clin Neurophysiol*, vol. 122, pp. 1295–313, Jul 2011.
- [150] H. Otsubo, A. Ochi, I. Elliott, S. H. Chuang, J. T. Rutka, V. Jay, M. Aung, D. F. Sobel, and O. C. Snead, “MEG predicts epileptic zone in lesional extrahippocampal epilepsy: 12 pediatric surgery cases,” *Epilepsia*, vol. 42, pp. 1523–30, Dec 2001.
- [151] S. Chitoku, H. Otsubo, T. Ichimura, T. Saigusa, A. Ochi, A. Shirasawa, K.-i. Kamijo, T. Yamazaki, E. Pang, J. T. Rutka, S. K. Weiss, and O. C. Snead, “Characteristics of dipoles in clustered individual spikes and averaged spikes,” *Brain Dev*, vol. 25, pp. 14–21, Jan 2003.
- [152] R. A. Chowdhury, J. M. Lina, E. Kobayashi, and C. Grova, “MEG source localization of spatially extended generators of epileptic activity: comparing entropic and hierarchical Bayesian approaches,” *PLoS One*, vol. 8, no. 2, p. e55969, 2013.
- [153] M. Scherg, T. Bast, and P. Berg, “Multiple source analysis of interictal spikes: goals, requirements, and clinical value,” *J Clin Neurophysiol*, vol. 16, pp. 214–24, May 1999.
- [154] G. Lantz, L. Spinelli, M. Seeck, R. G. de Peralta Menendez, C. C. Sottas, and C. M. Michel, “Propagation of interictal epileptiform activity can lead to erroneous source localizations: a 128-channel EEG mapping study,” *J Clin Neurophysiol*, vol. 20, no. 5, pp. 311–9, 2003.
- [155] M. Lau, D. Yam, and J. G. Burneo, “A systematic review on MEG and its use in the presurgical evaluation of localization-related epilepsy,” *Epilepsy Res*, vol. 79, pp. 97–104, May 2008.
- [156] Z.-P. Liang and P. C. Lauterbur, *Principles of magnetic resonance imaging*. SPIE Optical Engineering Press, 2000.
- [157] P. Sprawls, *Magnetic resonance imaging: principles, methods, and techniques*. Medical Physics Publishing, 2000.
- [158] K. K. Shung, M. Smith, and B. M. Tsui, *Principles of medical imaging*. Academic Press, 1992.
- [159] F. Bloch, “Nuclear induction,” *Physical review*, vol. 70, no. 7-8, p. 460, 1946.

-
- [160] E. M. Purcell, H. Torrey, and R. V. Pound, "Resonance absorption by nuclear magnetic moments in a solid," *Physical review*, vol. 69, no. 1-2, p. 37, 1946.
- [161] L. Ruthotto, H. Kugel, J. Olesch, B. Fischer, J. Modersitzki, M. Burger, and C. H. Wolters, "Diffeomorphic susceptibility artifact correction of diffusion-weighted magnetic resonance images," *Phys Med Biol*, vol. 57, pp. 5715–31, Sep 2012.
- [162] S. M. Smith, "Fast robust automated brain extraction," *Hum Brain Mapp*, vol. 17, pp. 143–55, Nov 2002.
- [163] M. Jenkinson, M. Pechaud, and S. Smith, "BET2: MR-based estimation of brain, skull and scalp surfaces," in *Eleventh annual meeting of the organization for human brain mapping*, vol. 17, 2005.
- [164] Y. Zhang, M. Brady, and S. Smith, "Segmentation of brain MR images through a hidden Markov random field model and the expectation-maximization algorithm," *IEEE Trans Med Imaging*, vol. 20, pp. 45–57, Jan 2001.
- [165] M. Oozeer, C. Veraart, V. Legat, and J. Delbeke, "Simulation of intra-orbital optic nerve electrical stimulation," *Med Biol Eng Comput*, vol. 43, pp. 608–17, Sep 2005.
- [166] C. Ramon, P. Garguilo, E. A. Fridgerisson, and J. Haueisen, "Changes in scalp potentials and spatial smoothing effects of inclusion of dura layer in human head models for EEG simulations," *Front Neuroeng*, vol. 7, p. 32, 2014.
- [167] M. W. Slutzky, L. R. Jordan, T. Krieg, M. Chen, D. J. Mogul, and L. E. Miller, "Optimal spacing of surface electrode arrays for brain-machine interface applications," *J Neural Eng*, vol. 7, p. 26004, Apr 2010.
- [168] T. E. J. Behrens, M. W. Woolrich, M. Jenkinson, H. Johansen-Berg, R. G. Nunes, S. Clare, P. M. Matthews, J. M. Brady, and S. M. Smith, "Characterization and propagation of uncertainty in diffusion-weighted MR imaging," *Magn Reson Med*, vol. 50, pp. 1077–88, Nov 2003.
- [169] S. Homma, T. Musha, Y. Nakajima, Y. Okamoto, S. Blom, R. Flink, and K. E. Hagbarth, "Conductivity ratios of the scalp-skull-brain head model in estimating equivalent dipole sources in human brain," *Neurosci Res*, vol. 22, pp. 51–5, Mar 1995.

-
- [170] Y. Lai, W. van Drongelen, L. Ding, K. E. Hecox, V. L. Towle, D. M. Frim, and B. He, “Estimation of in vivo human brain-to-skull conductivity ratio from simultaneous extra- and intra-cranial electrical potential recordings,” *Clin Neurophysiol*, vol. 116, pp. 456–65, Feb 2005.
- [171] R. Hoekema, G. H. Wieneke, F. S. S. Leijten, C. W. M. van Veelen, P. C. van Rijen, G. J. M. Huiskamp, J. Ansems, and A. C. van Huffelen, “Measurement of the conductivity of skull, temporarily removed during epilepsy surgery,” *Brain Topogr*, vol. 16, no. 1, pp. 29–38, 2003.
- [172] H. S. Wilson, “Continuous head-localization and data correction in a whole-cortex MEG sensor,” *Neurol Clin Neurophysiol*, vol. 2004, p. 56, 2004.
- [173] P. Küpper, “Combined EEG and MEG for improving source analysis in patients with focal epilepsy,” Master’s thesis, Beuth Hochschule für Technik Berlin, 2012.
- [174] C. H. Wolters, R. F. Beckmann, A. Rienäcker, and H. Buchner, “Comparing regularized and non-regularized nonlinear dipole fit methods: a study in a simulated sulcus structure,” *Brain Topogr*, vol. 12, no. 1, pp. 3–18, 1999.
- [175] S. Lew, C. H. Wolters, A. Anwander, S. Makeig, and R. S. MacLeod, “Improved EEG source analysis using low-resolution conductivity estimation in a four-compartment finite element head model,” *Hum Brain Mapp*, vol. 30, pp. 2862–78, Sep 2009.
- [176] C. H. Wolters, S. Lew, R. S. MacLeod, and M. Hämäläinen, “Combined EEG/MEG source analysis using calibrated finite elementhead models,” in *Proceedings of the 4th Annual Conference of the German Society for Biomedical Engineering (DGBMT’10)*, 2010.
- [177] A. Kumar, A. Bhattacharya, and N. Makhija, “Evoked potential monitoring in anaesthesia and analgesia,” *Anaesthesia*, vol. 55, no. 3, pp. 225–241, 2000.
- [178] J. S. Ebersole and S. M. Ebersole, “Combining MEG and EEG source modeling in epilepsy evaluations,” *J Clin Neurophysiol*, vol. 27, pp. 360–71, Dec 2010.
- [179] D. Güllmar, J. Haueisen, and J. R. Reichenbach, “Influence of anisotropic electrical conductivity in white matter tissue on the EEG/MEG forward and inverse solution. a high-resolution whole head simulation study,” *Neuroimage*, vol. 51, pp. 145–63, May 2010.

-
- [180] Z. Akalin Acar and S. Makeig, “Effects of forward model errors on EEG source localization,” *Brain Topogr*, vol. 26, pp. 378–96, Jul 2013.
- [181] M. Scherg, N. Ille, H. Bornfleth, and P. Berg, “Advanced tools for digital EEG review: virtual source montages, whole-head mapping, correlation, and phase analysis,” *J Clin Neurophysiol*, vol. 19, pp. 91–112, Apr 2002.
- [182] S. Gonçalves, J. C. de Munck, R. M. Heethaar, F. H. Lopes da Silva, and B. W. van Dijk, “The application of electrical impedance tomography to reduce systematic errors in the EEG inverse problem—a simulation study,” *Physiol Meas*, vol. 21, pp. 379–93, Aug 2000.
- [183] Ü. Aydin, J. Vorwerk, M. Dümpelmann, P. Küpper, M. Heers, H. Kugel, J. Wellmer, C. Kellinghaus, J. Haueisen, S. Rampp, H. Stefan, and C. H. Wolters, “Combined EEG/MEG can outperform single modality EEG or MEG source reconstruction in presurgical epilepsy diagnosis,” *PLoS One*, vol. -, no. -, accepted for publication, Jan. 2015.
- [184] I. Merlet, L. Garcia-Larrea, P. Ryvlin, J. Isnard, M. Sindou, and F. Mauguière, “Topographical reliability of mesio-temporal sources of interictal spikes in temporal lobe epilepsy,” *Electroencephalogr Clin Neurophysiol*, vol. 107, pp. 206–12, Sep 1998.
- [185] D. Zumsteg, A. Friedman, H. G. Wieser, and R. A. Wennberg, “Propagation of interictal discharges in temporal lobe epilepsy: correlation of spatiotemporal mapping with intracranial foramen ovale electrode recordings,” *Clin Neurophysiol*, vol. 117, pp. 2615–26, Dec 2006.
- [186] J. M. Badier and P. Chauvel, “Spatio-temporal characteristics of paroxysmal interictal events in human temporal lobe epilepsy,” *J Physiol Paris*, vol. 89, no. 4-6, pp. 255–64, 1995.
- [187] C. Plummer, M. Wagner, M. Fuchs, A. S. Harvey, and M. J. Cook, “Dipole versus distributed EEG source localization for single versus averaged spikes in focal epilepsy,” *J Clin Neurophysiol*, vol. 27, pp. 141–62, Jun 2010.
- [188] J. C. Mosher, M. E. Spencer, R. M. Leahy, and P. S. Lewis, “Error bounds for EEG and MEG dipole source localization,” *Electroencephalogr Clin Neurophysiol*, vol. 86, pp. 303–21, May 1993.

-
- [189] M. Fuchs, M. Wagner, and J. Kastner, “Confidence limits of dipole source reconstruction results,” *Clin Neurophysiol*, vol. 115, pp. 1442–51, Jun 2004.
- [190] A. G. Guggisberg, H. E. Kirsch, M. M. Mantle, N. M. Barbaro, and S. S. Nagarajan, “Fast oscillations associated with interictal spikes localize the epileptogenic zone in patients with partial epilepsy,” *Neuroimage*, vol. 39, pp. 661–8, Jan 2008.
- [191] A. C. Papanicolaou, E. Pataraiia, R. Billingsley-Marshall, E. M. Castillo, J. W. Wheless, P. Swank, J. I. Breier, S. Sarkari, and P. G. Simos, “Toward the substitution of invasive electroencephalography in epilepsy surgery,” *J Clin Neurophysiol*, vol. 22, pp. 231–7, Aug 2005.
- [192] A. Crouzeix, B. Yvert, O. Bertrand, and J. Pernier, “An evaluation of dipole reconstruction accuracy with spherical and realistic head models in MEG,” *Clin Neurophysiol*, vol. 110, pp. 2176–88, Dec 1999.
- [193] M. Dannhauer, E. Lämmel, C. H. Wolters, and T. R. Knösche, “Spatio-temporal regularization in linear distributed source reconstruction from EEG/MEG: a critical evaluation,” *Brain Topogr*, vol. 26, pp. 229–46, Apr 2013.
- [194] R. Bouet, J. Jung, C. Delpuech, P. Ryvlin, J. Isnard, M. Guenot, O. Bertrand, and F. Mauguière, “Towards source volume estimation of interictal spikes in focal epilepsy using magnetoencephalography,” *Neuroimage*, vol. 59, pp. 3955–66, Feb 2012.
- [195] C. Ramon, “Effect of dura layer on scalp EEG simulations,” *International Journal of Bioelectromagnetism*, vol. 14, no. 1, pp. 27–28, 2012.
- [196] T. E. J. Behrens, H. J. Berg, S. Jbabdi, M. F. S. Rushworth, and M. W. Woolrich, “Probabilistic diffusion tractography with multiple fibre orientations: What can we gain?,” *Neuroimage*, vol. 34, pp. 144–55, Jan 2007.
- [197] N. Tanaka, P. E. Grant, N. Suzuki, J. R. Madsen, A. M. Bergin, M. S. Hämäläinen, and S. M. Stuffebeam, “Multimodal imaging of spike propagation: a technical case report,” *AJNR Am J Neuroradiol*, vol. 33, pp. E82–4, Jun 2012.
- [198] Z. I. Wang, K. Jin, Y. Kakisaka, J. C. Mosher, W. E. Bingaman, P. Kotagal, R. C. Burgess, I. M. Najm, and A. V. Alexopoulos, “Imag(in)ing seizure propagation: MEG-guided interpretation of epileptic activity from a deep source,” *Hum Brain Mapp*, vol. 33, pp. 2797–801, Dec 2012.

-
- [199] N. Forss, R. Salmelin, and R. Hari, "Comparison of somatosensory evoked fields to airpuff and electric stimuli," *Electroencephalogr Clin Neurophysiol*, vol. 92, pp. 510–7, Nov 1994.
- [200] C. Pantev, M. Hoke, B. Lütkenhöner, and K. Lehnertz, "Tonotopic organization of the auditory cortex: pitch versus frequency representation," *Science*, vol. 246, pp. 486–8, Oct 1989.
- [201] C. Pantev, L. E. Roberts, T. Elbert, B. Ross, and C. Wienbruch, "Tonotopic organization of the sources of human auditory steady-state responses," *Hear Res*, vol. 101, pp. 62–74, Nov 1996.
- [202] K. Yamashiro, K. Inui, N. Otsuru, and R. Kakigi, "Change-related responses in the human auditory cortex: an MEG study," *Psychophysiology*, vol. 48, pp. 23–30, Jan 2011.
- [203] J. Hine and S. Debener, "Late auditory evoked potentials asymmetry revisited," *Clin Neurophysiol*, vol. 118, pp. 1274–85, Jun 2007.
- [204] I. Ozaki, Y. Suzuki, C. Y. Jin, M. Baba, M. Matsunaga, and I. Hashimoto, "Dynamic movement of N100m dipoles in evoked magnetic field reflects sequential activation of isofrequency bands in human auditory cortex," *Clin Neurophysiol*, vol. 114, pp. 1681–8, Sep 2003.
- [205] B. Yvert, A. Crouzeix, O. Bertrand, A. Seither-Preisler, and C. Pantev, "Multiple supratemporal sources of magnetic and electric auditory evoked middle latency components in humans," *Cereb Cortex*, vol. 11, pp. 411–23, May 2001.
- [206] C. Y. Jin, I. Ozaki, Y. Suzuki, M. Baba, and I. Hashimoto, "Dynamic movement of N100m current sources in auditory evoked fields: comparison of ipsilateral versus contralateral responses in human auditory cortex," *Neurosci Res*, vol. 60, pp. 397–405, Apr 2008.
- [207] P. Sörös, R. Dzierwas, E. Manemann, I. K. Teismann, and B. Lütkenhöner, "No indication of brain reorganization after unilateral ischemic lesions of the auditory cortex," *Neurology*, vol. 67, pp. 1059–61, Sep 2006.
- [208] A. Kanno, N. Nakasato, K. Nagamatsu, M. Iwasaki, K. Hatanaka, N. Murayama, and T. Yoshimoto, "Comparison of source localization for the P30m, P50m, and N100m peaks," *Helsinki University of Technology*, pp. 25–28, 2001.

-
- [209] C. Alain, A. Roze, and S. R. Arnott, “Chapter 9 - middle- and long-latency auditory evoked potentials: what are they telling us on central auditory disorders?,” in *Disorders of Peripheral and Central Auditory Processing* (G. G. Celesia, ed.), vol. 10 of *Handbook of Clinical Neurophysiology*, pp. 177 – 199, Elsevier, 2013.
- [210] J. P. Mäkelä, R. Hari, L. Valanne, and A. Ahonen, “Auditory evoked magnetic fields after ischemic brain lesions,” *Ann Neurol*, vol. 30, pp. 76–82, Jul 1991.
- [211] C. Pantev, O. Bertrand, C. Eulitz, C. Verkindt, S. Hampson, G. Schuierer, and T. Elbert, “Specific tonotopic organizations of different areas of the human auditory cortex revealed by simultaneous magnetic and electric recordings,” *Electroencephalogr Clin Neurophysiol*, vol. 94, pp. 26–40, Jan 1995.
- [212] C. Liégeois-Chauvel, A. Musolino, J. M. Badier, P. Marquis, and P. Chauvel, “Evoked potentials recorded from the auditory cortex in man: evaluation and topography of the middle latency components,” *Electroencephalogr Clin Neurophysiol*, vol. 92, pp. 204–14, May 1994.
- [213] H. v. Helmholtz, “Ueber einige gesetze der vertheilung elektrischer ströme in körperlichen leitern mit anwendung auf die thierisch-elektrischen versuche,” *Annalen der Physik*, vol. 165, no. 6, pp. 211–233, 1853.
- [214] S. Wagner, *An adjoint FEM approach for the EEG forward problem*. PhD thesis, Diploma Thesis (Mathematics), Institute for Biomagnetism and Biosignalanalysis and Institute for Computational and Applied Mathematics, University of Muenster, 2011.
- [215] K. R. Connolly, A. Helmer, M. A. Cristancho, P. Cristancho, and J. P. O’Reardon, “Effectiveness of transcranial magnetic stimulation in clinical practice post-FDA approval in the United States: results observed with the first 100 consecutive cases of depression at an academic medical center,” *J Clin Psychiatry*, vol. 73, pp. e567–73, Apr 2012.
- [216] S. Wagner, S. M. Rampersad, Ü. Aydin, J. Vorwerk, T. F. Oostendorp, T. Neuling, C. S. Herrmann, D. F. Stegeman, and C. H. Wolters, “Investigation of tDCS volume conduction effects in a highly realistic head model,” *J Neural Eng*, vol. 11, p. 016002, Feb 2014.
- [217] A. R. Brunoni, M. A. Nitsche, N. Bolognini, M. Bikson, T. Wagner, L. Merabet, D. J. Edwards, A. Valero-Cabre, A. Rotenberg, A. Pascual-Leone, R. Ferrucci,

- A. Priori, P. S. Boggio, and F. Fregni, “Clinical research with transcranial direct current stimulation (tDCS): challenges and future directions,” *Brain Stimul*, vol. 5, pp. 175–95, Jul 2012.
- [218] C. S. Herrmann, S. Rach, T. Neuling, and D. Strüber, “Transcranial alternating current stimulation: a review of the underlying mechanisms and modulation of cognitive processes,” *Front Hum Neurosci*, vol. 7, p. 279, 2013.
- [219] S. Ozen, A. Sirota, M. A. Belluscio, C. A. Anastassiou, E. Stark, C. Koch, and G. Buzsáki, “Transcranial electric stimulation entrains cortical neuronal populations in rats,” *J Neurosci*, vol. 30, pp. 11476–85, Aug 2010.
- [220] S. M. Rampersad, A. M. Janssen, F. Lucka, Ü. Aydin, B. Lanfer, S. Lew, C. H. Wolters, D. F. Stegeman, and T. F. Oostendorp, “Simulating transcranial direct current stimulation with a detailed anisotropic human head model,” *IEEE Trans Neural Syst Rehabil Eng*, vol. 22, pp. 441–52, May 2014.
- [221] A. M. Janssen, S. M. Rampersad, F. Lucka, B. Lanfer, S. Lew, U. Aydin, C. H. Wolters, D. F. Stegeman, and T. F. Oostendorp, “The influence of sulcus width on simulated electric fields induced by transcranial magnetic stimulation,” *Phys Med Biol*, vol. 58, pp. 4881–96, Jul 2013.
- [222] T. Zaehle, S. Rach, and C. S. Herrmann, “Transcranial alternating current stimulation enhances individual alpha activity in human EEG,” *PLoS One*, vol. 5, no. 11, p. e13766, 2010.
- [223] A. Datta, J. M. Baker, M. Bikson, and J. Fridriksson, “Individualized model predicts brain current flow during transcranial direct-current stimulation treatment in responsive stroke patient,” *Brain Stimul*, vol. 4, pp. 169–74, Jul 2011.
- [224] R. Salvador, A. Mekonnen, G. Ruffini, and P. C. Miranda, “Modeling the electric field induced in a high resolution realistic head model during transcranial current stimulation,” *Conf Proc IEEE Eng Med Biol Soc*, vol. 2010, pp. 2073–6, 2010.
- [225] F. Klauschen, A. Goldman, V. Barra, A. Meyer-Lindenberg, and A. Lunder-vold, “Evaluation of automated brain MR image segmentation and volumetry methods,” *Hum Brain Mapp*, vol. 30, pp. 1310–27, Apr 2009.
- [226] C. Ramon and M. D. Holmes, “Spatiotemporal phase clusters and phase synchronization patterns derived from high density EEG and ECoG recordings,” *Curr Opin Neurobiol*, vol. 31C, pp. 127–132, Oct 2014.

-
- [227] S. S. Dalal, S. Rampp, F. Willomitzer, and S. Ettl, “Consequences of EEG electrode position error on ultimate beamformer source reconstruction performance,” *Front Neurosci*, vol. 8, p. 42, 2014.
- [228] M. Theiß, “Registration of MRI and MEG data,” Master’s thesis, (Supervisors: Brinck H, Wolters, CH) Fachbereich Elektrotechnik und angewandte Naturwissenschaften, Westfälische Hochschule, 2014.
- [229] P. Reipke, “Development of an application for MEG/MRI co-registration,” Master’s thesis, (Supervisors: Brinck H, Wolters, CH) Fachbereich Elektrotechnik und angewandte Naturwissenschaften, Westfälische Hochschule, 2014.
- [230] P. Reipke, M. Theiß, Ü. Aydin, A. Wollbrink, C. Wolters, and H. Brinck, “Improving the MEG-MRI co-registration,” in *Innovative Verarbeitung bioelektrischer und biomagnetischer Signale (BBS2014)*, (Berlin), April 10-11 2014.
- [231] F. Willomitzer, S. Ettl, O. Arold, and G. Häusler, “Flying triangulation—a motion-robust optical 3D sensor for the real-time shape acquisition of complex objects,” in *AIP Conf. Proc.*, vol. 1537, pp. 19–26, 2013.
- [232] A. Sadeghzadeh, “Head tracking during magnetoencephalography (MEG) data recording via “flying triangulation,” Master’s thesis, (Supervisors: Ettl, S and Rampp, S) Friedrich-Alexander-Universität Erlangen-Nürnberg, 2013.
- [233] B. Lanfer, C. Röer, M. Scherg, S. Rampp, C. Kellinghaus, and C. Wolters, “Influence of a silastic ECoG grid on EEG/ECoG based source analysis,” *Brain Topogr*, vol. 26, pp. 212–28, Apr 2013.

Scientific Contributions

Journal Publications

1. **Aydin, Ü.**, Vorwerk, J., Dümpelmann, M., Küpper, P., Kugel, H., Heers, M., Wellmer, J., Kellinghaus, C., Haueisen, J., Rampp, S., Stefan, H., Wolters, C.H. (accepted for publication, Jan. 6, 2015) Combined EEG/MEG can outperform single modality EEG or MEG source reconstruction in presurgical epilepsy diagnosis. PLoS ONE.
2. **Aydin, Ü.**, Vorwerk, J., Küpper, P., Heers, M., Kugel, H., Galka, A., Hamid, L., Wellmer, J., Kellinghaus, C., Rampp, S., Wolters, C.H. (2014) Combining EEG and MEG for the reconstruction of epileptiform activity using a calibrated realistic volume conductor model of the patients head. PLoS ONE 9(3).
3. Rampersad, S.M., Janssen, A.M., Lucka, F., **Aydin, Ü.**, Lanfer, B., Lew, S., Wolters, C.H., Stegeman, D.F., Oostendorp, T.F. (2014) Simulating transcranial direct current stimulation with a detailed anisotropic human head model. IEEE Trans. Neur. Sys. and Rehab. Eng., 22(3), pp. 441-452.
4. Wagner, S., Rampersad, S.M, **Aydin, Ü.**, Vorwerk, J., Oostendorp, T.F., Neuling, T., Hermann, C.S., Stegeman, D.F., Wolters, C.H. (2014). Investigation of tDCS/tACS volume conduction effects in a highly realistic head model. J. Neural Eng., 11:016002(14pp).
5. Janssen, A.M., Rampersad, S.M., Lucka, F., Lanfer, B., Lew, S., **Aydin, Ü.**, Wolters, C.H., Stegeman, D.F., Oostendorp, T.F. (2013) The influence of cortical surface geometry on simulated electric fields induced by transcranial magnetic stimulation. Phys. Med. Biol., 58(14), pp.4881-4896.

Peer-reviewed proceedings

1. Hamid, L., **Aydin, Ü.**, Wolters, C. H., Stephani, U., Siniatchkin, M., Galka, A. MEG-EEG Fusion by Kalman Filtering within a Source Analysis Framework. 35th Ann. Int. IEEE EMBS Conference, Osaka, Japan, (2013).

Invited talks

1. Combined EEG/MEG can outperform single modality EEG or MEG source analysis in presurgical epilepsy diagnosis. German EEG/EP mapping meeting (2014).

Abstracts

1. **Aydin Ü.**, Vorwerk J., Dümpelmann M., Küpper P., Kugel H., Wellmer J., Kellinghaus C., Haueisen J., Rampp S., Stefan H., Wolters, C.H. Combined EEG/MEG can outperform single modality EEG or MEG source reconstruction in presurgical epilepsy diagnosis. 19th Int. Conf. on Biomagnetism (BIOMAG), Halifax, Canada (2014).
2. **Aydin Ü.**, Vorwerk J., Dümpelmann M., Küpper P., Kugel H., Wellmer J., Kellinghaus C., Haueisen J., Rampp S., Stefan H., Wolters, C.H., Comparison of EEG, MEG and Combined EEG/MEG Localizations of Epileptic Activity Based on Subaverages. 20th Annual Meeting of the Organization for Human Brain Mapping, Hamburg, Germany (2014).
3. **Aydin Ü.**, Vorwerk J., Dümpelmann M., Küpper P., Kugel H., Wellmer J., Kellinghaus C., Haueisen J., Rampp S., Stefan H., Wolters, C.H. Effects of Spike Averaging on EEG, MEG and Combined EEG/MEG Source Analysis of Epileptic Activity. 30th Int. Cong. on Clinical Neurophysiology (ICCN), Berlin, Germany (2014).
4. **Aydin Ü.**, Vorwerk J., Küpper P., Heers, M., Kugel, H., Wellmer J., Kellinghaus C., Scherg M., Rampp S., Wolters C. Combined EEG/MEG Source Analysis of Epileptic Activity: Effects of Volume Conduction and Spike Averaging. First Int. Conf. on Basic and Clinical multimodal Imaging (BaCI), Geneva, Switzerland (2013).

5. Lucka F., **Aydin Ü.**, Vorwerk J., Burger M., Wolters C.H. Hierarchical Fully-Bayesian Inference for Combined EEG/MEG Source Analysis of Evoked Responses: From Simulations to Real Data. First Int. Conf. on Basic and Clinical multimodal Imaging (BaCI), Geneva, Switzerland (2013).
6. Wagner S., **Aydin Ü.**, Vorwerk J., Herrmann, C., Burger M., Wolters C.H. Volume conduction and optimized stimulation protocols in transcranial current stimulation. First Int. Conf. on Basic and Clinical multimodal Imaging (BaCI), Geneva, Switzerland (2013).
7. Heers M., Jacobs-Le Van J., Hirschmann J., Dümpelmann M., **Aydin Ü.**, Wolters C., Rampp S., Stefan H., Schnitzler A., Wellmer J. Spike associated high frequency oscillations in magnetoencephalography co-localize with focal cortical dysplasia type IIB. 30th Int. Epilepsy Cong., Montreal, Canada (2013).
8. Wagner S., Rampersad S., **Aydin Ü.**, Vorwerk J., Neuling T., Herrmann C.S., Stegeman D.F., Wolters C.H. Volume conduction effects in tDCS using a 1mm geometry-adapted hexahedral Finite element head model. Biomedical Engineering, 57(Suppl.1), p.329 (2012).
9. **Aydin Ü.**, Vorwerk J., Lucka F., Rampp S., Heers M., Kellinghaus C., Wellmer J., Stefan H. Wolters C.H. Combined EEG and MEG Source Analysis of Epileptic Activity. 18th Int. Conf. on Biomagnetism (BIOMAG), Paris, France (2012).
10. **Aydin Ü.**, Vorwerk J., Lucka F., Pantev C., Wolters C.H. Combining EEG and MEG to Study Auditory Tonotopy. 18th Int. Conf. on Biomagnetism (BIOMAG), Paris, France (2012).

Oral presentations on conferences

1. **Aydin Ü.**, Vorwerk J., Küpper P., Heers, M., Kugel, H., Wellmer J., Kellinghaus C., Scherg M., Rampp S., Wolters C. Combined EEG/MEG Source Analysis of Epileptic Activity: Effects of Volume Conduction and Spike Averaging. First Int. Conf. on Basic and Clinical multimodal Imaging (BaCI), Geneva, Switzerland (2013).

Poster presentations on conferences

1. **Aydin Ü.**, Vorwerk J., Dümpelmann M., Küpper P., Kugel H., Wellmer J., Kellinghaus C., Haueisen J., Rampp S., Stefan H., Wolters, C.H., Comparison of EEG, MEG and Combined EEG/MEG Localizations of Epileptic Activity Based on Subaverages. 20th Annual Meeting of the Organization for Human Brain Mapping, Hamburg, Germany (2014).
2. **Aydin Ü.**, Vorwerk J., Dümpelmann M., Küpper P., Kugel H., Wellmer J., Kellinghaus C., Haueisen J., Rampp S., Stefan H., Wolters, C.H. Effects of Spike Averaging on EEG, MEG and Combined EEG/MEG Source Analysis of Epileptic Activity. 30th Int. Cong. on Clinical Neurophysiology (ICCN), Berlin, Germany (2014).
3. **Aydin Ü.**, Vorwerk J., Lucka F., Rampp S., Heers M., Kellinghaus C., Wellmer J., Stefan H. Wolters C.H. Combined EEG and MEG Source Analysis of Epileptic Activity. 18th Int. Conf. on Biomagnetism (BIOMAG), Paris, France (2012).
4. **Aydin Ü.**, Vorwerk J., Lucka F., Pantev C., Wolters C.H. Combining EEG and MEG to Study Auditory Tonotopy. 18th Int. Conf. on Biomagnetism (BIOMAG), Paris, France (2012).

Erklärung

Ich versichere, dass ich die vorliegende Arbeit ohne unzulässige Hilfe Dritter und ohne Benutzung anderer als der angegebenen Hilfsmittel angefertigt habe. Die aus anderen Quellen direkt oder indirekt übernommenen Daten und Konzepte sind unter Angabe der Quelle gekennzeichnet.

Weitere Personen waren an der inhaltlich-materiellen Erstellung der vorliegenden Arbeit nicht beteiligt. Insbesondere habe ich hierfür nicht die entgeltliche Hilfe von Vermittlungs- bzw. Beratungsdiensten (Promotionsberater oder anderer Personen) in Anspruch genommen. Niemand hat von mir unmittelbar oder mittelbar geldwerte Leistungen für Arbeiten erhalten, die im Zusammenhang mit dem Inhalt der vorgelegten Dissertation stehen.

Die Arbeit wurde bisher weder im In- noch im Ausland in gleicher oder ähnlicher Form einer Prüfungsbehörde vorgelegt. Ich bin darauf hingewiesen worden, dass die Unrichtigkeit der vorstehenden Erklärung als Täuschungsversuch bewertet wird und gemäß § 7 Abs. 10 der Promotionsordnung den Abbruch des Promotionsverfahrens zur Folge hat.

Ilmenau, den 12.01.2015

Ümit Aydın